Modeling and Torque Control Implementation for an 8/6 Switched Reluctance Motor

By Sen Wang
University of KwaZulu-Natal
2006

Submitted in fulfillment of the academic requirement for the degree of Master of Science in Engineering in the School of Electrical, Electronic and Computer Engineering, University of KwaZulu-Natal in South Africa, 2006

PREFACE

The research work in this dissertation was performed by Sen Wang, under the supervision of supervisor Mr. Bruce Burton and co-supervisor Professor Ron Harley at the school of Electrical, Electronic and Computer Engineering, University of KwaZulu-Natal.

This work was partially supported by the National Research Foundation (NRF), the Eskom Tertiary Education Support Programme (TESP), the South African Technology and Human Resources for Industry Programme (THRIP), the University of Arkansas (USA), and the Baldor Motor Corporation (USA).

Parts of this dissertation have been presented by the author at the SAUPEC'04 conference at the University of Stellenbosh, South Africa, IEEE AFRICON 2004 in Botswana and the SAUPEC'05 conference at the University of the Witwatersrand, Johannesburg, South Africa. One conference paper has been accepted as a journal paper for the Transactions of the SAIEE (The South African Institute of Electrical Engineers).

The entire dissertation, unless specifically indicated to the contrary in the text, is the author's own work and has not been submitted in whole or in part to any other university.

ABSTRACT

This thesis begins with a brief introduction of the basic principles of operation of SRMs, and explains how flux characteristics are derived from voltage and current measurements, and presents results obtained from an 8/6 SRM. Torque characteristics are derived from these flux characteristics using both the inductance and co-energy methods. Comparison of these results with direct torque measurements shows that the co-energy method is significantly more accurate than the inductance method. Electrical and mechanical simulation models are derived from inductance and torque characteristics, and implemented in Matlab/Simulink. Simulated results are shown to agree with measurements obtained from physical locked and free rotor alignment experiments. These models are also used to illustrate the need for sophisticated commutation strategies and high performance current control loops to achieve low ripple torque control.

The Matlab/Simulink models are transferred to PSCAD to compare the current control abilities, cost, complexity and robustness of the Asymmetrical Half Bridge (AHB), n+1 switch, and C-dump SRM converter topologies. The relatively high cost of the AHB converter is justified in terms of its robustness, simplicity and superior capabilities for current and torque control. The torque sharing function commutation strategy for low ripple torque control is presented and simulated with hysteresis current control for the 8/6 SRM fed from a four phase AHB converter.

A DSP implementation of the current and torque control loops is also presented and tested under various dynamic speed and load conditions and recommendations are made for future work.

ACKNOWLEDGEMENTS

I would like to give a special thanks to Mr. Bruce Burton as my supervisor for his encouragement, guidance, patience and constant support through my studies.

I also wish to thank:

- My parents and friends for their constant support and encouragement through good and bad times
- James Ireland for his assistance and technical advice on DSP
- My colleagues: Rao, Rudy, Jayesh, Lance and Jerry for their encouragement and advice
- The workshop staff, especially Mr. Roos, Mr Munnik, Swanni, Bazil and Innocent for their assistance with hardware setup and mechanical work
- Larisha Soodhoo for counselling

Thanks also go to School of Electrical, Electronic and Computer Engineering, the National Research Foundation (NRF), the Eskom Tertiary Education Support Programme (TESP), the South African Technology and Human Resources for Industry Programme (THRIP), the University of Arkansas (USA), and the Baldor Motor Corporation (USA). Without their financial support, this work would not have been possible.

TABLE OF CONTENTS

CHAPTER 3 POWER CONVERTER STRATEGIES FOR SRM

LIST OF FIGURES AND TABLES

FIGURES

CHAPTER 2

CHAPTER 3

CHAPTER 4

CHAPTER 5

TABLES

LIST OF ABBREVIATIONS AND SYMBOLS

ABBREVIATIONS

ADC	Analogue-to-Digital Converter
ANSI	American National Standards Institute
AHB	Asymmetrical half bridge
DC	Direct Current
DSP	Digital System Processor
EMTDC	Electromagnetic Transients including DC
EVA	Event Manger A
EVB	Event Manger B
IDE	Integrated Development Environment
IGBT	Insulated Gate Bipolar Transistor
JTAG	Joint Test Action Group
MOSFET	Metal-Oxide-Semiconductor Field Effect Transistor
PSCAD	Power Systems CAD
PWM	Pulse Width Modulation
RAM	Random Access Memory
SCI	Serial Communications Interface
SRM	Switched Reluctance Motor
TSF	Torque Sharing Function

SYMBOLS

Switched Reluctance Motor Related Symbols

8/6	8 stators and 6 rotors
S1, S2, S3, S4, S1', S2', S3', S4'	Stator poles 1, 2,3,4,5,6,7,8
S1-S1'	Phase 1
S2-S2'	Phase 2
S3-S3'	Phase 3

S4-S4'	Phase 4
$\Re$	Reluctance
φ	Flux
μ	Permeability of the magnetic material
l	Length of magnetic path
B	flux density
S	cross section area of magnetic path
λ	Flux linkage
i	phase current
N	number of turns per phase
R	phase resistance
$\lambda(\theta,i)$	Magnetic Flux
$L(\theta,i)$	Inductance
J	Rotor's inertia moment
B_m	Viscous friction coefficient of the rotor
T_L	Load torque
ω	Rotor's angular speed
θ	Rotor position with respect to starting position
θ_j	Rotor position with respect to the jth phase
i_{j1}	jth phase current
λ_j	Flux with respect to the jth phase
T_{ej}	Torque generated by the jth phase
L_a	Phase inductance at aligned position
L_{un}	Phase inductance at unaligned position
P	Electrical input power
$P_{resistance}$	Resistance loss
P_{iron}	Iron loss
P_{mag}	Rate of change of stored magnetic energy
P_{mech}	Mechanical output power
W_f	Stored field energy

W'	Coenergy

Power Converter Related Symbols

V_{fd}	Forward diode voltage drop
Q11	Gate signal for phase 1 top switch
Q12	Gate signal for phase 1 bottom switch
Q0	Common switch
Vdc	DC link voltage
G1	phase 1 variable inductance
Vcd	capacitor voltage
V_IGBT	measured IGBT characteristic
V_diode	measured diode characteristic

Torque Control Related Symbols

$f_T(\theta)$	Contour function
T_{ref}	Torque reference
T_{all}	Torque derived from lookup table
T_a	Torque reference for phase 1
T_b	Torque reference for phase 2
T_c	Torque reference for phase 3
T_d	Torque reference for phase 4
I_a	Current reference for phase 1
I_b	Current reference for phase 2
I_c	Current reference for phase 3
I_d	Current reference for phase 4

CHAPTER ONE

INTRODUCTION

1.1 General

The first reference to the term "switched reluctance" was made by Nasar in a paper in the IEE Proceedings in 1969 [1.1]. The origin of this motor can be tracked back to 1842, but it became popular from the 1980s onwards due to the advent of inexpensive, high-power switching devices. Low ripple torque and speed control remains a challenge, but the ever increasing power and decreasing cost of microprocessors capable of executing advanced control algorithms continues to increase the viability of Switched Reluctance Motor (SRM) drives as viable candidates for various adjustable speed and torque applications. Combining the unique features of an SR motor with its relatively simple and efficient power converter results in a motor drive that may be preferable for many applications compared to other ac or dc drive systems. The main advantages of an SRM drive are:

a) Simple, robust, and low-cost machine construction due to the absence of rotor windings or permanent magnets,
b) no shoot-through faults between the dc busses in the SR motor drive converter since the stator windings are connected in series with the top and bottom switching devices,
c) simple and reliable converter topologies as bidirectional torque can be generated with unidirectional current,
d) low rotor inertia and high torque/inertia ratio,
e) high fault tolerance and robustness as stator phases can be controlled independently,
f) high temperature and vibration tolerance of SRMs, and
g) most of the heat is generated in the stationary stator which is relatively easy to cool.

The main disadvantage of currently available SRM drives are that the highly salient SRM structure poses severe challenges with respect to torque ripple and acoustic noise minimization than other motor types [1.2]. However, the continuing development and application of advanced motor design techniques and high performance control algorithms continues to improve the suitability of SRM drives in an ever widening range of applications.

This thesis presents a theoretical and experimental implementation and analysis of a torque and current control strategy designed to minimize torque ripple.

1.2 Thesis Project Background and Objectives

The objectives of this thesis are to:

1. develop SRM simulation models for power converter and torque control studies,
2. simulate and analyze a suitable torque ripple minimization control strategy,
3. implement and test a prototype torque controller.

SRM Modeling and Parameter Measurements

On the surface, the electrical SRM model appears to be quite simple, and very similar to that of the DC motor. However, because of the doubly salient structure of the SRM, it is inherently nonlinear. The reluctance of the air gap between the salient stator and rotor poles must vary significantly with rotor position in order for significant torque to be produced. The stator phase inductance is therefore a nonlinear function not only of phase current, but also rotor angle. The torque is also a nonlinear function of instantaneous flux, and hence current and rotor angle. The SRM usually operates well into the magnetic flux saturation to yield a higher torque to mass ratio and overall efficiency. Accurate models of the magnetic nonlinearities are therefore required to develop SRM simulation models suitable for evaluating and optimizing power converter designs and torque control strategies. The required data could be obtained from detailed finite element analysis in the motor design stage, or from experimental measurements. This thesis employs several experimental measurement and data manipulation techniques to obtain nonlinear lookup tables for each function of interest. This experimental approach is very time intensive, but can yield motor characteristics which are more accurate than those obtained through mathematical modeling (without measurement), owing to the difficulty of accurately mathematically modeling and calculating the nonlinear electromagnetic characteristics.

There are two main groups of methods of torque measurement for the SRM [1.3]. The first group uses measured variables to calculate instantaneous torque from measured/analytical magnetic characteristics. This is termed indirect torque measurement. The other group uses sensors to measure the torque directly. All indirect methods derive the torque either from the

magnetic flux characteristic or derived inductance characteristic. Such methods are prone to errors due to the accuracy of the flux/inductance characteristic and instantaneous flux estimates (integrator offset) or arithmetic involving division by small measured current values. Direct torque measurement methods avoid these problems. It is impractical to use torque transducers for online torque measurements in most applications, but it is possible to measure the torque vs current and rotor angle characteristics of a particular motor in a laboratory environment, and to then obtain online torque estimates by feeding instantaneous current and rotor angle into the resulting lookup table. While this approach is not prone to calculation errors, it is still not commonly used due to the considerable amount of work required to obtain the required measurements.

SRM Converter Topologies

Continuous torque can be produced by intelligently synchronizing each phase's excitation with the rotor position. The amount of current flowing through the SRM winding is controlled by switching a DC bus/link with power electronic devices, such as MOSFETs (Metal-Oxide-Semiconductor Field Effect Transistor) or IGBTs (Insulated Gate Bipolar Transistor). The power converter topology is an important issue in SRM control because it largely dictates how the motor can be controlled. Several different converter configurations have been researched and developed for SRM drives to address different basic technical and economical requirements and constraints. The converter selection process boils down to a trade-off between the cost of the converter components and torque/speed control capability (independent control of phases, etc.).

SRM Speed and Torque Control

There are several ways of controlling an SRM [1.4]. The simplest is the single pulse method, where a single (narrow) voltage pulse is applied to each phase so that the current builds up to the level required to achieve the desired average torque/speed. This method is used in high-speed operation. At lower speeds the pulse width exceeds the current settling time, so it is possible to regulate the current at the required level by PWM (Pulse Width Modulation) or hysteresis voltage switching/chopping. There are two types of voltage chopping. Soft chopping implies that the voltage applied to the phase winding switches between the DC rail and zero. Hard chopping implies that the phase winding is switched between $+V_{DC}$ rail and $-V_{DC}$ rail or higher (as is possible with several converter topologies). The amount of torque

ripple in either case will depend on the sequence and shape of the resulting current pulses with respect to rotor angle.

Torque Ripple

The high efficiency of SRMs comes at the price of inherently high torque ripple, especially when operated in single-pulse voltage control mode. For many applications where the machine is operating at relatively high speeds, this is mitigated by the fact that the mechanical time-constant is significantly longer than the torque ripple period. Low torque ripple performance (for a given machine design or current-angle-torque characteristic) requires the development of nonlinear torque control strategies to optimize instantaneous torque contribution of each phase. These strategies also need to take the practical limitations of the power supply and converter and real time computing hardware into account.

Practical Implementation

Practical implementations of SRM drives incorporate several hardware and software components. The core hardware component is the control platform. DSPs are preferred because of their relatively high speed and large memory. There are also several DSPs which incorporate application specific hardware functions as ADC (Analogue-to-Digital Converter) and Quadrature Encoder Pulse inputs, and polyphase PWM outputs.

All of the above aspects of SRM drives are covered in more detail in the body of this thesis.

1.3 Thesis Layout

This thesis has been arranged into the following six chapters and four appendices.

Chapter 1

The first chapter gives an overview of the switched reluctance motor and states the objectives and contributions of this thesis.

Chapter 2

The principle of operation and mathematical model of the switched reluctance motor are introduced and it is shown how measurements can be performed to obtain the motor parameters and flux/inductance characteristics. Torque characteristics derived by the (i) flux and (ii) co-energy methods are then discussed and compared with direct measurement from a transducer. The two possible phase connection methods (single/aligned vs. dual/opposing flux) are also considered and the corresponding flux and torque characteristics compared. A Matlab/Simulink model of the prototype 8/6 SRM is presented and validated by means of locked rotor and free rotor alignment tests.

Chapter 3

The three main classes of SRM power converter topology are introduced in this chapter, namely the Asymmetrical Half Bridge (AHB) converter, (n+1) power converter, and C-Dump converters. Their structure and operation in both chopping modes (hard chopping and soft chopping) are also explained and analyzed by means of PSCAD simulations. The AHB converter is chosen for the 8/6 SRM used in this thesis because of its relatively high control performance and robustness, and relatively low complexity. The Matlab/Simulink SRM model presented in Chapter 2 is re-implemented in PSCAD. The combine SRM and AHB model are then validated by means of locked rotor and free rotor alignment tests.

Chapter 4

This chapter considers the problem of SRM torque control. The relatively simple method of torque control via commutation angle is briefly introduced and simulated results show the effects of turn-on and turn-off angle variations on average torque and torque ripple. The Torque Sharing Function method (with hysteresis current control) is then presented in detail, and analyzed under various locked rotor and speed controlled load conditions by means of PSCAD simulations.

Chapter 5

This chapter starts with a brief overview of the hardware and software used to implement the four-phase (8/6) SRM TSF torque and current control strategy presented in Chapter 4. It explains how all required functionality is provided by a Texas Instruments F2812 DSP motherboard and in-house developed daughter boards for PWM, ADC, quadrature encoder

and communications interfaces. Measured results are presented for several tests under various locked rotor and speed controlled load conditions in both motoring and generating modes. Close agreement is observed between these measurements and corresponding torque and current responses, despite several problems with the versions of the DSP development tools (and hence the real time code) available at the time of writing this thesis.

Chapter 6

This chapter concludes the main body of the thesis, summarizing important results and observations and consolidating various suggestions for the future work.

Appendices

8/6 SRM data and Matlab code/models, power converter details and lookup tables, PSCAD diagram details for current and torque control, and practical implementation details are arranged into four appendices.

1.4 Contributions

This thesis makes the following contributions to SRM research with respect to simulation methods and models, parameter measurements and real-time implementation.

- Accurate Matlab/Simulink and PSCAD SRM models are developed, which are suitable for controller and power converter design and evaluation.
- Different approaches to derive SRM torque characteristics are explained in detail and compared with each other and with accurate measurements.
- Two different phase connection methods (inline and opposing) are compared.
- Different power converters are modeled in PSCAD and compared in both hard and soft chopping modes with and without current control.
- Detailed analyses, explanations and comparisons of measured and simulated steady state current and torque control responses are presented for key locked rotor and constant speed load conditions in both motoring and generating mode.

1.5 Research Publications

Two papers on various aspects and findings of the work of this thesis have been presented at local conferences [1.5, 1.6]. One of these was also presented at an international conference [1.7], and has subsequently also been selected for publication in a Journal.

1.6 Summary

This thesis investigates the practical implementation of a TSF (Torque Sharing Function) method for torque control and ripple minimization with an 8/6 SRM. The main objectives of this work are to develop SRM simulation models for power converter and torque control studies, to simulate and analyze a suitable torque ripple minimization control strategy, and to implement and test a prototype torque controller.

In achieving these objectives, the work of this thesis makes contributions to the field of SRM control and drives research by developing accurate Matlab/Simulink and PSCAD models, comparing the results of the two main approaches of deriving SRM torque characteristics with accurate torque measurements, comparing the characteristics for the two possible phase connection methods (inline and opposing). It also compares the three main types of power converter topologies in both hard and soft chopping modes with and without current control, and presents detailed analyses, explanations and comparisons of measured and simulated steady state current and torque control responses for key locked rotor and constant speed load conditions in both motoring and generating mode.

Chapter 2 begins with an introduction to the fundamental SRM operating principles. Methods for parameter measurements and modeling of an 8/6 prototype SRM in Matlab/Simulink are then presented, and validated by means of practical locked rotor and free rotor alignment tests.

CHAPTER TWO

SWITCHED RELUCTANCE MOTOR MEASUREMENTS AND SIMULATION MODELS

2.1 Switched Reluctance Motor Fundamentals

2.1.1 Introduction

The structure and operating principle of the Switched Reluctance Motor (SRM) are different from other conventional motors. The torque of SRM is not produced by the interaction of two magnetic fields but by the distortion of one magnetic field. Its physical doubly salient structure and highly saturated magnetic property decides the phase flux, phase inductance and motor torque are all nonlinear functions of phase current and rotor position. Because of this nonlinear function, it is difficult to get the SRM parameters compared with other motors. There are basically two approaches for modeling the nonlinear magnetic characteristics of SRM, which is the base for the whole motor parameter measurements and modeling: the first is the finite-element method; the second one is the static test. However, in the finite-element method, the process is quite complicated and very time consuming so the second approach is chosen in this thesis. After obtaining all the information from the static test, there are also two ways for modeling: analytical formulations, which are easy to implement but lack accuracy; lookup tables which can store all the characteristics. The latter method is chosen here because an accurate simulation model is crucial for the good performance of torque and current control of SRM. In this chapter, the prototype SRM structure, principle of operation and mathematic equations are introduced first. Then, parameter measurement results and simulation models in MATLAB and SIMULINK are given. Finally, current and rotor position responses under locked and free rotor conditions are shown to closely agree with the practical measurements to confirm the validity of this model.

2.1.2 SRM Structure and Phase Connection

The Switched Reluctance Motor is a kind of motor in which both the rotor and stator have different numbers of salient poles. The rotor is composed of laminated iron sheets. Magnetic flux is produced by stator coils. The stator windings on diametrically opposite poles are

connected in series to form one phase of the motor.In this thesis, a four phase, 8/6 switched reluctance motor shown in Fig. 2.1 is the prototype which will be discussed. It has 8 stator poles (S1, S2, S3, S4, S1', S2', S3', S4') and 6 rotor poles (A to G), as shown in Fig. 2.2. In this motor, the four stator phases are created by connecting opposite stator coil pairs in series (S1-S1', S2-S2', S3-S3', S4-S4') so that they are energised simultaneously.

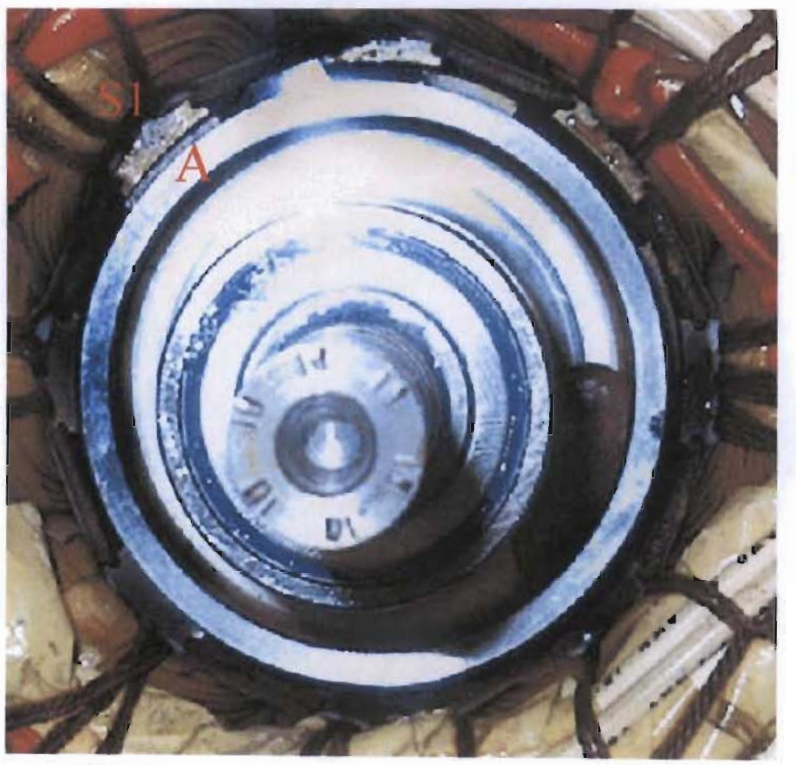

Fig. 2.1 Photo of 8/6 SRM at 0° position

2.1.3 Basic Principle of Operation for SRM

When a stator phase is energized, the most adjacent rotor pole-pair is attracted towards the energized stator in order to minimize the reluctance of the magnetic path. Therefore, by energizing consecutive phases in succession it is possible to develop constant torque in either direction of rotation. [2.1][2.2]

2.1.4 Definition of Aligned Position and Unaligned Position

When the rotor poles are fully aligned with the energized stator poles, this position is called the aligned position for that energized phase. The reluctance of the magnetic circuit [2.3] which is given by eq. (2.1) is at its minimum, and inductance which is given by eq. (2.2), is at its maximum.

$$\Re = \frac{F}{\varphi} = \frac{Hl}{BS} = \frac{l}{\mu S} \tag{2.1}$$

where $\Re$ is the reluctance, F is the magneto motive force (mmf), φ is flux, H is the magnetizing force in the air gap, μ is the permeability of the magnetic material, l is the length of magnetic path, B is the flux density, S is the cross section area of magnetic path.

$$L = \frac{\lambda}{i} = \frac{N\varphi}{i} = \frac{N^2}{\Re} \tag{2.2}$$

where λ is the flux linkage, i is the phase current, N is the number of turns per phase.

Conversely, if the inter-polar axis of the rotor is aligned with the stator poles of a particular phase, this position is called the unaligned position for that phase. The reluctance in this position is at its maximum value.

The rotor position is defined to be 0° when the rotor pole pair A-D is aligned with S1-S1' as shown in Fig. 2.1 and Fig. 2.2. Positive rotation is defined in the anti-clockwise direction. The rotor position is defined from 0° to 360°, as shown in Fig. 2.2 (a), irrespective of the direction of rotation.

In Fig. 2.2 (a), rotor pole pairs A-D and C-F are completely unaligned with phase S1-S1'. Energising only S1-S1' in this position will produce no net torque, as the two adjacent rotor pole pairs will both be equally attracted to the energised S1 poles. Each stator phase, however, is usually only energised when a rotor pole is unaligned by 15° or less for an 8/6 SRM [2.4].

In Fig. 2.2 (b), for example, rotor pole pair A-D is aligned with S1-S1'. Energising only S2-S2' in this position can move the rotor through 15° to align rotor pole pair B-E with S2-S2'. Subsequent individual energization of S3-S3' and then S4-S4' can therefore move the rotor through a further 15° each. One stator cycle is defined as one such sequence of individual energization of the four phases, and can therefore only move the rotor through $4 \times 15^\circ = 60^\circ$. Six stator cycles are therefore required to move the rotor of an 8/6 SRM though one complete revolution (360°).

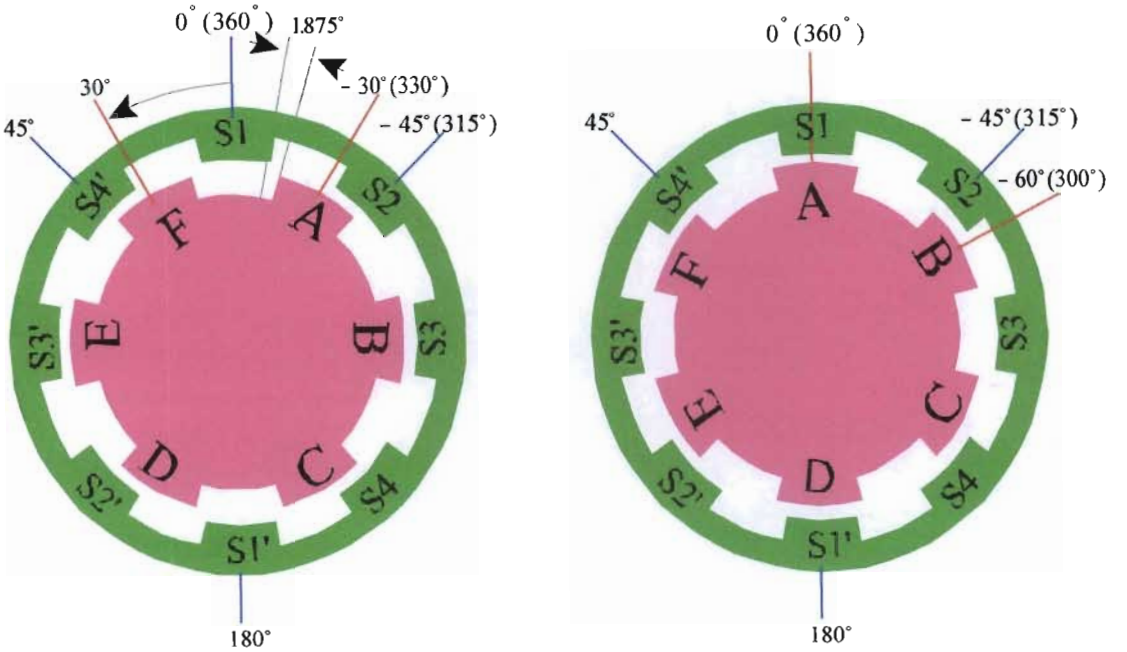

(a) 1st Stator phase unaligned (30° and 330°) *(b) 1st Stator phase aligned (0°)*

Fig. 2.2 Cross section of an 8/6 SRM

The next section develops the mathematical models for numerical simulation of SRM.

2.2 SRM Mathematical Models

2.2.1 Mathematic Equations of the SRM

To derive a mathematical model for the SRM, the following simplifying assumptions are made:

- mutual coupling between phases is negligible;
- hysteresis and eddy current losses in the magnetic circuit are neglected;
- The winding resistance is assumed to be constant and independent of the current waveform or frequency.

The electrical circuit for one phase of the SRM is shown in Fig. 2.3.

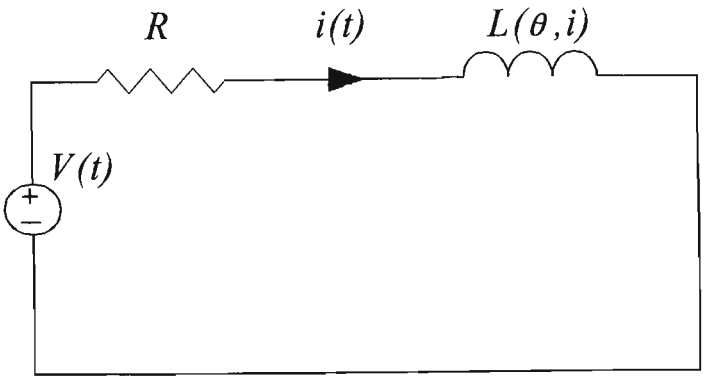

Fig. 2.3 Equivalent circuit for one stator phase

Applying Kirchhoff voltage law (and omitting the longhand notation for time dependencies (t) for simplicity) gives

$$V = iR + \frac{d\lambda(\theta,i)}{dt} \tag{2.3}$$

where R is the phase resistance (assumed to be constant).

Magnetic flux $\lambda(\theta,i)$ is given by

$$\lambda(\theta,i) = L(\theta,i)i \tag{2.4}$$

where $L(\theta,i)$ is the phase inductance, which varies as a function of rotor position (due to varying reluctance) and phase current (due to magnetic saturation).

Eq. (2.3) can be solved to calculate the magnetic flux at various rotor angles and current magnitudes from measured stator voltages, currents and resistance as shown in eq. (2.5).

$$\lambda(\theta,i) = \int (V - iR)dt \tag{2.5}$$

A lookup table can then be constructed to determine the per phase values of inductance for various rotor angles and current magnitudes using eq. (2.6) from flux linkage information (as shown in section 2.3).

$$L(\theta,i) = \frac{\lambda(\theta,i)}{i} \tag{2.6}$$

The current response to a particular voltage input can be then simulated using eq. (2.7), as shown in section 2.3.

$$i = \frac{\int (V - iR)dt}{L(\theta,i)} \tag{2.7}$$

The electrical model of the SRM can be compared with that of a DC motor by substituting eq. (2.4) into eq. (2.3) as follows.

$$V = iR + \frac{d(L(\theta,i)i)}{dt} = iR + L(\theta,i)\frac{di}{dt} + i\frac{d(L(\theta,i))}{dt} \quad (2.8)$$

$$= iR + L(\theta,i)\frac{di}{dt} + i\frac{d\theta}{dt}\frac{d(L(\theta,i))}{d\theta}$$

$$= iR + L(\theta,i)\frac{di}{dt} + i\omega\frac{d(L(\theta,i))}{d\theta} \quad (2.9)$$

The mechanical rotor speed is $\omega = \frac{d\theta}{dt}$. The armature back emf in DC motors is analogous to the term

$$i\omega\frac{d(L(\theta,i))}{d\theta} = \mathrm{E} \quad (2.9a)$$

in eq. (2.9) [2.5], and shows that higher supply voltage is required to achieve higher rotor speed.

In general, the mechanical model of an SRM is as follows:

$$J\frac{d\omega}{dt} = T_e - B_m\omega - T_L \quad (2.10)$$

$$T_e = \sum_{j=1}^{m} T_{ej} \quad (2.11)$$

$$T_{ej} = \int_0^{i_{j1}} \frac{\partial\lambda_j}{\partial\theta} di_j \quad (2.12)$$

where J is the rotor's inertia moment, B_m is the viscous friction coefficient of the rotor and T_L is the load torque; ω denotes the rotor's angular speed; θ denotes the rotor position with respect to starting position; θ_j denotes the rotor position with respect to the jth phase; i_{j1} denotes the jth phase current; λ_j denotes the flux with respect to the jth phase, while T_{ej} denotes the torque generated by the jth phase.

2.2.2 Ideal Phase Inductance Curve and Analysis

Fig. 2.4 shows an idealised curve of S1-S1' phase inductance vs rotor position for the 8/6 SRM in Fig. 2.1 and Fig. 2.2. (for one value of phase current)

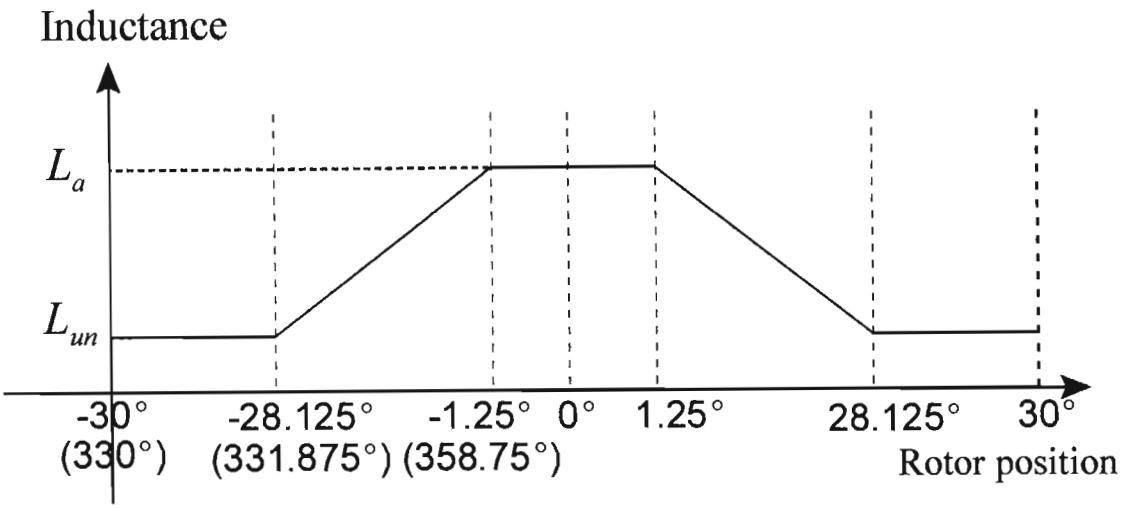

Fig. 2.4. Idealised curve of phase S1-S1' inductance vs. rotor position for one value of phase current in an 8/6 SRM

In this curve, L_a is the phase inductance at the A-D rotor pair aligned position ($0°$) and L_{un} is the phase inductance at the two completely unaligned positions ($30°$ and $330°$). This curve is symmetrical about the aligned position. Fig. 2.1 shows that the rotor pole faces are slightly longer than the stator pole faces. The S1-S1' stator poles and A-D rotor poles therefore completely overlap each other for rotor angles from $358.75°$ to $1.25°$. The idealized inductance then begins to decrease as the amount of overlap decreases to zero in both directions. The constant minimum idealized inductance L_{un} is reached for zero overlap on each side of the stator pole (outside of $[331.875°, 28.125°]$).

2.2.3 Torque Characteristics of SRM

SRM phase torque is a nonlinear function of phase current and rotor position. An accurate knowledge of the torque characteristic is crucial for torque control. The torque characteristics are normally obtained by locking the rotor at different positions (from unaligned position to aligned position) and energizing the stator phase.

There are two ways to get the torque information:

1) Directly measuring shaft torque by torque transducer
2) Using two different analytical methods to estimate the torque

In the two analytical methods, the first one is that the SRM torque characteristic can be derived from the nonlinear phase inductance characteristics. The second one is the torque characteristic can be derived from phase flux characteristics. In the remainder of this section, the power flow of SRM will be first shown, which explains how the torque can be derived from phase inductance; secondly, it will be shown how the torque characteristic be derived from phase flux.

Power Flow of SRM

Fig. 2.5 shows the power flow through the SRM as follows.

$$P = P_{resistance} + P_{mag} + P_{iron} + P_{mech} \tag{2.13}$$

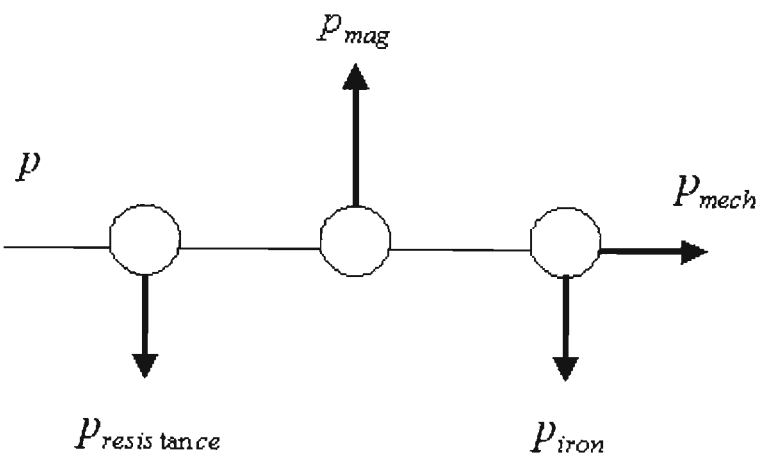

Fig. 2.5 SRM power flow diagram

In motor mode, the electrical input power P is equal to the sum of: (i) resistance loss $P_{resistance}$, (ii) iron loss P_{iron}, (iii) rate of change of stored magnetic energy P_{mag}, and (iv) mechanical output power P_{mech}.

Torque Characteristics Derived from Phase Inductance

Idealised/measured inductance vs. position curves for various current values can be used to determine corresponding idealised/measured torque curves by *assuming negligible iron losses* ($P_{iron} = 0$) and equating instantaneous air gap power to mechanical output power. The instantaneous electrical input power for each stator phase is given by the product of instantaneous voltage and current.

$$T(\theta,i)=\frac{\partial}{\partial\theta}\int_0^i\lambda(\theta,i)di \tag{2.25}$$

If there is no magnetic saturation, the magnetization curve at each angle is a straight line ($\lambda(\theta,i)=L(\theta)i$). In this case, at any rotor position θ, the coenergy and the stored magnetic energy are equal, and given by:

$$W_f=W'=\frac{1}{2}L(\theta)i^2 \tag{2.26}$$

Then the instantaneous torque reduces to

$$T(\theta,i)=\frac{\partial W'}{\partial\theta}=\frac{1}{2}i^2\frac{dL(\theta)}{d\theta} \tag{2.27}$$

From eq. (2.25), the torque characteristics can be derived from the derivative of phase flux with respect to rotor position. Flux is obtained from locked rotor tests using eq. (2.5). Real measured torque characteristics from the above two analytical methods will be shown in section 2.3 and compared with torque transducer results to show their utility and importance for SRM simulation and control implementation.

2.3 Phase Inductance and Torque Measurements

Fig. 2.9 shows a block diagram of the experimental setup used to make all of the practical SRM measurements presented in this section. Fig. 2.10 shows 31 measured voltage and current curves obtained by switching a 12V battery across the terminals of the series S1-S1' circuit with the rotor locked in steps of 1° from 0° to 30°. The stator terminal voltage droops with increasing current due to the internal battery resistance, cable resistance and forward IGBT voltage characteristic.

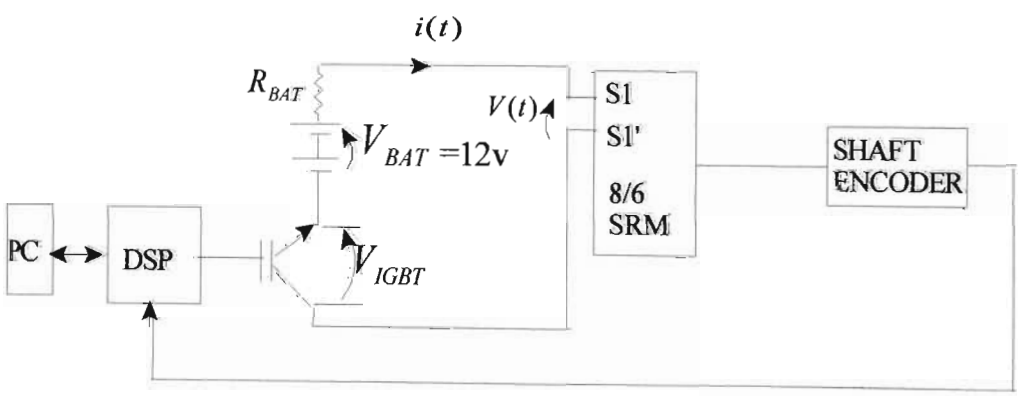

Fig. 2.9 Block diagram of SRM measurement setup

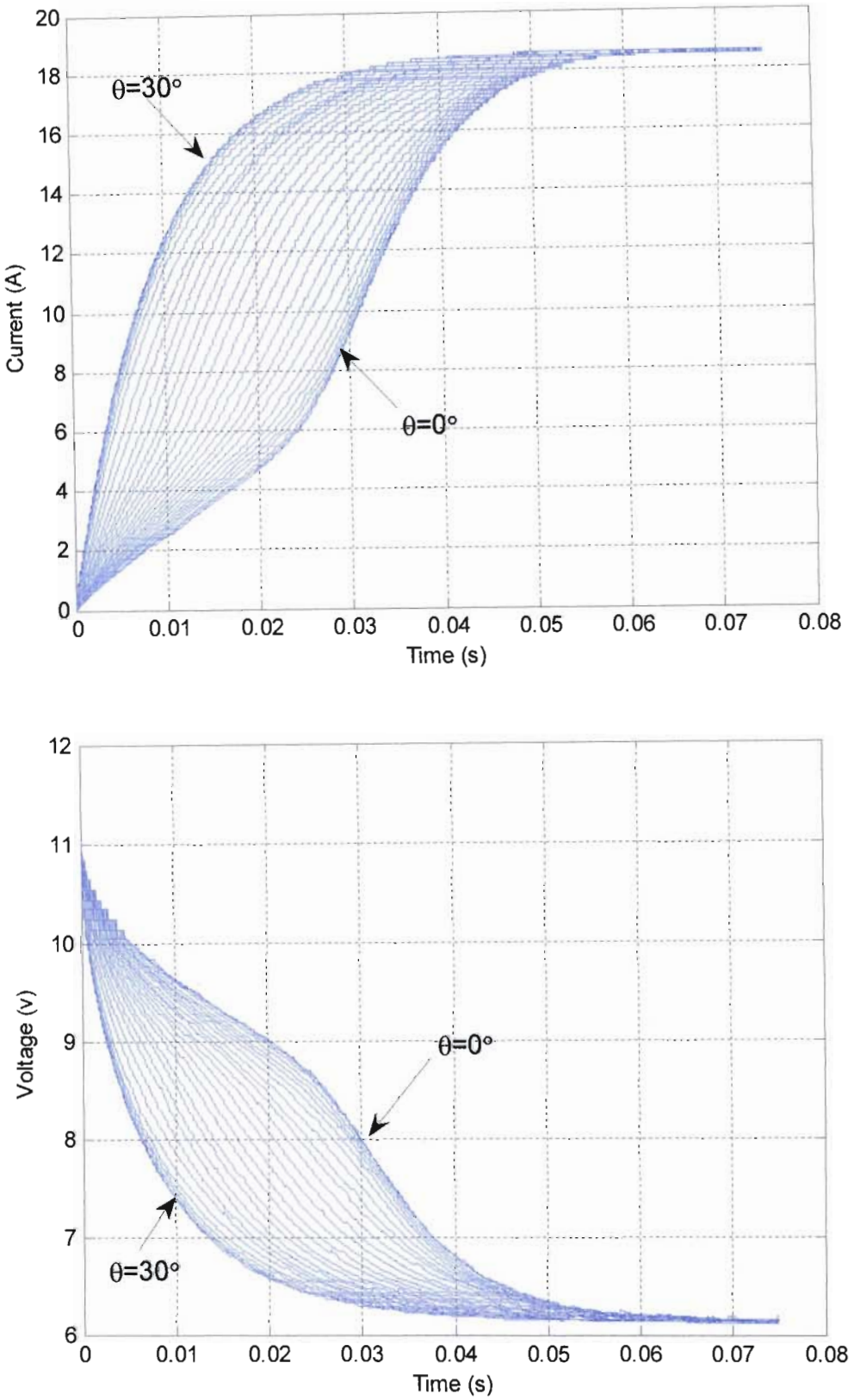

Fig. 2.10 Measured phase current and voltage with rotor is locked at fixed angles

$$\theta \in \{0^\circ, 1^\circ, 2^\circ, \ldots, 30^\circ\}$$

Fig. 2.11 shows graphs of flux vs current for each locked rotor position in Fig. 2.10. These graphs were calculated by substituting corresponding graphs of voltage and current into eq. (2.5).

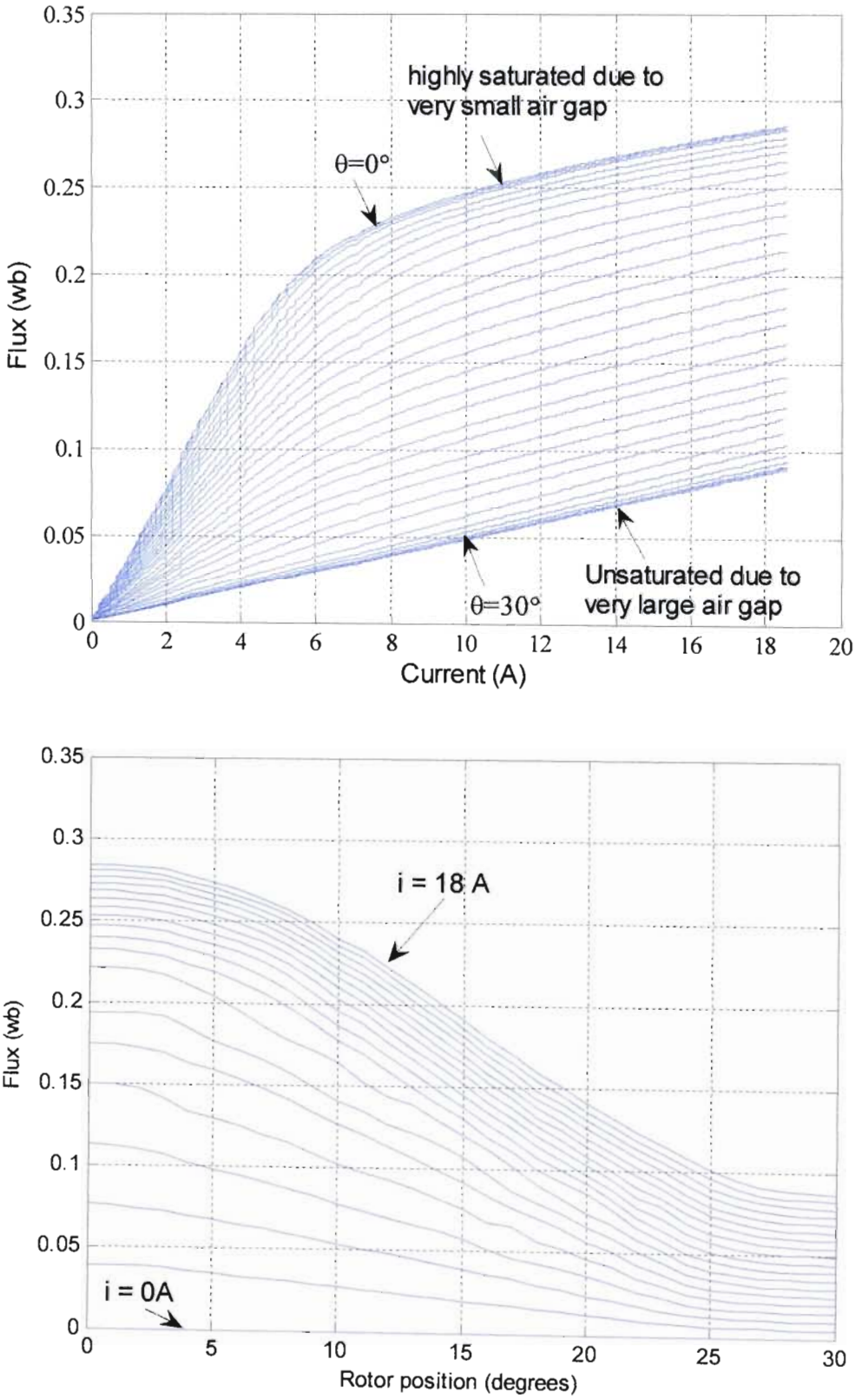

Fig. 2.11 Flux vs current for different locked rotor positions $\theta \in \{0^\circ, 1^\circ, 2^\circ, \ldots, 30^\circ\}$

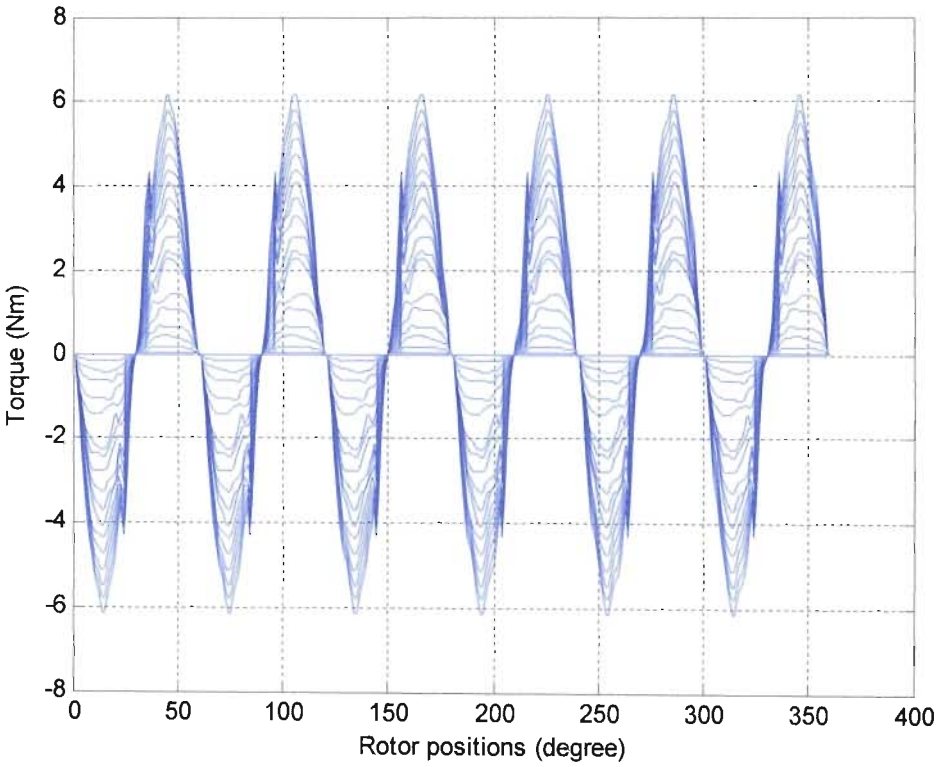

(a) Torque derived from inductance

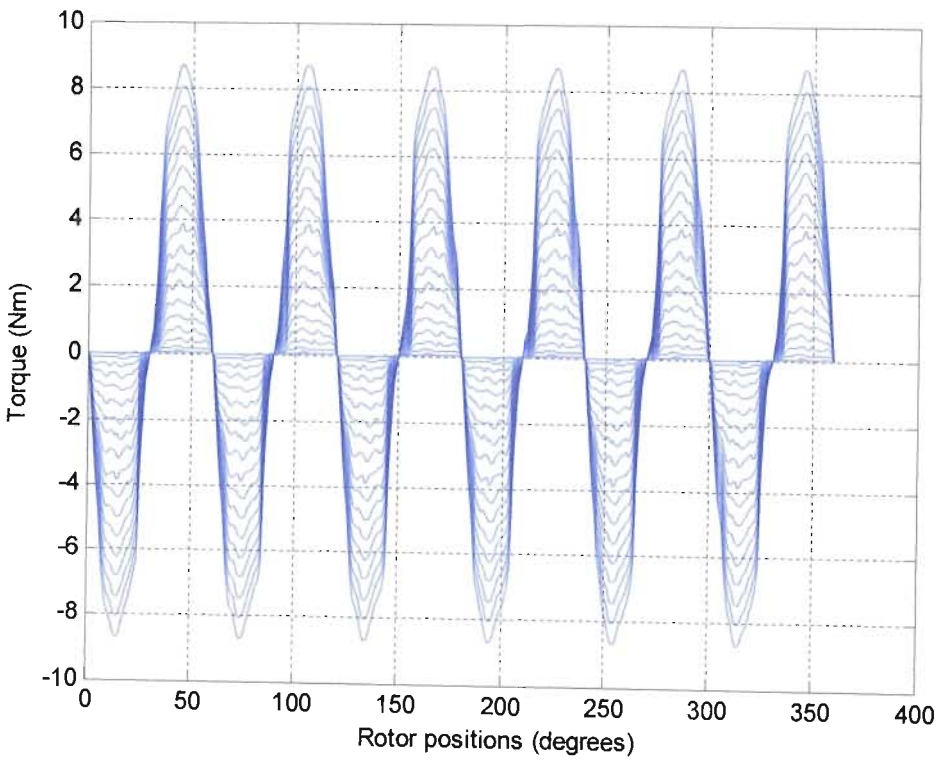

(b) Torque derived from flux

Fig. 2.15 Periodic torque of 1st stator phase vs rotor position from 0° to 360° for different fixed current values

2.4 Comparison of Torque from Calculation and from Torque Transducer Measurement

In this section, the two different analytical methods of estimating the phase torque characteristics introduced in section 2.2 are discussed and compared with direct measurements.

The torque characteristics obtained from eq. (2.19), which are derived from phase inductance, must be numerically smoothed, as shown in Fig. 2.16, before they can be incorporated into an invertible lookup table [1.7]. The smoothing procedure and programs can be found in Appendices A.2 and A.3. Fig. 2.17 shows significant errors between torques measured with a torque transducer and those calculated from eq. (2.19). Fig. 2.19 shows that the torque obtained by eq. (2.25) is much closer to the transducer measurements, but still requires smoothing before it is stored as a lookup table. The comparison before smoothing and after smoothing is shown in Fig. 2.18.

Close agreement between co-energy derived torque curves and measured curves establishes good confidence in the practical flux measurement method used and the resulting flux characteristics. The inductance characteristics are derived directly from these flux characteristics, but future work could include a detailed analysis of the assumptions leading to the inductance derived torque curves to determine the causes for their significant deviation from the measured curves and co-energy derived curves.

The torque transducer measurement is the best option to get the accurate torque characteristics. If a torque transducer is not available, eq. (2.25) should be used to estimate the torque characteristics because it is closer to real measurement than the one derived from eq. (2.19). In the remainder of this thesis, the torque transducer measured result is chosen as the torque characteristic for the 8/6 SRM used in this thesis.

Future work could also include a detailed comparison of the simulated and measured results obtained with the co-energy derived torque characteristic, and those obtained using the measured torque characteristic.

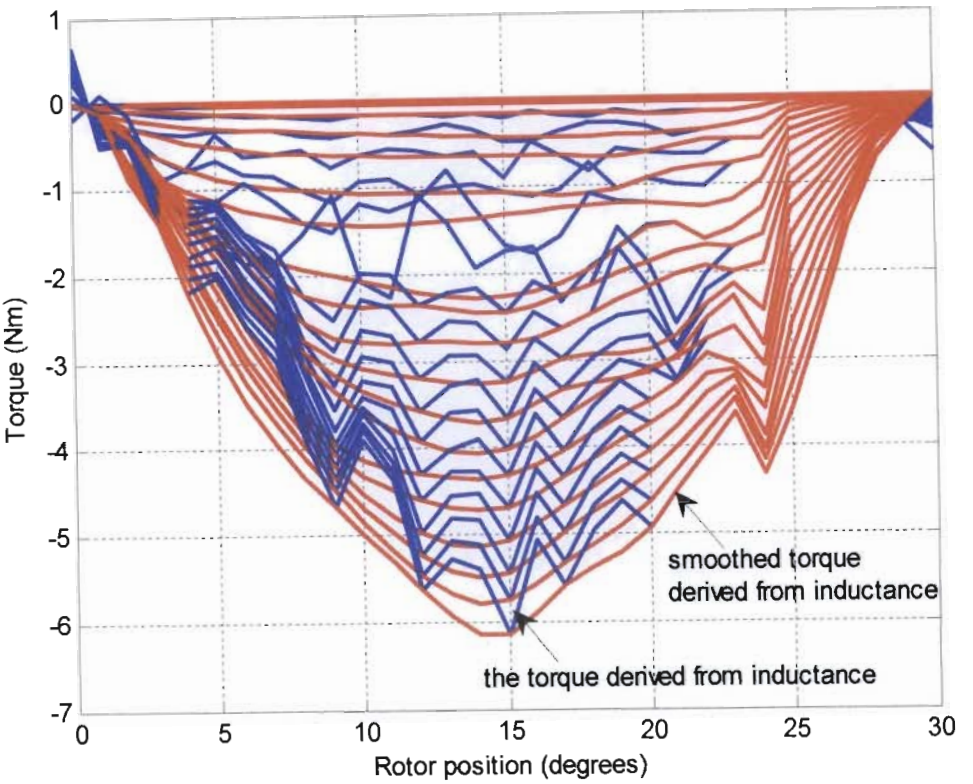

Fig. 2.16 Torque characteristics smoothed from eq. (2.19) and from eq. (2.19)

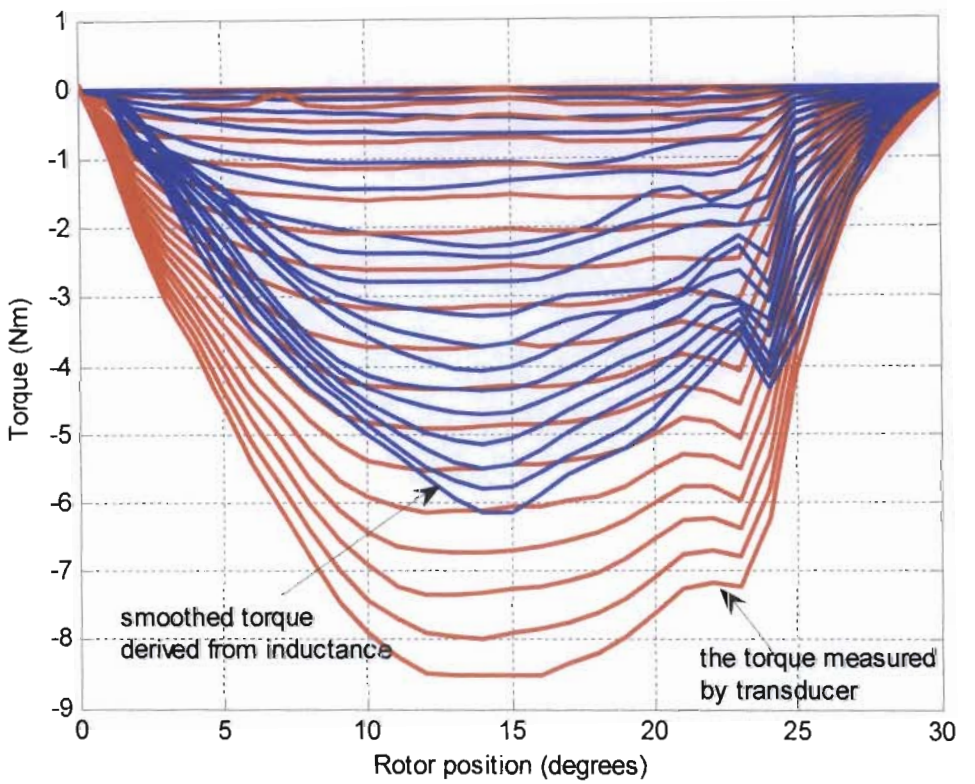

Fig. 2.17 Torque characteristics smoothed from eq. (2.19) and from transducer

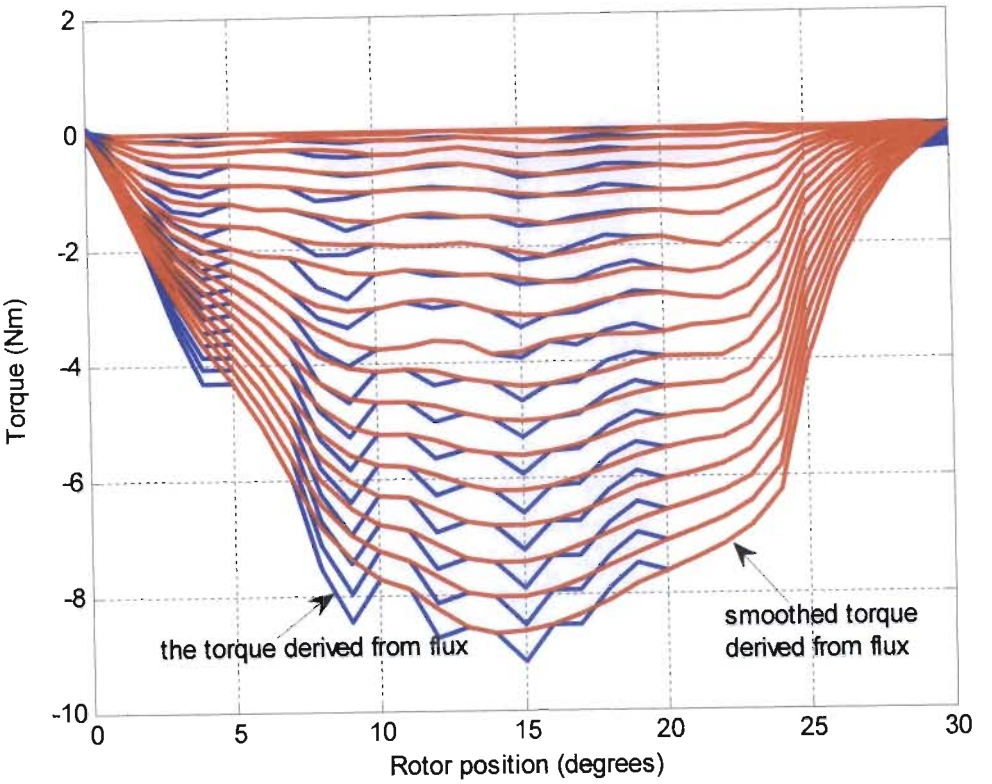

Fig. 2.18 Torque characteristics smoothed from eq. (2.25) and from eq. (2.25)

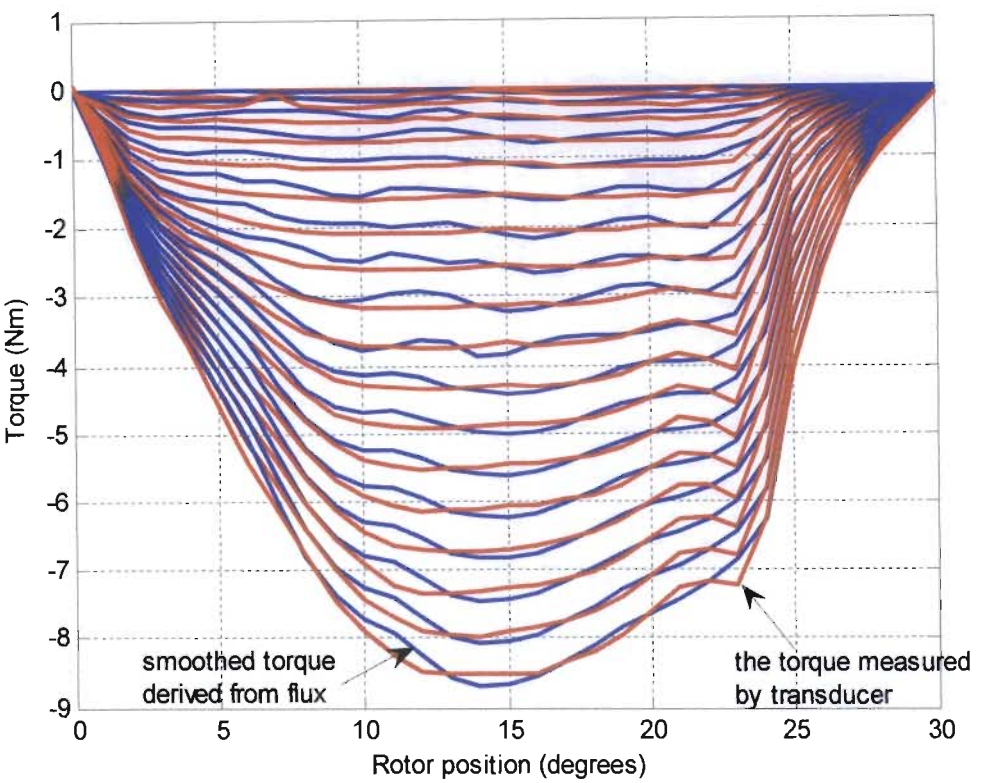

Fig. 2.19 Torque characteristics smoothed from eq. (2.25) and from transducer

2.5 Comparison of Different Connection of Each Stator Phase

As introduced in section 2.1, the opposite stator poles are connected in series to form one phase. Here, two ways of connection need to be discussed in detail. When two opposite stator poles are connected in series with the same/opposite polarity of flux, as shown in Fig. 2.20, this is called an inline/opposing connection.

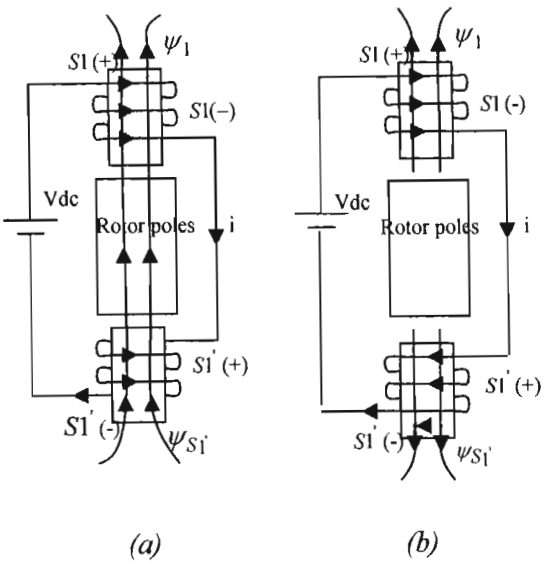

Fig. 2.20 Phase 1 connection: (a) S1-S1' inline connection, (b) S1-S1' opposing connection

Fig. 2.21 shows that the inline connection produces a larger measured torque than the opposing connection. For small current, both torqueses are close to ideal (flat). Both connections give less ideal torque characteristics with increasing current, but the inline connection is more ideal in the region of peak torque, and would hence facilitate better torque control performance.

Fig. 2.22 shows that the saturated flux produced by the inline connection is larger than that produced by the opposing connection, due to a lower reluctance in the flux path of the inline connection. The gradient of the inline flux is also higher before saturation. Eq. (2.19) and eq. (2.25) therefore also estimate larger torques in the inline configuration. In physical terms, the torque produced by the inline connection is significantly higher because the reluctance in the aligned position is significantly lower. The next section develops Matlab and Simulink models from the measured phase inductance and torque characteristics obtained from torque transducer measurement of the SRM in the inline phase connection. The simulated and measured results are compared under locked rotor and free rotor test conditions.

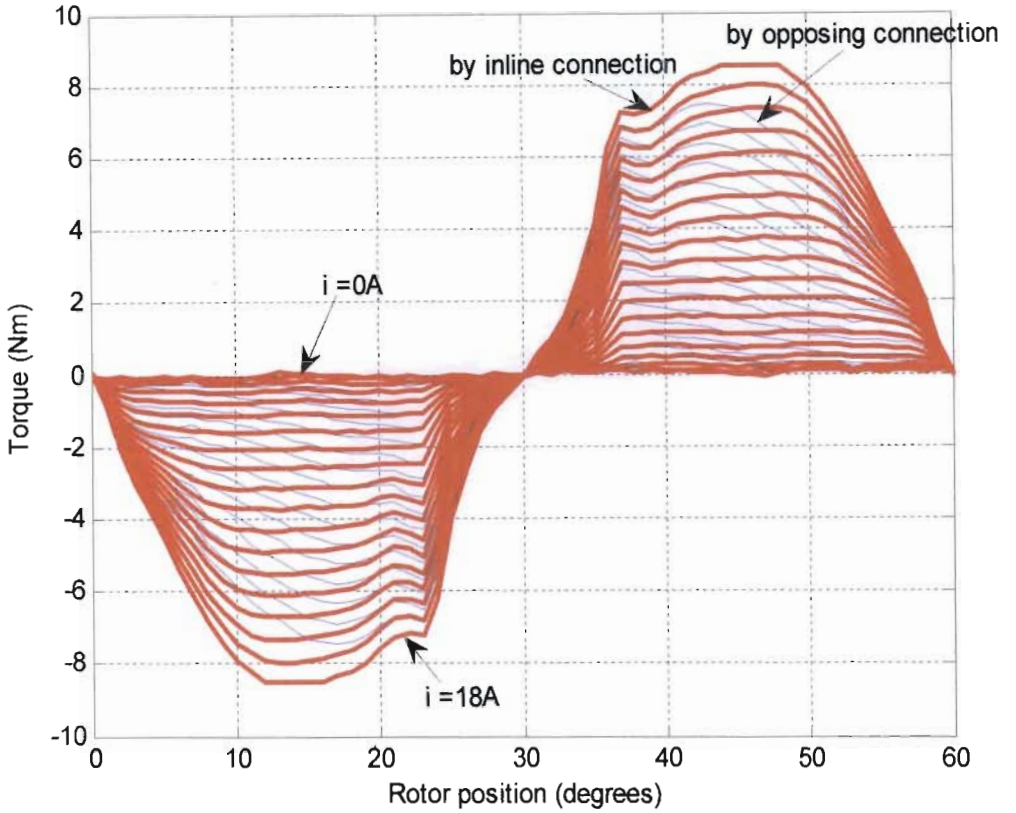

Fig. 2.21 Torque characteristics by inline connection and opposing connection

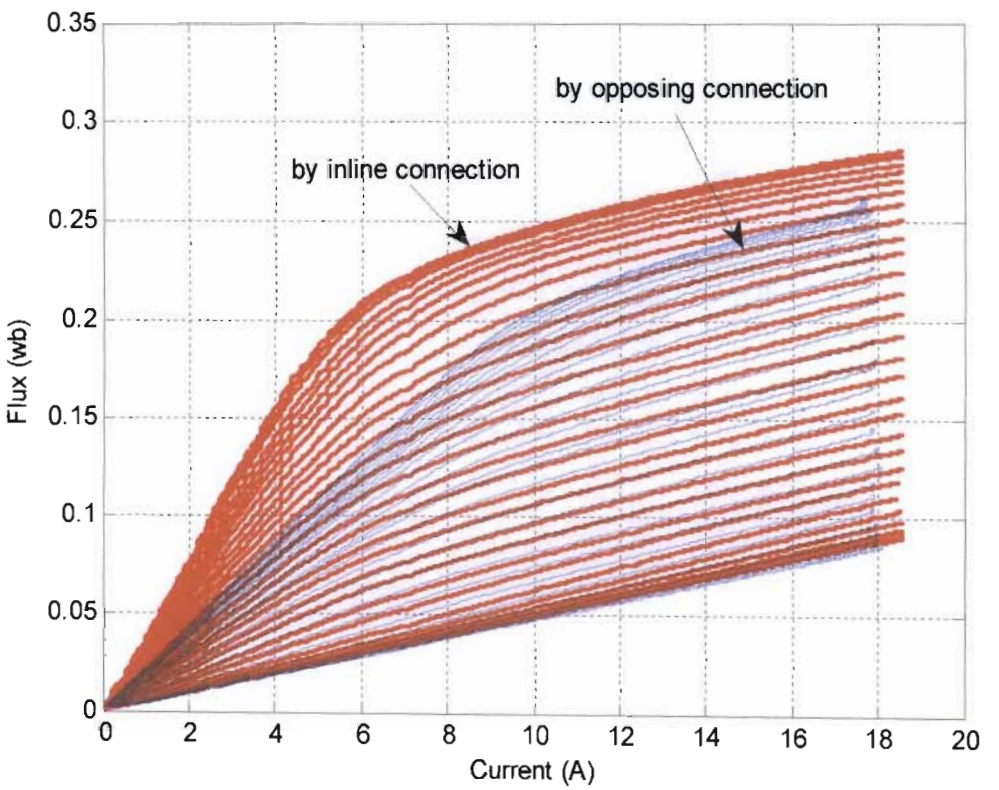

Fig. 2.22 Flux by inline connection and opposing connection

2.6 Simulation and Measured Results

2.6.1 Electrical Simulation Model and Locked Rotor Test

Fig. 2.23 shows a Simulink implementation of the electrical model presented in section 2.2.1. The experiment circuit is same as Fig. 2.9. Eq. (2.7) is used to obtain the locked rotor current response to the particular measured terminal voltage curve shown in Fig. 2.24. The inductance curves in Fig. 2.12 are incorporated in the form of a 2-D lookup table with current and position indices.

Fig. 2.24 and Fig. 2.25 compare simulated and measured phase voltage and current responses for a locked rotor position of 5° (similar results were produced at other rotor angles). The Vdc to VSRM block accounts for the voltage drops of power converters in the practical system, as shown in Fig. 2.23. The close agreement between the measured and simulated current and voltage responses confirms the validity of the mathematical and simulation models of each stator circuit under locked rotor conditions.

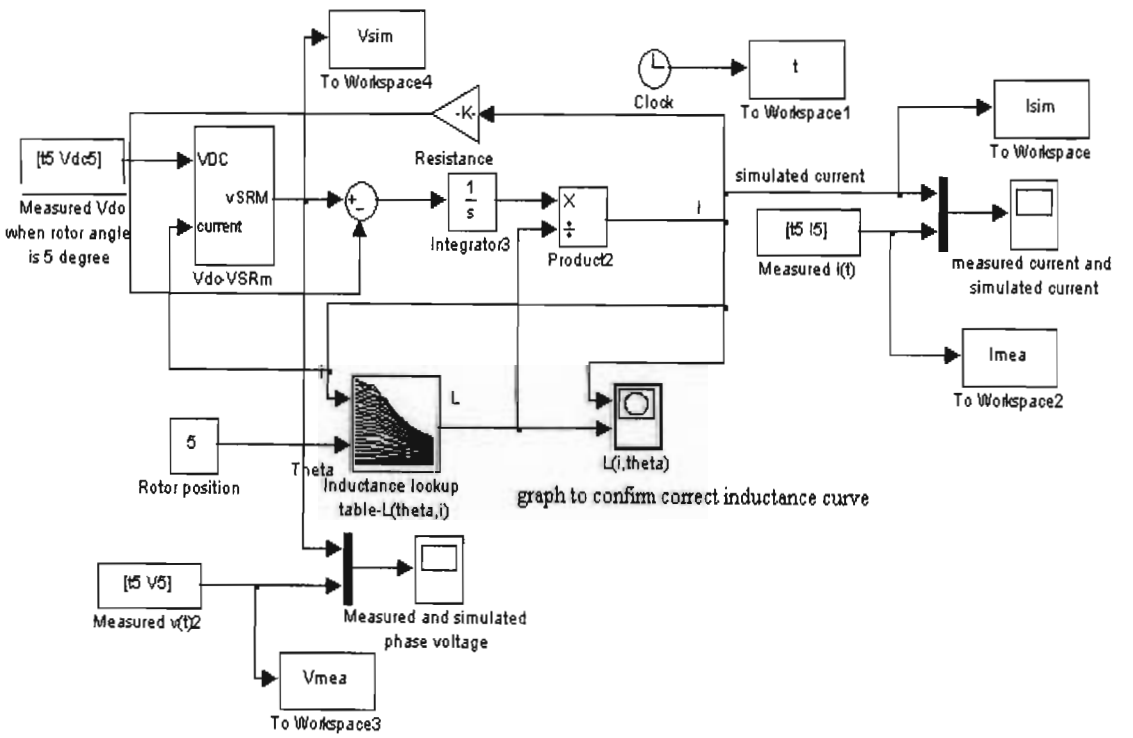

Fig. 2.23 Electrical model for each SRM stator phase with locked rotor

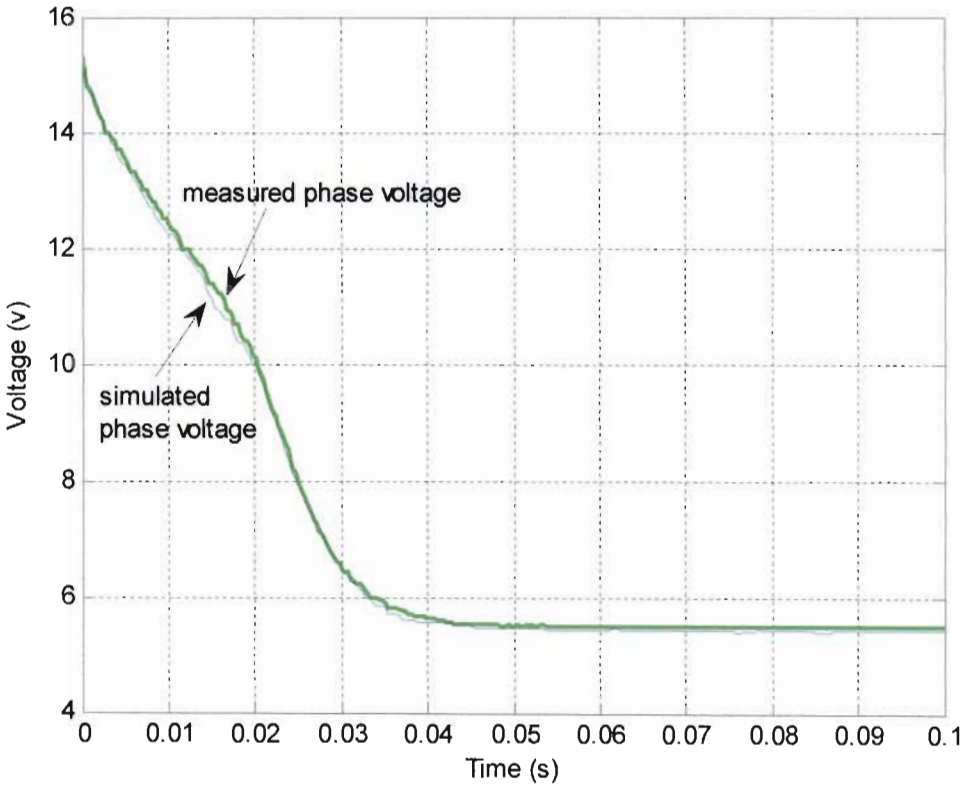

Fig. 2.24 Simulated and measured phase voltage for a locked rotor position of 5°

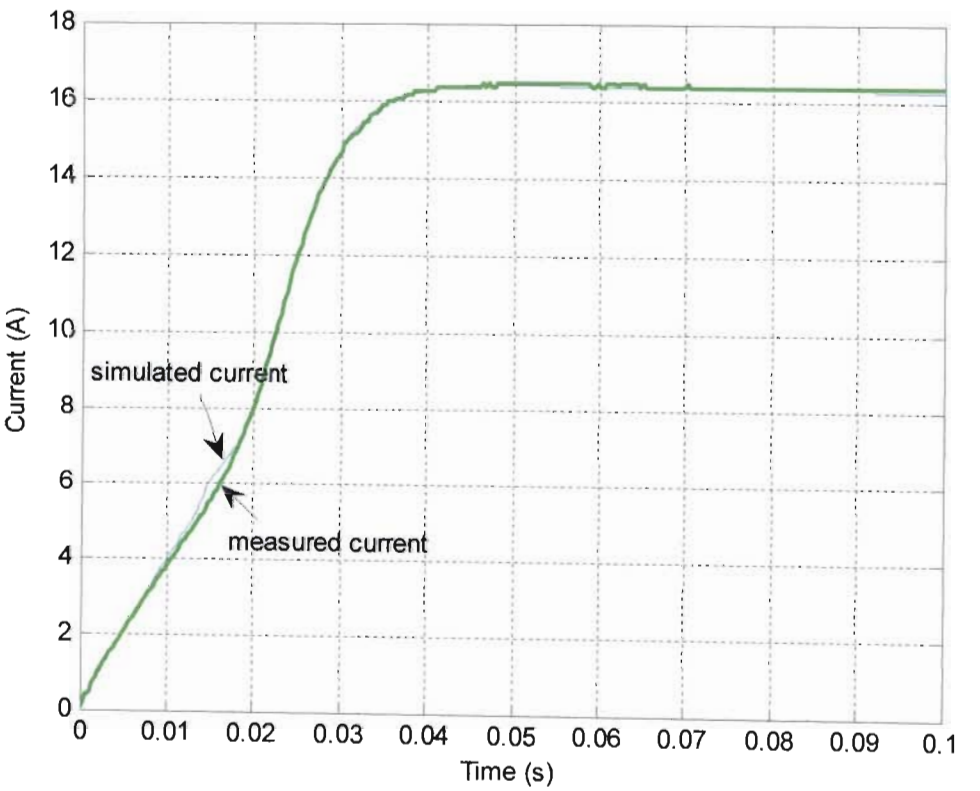

Fig. 2.25 Simulated and measured current responses for a locked rotor position of 5°

2.6.2 Mechanical Model and Free Rotor Alignment Test

The simulation of free rotor alignment test requires the inclusion of model to determine the mechanical position and speed responses to the torque produced by the SRM. In this test, the SRM was not connected to any other mechanical system (apart from the rotor locking mechanism, which was removed during free rotor alignment test) which means eq. (2.10) can be used and $T_L = 0$ .Therefore the first order model in eq. (2.10) is shown in Fig. 2.26 to account for the SRMs own inertia and viscous friction.

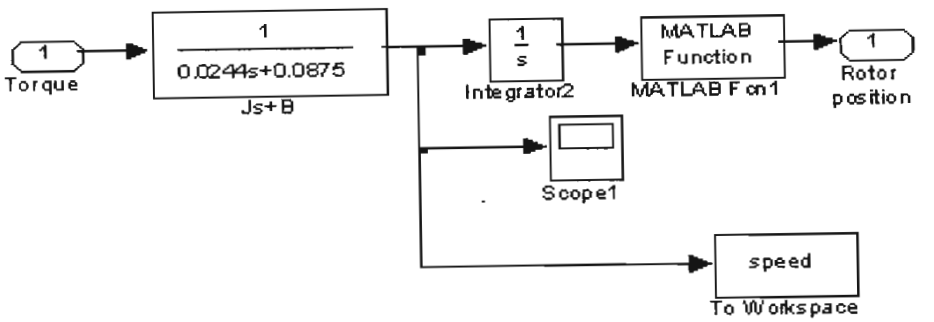

Fig. 2.26 Mechanical shaft model

Fig. 2.27 shows how the electrical model of Fig. 2.23 was combined with the torque characteristic stored as a lookup table and the mechanical model of Fig. 2.26 to simulate the free rotor alignment test response when a 12V battery was switched across the terminals of the series S1-S1' circuit. The torque characteristic is entered in the form of a 2-D lookup table with current and position indices. The range of the angle index is limited to $[330°,30°]([-30°,30°])$, because the rotor position is not expected to exceed this range for initial rotor positions inside it. The initial rotor position is entered (in radians) in the form of an initial condition on integrator2 in Fig. 2.26.

Fig. 2.28 compares simulated and measured current and rotor position responses when the rotor is free to move from an initial position of $15°$. The measured voltage across the phase S1-S1'is also used as the input voltage in this simulation. Fig. 2.28 shows that the simulated phase current and rotor position response closely agree with measured current and rotor angle. The results prove that the torque characteristics and mechanical model for the one phase SRM simulation model are working well. In addition, the electrical model is also shown to be valid under free rotor conditions, and all three models have been correctly combined to simulate one phase of the whole SRM.

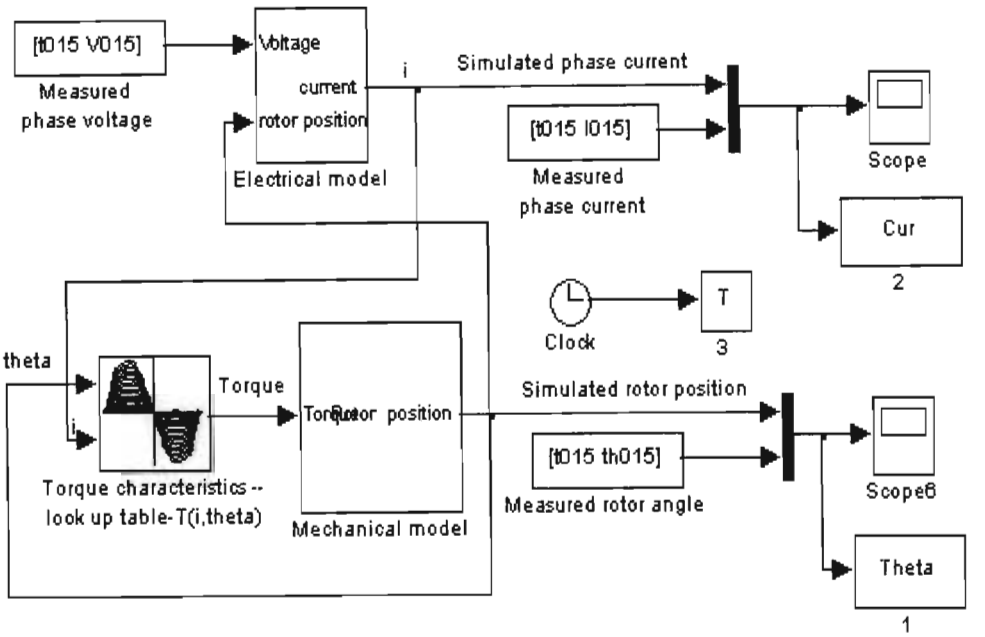

Fig. 2.27 One phase SRM simulation model under free rotor alignment test

The next section discusses the simulation of the complete 8/6 SRM by combining four one phase models and a simple torque control strategy study that only controls the turn on and turn off angles.

2.7 Four Phase Simulation Model and Simple Torque Control Strategy for 8/6 SRM

Fig. 2.29 shows the four phase individually energized model for an 8/6 SRM. A constant current source is sequentially switched into one phase circuit at a time. A current source is chosen in this hypothetical controller to illustrate the need for current control to implement any effective torque control strategy in practice. The initial rotor angle is set to 345°, as explained in section 2.2. Each complete rotor revolution is then produced by commutating the current source from one phase to the next at the end of each corresponding 15° change in rotor angle. One complete rotor revolution therefore requires six stator cycles.

Fig. 2.30 shows the simulated torque and speed responses produced by this hypothetical strategy. Replacement of the ideal current source commutation scheme in Fig. 2.29 with a practical current controlled voltage source will result in a more discontinuous torque response than that seen in Fig. 2.30 (a), due to practical limitations on the current rise and fall times. A completely different approach is therefore required to achieve smooth (low ripple) torque responses, as shown in chapter 4.

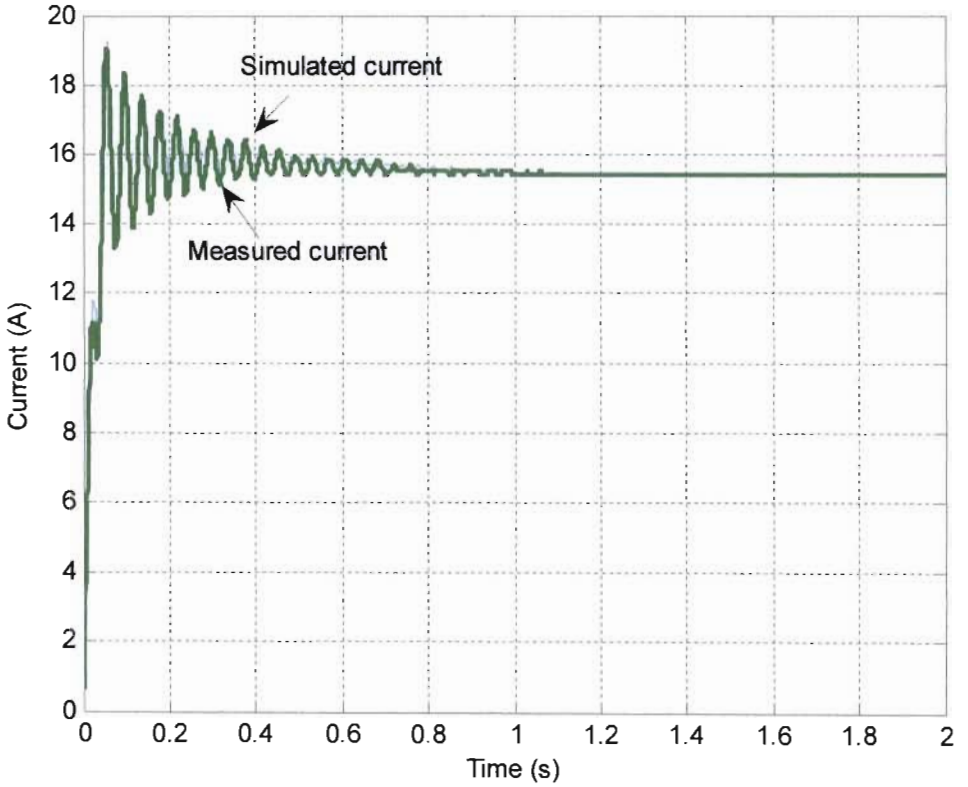

(a) Measured and simulated current curve

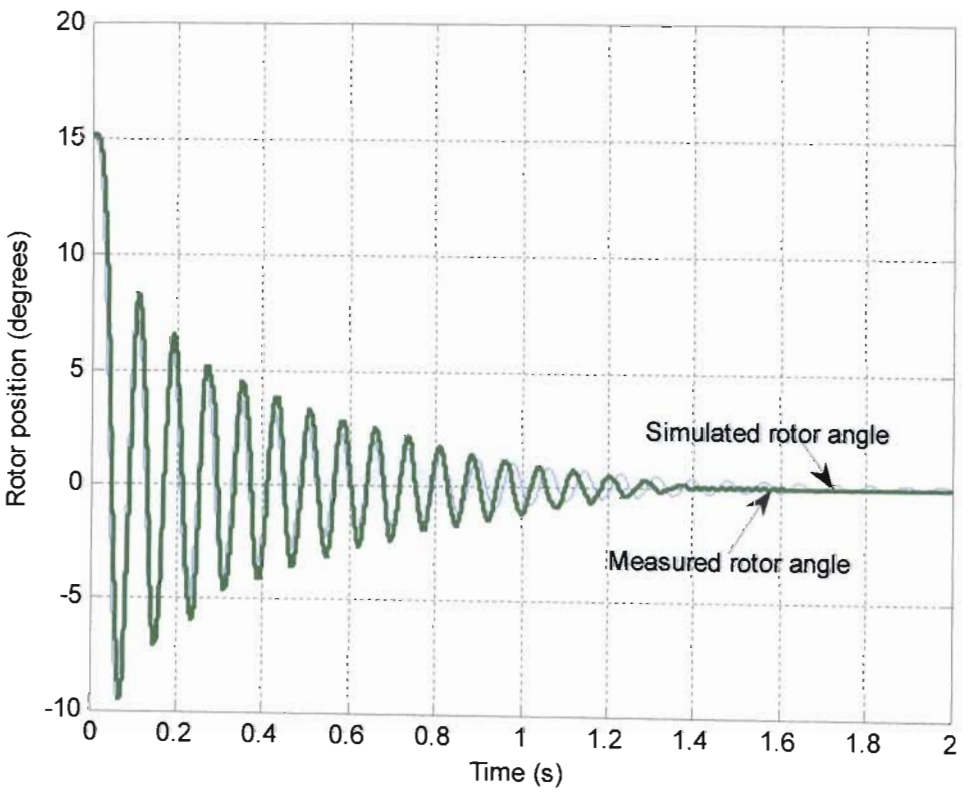

(b) Measured and simulated rotor position curve

Fig. 2.28 Free rotor alignment test results when rotor starts from 15°

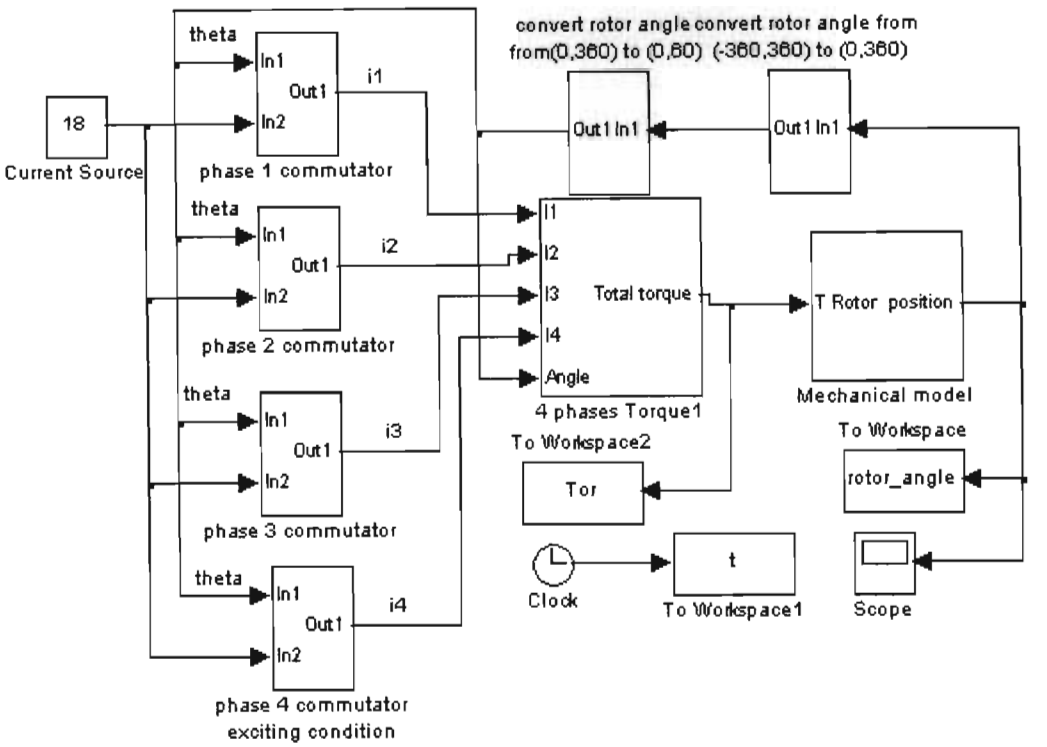

Fig. 2.29 Four phase simulation model for an 8/6 SRM with commutated current source

Subplots (a) to (d) in Fig. 2.31 show the torque which can be produced in each rotor position for various values of current in each of the four phases of the 8/6 SRM. Any two of these four sets of torque curves can be added together in only 6 unique ways. Subplot (e) shows the 6 combined torque curves for maximum current of 18A. Combining more than two phase torques at a time would serve no practical purpose as only two phase torques will have the same sign for any given rotor angle. It can be seen that two of these combinations (phase 1 plus 3, and phase 2 plus 4) produce near zero torque, but the other four combinations produce torques which (i) have a higher peak magnitude than each phase torque, but (more importantly) (ii) overlap with each other. This means any constant or time varying torque value (inside the envelope defined by these four curves) can be achieved by forcing any appropriate combination of currents to flow in the appropriate two phases for a given instantaneous rotor angle.

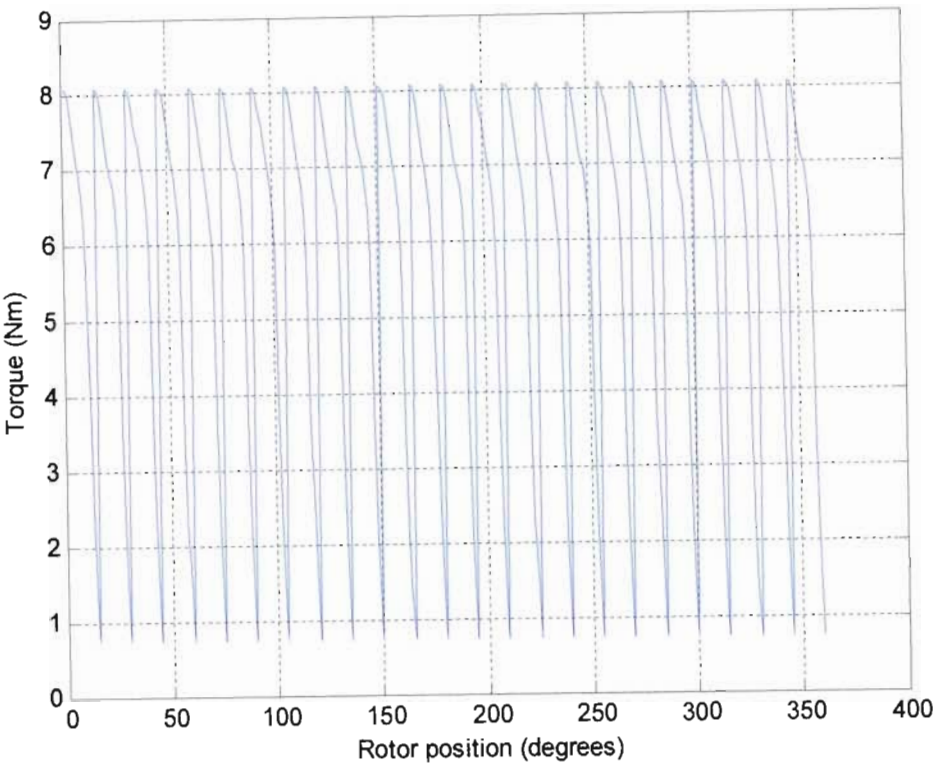

(a) Torque response

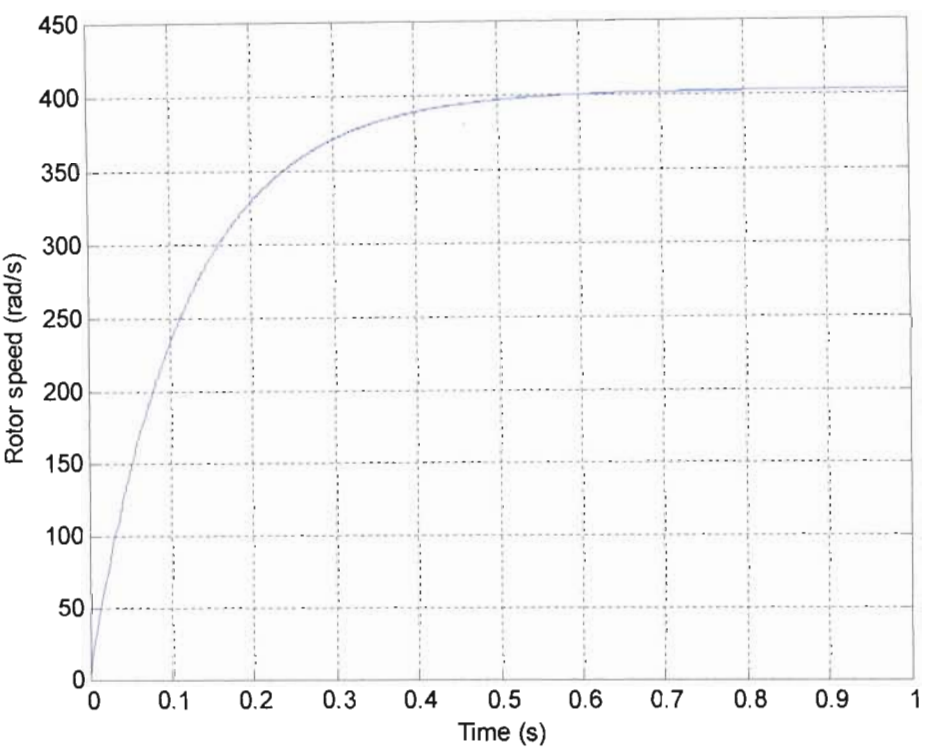

(b) Speed response

Fig. 2.30 Torque and speed responses produced by simulation of ideal current source commutation

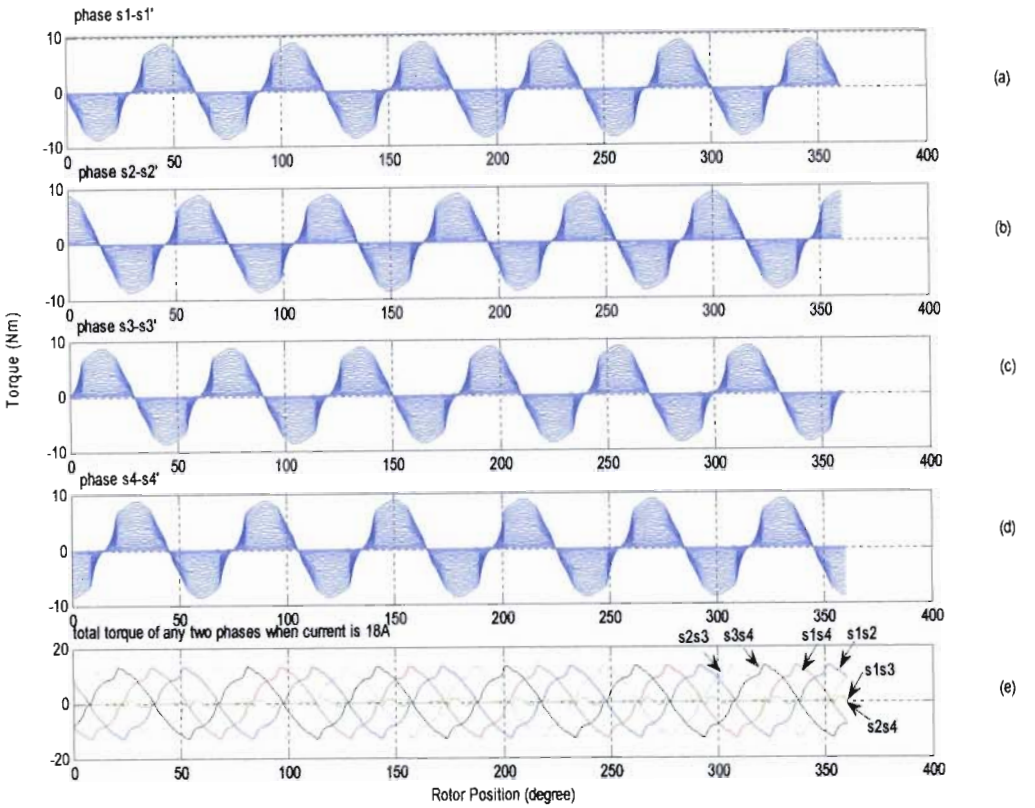

Fig. 2.31 (a) – (d) Four phase torques vs rotor angle for various fixed current magnitudes and (e) sum of maximum torque curves for all six unique phase pairs

Practical implementation of this bi-phase torque control strategy for four phase SRMs (such as the 8/6 motor considered in this thesis) will require the development of (i) algorithms to determine appropriate instantaneous current values for all four phases, and (ii) converter hardware and current control algorithms to track the resulting current trajectories. The torque control design for the 8/6 SRM which is based on torque ripple minimization and torque sharing function will be presented in chapter 4 and its simulation results are also shown and explained. In the next chapter, the power converters for a SRM are introduced and compared in detail. The PSCAD model of a SRM is also given and validated by locked rotor and free rotor alignment test.

2.8 Summary

This chapter first introduced the fundamental principle of an 8/6 Switched Reluctance Motor and then described an experimental process used to produce a model in Matlab and Simulink for a prototype 8/6 Switched Reluctance Motor, and some methods used to validate the model. The inductance, flux and torque characteristics of switched reluctance motors are nonlinear, and must usually be numerically determined from real experimental data.

Torque can be measured directly or calculated from measured phase current and rotor position, and numerically-determined inductance or indirectly from phase flux. These analytical methods of obtaining torque characteristics were also evaluated by comparison with practical torque measurements, which were also used to determine the optimal phase winding configuration.

This chapter explained how two different lookup tables (for inductance and torque characteristics) are used to simulate the electrical, magnetic and mechanical characteristics of the motor. Simulation results were shown to closely agree with practical current and rotor position responses under locked and free rotor conditions. It was also explained how the validated simulation models will be used for the torque control design.

In the next chapter, different power converter strategies for a SRM will be discussed and compared in PSCAD. The PCSAD model for 8/6 SRM is also given and validated by locked rotor and free rotor alignment tests.

CHAPTER THREE

POWER CONVERTER STRATEGIES FOR SWITCHED RELUCTANCE MOTOR

3.1 Introduction

Chapter 2 presented methods for measuring the parameters of and simulating a prototype 8/6 SRM. The first step in designing and implementing current and torque control for this motor, is the selection of a power converter. There are many different SRM converter topologies which all exploit the fact that only unipolar current is required for bidirectional torque production. The most popular converter topologies for SRMs [3.1] [3.2] include

1. Asymmetrical Half Bridge (AHB),
2. (n+1) Switch (N1S),
3. Modified C-Dump (MCD), and
4. Cost Effective C-Dump (CECD).

This chapter compares the capabilities and performance of these topologies with respect to current and torque control. The various topologies are compared using custom models and simulations in the simulation program Power Systems Computer Aided Design (PSCAD). The relative complexity, cost and robustness of these topologies is also considered.

Section 3.2 presents a brief introduction to the main properties of SRM converters in general. Section 3.3 follows with an overview of PSCAD. Sections 3.4 to 3.7 explain the operation of each selected topology, and present PSCAD simulation results as a basis for their comparison with respect to current control performance. Section 3.8 explains the selection of the AHB converter topology for the practical work of this thesis. Section 3.9 presents PSCAD locked and free rotor alignment simulation results for the AHB topology, and shows that these are in close agreement with measured results.

3.2 Generic Properties of SRM Power Converters

The main differences between converters for SRM and other converters [3.3] are as follows.

1. It is possible to use only one switch for each phase. This is big saving compared with AC motors which need two switches for each phase.
2. Shoot through faults can be avoided because the phase winding is in series with top and bottom devices in each converter leg.
3. Device failure in one phase has no effect on other phases.
4. The SRM has zero rotor current and therefore zero short-circuit current and zero open-circuit voltage in generating mode, irrespective of speed. Thus, there are less over-voltage and over-heating problems accompanied with faults.

The main requirements [3.1] for SRM converters to get good drive performance are as follows.

1. Each phase of an SRM should work independently for reliability and robustness.
2. The converter should have the ability to demagnetize the phase fast enough so that the motor will not work in the undesired opposite mode (motor or generator).
3. The converter should have the ability to magnetize one phase while demagnetizing another phase. (Phase sharing available for higher motor torque)
4. When the phase is demagnetized, the phase energy stored must be returned to the source or used to energize another phase.
5. The converter can energize and demagnetize each phase quickly and accurately (Low torque ripple and noise).
6. The converter can offer a freewheeling option which can reduce the switching frequency (High efficiency).

The next section presents an overview of the PSCAD software used to simulate and compare four specific SRM power converters in subsequent sections.

3.3 PSCAD Overview

PSCAD [3.4] is a powerful and flexible graphical user interface to the well established EMTDC (Electromagnetic Transients including DC) simulation engine. By using PSCAD software with a suitable FORTRAN compiler, users can construct a circuit, run a simulation, analyze the results, and manage the data in a completely integrated, graphical environment. Online plotting functions, controls and meters are also included so that the system parameters and results during a simulation run can be viewed.

EMTDC represents and solves differential equations (for both electromagnetic and electromechanical systems) in the time domain; Solutions are calculated based on a fixed time step trapezoidal method, and the program structure allows for the representation of circuits and control systems, either with or without electromagnetic or electromechanical components.

Chapter 2 showed MATLAB and Simulink SRM simulation results which agree closely with practical motor measurements, but PSCAD is preferred for detailed simulation of various power converter models due to the ease with which these can be implemented using the graphical interface and standard component libraries. The MATLAB and Simulink SRM model presented in chapter 2 was thus re-implemented in PSCAD. This implementation is discussed in detail in Section 3.9, where simulation results are also shown to closely agree with measured results. Sections 3.4 to 3.7 first explain the operation of the four selected converter topologies, and present PSCAD simulation results (using only the electrical part of the PSCAD SRM model) as a basis for their comparison with respect to current control performance.

3.4 The Asymmetrical Half Bridge Converter

3.4.1 AHB Converter Introduction and Principle of Operation

The Asymmetrical Half Bridge (AHB) converter is the most popular converter for SRMs due to the following advantages.

1. Robustness in the case of switching element or driver failures because each phase operates independently.
2. Efficiency due to recovery of commutation energy.
3. "Hard" and "soft" chopping options for improved torque and current control.
4. Phases can be overlapped to minimize torque ripple.

Each machine phase is connected to an asymmetric half bridge consisting of two power switches and two diodes. The figure below illustrates its configuration for a four phase (8/6) SRM [3.5].

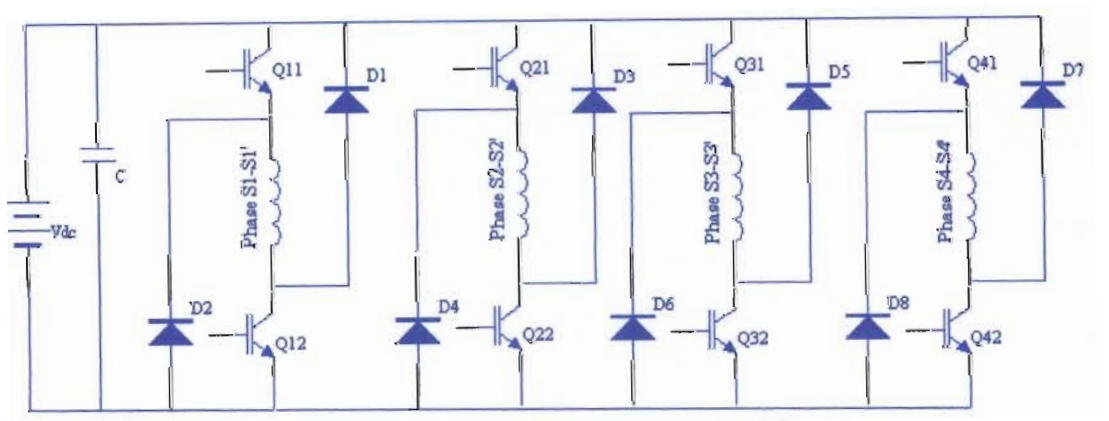

Fig. 3.1 AHB converter for a four phase SRM

Vdc is applied on phase S1-S1' when the top switch Q11 and bottom switch Q12 are turned on simultaneously, as shown in Fig. 3.2 (a). This is called the on commutation or "hard" chopping "on" mode. This mode can be initiated before the rotor and stator poles start overlapping so that the phase current approaches the reference value as quickly as possible before the phase inductance begins to increase. C is the DC link capacitor which reduces the DC link ripple caused by the flow of current through the internal resistance of the DC source.

When the current reaches the reference value, the converter goes into current regulation mode or "soft" chopping mode, as shown in Fig. 3.2 (b). The phase S1-S1' current is

maintained at the reference value by PWM or hysteresis switching of Q12 while leaving Q11 on continuously or switching Q11 while leaving Q12 on continuously (advanced scheduling of these two modes can be performed to ensure equal distribution of conduction and switching losses between all devices).

Fig. 3.2 (c) shows the phase S1-S1' commutating current path when Q11 and Q12 are off. This is called the hard chopping "off" mode, used for rapid off phase commutation. The current flows through diode D1, the dc source, D2 and phase S1-S1'. The voltage across the phase is –Vdc-2V_{fd}, where V_{fd} is the forward diode voltage drop.

While one phase is demagnetizing, another phase can be magnetized. This helps to reduce the torque ripple during the commutation as shown in Fig.2.31 (e).

This converter provides a high degree of control flexibility in that the current control can be totally independent for each phase, allowing operation with any desired phase overlap. This is a critical feature for achieving torque ripple minimization control performance as discussed in section 2.7.

The nominal voltage rating of all the switching devices and diodes is $\pm$Vdc, which is relatively low. The energy from the commutating phases is also transferred back to the source, which is the efficient utilization of energy.

The disadvantage of this converter is the high number of power switches for each phase (two switches and two diodes), which makes the converter cost relatively high.

3.4.2 Locked Rotor Test for Different Operation Modes of AHB Converter for Phase S1-S1'

There are two different tests for each power converter in PSCAD to show their characteristics. The first is the hard chopping on and off test which means the top and bottom switches are both on or both off; the second is the freewheeling test which means one switch is kept on all the time, while the other is toggled to regulate the current. This is also called the soft chopping mode. Details of the per phase SRM electrical model (a 0.316Ω resistor and variable inductor G1 connected in series) are discussed in detail in Section 3.9. The

same model is first used to compare the commutation and current regulation performance of the four selected converter topologies at an arbitrary locked rotor angle of 5°.

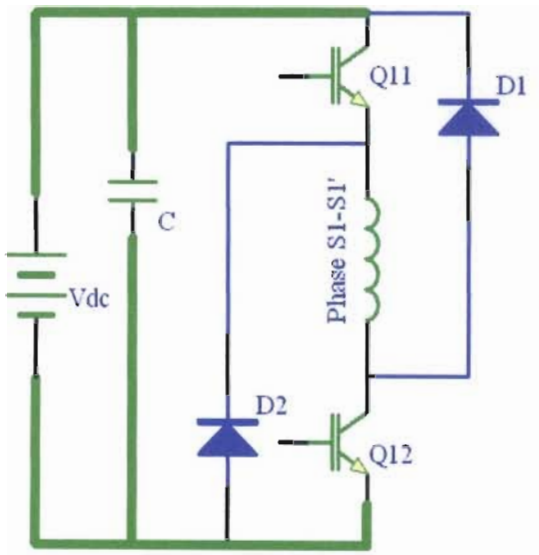

a) Hard on mode for phase S1-S1'

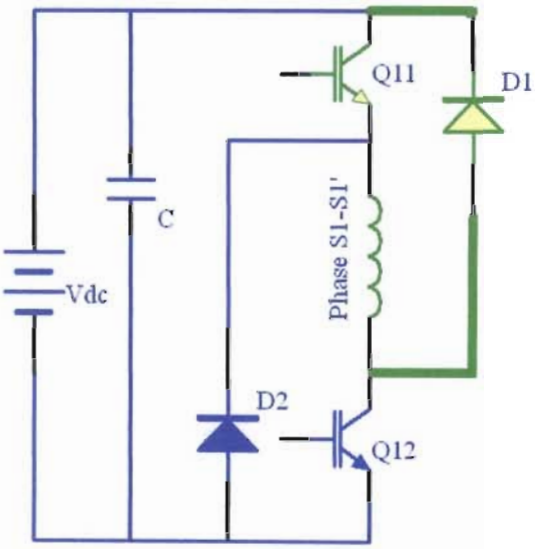

b) Freewheeling (soft chopping) mode for phase S1-S1'

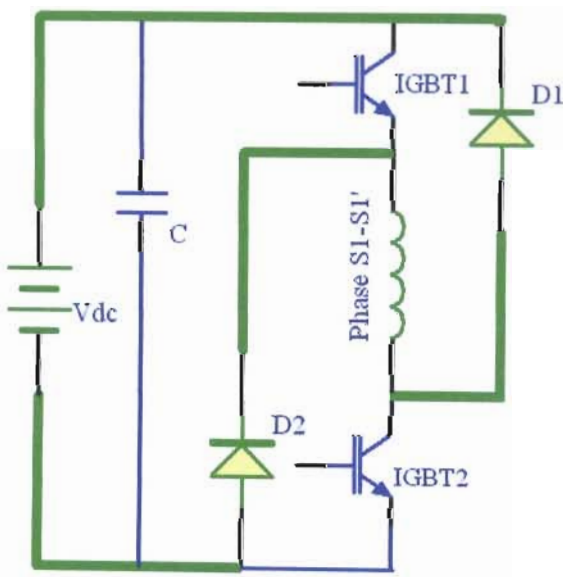

c) Hard off mode for phase S1-S1'

Fig. 3.2 Modes of operation of the AHB converter

- **Hard Chopping Mode**

Hard chopping on and off for phase S1-S1'is achieved by feeding the Q1 signal shown in Fig. 3.3 and to the bases of both Q11 and Q12, as shown in Fig 3.4.

In Fig. 3.4, the Q1 signal is scaled by a gain of 20 for clarity, and labeled 20*Q1. The effect of phase inductance saturation can be seen in the response of current I1 when Q1 switches from 0 to 1 (on) at t = 0s. The I1 response when Q1 switches from 1 to 0 (off) at t = 0.1s is faster due to the difference between the on and off commutation voltage, as shown on the E11 curve in Fig. 3.4.

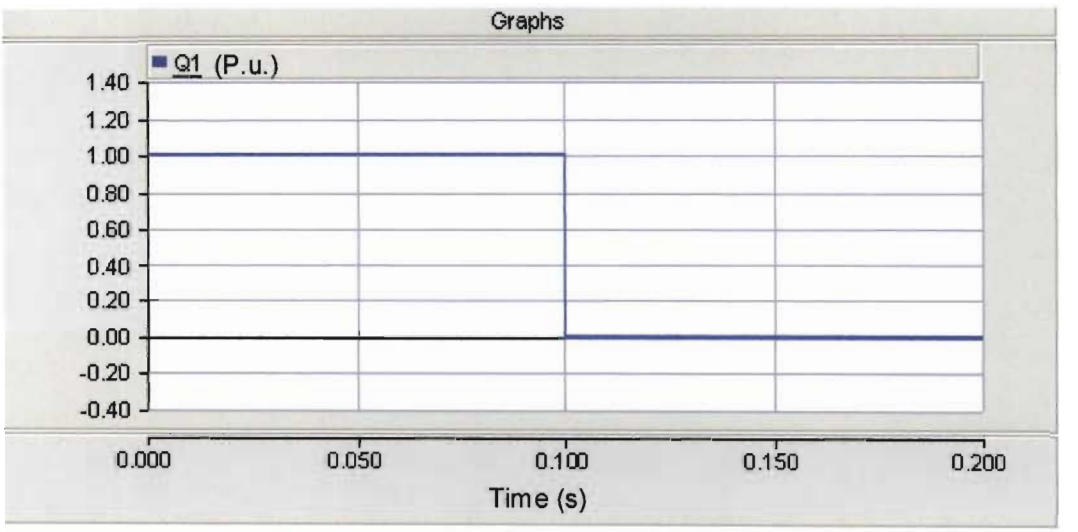

Fig. 3.3 Switching signals for hard chopping

- **Soft vs Hard Chopping Current Control**

The relative current control performance of the four selected topologies is investigated by enabling a simple hysteresis controller (with lower and upper thresholds at 4.5A and 5.5A) at t=0.1s, instead of simply switching Q11 and Q12 off at this time (off commutation). Fig. 3.5 (a) shows the soft chopping current response of phase S1-S1'. This was obtained by using Q11=1 and Q12=Q, as shown in Fig. 3.6(a). Fig. 3.5(b) shows the current control performance with hard chopping. This was obtained by using Q11=Q12=Q, as shown in Fig. 3.6(b). The soft and hard chopping hysteresis current control circuits can be seen in Appendix B.1.

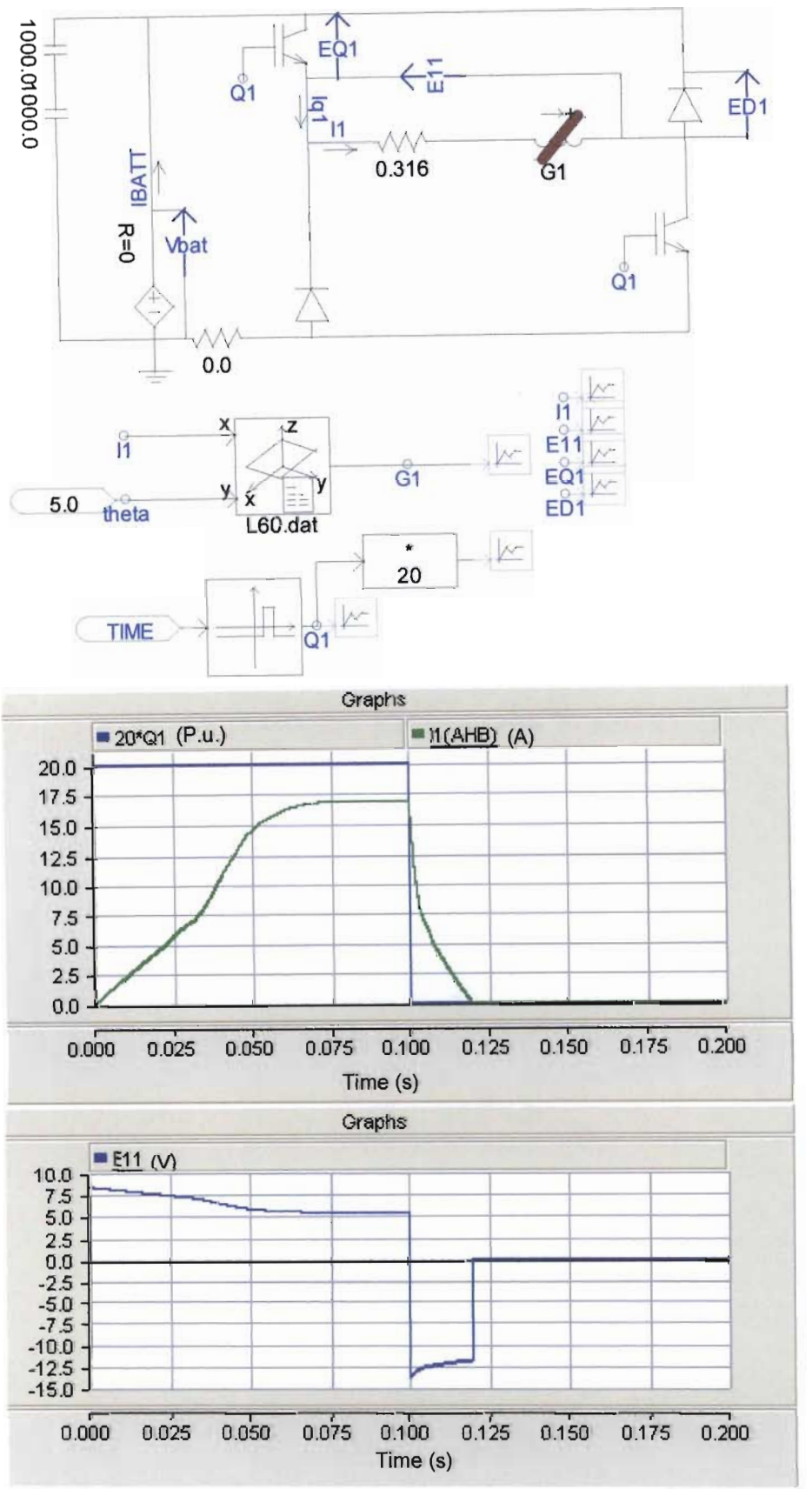

Fig. 3.4 AHB hard chopping circuit and phase current I1 (A) and phase voltage E11 (V) results (logic switching signal Q1 is multiplied by 20 to make it more visible)

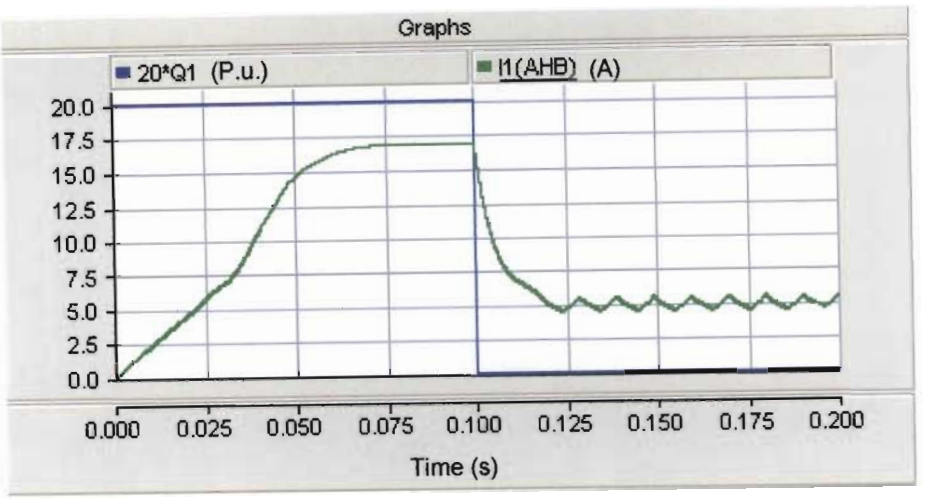

(a) Soft chopping

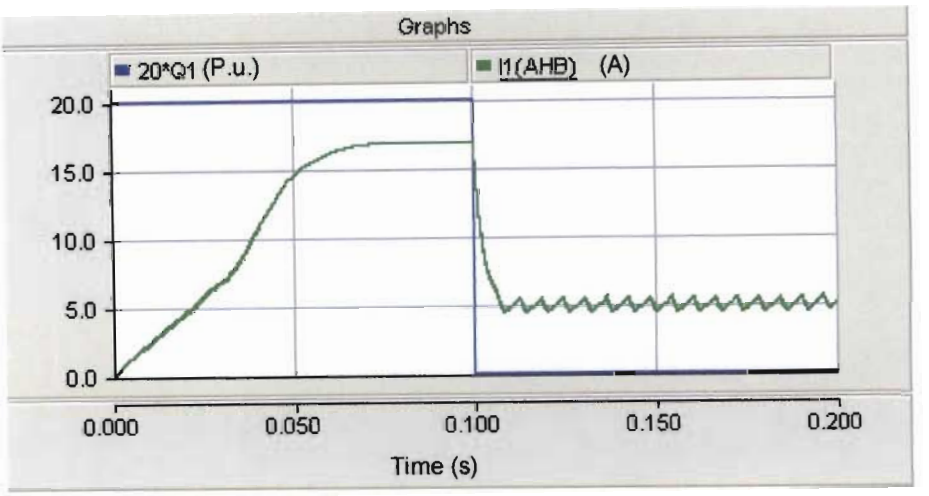

(b) Hard chopping

Fig. 3.5 Phase current of AHB converter under soft chopping and hard chopping with hysteresis current control

It can be seen from Fig. 3.5 that the current switching frequency in soft chopping is less than that in hard chopping for the same hysteresis band. Lower energy means fewer switching energy loss events per unit time. Soft chopping is thus more efficient than hard chopping. Especially the smaller phase voltage excursions in soft chopping also produce lower current ripple (and therefore lower torque ripple), in digital hysteresis control schemes where the error signal is sampled at a fixed frequency. Comparison of the current response immediately after 0.1s, however, shows that the commutation current tracking error is less for hard chopping. It will thus produce less commutation torque ripple. The control methods presented in chapters 4 and 5 of this thesis therefore use only hard chopping. Optimal use of both hard and soft chopping could form part of future work.

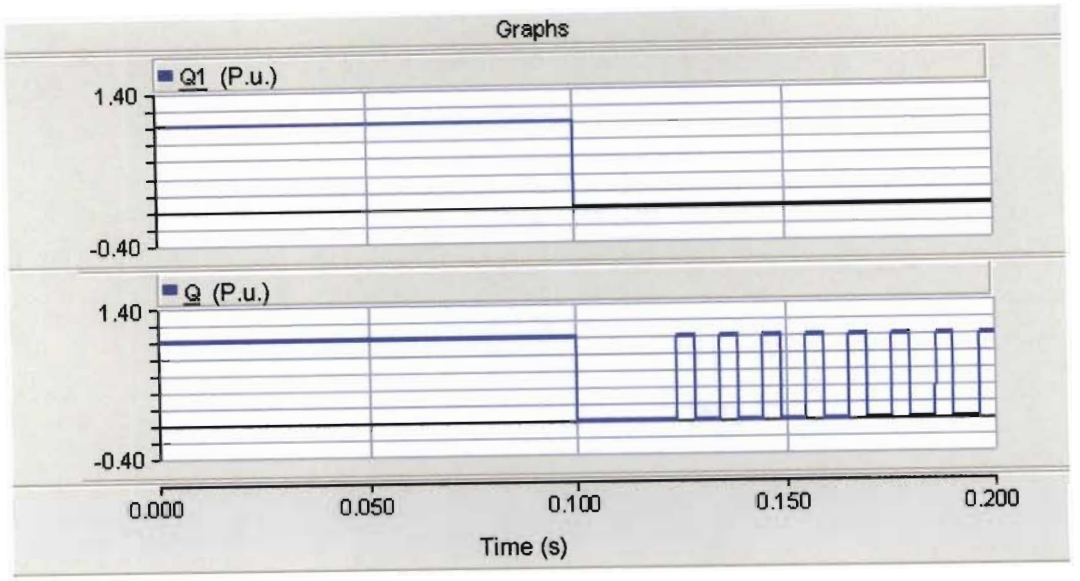

(a)

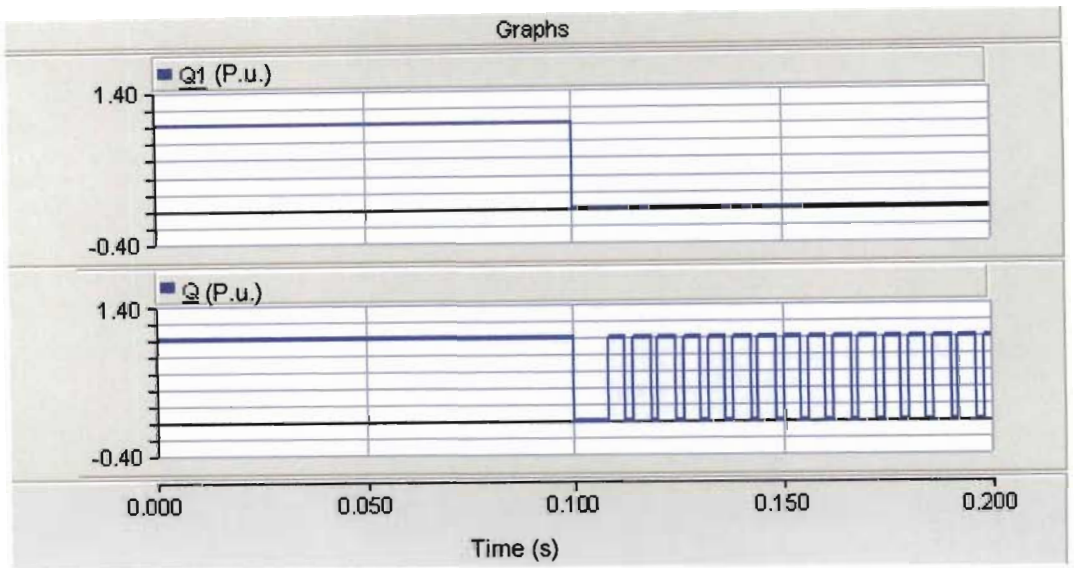

(b)

Fig. 3.6 Switching signals for soft (a) vs hard (b) chopping current control

The AHB converter topology is robust and flexible. It is also easy to achieve current and torque control with phase overlap, which is crucial for torque ripple minimization. The main disadvantage of the AHB is the relatively high number of power switches per phase. This results in a relatively low converter efficiency and relatively high cost. All other converters try to reduce the number of power switches and/or use a capacitor to minimize commutation (switch on and off) times. In the next section, the (n+1) switch converter is introduced because it uses less power switches compared with the AHB converter. Capacitor assisted commutation schemes are presented in sections 3.6 and 3.7.

3.5 The (n + 1) Switch Converter

3.5.1 N1S Converter Introduction and Principle of Operation

The AHB converter requires two switches and two diodes per phase, i.e. 2n switches and 2n diodes for an n-phase motor. The (n+1) switch (N1S) converter requires only (n+1) switches and (n+1) diodes for an n-phase motor. A four phase (8/6) SRM therefore requires five switches and five diodes, as shown in Fig. 3.7, where Q0 is the "+1"/common/main switch.

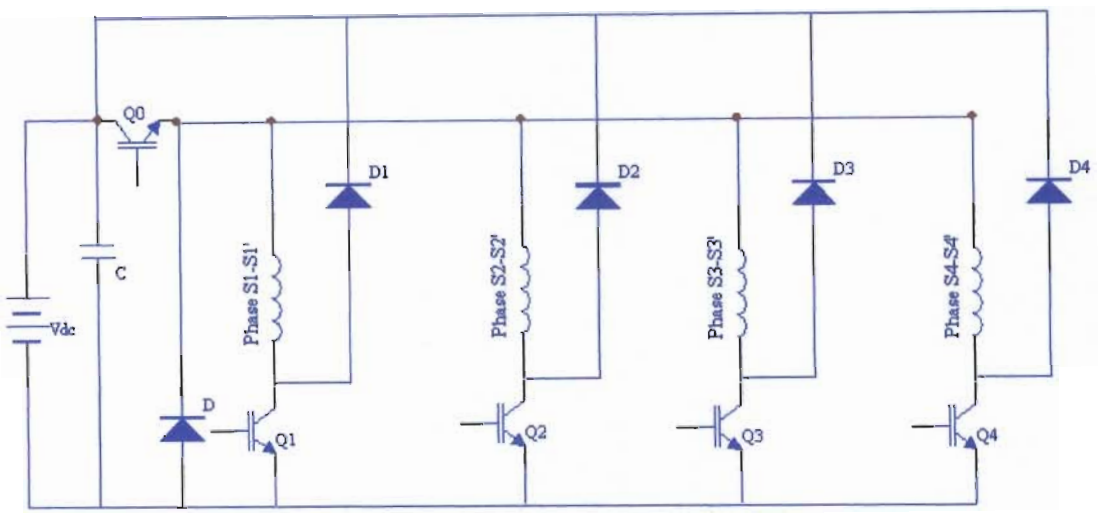

Fig. 3.7 N1S converter for a four phase SRM

There are three modes of operation in this converter. During the conduction phase, the common switch and conducting phase switch (Q0 and Q1 for phase S1-S1') are in the on state as shown in Fig. 3.8 (a). In the current regulation mode, common switch Q0 is turned off, and the current free wheels through the diode and the phase switch (D and Q1). The current is maintained at the reference value by using chopping on the common switch (Q0) while the phase switch (Q1) is left continuously on as shown in Fig. 3.8 (b).

The commutation occurs by turning both the common switch Q0 and the phase switch Q1 off as shown in Fig. 3.8 (c). The phase energy flows back to the source via two diodes. A voltage equal to $-\text{Vdc} - 2V_{fd}$ thus results across the phase during commutation.

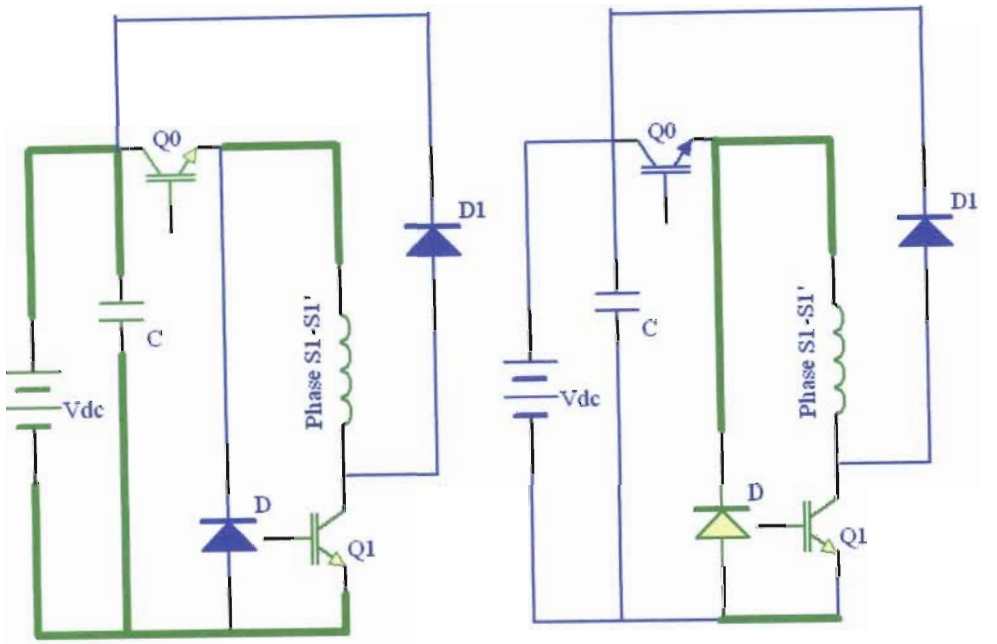

a) Hard on mode for phase S1-S1' *b) Freewheeling mode for Phase S1-S1'*

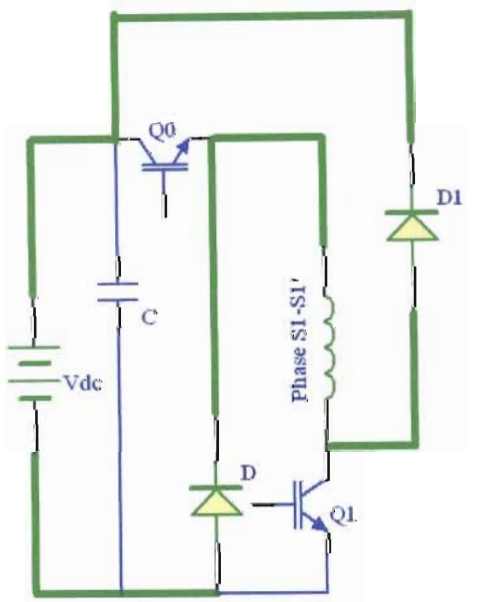

c) Hard off mode for phase S1-S1'

Fig. 3.8 Modes of operation of the N1S converter

The next phase cannot be turned on without putting the off going phase into freewheel (soft off) mode. The off going phase must therefore be completely demagnetized before the next phase is switched on via the common switch Q0. It is therefore not possible to implement independent or overlapping current control for torque ripple minimization. The main advantage of this topology is the lower number of switching devices.

3.5.2 Locked Rotor Test for Different Operation Modes of N1S Converter for Phase S1-S1'

Fig. 3.9 and Fig. 3.10 show that the (n+1) switch converter has the same performance as AHB converter when only one phase is working in both hard chopping and soft chopping mode. The advantage of this converter is that it has fewer switches, and therefore slightly less cost. The main disadvantage is its inability to implement effective torque ripple minimization because the phases are not independently controlled (which also results in lower robustness). It is, however, possible to improve the commutation performance of this type of converter by using a capacitor to supply and absorb the phase magnetization energy. Sections 3.6 and 3.7 consider two methods of implementing this strategy.

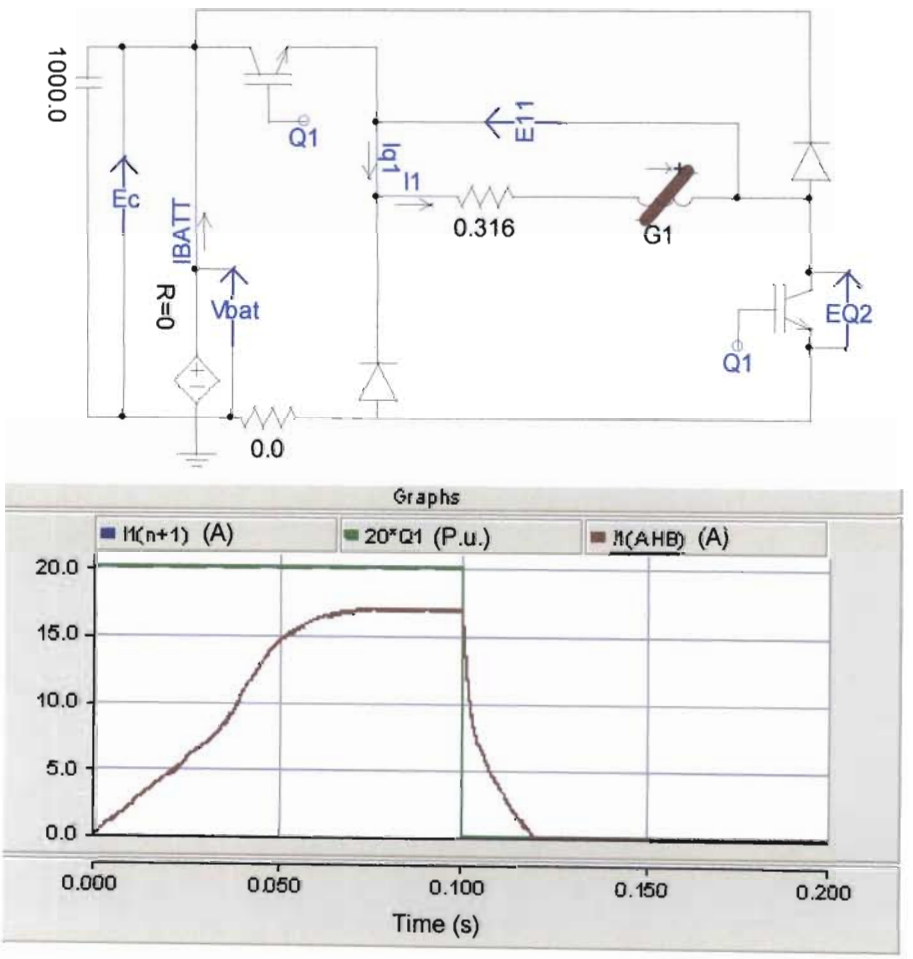

Fig. 3.9 N1S hard chopping circuit and phase current

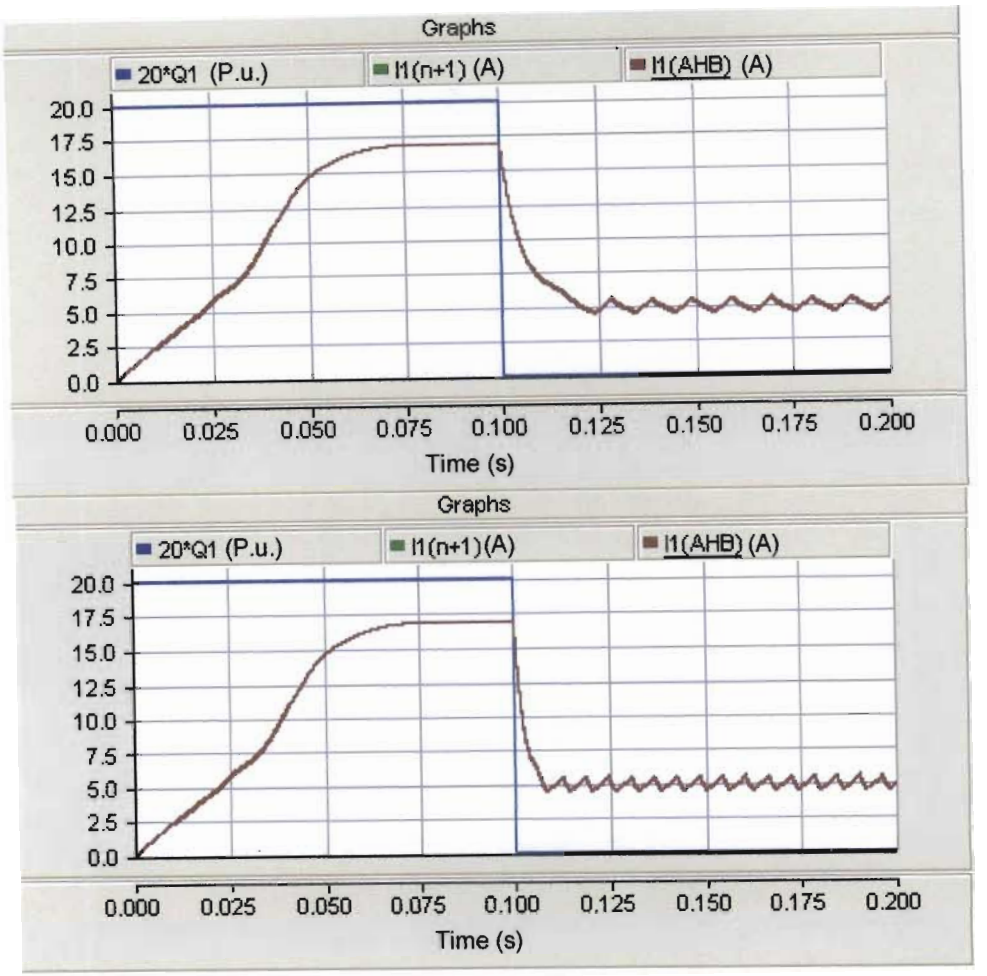

Fig. 3.10 N1S and AHB phase current under soft chopping and hard chopping with hysteresis current control

3.6 The Modified C-dump Converter

3.6.1 MCD Converter Introduction and Principle of Operation

There are several types of so called C-dump converters which make use of capacitor energy storage for faster on and off switching. Two particular C-dump variants considered in this chapter are modified C-dump (MCD) and cost effective C-dump (CECD) converter. These two converter types illustrate all of the key characteristics and advantages and disadvantages of this class.

Fig. 3.11 shows the MCD converter circuit [3.2]. This topology improves on the original C-dump converter [3.6] by eliminating the inductor in the original dump circuit. The capacitor feeds the phase demagnetization energy to the next phase to be turned on instead of the

voltage source. The resulting commutation is faster than in the AHB or N1S topologies because the commutating voltage is significantly higher than the source voltage.

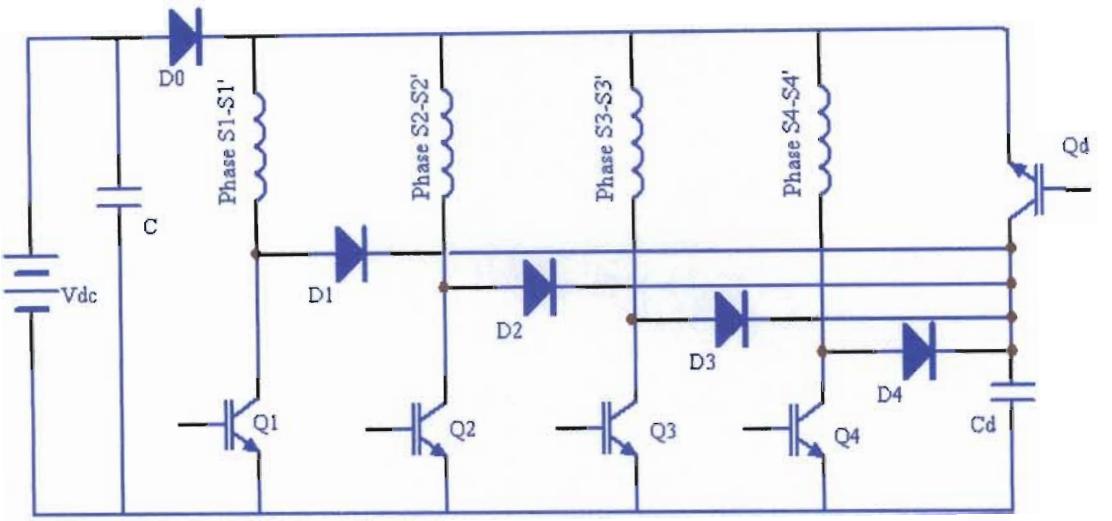

Fig. 3.11 MCD converter for a four phase SRM

Fig. 3.12 (a) to (c) shows the sequence in which switches and diodes are commutated to energize and de-energize phase S1-S1'. Fig. 3.12 (d) shows the first step in the sequence for phase S2-S2'.

In Fig. 3.12 (a), both Qd and Q1 are closed. If the capacitor voltage Vcd is larger than Vdc, phase S1-S1' is energized by Vcd. Otherwise, phase S1-S1' is energized by the DC link. In Fig. 3.12 (b), the phase S1-S1' is demagnetized through freewheeling diode D1 and dump switch Qd. In Fig. 3.12 (c), both Qd and Q1 are turned off and phase S1-S1' is demagnetized through D1, capacitor Cd and input voltage source Vdc. The capacitor is thus charged with some of the demagnetization energy from the S1-S1' phase winding (the balance is regenerated into the DC supply and dissipated in the supply resistance and freewheeling diodes). Fig. 3.12 (d) shows phase S2-S2' energized which is equivalent to the model shown in Fig. 3.12 (a).

During the commutation, the voltage across the phase is the difference between the capacitor voltage and the source voltage. The capacitor voltage depends on the capacitor size and the amount of energy which is dumped ($\because E = \frac{1}{2}CV^2 \therefore V = \sqrt{\frac{2E}{C}}$). Higher capacitor voltage results in a faster turn off (and turn on of the next phase), but requires diodes and switching devices with higher voltage ratings.

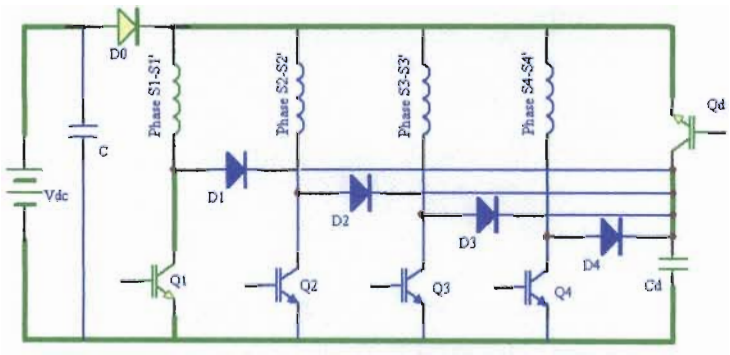

a) Hard on mode for Phase S1-S1'

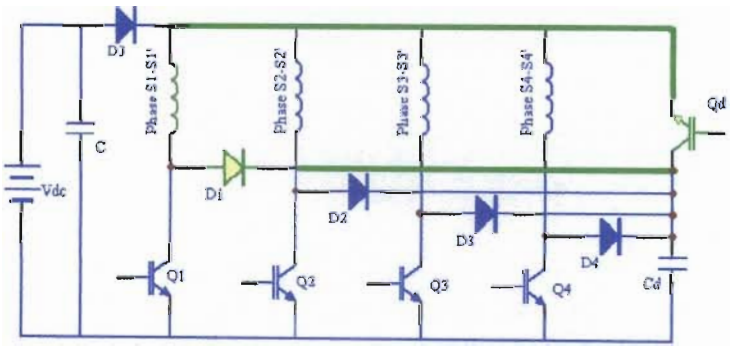

b) Freewheeling mode for Phase S1-S1'

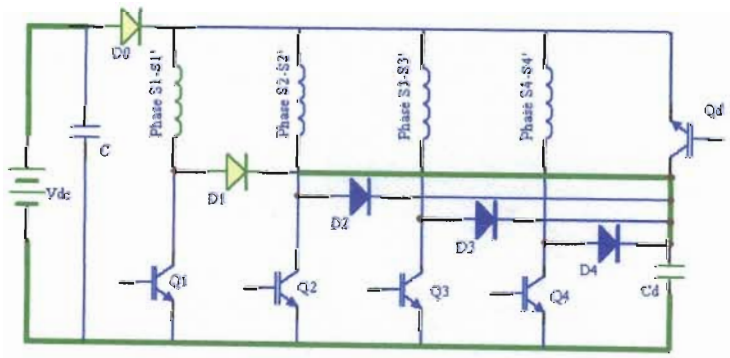

c) Hard off mode for Phase S1-S1'

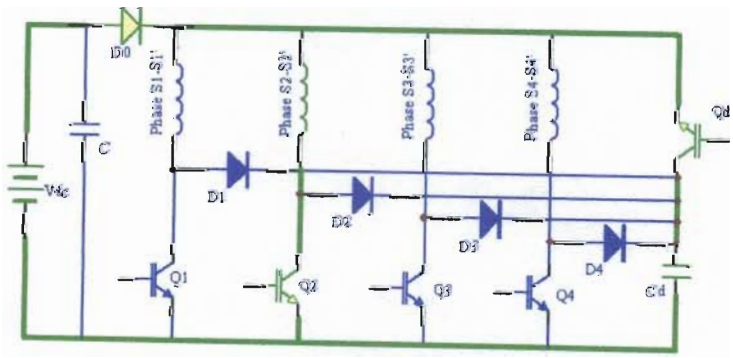

d) Hard on mode for Phase S2-S2'

Fig. 3.12 Modes of operation of the MCD converter

3.6.2 Locked Rotor Test for Different Operation Mode of MCD Converter for Phase S1-S1'

Fig. 3.13 shows the MCD converter circuit. Q1 is same switching signal shown in Fig. 3.3. Fig. 3.14 shows the phase current and capacitor voltage results with hard chopping when the initial condition of the $10\,\mu F$ capacitor is zero. Fig. 3.15 shows the phase current and capacitor voltage result when the capacitor has a non-zero initial condition (achieved by switching signal Q1a as shown in Fig. 3.16).

The performance of the MCD is strongly dependent on the size of the dump capacitor. Fig. 3.17 and Fig. 3.18 show how the performance changes for lower and higher values of capacitance. When Cd is smaller, the voltage across it will be higher (about 1800V for 1 μF and about 200V for 100 μF) and the hard chopping rate of change of phase current di/dt will be higher.

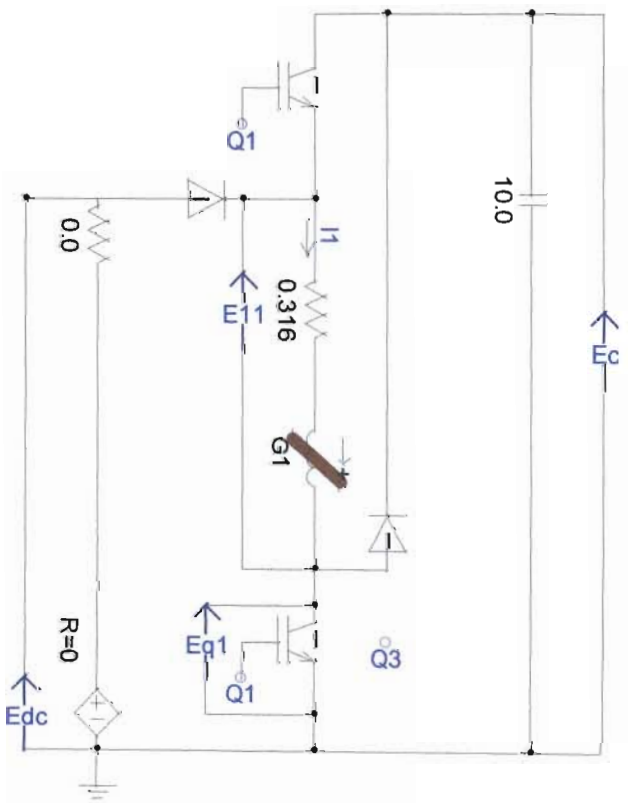

Fig. 3.13 MCD hard chopping circuit

Fig. 3.19 compares the AHB and MCD converter performance in the hard chopping mode (with zero initial dump capacitor voltage). The MCD phase current drops much faster the AHB current at the expense of significantly higher device voltages (the same is true with

respect to rate of rise of phase current for non-zero initial dump capacitor voltage, as shown in Fig. 3.15). The steady state current in the MCD converter is slightly higher than in the AHB converter because there is no voltage drop across the top switch when the capacitor initial condition is less than Vdc (no current flows through the top switch). The diode voltage drop in the MCD converter is also less than the top switch voltage drop in AHB converter.

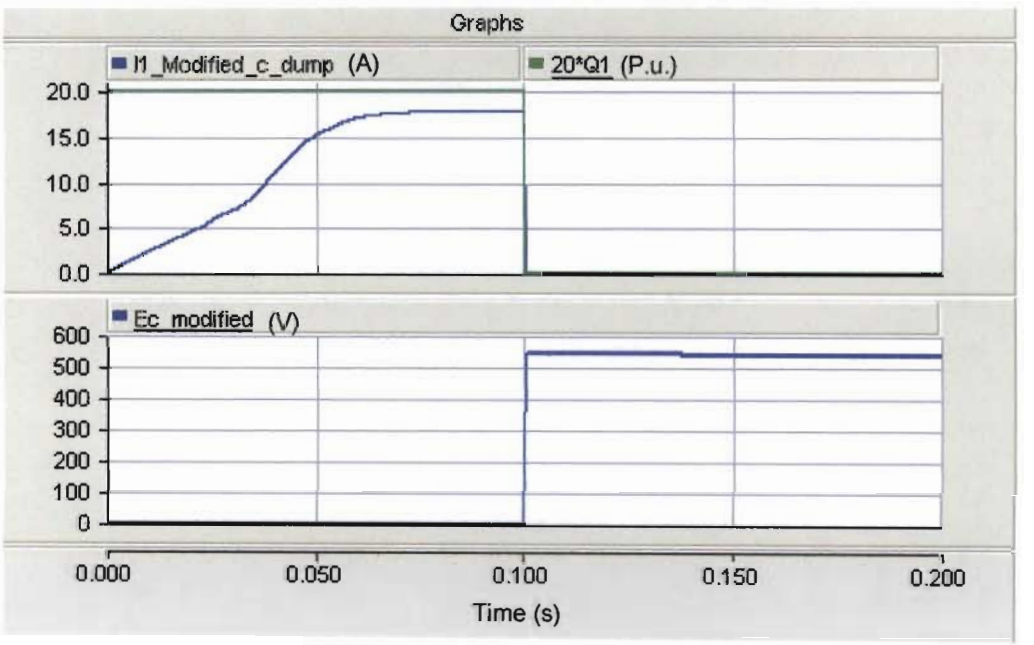

Fig. 3.14 MCD hard chopping phase current and capacitor voltage

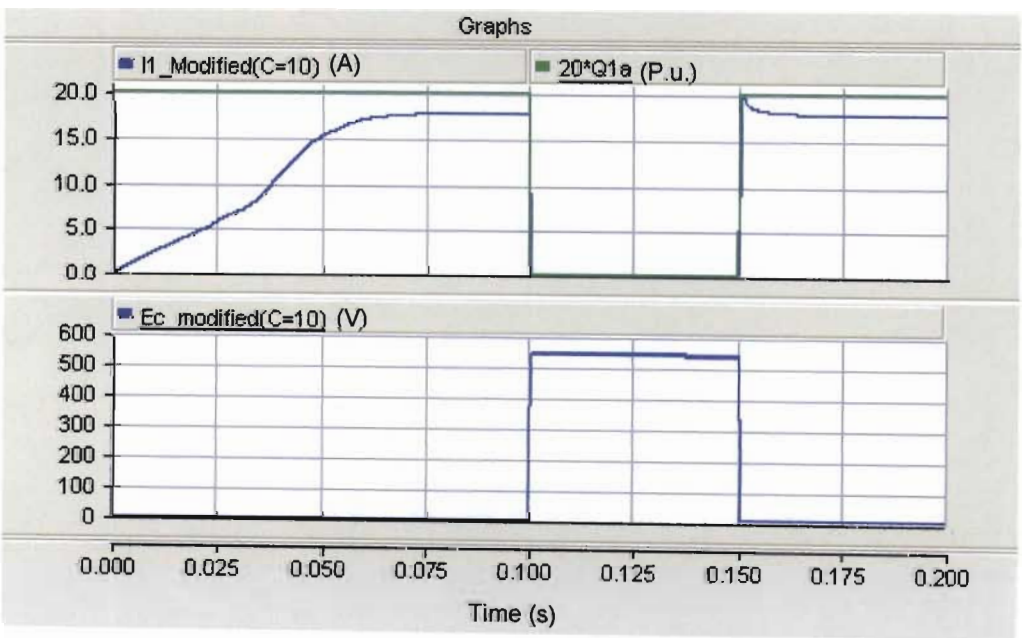

Fig. 3.15 MCD hard chopping phase current and capacitor voltage with non-zero initial capacitor voltage

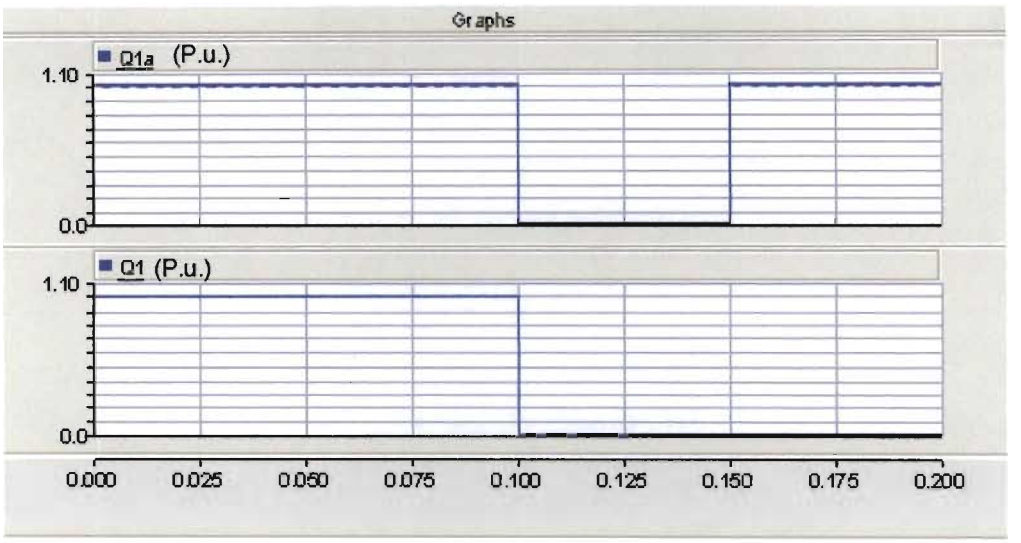

Fig. 3.16 MCD hard chopping switching signals for non-zero initial capacitor voltage test

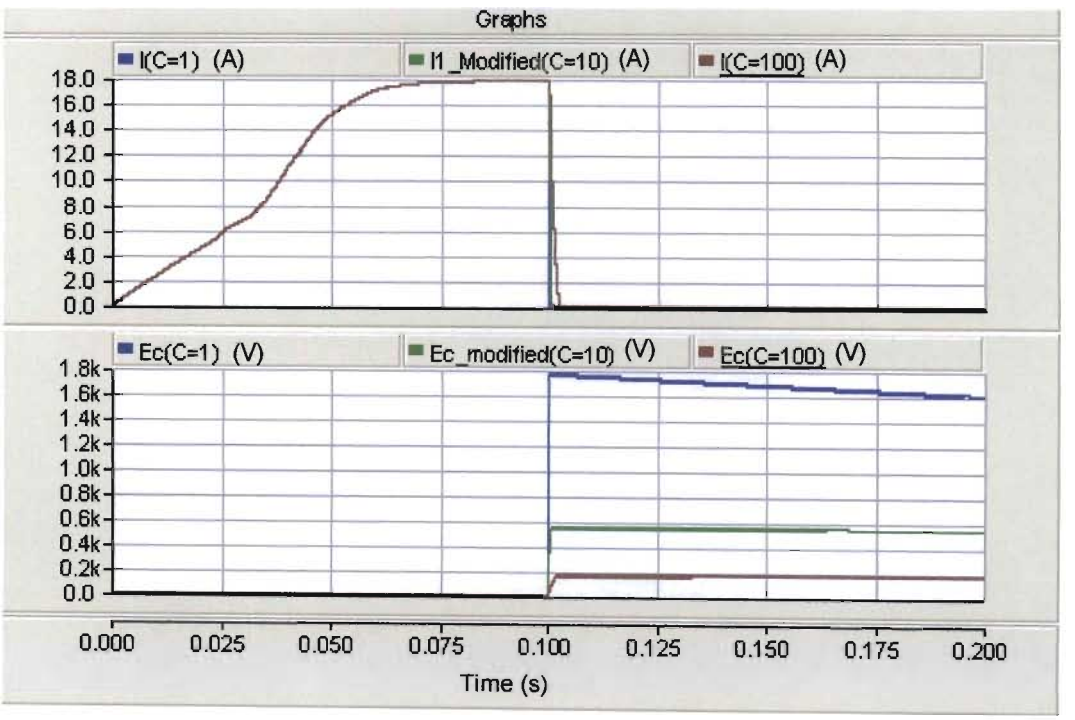

Fig. 3.17 MCD phase current and capacitor voltage under hard chopping condition for Cd ∈ {1, 10,100} μF

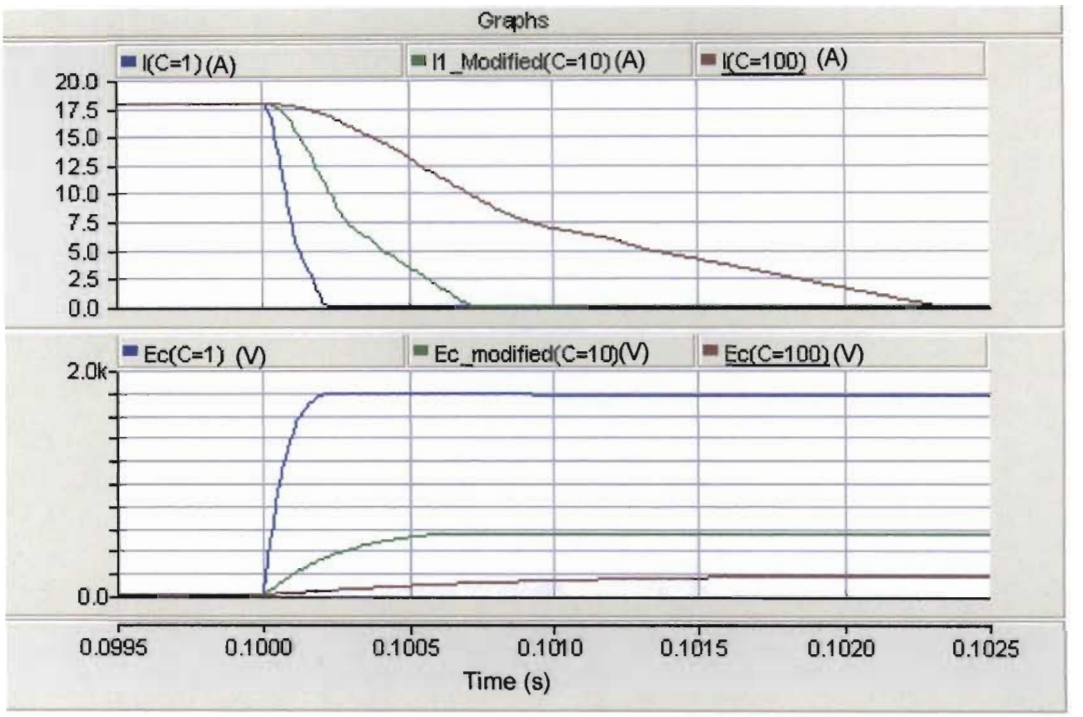

Fig. 3.18 MCD phase current and capacitor voltage under hard chopping condition for Cd ∈ {1, 10,100} μF (zoom of Fig. 3.17)

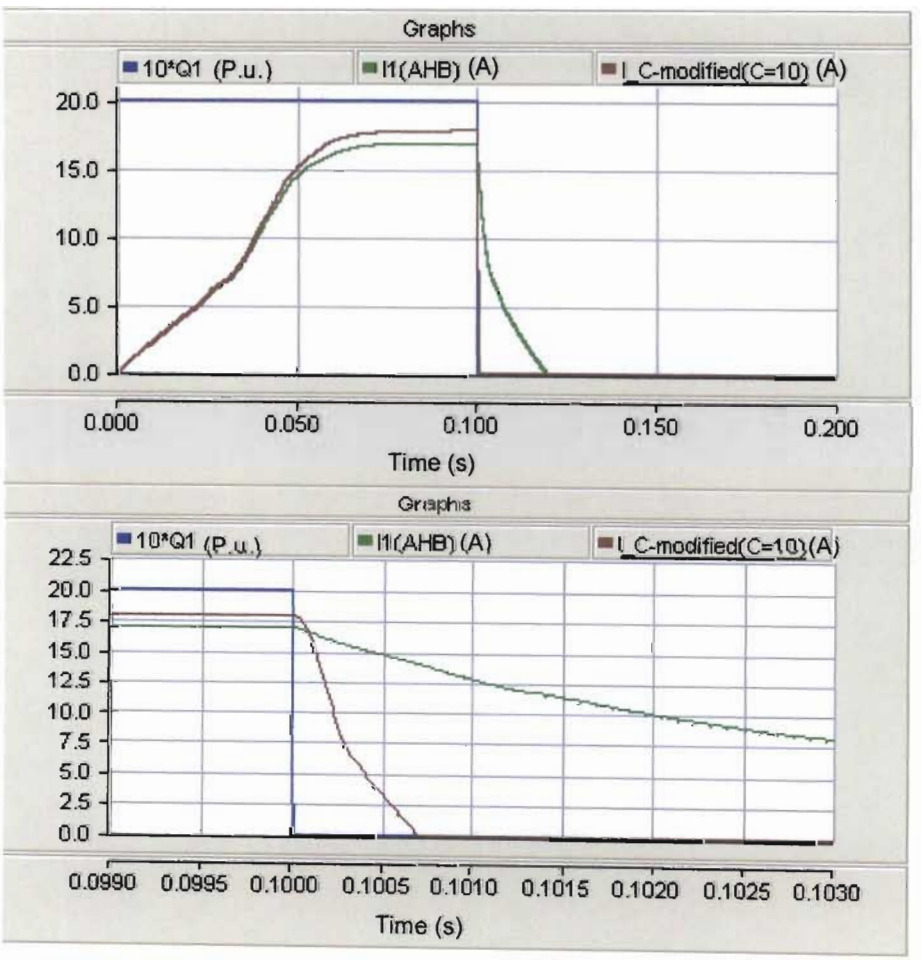

Fig. 3.19 AHB and MCD Phase current

Fig. 3.20 compares the AHB and MCD converter performance in the soft and hard chopping hysteresis current control modes.

It can be seen from Fig. 3.20 that, as in the case of the AHB, the soft chopping switching frequency is less than for hard chopping. The voltage across the capacitor is also much less than that for hard chopping. The main benefit of this converter is that very rapid commutation can be obtained at the expense of devices with higher nominal voltage ratings. A trade-off can be made between device voltage ratings and commutation speed by using a larger value of dump capacitance, as shown in Fig. 3.17, but impractically high capacitance values would generally be needed to keep the voltage increase below one order of magnitude. A further alternative is to implement a dump capacitor voltage regulation scheme, whereby the hard off mode is used until a predetermined voltage is reached. The remainder of the demagnetization would then have to be achieved via freewheeling and/or simultaneous magnetization of the next phase. A further drawback of this scheme is that the demagnetization current has to flow through the source and the dump capacitor in series in the hard off mode, as shown in Fig. 3.12(c). Vcd therefore has to be regulated to at least 2Vdc [3.1, 3.2, 3.7 and 3.8] in order to provide an off commutation voltage equal to –Vdc (the AHB and N1S value). The cost of the MCD converter is thus relatively high due to the higher voltage rating of the circuit components. The next section presents a cost-effective version of this topology which permits regulation of Vcd down to Vdc, instead of 2Vdc [3.1, 3.2, 3.7, and 3.8].

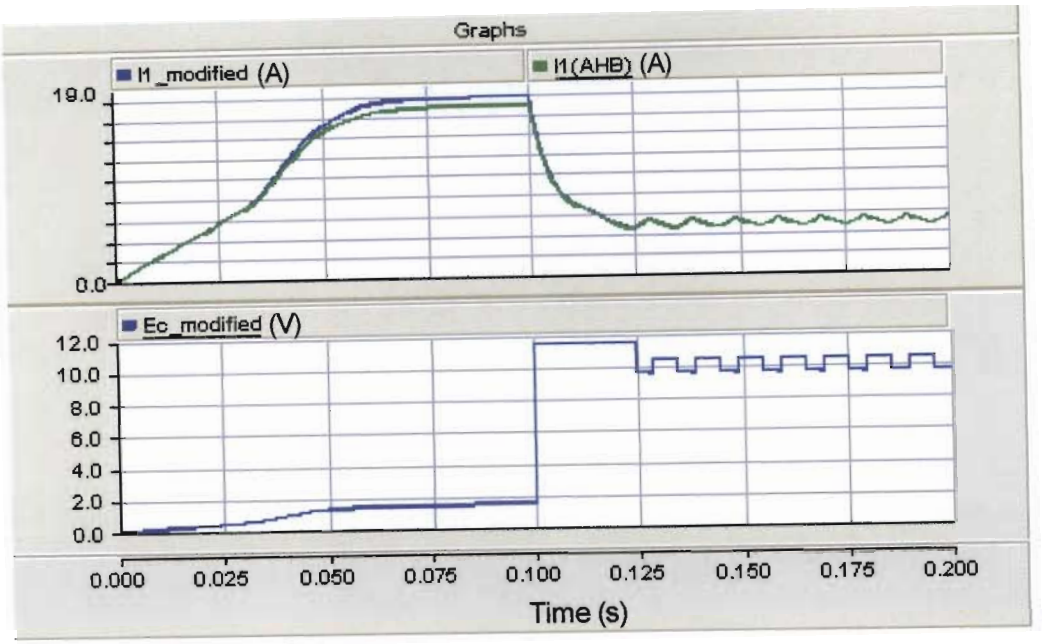

(a) Soft chopping

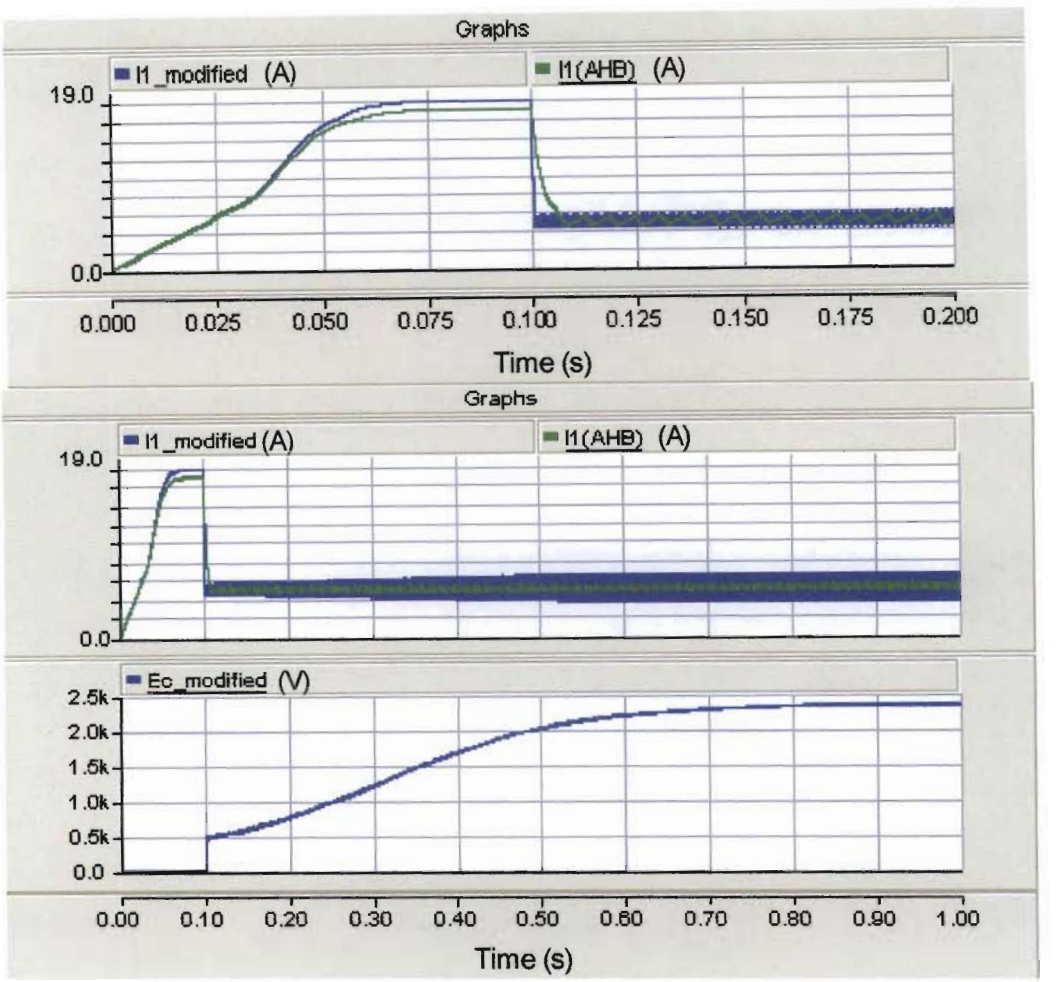

(b) Hard chopping

Fig. 3.20 MCD soft chopping and hard chopping phase current and capacitor voltage

3.7 The Cost-effective C-dump Converter

3.7.1 CECD Converter Introduction and Principle of Operation

The cost-effective C-dump (CECD) converter circuit [3.7] is shown in Fig. 3.21. Inclusion of diodes Dc and Dd into the MCD structure enables a commutation voltage of –Vdc to be obtained with a regulated dump capacitor voltage of Vdc, instead of 2Vdc. This is made possible by removing the voltage source from the demagnetization circuit in the hard off mode. This significantly reduces the voltage ratings for the switching devices, (as shown in Fig 3.22(c)), and hence the cost of the converter. A further advantage of this approach is that one phase can be operated in the hard off mode while the next phase is operated in the hard on mode, as shown in Fig 3.22(d).

During the conduction mode (Fig. 3.22 (a)), phase S1-S1' starts to magnetize with both Q1 and Qd on. If Vcd is regulated to a value higher than Vdc (at the expense of higher device voltage ratings), then the phase is energized from the capacitor until the capacitor voltage drops to the level of input voltage Vdc. The blocking diode Db then becomes forward biased and the source begins to feed energy to the phase S1-S1'. The current is regulated to the reference value by switching Q1 on and off (Fig. 3.22 (b)). The phase current freewheels through diode D1 and Qd when Q1 is off. The current commutates with Q1 and Qd off (Fig. 3.22(c)), and charges the dump capacitor until the required Vcd limit is reached, when Qd must be switched on (i.e. freewheeling is resumed). Diode Dd prevents the demagnetizing current from flowing through the source. While phase S1-S1' is being demagnetized, phase S2-S2' can be magnetized by turning Q2 on (Fig. 3.22 (d)). During this period, the current through phase S2-S2' can be regulated by dumping energy into the capacitor [3.8].

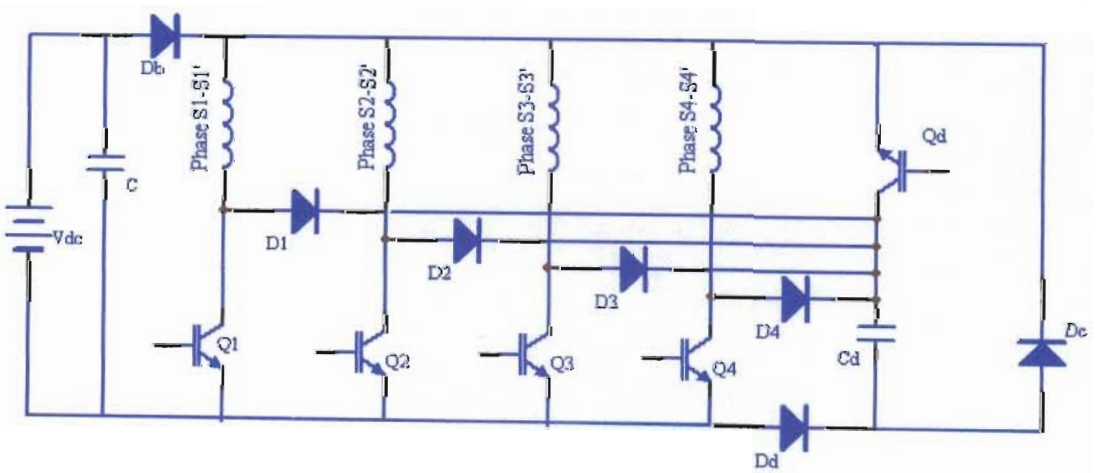

Fig. 3.21 CECD converter for a four phase SRM

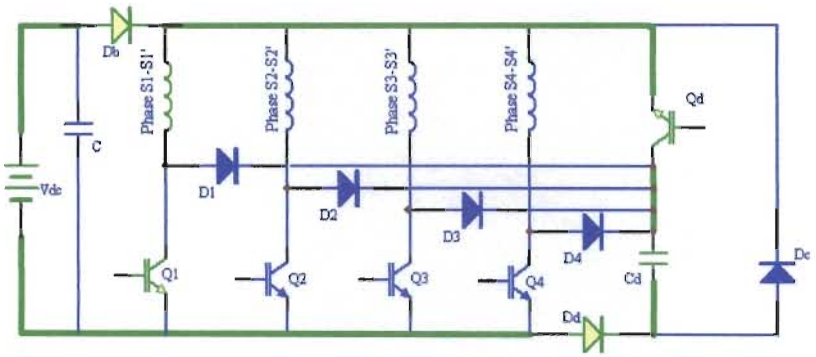

a) Hard on mode for Phase S1-S1'

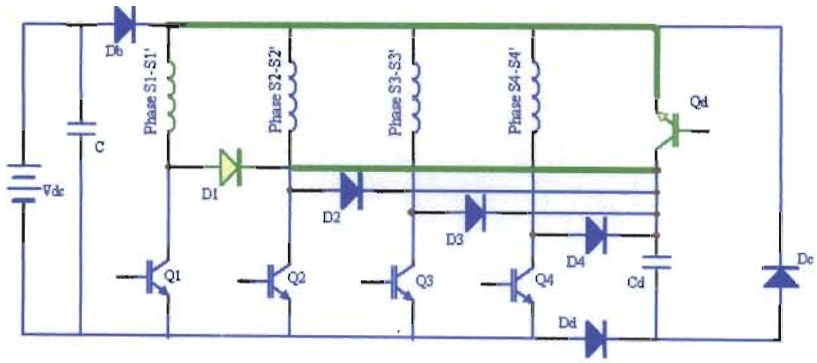

b) Freewheeling mode for Phase S1-S1'

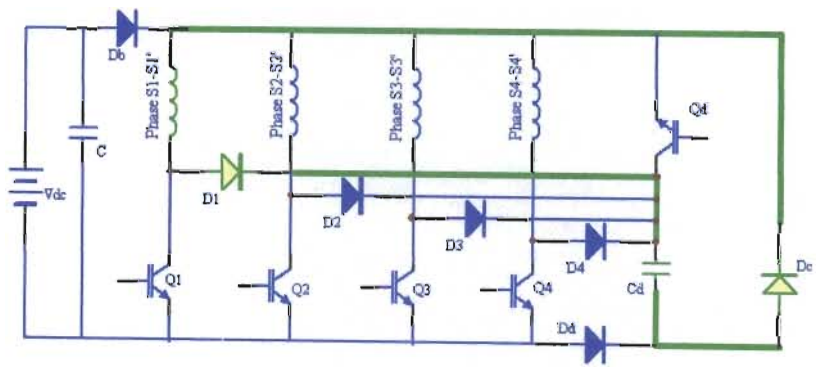

c) Hard off mode for Phase S1-S1'

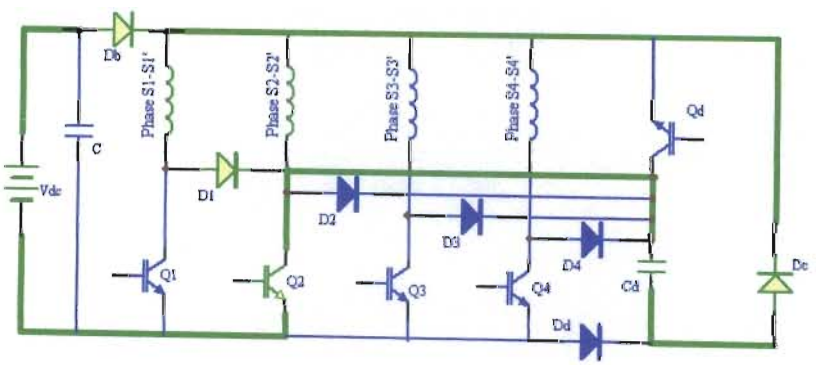

d) Hard on mode for Phase S2-S2'

Fig. 3.22 Modes of operation of the CECD converter

3.7.2 Locked Rotor Test for Different Operation Mode of CECD Converter for Phase S1-S1'

- **Hard Chopping Mode**

Fig. 3.23 shows the CECD converter circuit. The MCD and CECD hard on and off phase current and capacitor voltage are compared in Fig. 3.24 (for zero initial capacitor voltage). It can be seen that these responses are almost identical as can be expected due to the similarity of their conduction paths in this mode (CECD only has two more diodes than MCD).

- **Soft vs Hard Chopping Current Control**

Fig. 3.25 shows the voltage across the capacitor in CECD converter is much less than MCD converter in soft chopping mode so that the power switches' ratings for CECD converter can be much less as well.

Fig. 3.26 shows that the MCD converter capacitor needs to handle higher voltages to give the same hysteresis current control performance compared with the CECD converter when Vcd is not regulated. The phase current of CECD converter also shows that current can be regulated in the same hysteresis band with a lower switching frequency, and hence lower switching losses.

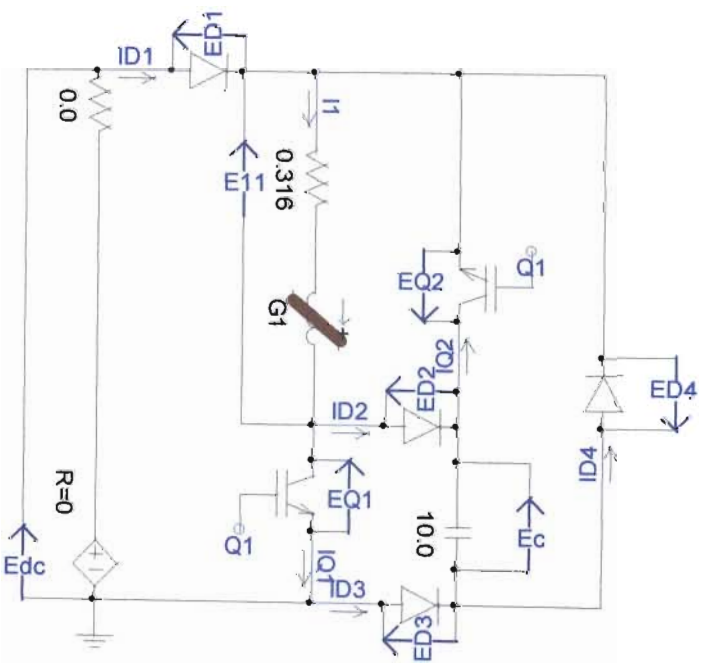

Fig. 3.23 Cost-effective C-dump converter circuit

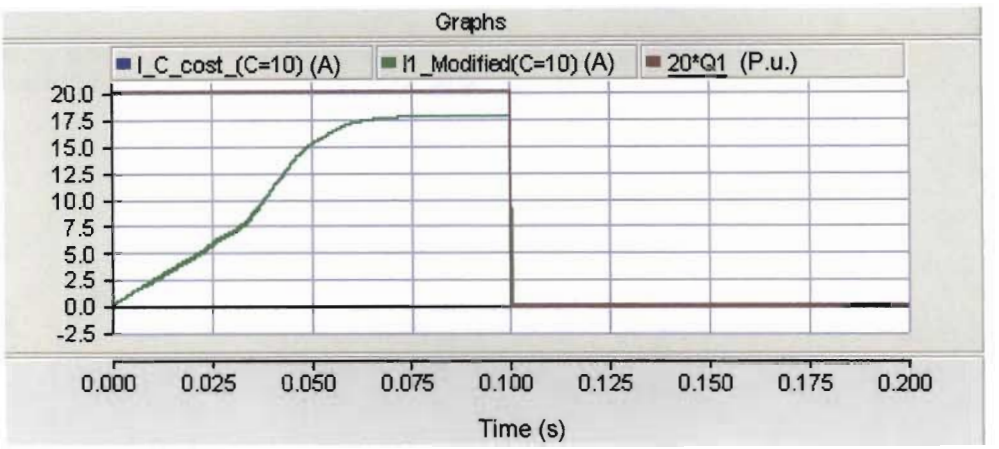

(a) Phase current

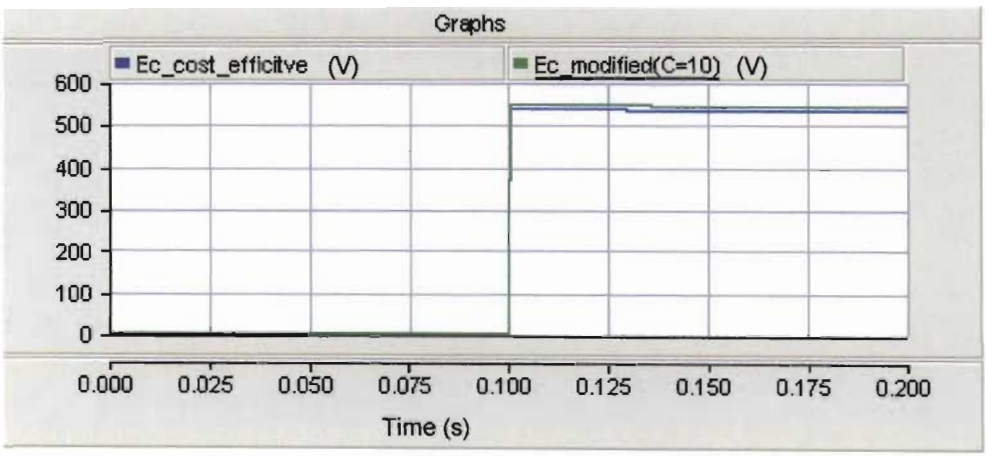

(b) Voltage across capacitor

Fig. 3.24 CECD hard chopping phase current and capacitor voltage

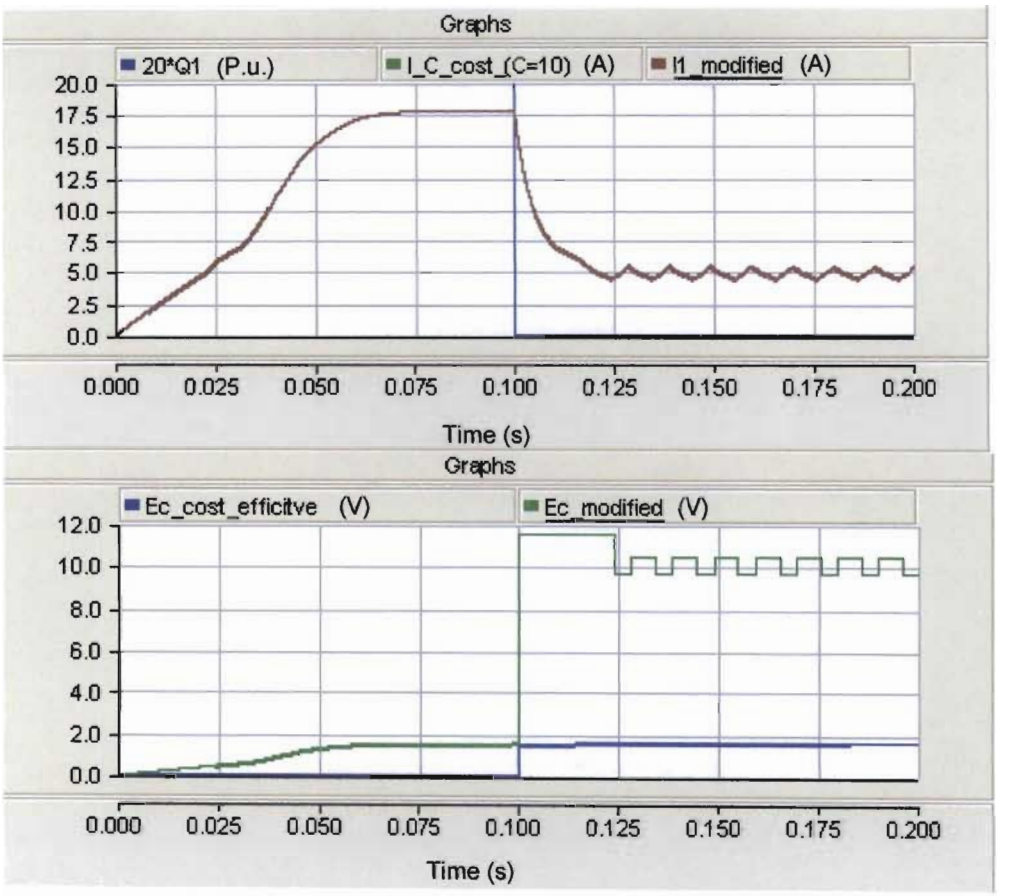

Fig. 3.25 Phase current and capacitor voltage with hysteresis current control on soft chopping mode

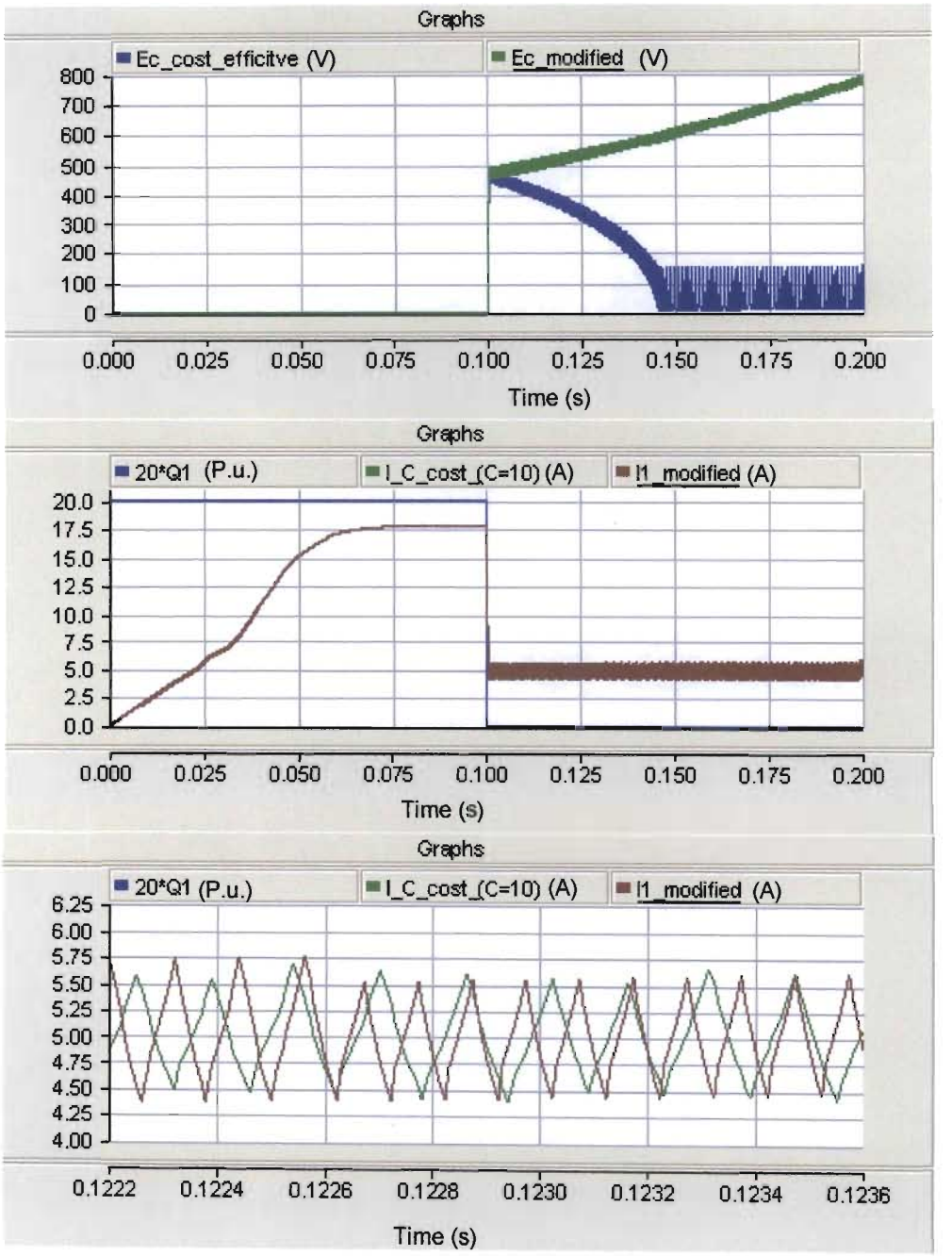

Fig. 3.26 Phase current and capacitor voltage with hysteresis current control on hard chopping mode

3.8 SRM Converter Topology Selection

Sections 3.4 to 3.7 have explained the operation and compared the commutation and current regulation performance of the AHB, N1S, MCD and CECD converter topologies.

In all of the converters discussed, there is a trade off between the performance and the cost of the converter. From the AHB converter to the C-dump converter, the reduction in the number of switching devices and voltage drops per phase is achieved at the cost of increased control algorithm complexity. Converters with a reduced number of switches are also typically less fault tolerant. The fault tolerance of a converter is a prime consideration for the reliability of the drive.

Table 3.1 presents a simple qualitative comparison of these topologies. In this comparison, each converter type is ranked according to several economy and performance criteria, where a ranking of 1 indicates the best topology, and 4 indicates the worst topology. All criteria are equally weighted to obtain an overall total ranking. The lowest total corresponds to the best overall topology. This ranking procedure shows the AHB to be the best overall topology.

The AHB converter is robust, stable and can achieve better performance for torque ripple minimization, which is the main concern in this thesis so that it is chosen as the converter strategy for the four phase 8/6 SRM drive from now.

It is explained in chapter 5 how three individual three-phase converters were configured to produce a four-phase AHB converter for the practical work of this thesis. The next section shows how the PSCAD SRM and AHB models are validated by means of the same locked rotor and free rotor alignment tests used to validate the Matlab/Simulink models presented in Chapter 2.

Type	Economy			Performance			Total
	Device Count	Voltage Rating	Control Simplicity	Commutation	Independence	Ripple	
AHB	4	1	1	3	1	1	11
N1s	1	1	2	3	4	2	13
MCD	2	4	3	1	3	4	17
CECD	3	3	4	2	2	3	17

Table 3.1 Performance comparison of four converter topologies

3.9 Validation of PSCAD AHB/SRM Model

3.9.1 Locked Rotor Test for PSCAD SRM Model

In the locked rotor test, the rotor is fixed at an angle of 5° (i.e. the same condition presented for the Matlab/Simulink model in chapter 2). The Matlab/Simulink electrical model block diagram is explicitly built to solve the SRM phase voltage equation. This equation is implicitly solved in the PSCAD model by constructing the equivalent circuit diagrams of the SRM phases, i.e. a resistance of 0.316Ω in series with variable inductance G1. The model shown in Fig. 3.27 therefore only needs an inductance lookup table to reproduce the simulated phase voltage and current response shown in Fig.2.12. The phase inductance G1 is obtained from the lookup table L60.dat shown in appendix B.2.

The variable inductance component G1 is not a standard library component at the time of writing this thesis. It was obtained from Manitoba Hydro (the makers of PSCAD) upon special request because the standard variable inductance component did not work for this application. The standard variable inductance component can only be used to specify different inductance values at the start of a simulation, because it uses the differential equation V=Ldi/dt. The G1 component, however, can be used to simulate SRMs because it uses the equation V=d(Li)/dt, where L can be varied according to the required nonlinear function of rotor position and phase current (or an equivalent lookup table).

In Fig 3.27, three lookup tables (Vph_mea.dat, Vdc_mea.dat and I_mea.dat) are used to plot graphs of measured values (measured phase voltage, DC battery voltage (the DC battery voltage droops during the test) and phase current obtained during the corresponding practical locked rotor test) on the same axes as the PSCAD simulation results. In the results of Fig. 3.28, I1 and E11 are the simulated phase current and voltage result with the rotor locked at 5°, I_mea and Vph_mea are the measured phase current and voltage result with the rotor locked at 5°.

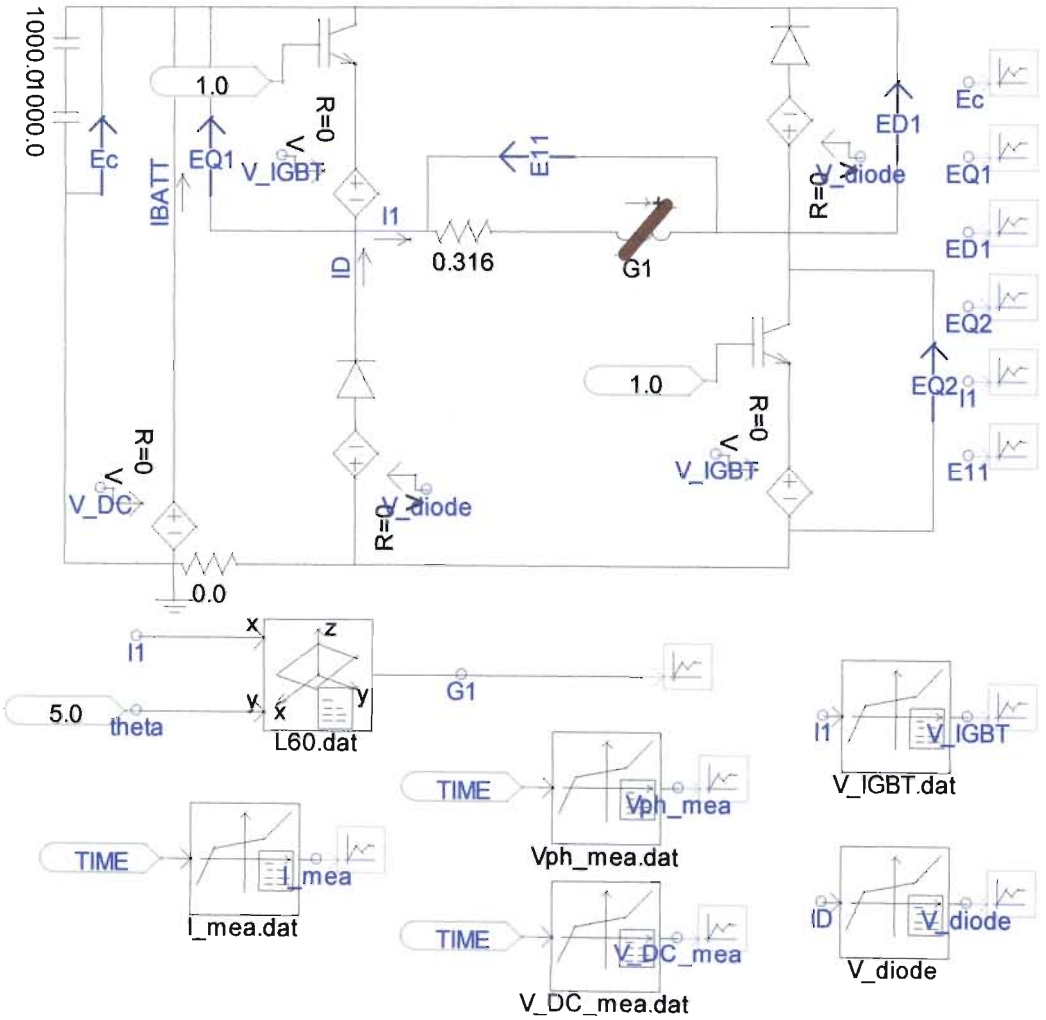

Fig. 3.27 One phase locked rotor PSCAD SRM and AHB converter model

The characteristics of the AHB IGBTs and diodes are highly nonlinear with respect to current, and therefore cannot be accurately represented by simply setting the PSCAD converter and diode block parameters. Measured characteristics are therefore used by means of lookup tables to accurately simulate these components. V_IGBT and V_diode are the measured IGBT and diode characteristics respectively seen in appendix B.3.

Fig. 3.28 compares the PSACD phase current and phase voltage responses (at a fixed angle of 5°) with the corresponding measured responses. The close agreement between the simulated current and voltage responses and the measured responses validates the PSCAD *electrical* SRM and AHB models under these test conditions.

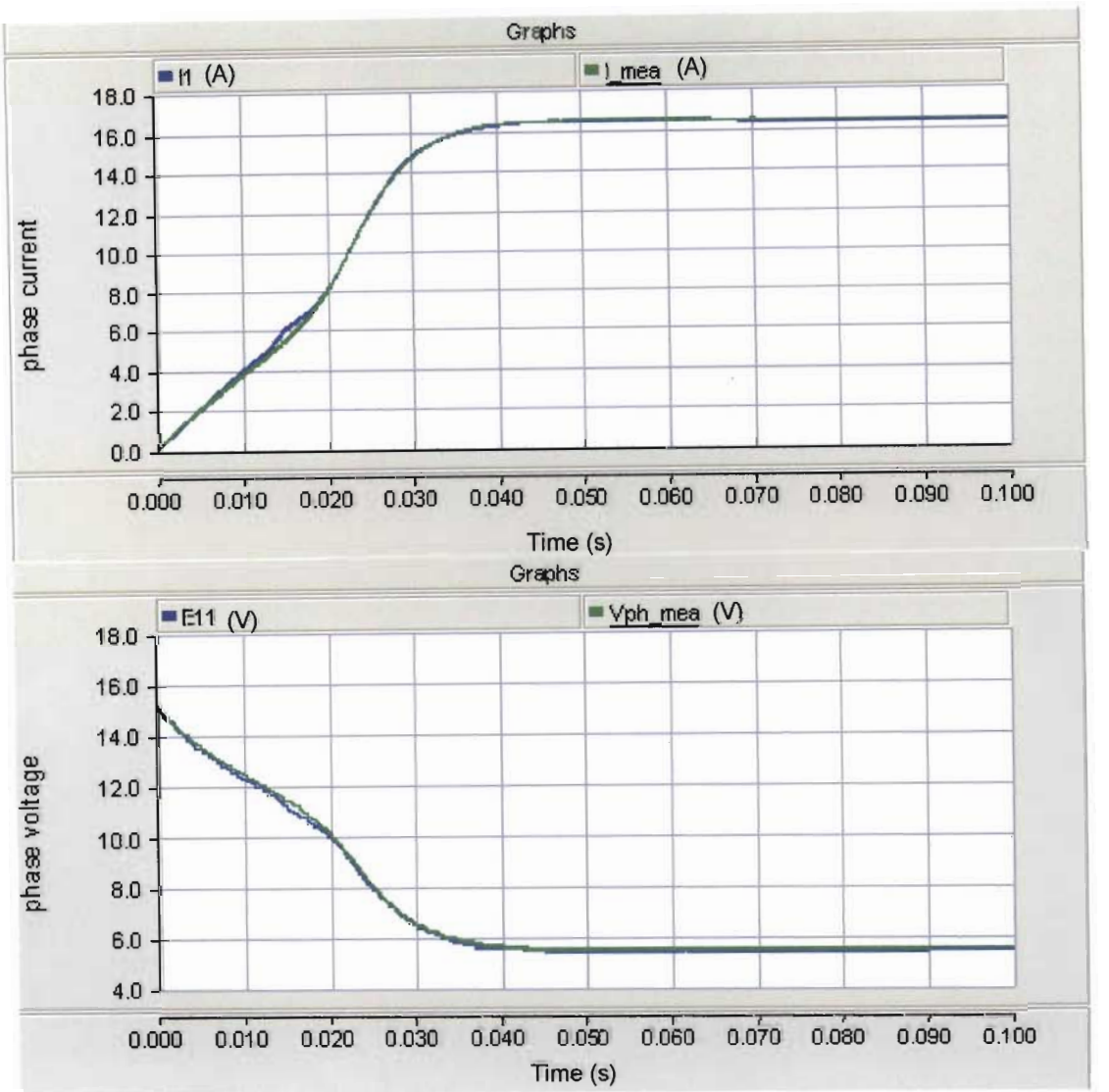

Fig. 3.28 Phase current for a fixed rotor position at 5°

3.9.2 Free Rotor Alignment Test for PSCAD SRM Model

The free rotor alignment test circuit is explained in section 2.6 and shown in Fig.2.27. The phase S1-S1' is energized with 12 Vdc when the initial rotor angle is 15°. The rotor moves to the aligned position (0°) due to the corresponding electrical torque response. The PSCAD model is shown in Fig. 3.29. The one phase torque characteristic is contained in lookup table

TORQUE60yx4.dat shown in Appendix B.2. L3030.dat is the lookup table of phase inductance characteristics for rotor angles from -30° to 30°. The moment of inertia J and friction coefficient B of the experimental rig are measured as 0.0244 kgm^2 and 0.0875Nm/s respectively. The "0to360" and "360to60" blocks wrap the rotor angle first from of 0° to 360°, and then from 0° to 60° respectively. Four lookup tables are used to plot graphs of measured values on the same axes as the PSCAD simulation results. Vdc015.dat is the measured Vdc, i015.dat is the measured phase current, th015.dat is the measured rotor angle, and Vp015 is the measured phase voltage.

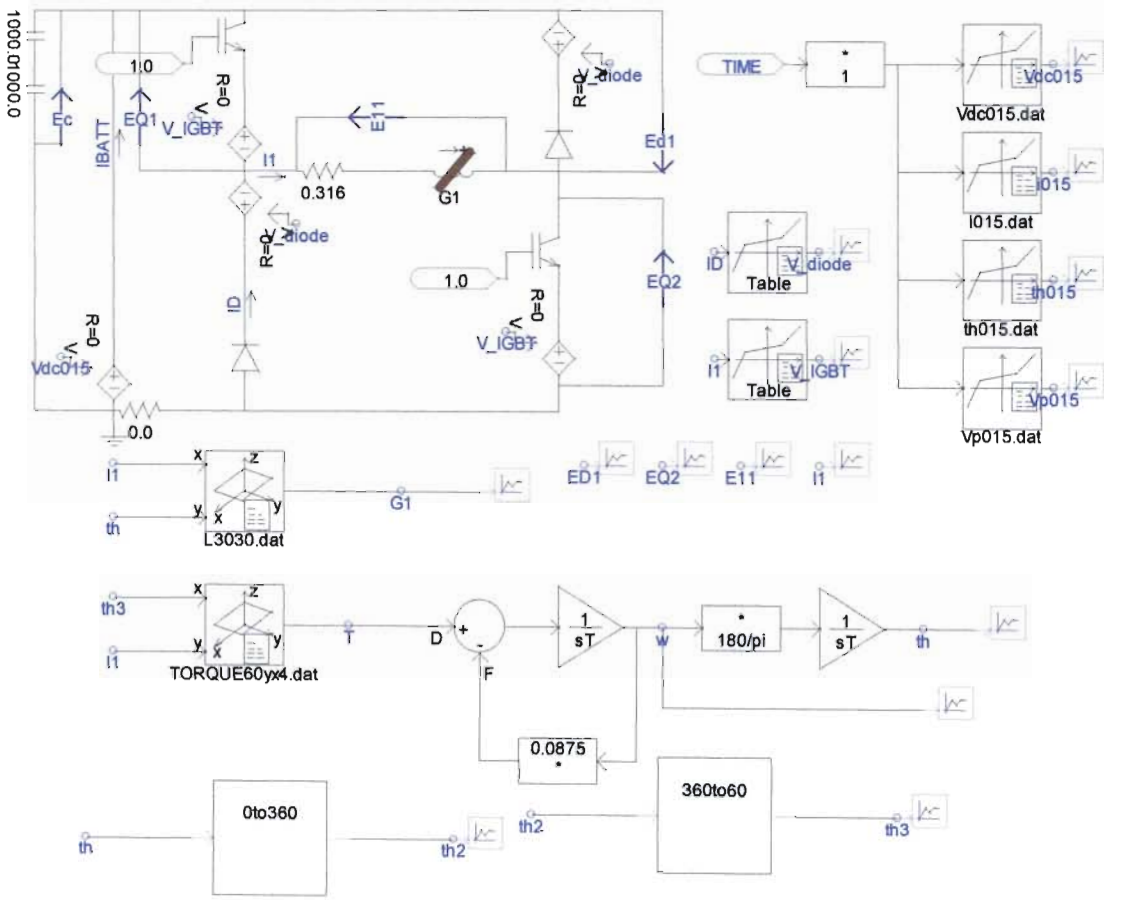

Fig. 3.29 One phase free rotor PSCAD SRM and AHB model

Fig. 3.30 compares measured and simulated phase voltage, current and rotor angle results under free rotor alignment test. The PSCAD *electrical* SRM and AHB, and mechanical models are all validated under these test conditions by the close agreement observed between the simulated and measured current, voltage, and rotor angle responses.

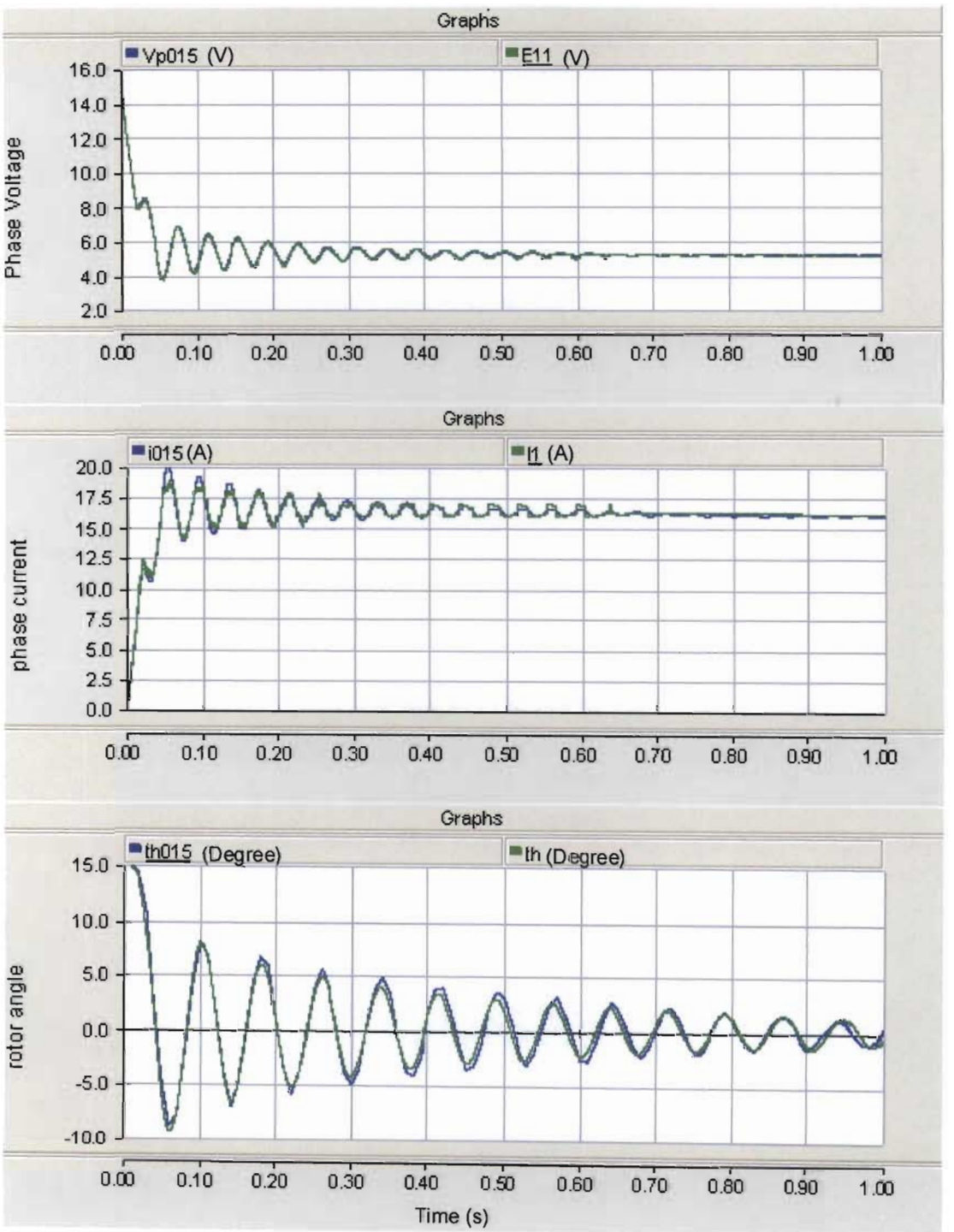

Fig. 3.30 Free rotor alignment test results when rotor starts from 15°

3.10 Summary

This chapter has explained the principle of operation, and used PSCAD models and simulations to compare the performance of four different SRM power converter topologies under various operating conditions. The AHB converter topology is selected for the experimental work of this thesis due to

1. its relative simplicity with respect to phase commutation and current control,
2. its ability to enable independent phase commutation and current control for torque ripple minimization, and
3. its relatively good phase commutation and current control performance.

It is, however, proposed that future work should aim to minimize the control complexity and exploit the potential advantages of faster independent phase commutation and tighter current control offered by the cost-effective c-dump topology.

This chapter has also presented and validated PSCAD SRM and AHB models by means of locked and free rotor alignment tests. The next chapter makes use of these models to develop and test a PSCAD torque control strategy based on optimal simultaneous phase commutation and current control.

CHAPTER FOUR

SRM TORQUE CONTROL

4.1 Introduction

Chapter 3 introduced and compared different SRM power converter topologies. PCSAD models for the 8/6 SRM and the chosen AHB converter were also presented and validated. This chapter uses these PSCAD models to develop and test a torque control strategy for the four-phase 8/6 SRM under steady state conditions (transient conditions are investigated in Chapter 5).

The highly nonlinear torque characteristic makes low ripple SRM torque control much more difficult than for other machines. The doubly salient structure causes the torque to be a nonlinear function of both phase current and rotor position.

There are several popular approaches to SRM torque control. Section 4.2 presents one of the simplest methods, which is based purely on static or dynamic adjustment of phase commutation angles (i.e. no phase current control) [4.1-4.5]. Section 4.3 presents a more sophisticated approach, which uses a Torque Sharing Function (TSF) and closed loop current controllers to achieve the instantaneous torque requirement using one or two phases, depending on the corresponding instantaneous angle [4.6, 4.7].

4.2 Torque Control via Commutation Angle

The simplest SRM torque control method adjusts the phase commutation (turn-on and turn-off) angles. When a phase turns on, the DC link voltage (minus the power converter voltage drops) is applied to that phase; when the phase turns off, the inverse DC voltage (plus power voltage drops) is applied to that phase. The performance of this method is investigated using the PSCAD SRM and AHB converter models presented in Chapter 4. Fig. 4.1 shows the PSCAD model used to investigate the current and torque responses for various commutation angles (all of the block diagrams and their functions are explained in Appendix C). A constant speed load is preferred for this study because it provides a consistent basis for comparison of the different torque and current responses.

Fig. 4.2(a) shows the four-phase current and torque responses resulting for a turn-on angle of 30°, and a turn-off angle of 60° at a constant speed of 150 rpm, and a DC supply of 12V. The initial transient in the torque response is due to the zero initial condition in I2. The phase torque goes slightly negative during turn-off. Fig 4.2(b) isolates the phase 1 current and torque, and shows the corresponding phase inductance. Comparison of the phase 1 current and inductance shows that negative torque is produced due to the coincidence of non-zero phase current and negative $dL/d\Theta$ (i.e. $dL/dt < 0$ and $d\Theta/dt > 0$). This negative torque results in a reduction in the average torque. It is therefore possible to increase or decrease (i.e. crudely control) the average torque by adjusting the turn-off angle. However, adjusting both the turn-off and turn-on angles will result in a higher degree of control and better efficiency.

Fig. 4.3 shows the current and torque responses produced after experimental adjustment of the turn-on and turn-off angles in an attempt to increase the average torque. Slight advancement of the turn-on angle from 30° to 27° causes negative torque until the angle reaches 30°. This negative torque, however, is very small due to the low $dL/d\Theta$ in this range and relatively slow current response, but this is more than compensated by the resulting increase in the coincidence of high values of current and positive $dL/d\Theta$. The turn-off angle is also advanced from 60° to 51° to prevent the coincidence of non-zero current with large negative values of $dL/d\Theta$, and hence significant negative torque values.

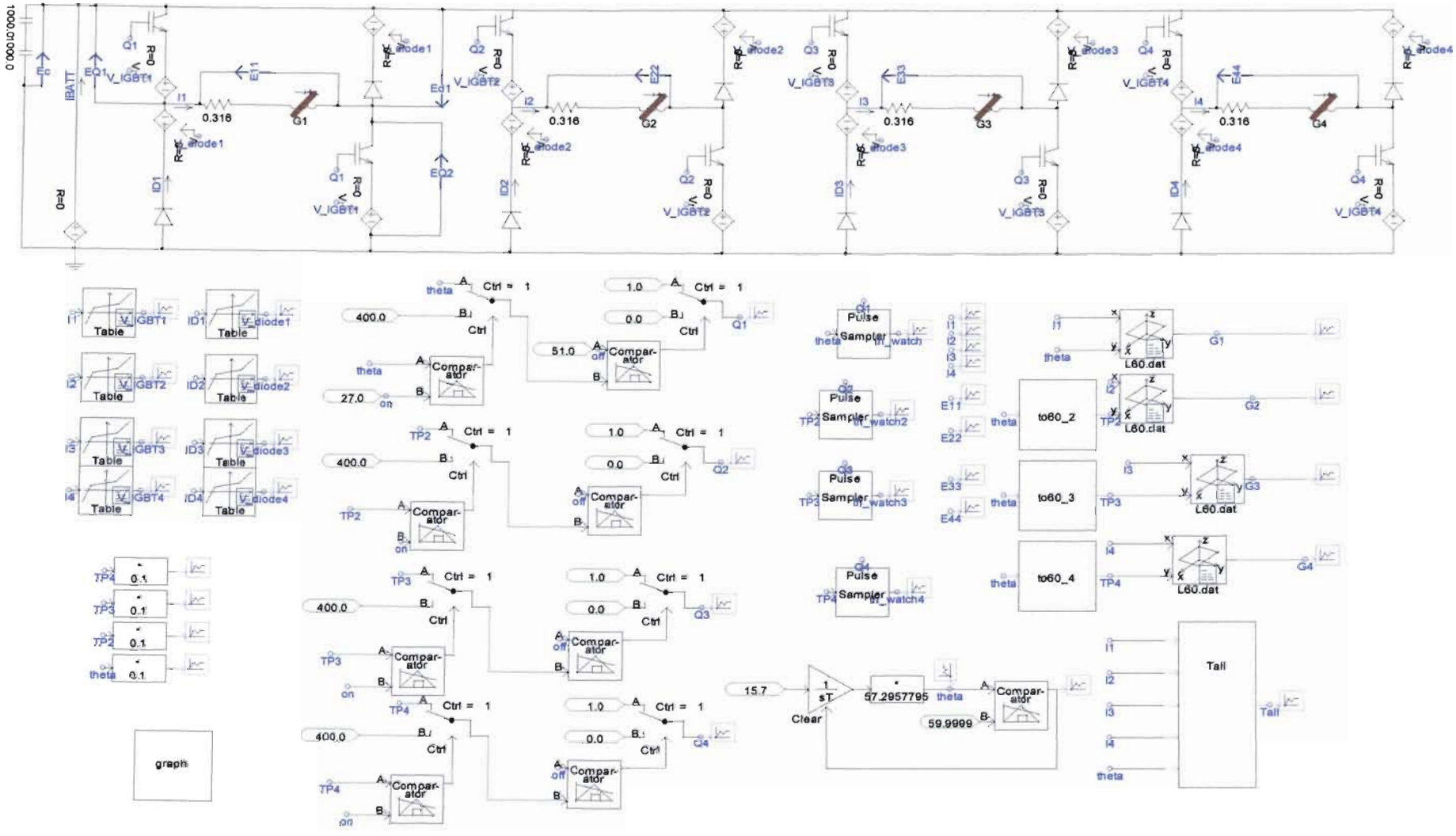

Fig. 4.1 Four phase torque control via commutation angle

Comparison of Fig 4.3 and Fig. 4.4 shows the effect of increasing the speed from 150 rpm to 500rpm. The higher back emf results in lower average current (due to lower peak value and slower response), and hence lower average torque.

Fig. 4.5 shows the effects of turn-on and turn-off angle adjustments on the combined torque response of all four phases at a speed of 150rpm. Fig. 4.5 (a) shows the effect of retarding the turn-off angle from 51° to 55° with a constant turn-on angle of 27°. It can be seen that this increases the average torque despite increased co-incidence of non-zero current and negative dL/dΘ (the percentage ripple is also increased).

Fig. 4.5 (b) shows the effect of advancing the turn-off angle from 51° to 47° with a constant turn-on angle of 27°. It can be seen that this decreases the average torque with no co-incidence of non-zero current and negative dL/dΘ (the percentage ripple is also decreased).

Fig. 4.5 (c) shows the effect of retarding the turn-on angle from 27° to 31° with a constant turn-off angle of 51°. It can be seen that this decreases the average torque with no co-incidence of non-zero current and negative dL/dΘ (the percentage ripple is also decreased).

Fig. 4.5 (d) shows the effect of advancing the turn-on angle from 27° to 23° with a constant turn-off angle of 51°. It can be seen that this increases the average torque despite increased co-incidence of non-zero current and negative dL/dΘ (the percentage ripple is also increased).

Effective torque control by automatic adjustment of commutation angles therefore requires complex optimization algorithms (such as neural networks [4.8, 4.9] and/or fuzzy logic [4.10]) to achieve the desired average torque with minimum torque ripple, and maximum efficiency. The next section presents an alternative approach, which attempts to achieve zero torque ripple by cyclic allocation of the instantaneous torque requirement to one or two phases, depending on the corresponding instantaneous angle.

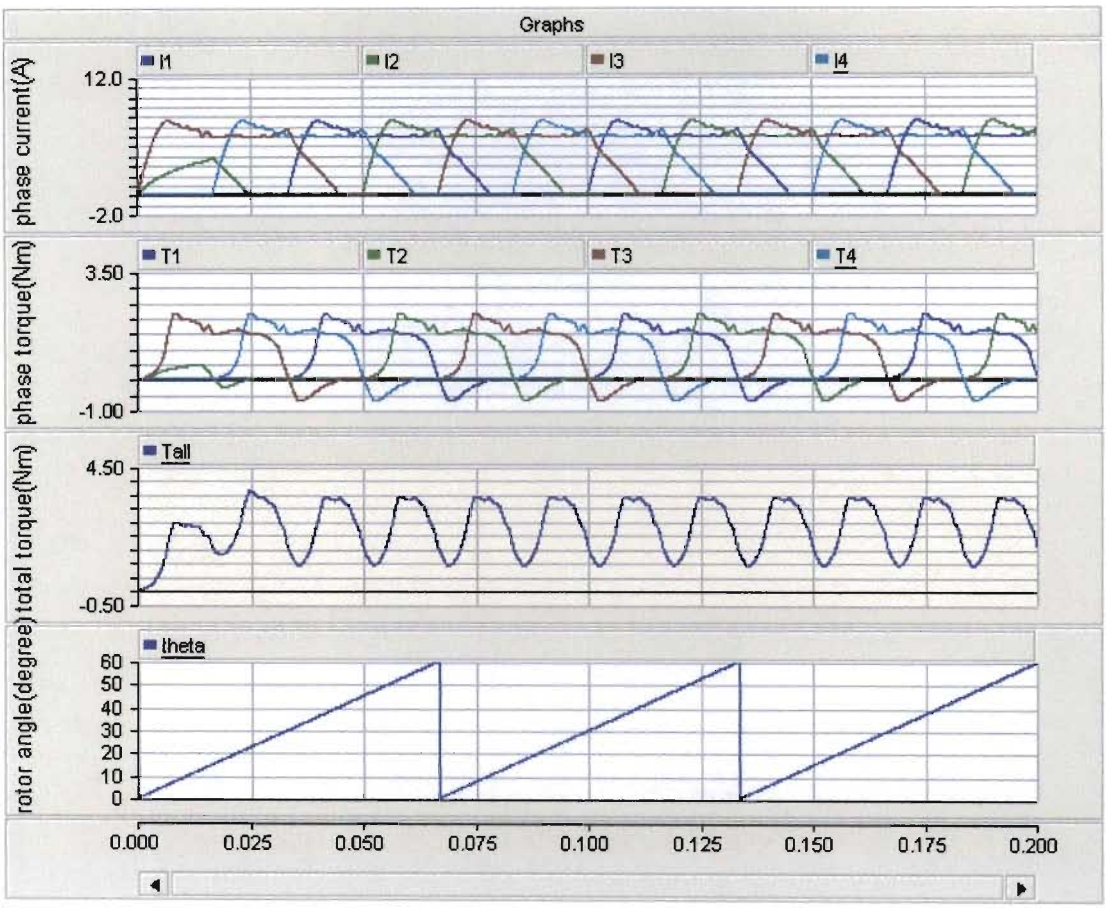

(a)

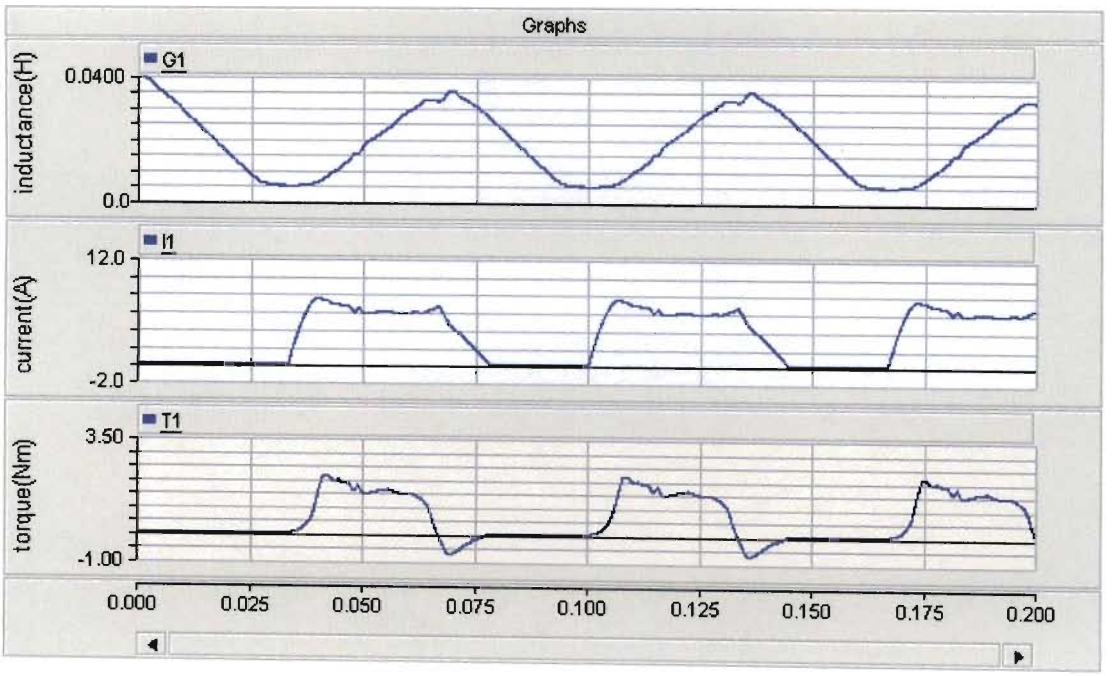

(b)

Fig. 4.2 Commutation control results at ***150rpm*** *with* 30° *turn-on angle and* 60° *turn-off angle*

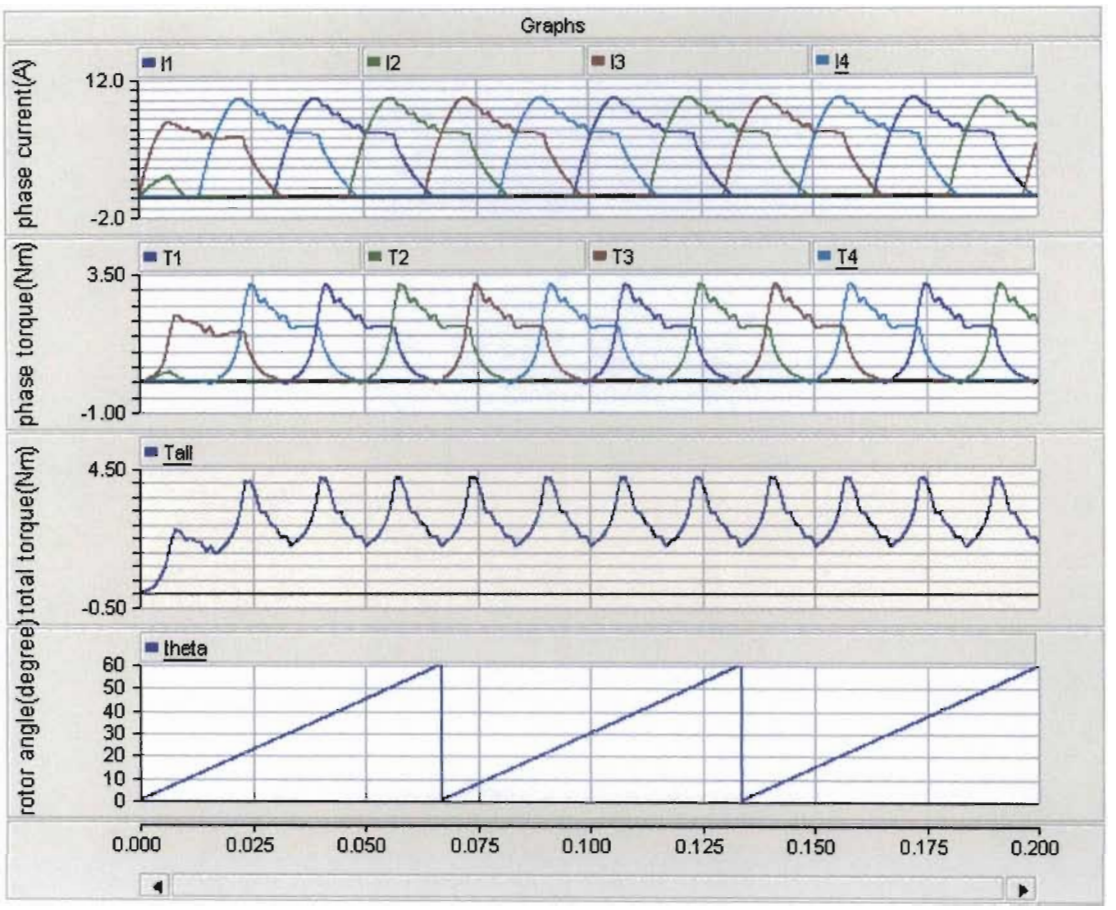

(a)

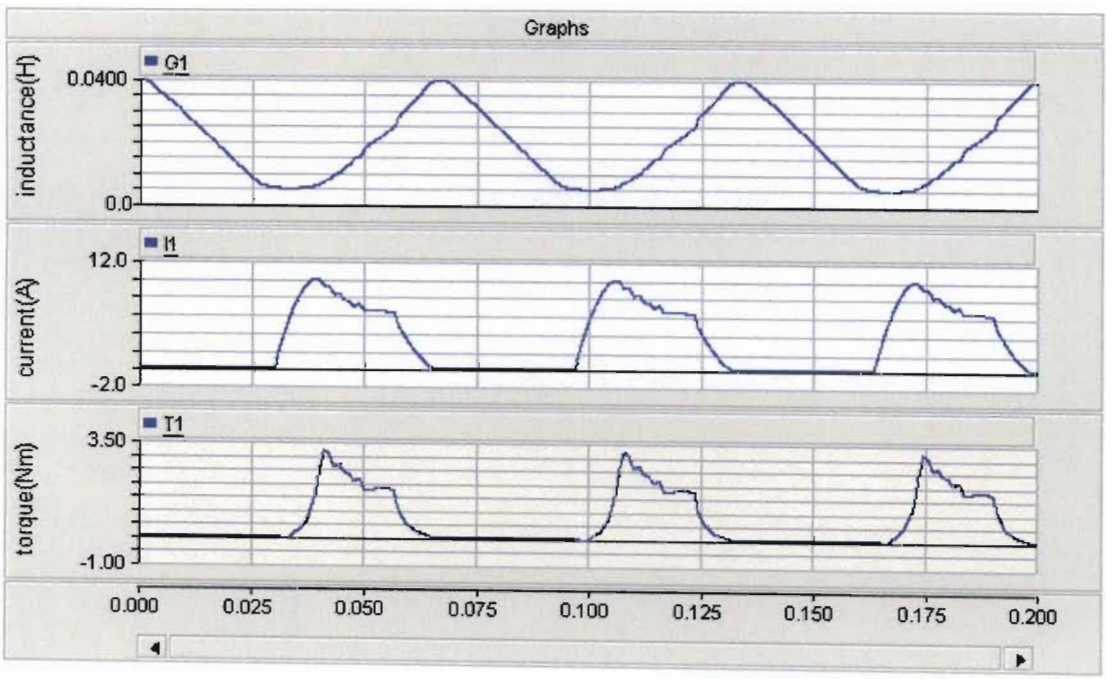

(b)

Fig. 4.3 Commutation control results at ***150rpm*** *with turn-on angle* 27° *and turn-off angle* 51°

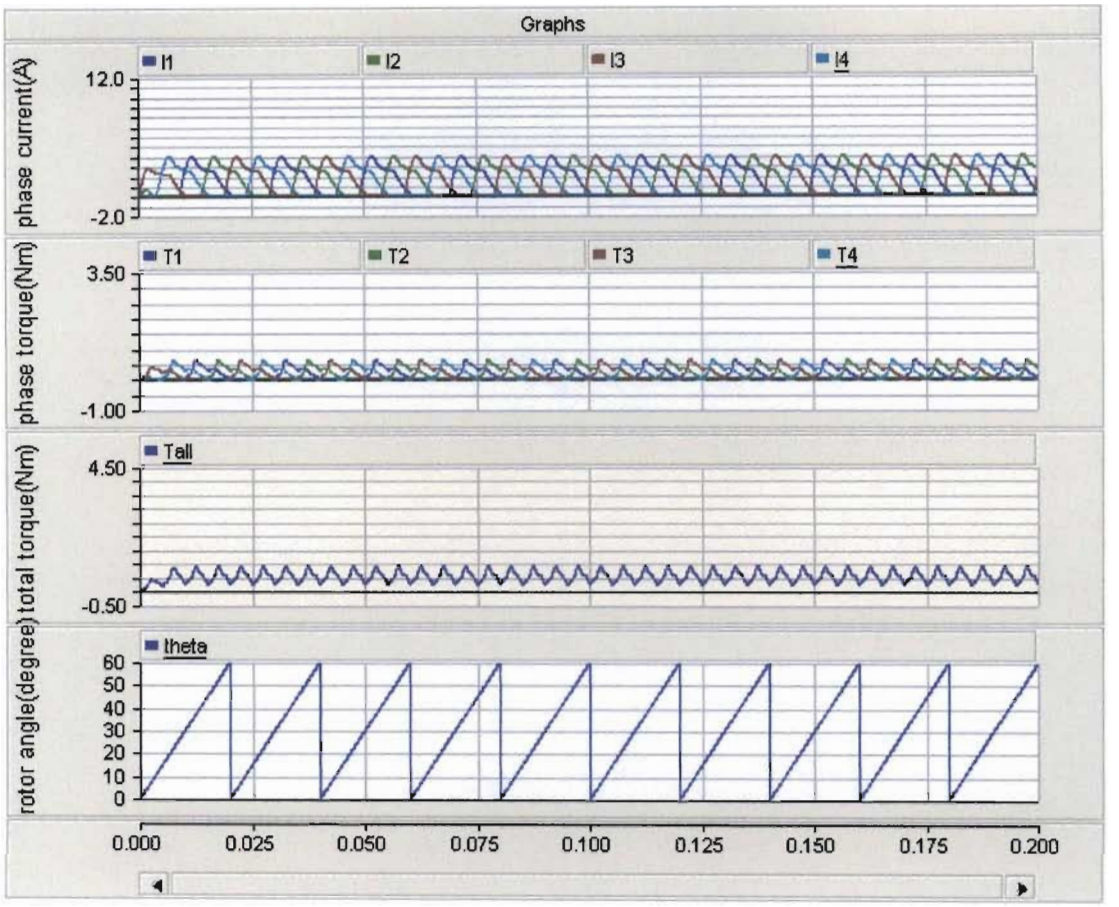

(a)

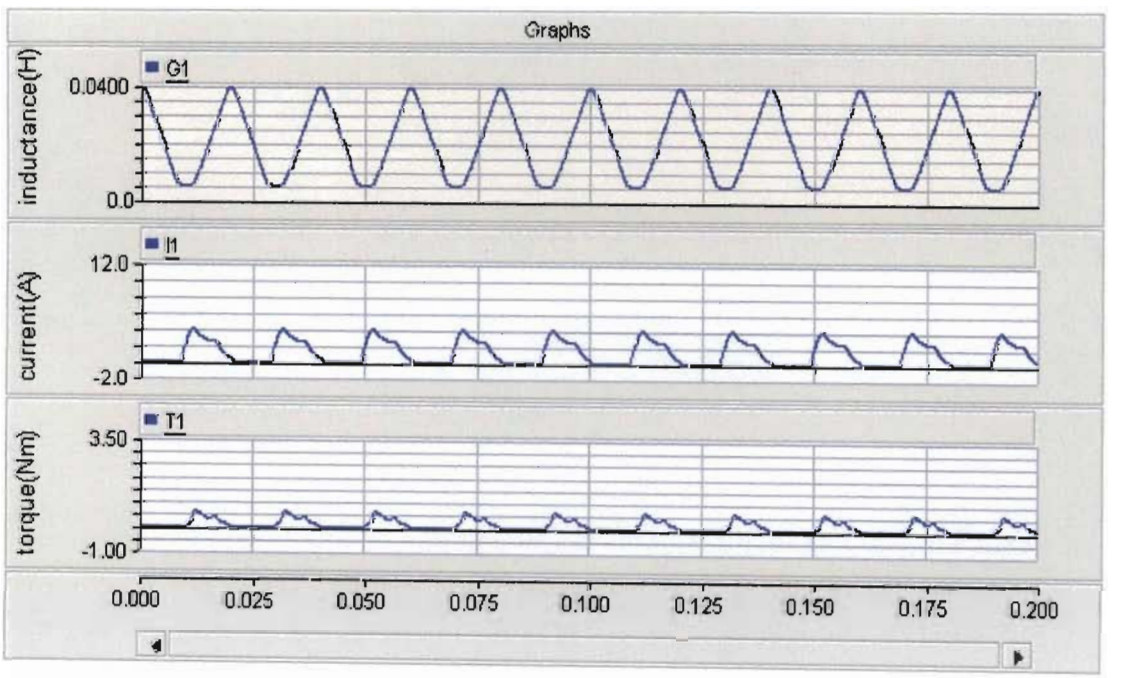

(b)

Fig. 4.4 Commutation control results at ***500rpm*** *with turn-on angle* 27° *and turn-off angle* 51°

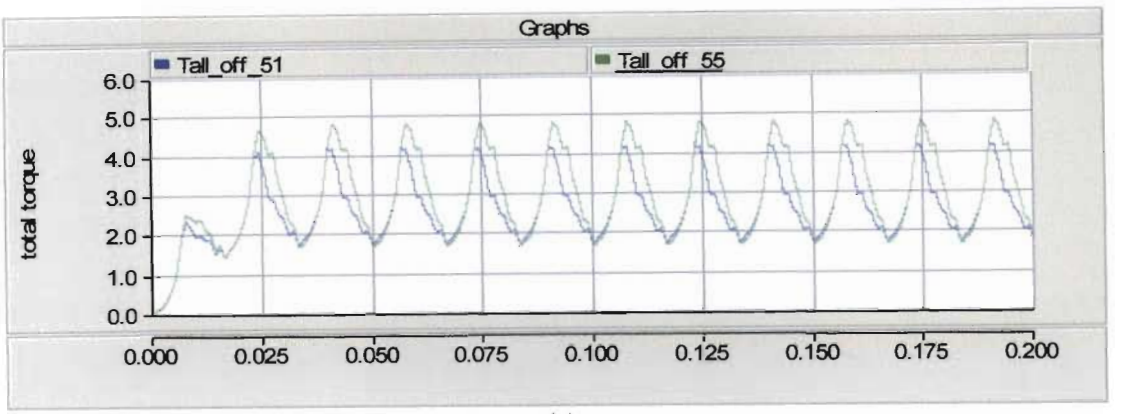

(a)

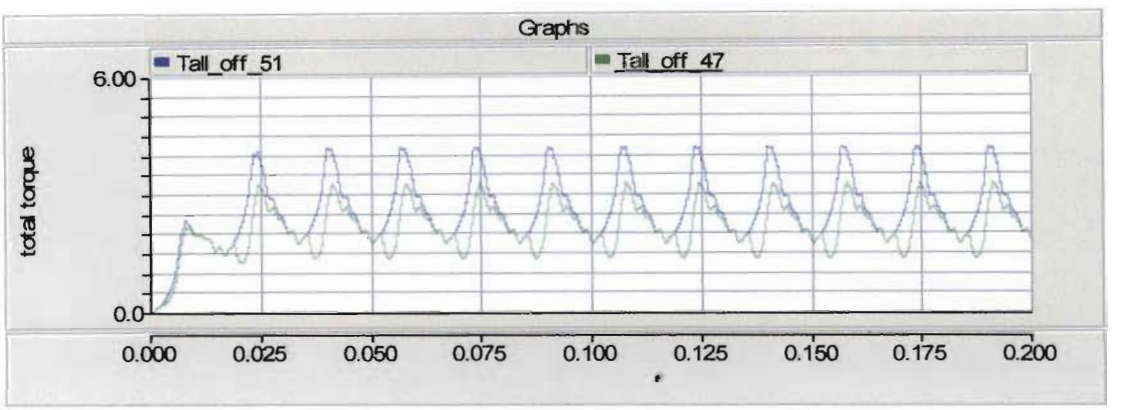

(b)

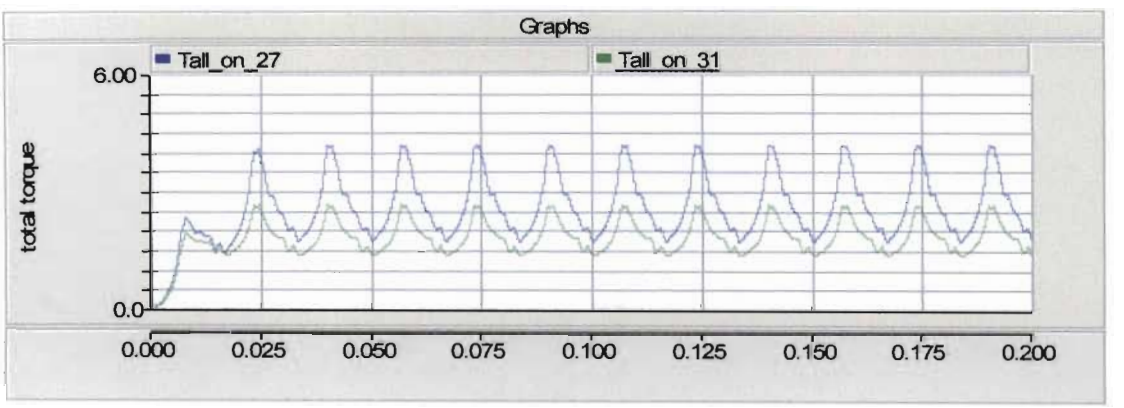

(c)

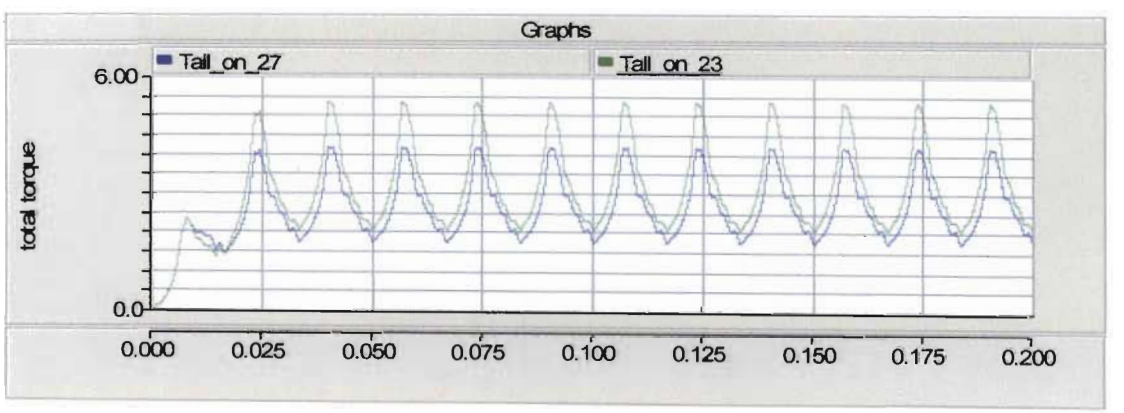

(d)

Fig. 4.5 Torque results with different turn-on and turn-off angle combination

4.3 Torque Control Strategy Based on Torque Sharing Function

The use of torque sharing functions (TSFs) to minimize torque ripple in general is discussed in detail in [4.5]. The particular TSF used for the 8/6 SRM in this thesis is adopted from [4.6]. This TSF is defined by a contour function which describes each phase contribution to the total torque reference, as a function of instantaneous angle. The contour function $f_T(\theta)$ is defined by

$$T_{total} = T_{ref} f_T(\theta) \tag{4.1}$$

where

$$f_T(\theta) = \sum_{i=1}^{n} f_i(\theta) = 1 \tag{4.2}$$

and i represents phase number (from 1 to 4 for the 8/6 SRM). The contour function $f_T(\theta)$ used in this thesis for the four-phase 8/6 SRM is shown in Fig. 4.6, and eq. (4.3).

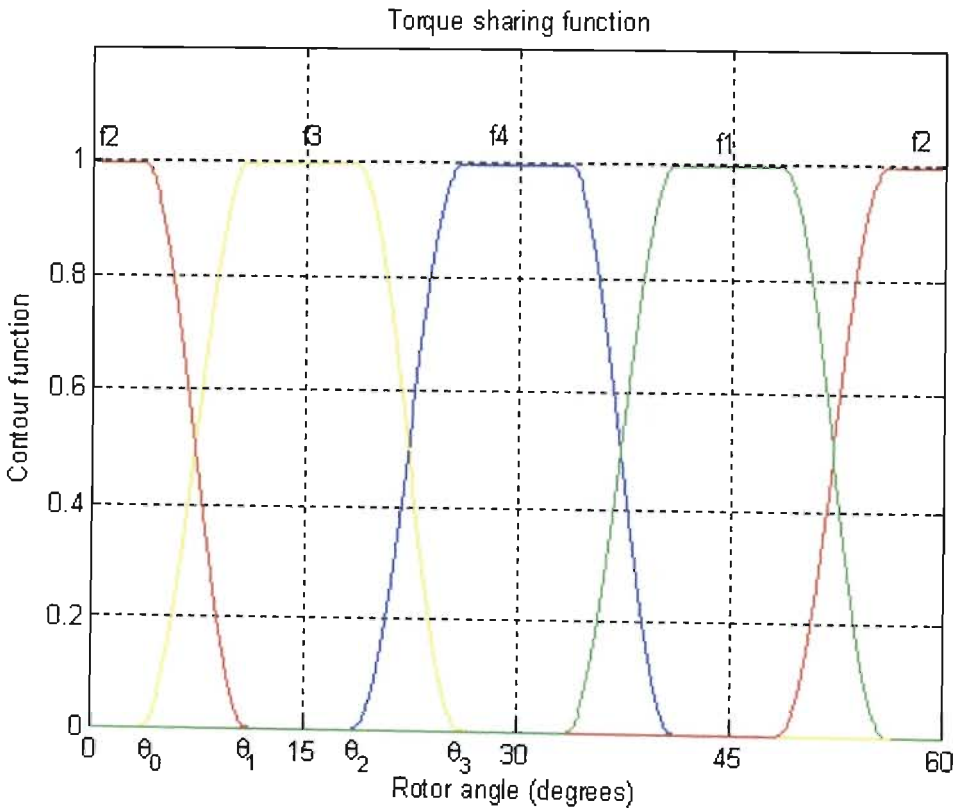

Fig. 4.6 Contour function of four phase SRM

$$f_i(\theta) = \begin{cases} 0.5 - 0.5\cos 24(\theta - \theta_0) & \theta_0 \le \theta < \theta_1 \\ 1 & \theta_1 \le \theta < \theta_2 \\ 0.5 + 0.5\cos 24(\theta - \theta_2) & \theta_2 \le \theta < \theta_3 \\ 0 & \text{otherwise} \end{cases} \quad (4.3)$$

It can be seen from eq. (4.3) that phase (i+1) has the same equation as phase i with a 15° delay. Angles θ_0 to θ_3 need to be adjusted according to the number of phases. In this thesis $\{\theta_0, \theta_1, \theta_2, \theta_3\} = \{3.5°, 11.5°, 18.5°, 26.5°\}$ to suit a four-phase motor [4.6]. Future work will investigate possible static and dynamic optimizations of these angles.

For the four-phase 8/6 SRM, the total instantaneous torque reference is therefore calculated as

$$T^* = T_{ref} f_1 + T_{ref} f_2 + T_{ref} f_3 + T_{ref} f_4 = T_a + T_b + T_c + T_d = T_{ref} \quad (4.4)$$

where T_a, T_b, T_c, T_d represent torque reference for phase1 to 4.

To get the corresponding reference current for each phase, the torque-angle-current $(T - \theta - i)$ characteristic is needed. It is obtained from offline static tests in which phase current and voltage are measured with the rotor locked at each position from 0° (the aligned position) to 30° (the fully unaligned position) with a 1° interval. The measured information is then stored as a look up table $(\theta - i - T)$ to estimate each phase torque in the simulation model, and as $(T - \theta - i)$ to obtain the current reference for each phase as a function of the instantaneous torque reference and rotor angle.

The resulting TSF based torque and current control strategy consists of six steps.

1. Measure rotor position θ
2. Obtain T_{ref} from speed controller and/or from direct input
3. Obtain contour function $f_i(\theta)$ for each phase

4. Obtain torque reference for each phase by $T_i = T_{ref} f_i(\theta)$

5. Obtain current reference for each phase from $(T-\theta-i)$ tables

6. Output phase voltages required to track current references (current control)

Accurate knowledge of the torque characteristics of the motor is therefore essential to the success of such an approach. The next section presents a PSCAD implementation of the above six step TSF torque control method, and simulation results under several locked and free rotor operating conditions.

4.4 Torque Control PSCAD Model and Results

This section presents a PSCAD model and simulation study of a TSF SRM torque controller. The TSF in eq. (4.3) is used to determine torque references for each phase. These torque references are then converted into corresponding current references by means of $(T-\theta-i)$ lookup tables.

Section 4.4.1 tests the TSF strategy by feeding the current references directly into the torque model ($\theta-i-T$ lookup table), i.e. assuming perfect/ideal current control. Section 4.4.2 introduces (i) the voltage-fed electrical model for each phase, (ii) the AHB converter, and (iii) hysteresis current controllers, and tests the performance of the full system under several locked and free rotor operating conditions.

4.4.1 TSF Torque Control with Ideal Current Controllers

As shown in Fig. 4.7, the TSF block transforms the instantaneous torque reference T_{ref} and rotor position θ into individual phase torque references (T_a, T_b, T_c, T_d). The $T-\theta-i$ block then transforms these into corresponding current references (I_a, I_b, I_c, I_d). The $i-\theta-T$ block incorporates the SRM phase torque model presented in Chapter 2, and calculates the total torque T_{all} produced by all four phases. Fig. 4.8 shows the PSCAD implementation of Fig. 4.7.

The simulated torque T_{all} is compared with the torque reference T_{ref} to evaluate the performance of the TSF and accuracy of the $T-\theta-i$ characteristic (and $i-\theta-T$

characteristic). Details for the TSF, $T-\theta-i$ and $i-\theta-T$ blocks are presented in Appendices C.7 and C.8.

TORQUE60yx4.dat is the lookup table for the $i-\theta-T$ block, which incorporates the accurate torque characteristics derived from the torque transducer measurements shown in Fig.2.17 in chapter2 (and tabulated in appendix B.2). The inverse of this table with respect to current and torque is stored in CurrentRefyx4.dat, and is used for the $T-\theta-i$ block (to obtain the phase current references). The rotor angle (labeled "theta") is wrapped to span the range of angles from one completely aligned position ($0°$) to the next ($60°$), i.e. with the completely unaligned position in the centre of this range ($30°$).

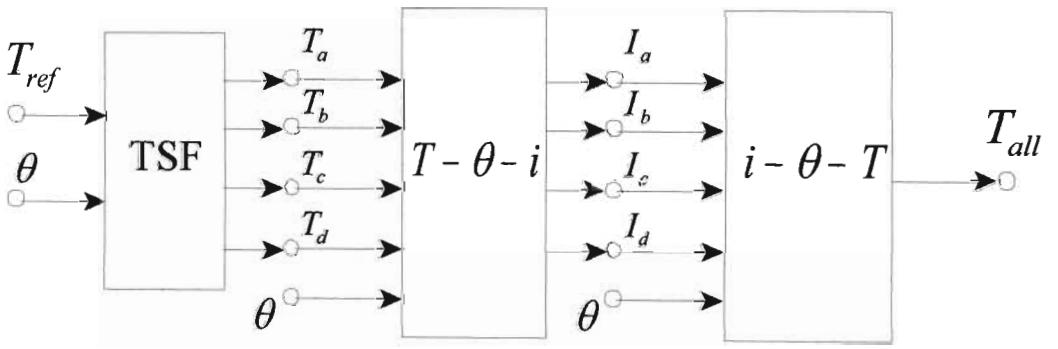

Fig. 4.7 TSF torque controller with ideal current control

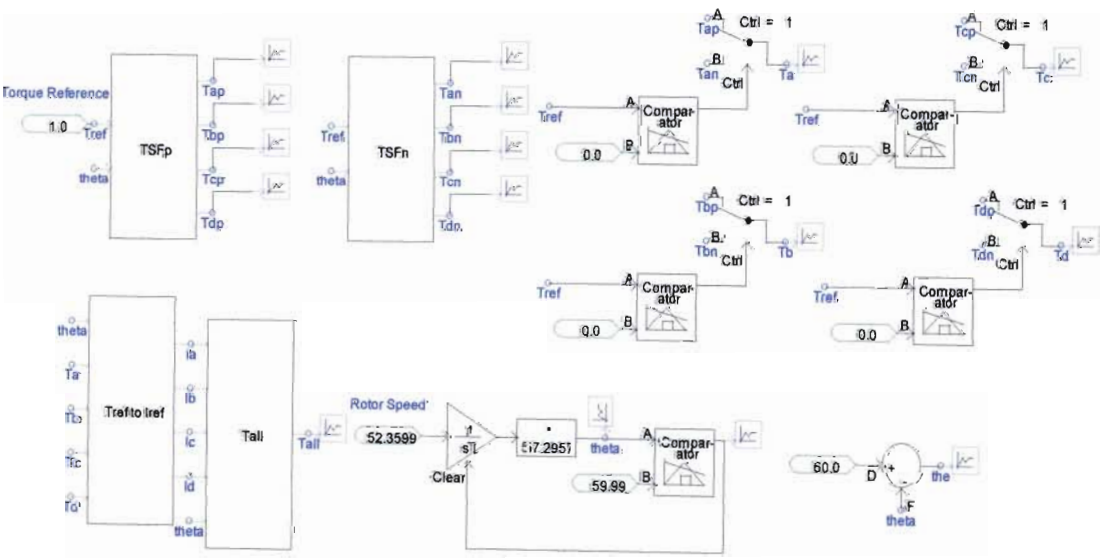

Fig. 4.8 PSCAD TSF Torque Controller with ideal current control

Locked Rotor TSF Torque Control Results with Ideal Current Control

Table 4.1 shows the T_{all} values produced by the $T-\theta-i$ and $i-\theta-T$ blocks for torque references T_{ref} of $(0,\pm 1Nm,\pm 2Nm,\pm 4Nm,\pm 7Nm)$ at *locked* (ω = 0) rotor angles θ of$(0^{\circ},5^{\circ},10^{\circ},15^{\circ},25^{\circ},30^{\circ})$. The only two possible sources of error between T_{all} and T_{ref} are

1. errors in the inversion of $i-\theta-T$ to obtain $T-\theta-i$,and
2. linear interpolation error.

Fig. 4.9 shows plots of the percentage error between T_{all} and T_{ref} as a function of T_{ref} (calculated using the data in Table 4.1). It can be seen that the error incurred in using the$T-\theta-i$ block (required for TSF torque control) is in the order of ±0.5% (i.e. an envelope of 1%) under these locked rotor test conditions.

θ (degrees) → T_{ref} (Nm) ↓	0	5	10	15	25	30
-7	-6.99883	-7.00414	-6.99828	-6.99883	-6.99828	-6.99883
-4	-4.00323	-4.00338	-3.99924	-4.00323	-3.99924	-4.00323
-2	-1.9995	-2.01109	-1.9939	-1.9995	-1.9939	-1.9995
-1	-1.0044	-0.99636	-1.00585	-1.0044	-1.00585	-1.0044
0	0	0	0	0	0	0
1	1.004395	0.998794	1.00082	1.004395	1.00082	1.004395
2	1.999503	2.002411	1.99435	1.999503	1.99435	1.999503
4	4.003229	3.993122	4.01294	4.003229	4.01294	4.003229
7	6.998827	6.994637	7.006115	6.998827	7.006115	6.998827

Table 4.1 Locked rotor total torque T_{all} with ideal current control

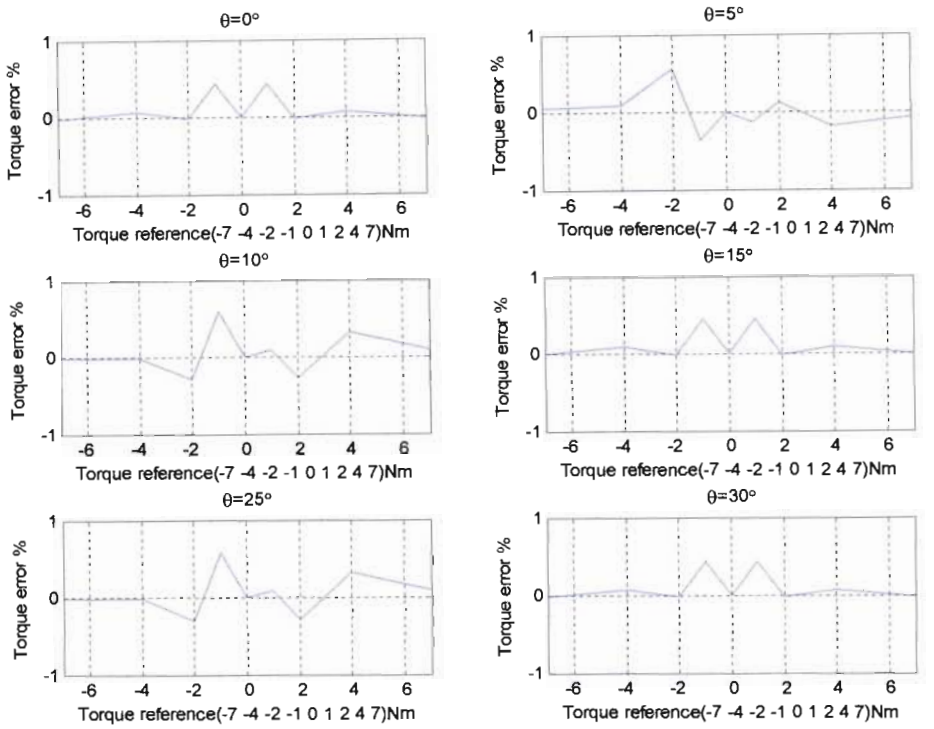

Fig. 4.9 Torque error by percentage between torque reference and simulated torque obtained from Table 4.1

Free Rotor TSF Torque Control Results with Ideal Current Control

Figs. 4.10 to 4.15 show the total torque response T_{all} for torque references T_{ref} of $(0,\pm 1Nm,\pm 2Nm,\pm 4Nm,\pm 7Nm)$ at constant rotor speeds ω of. (±500rpm, ±1000rpm, ±1500rpm).

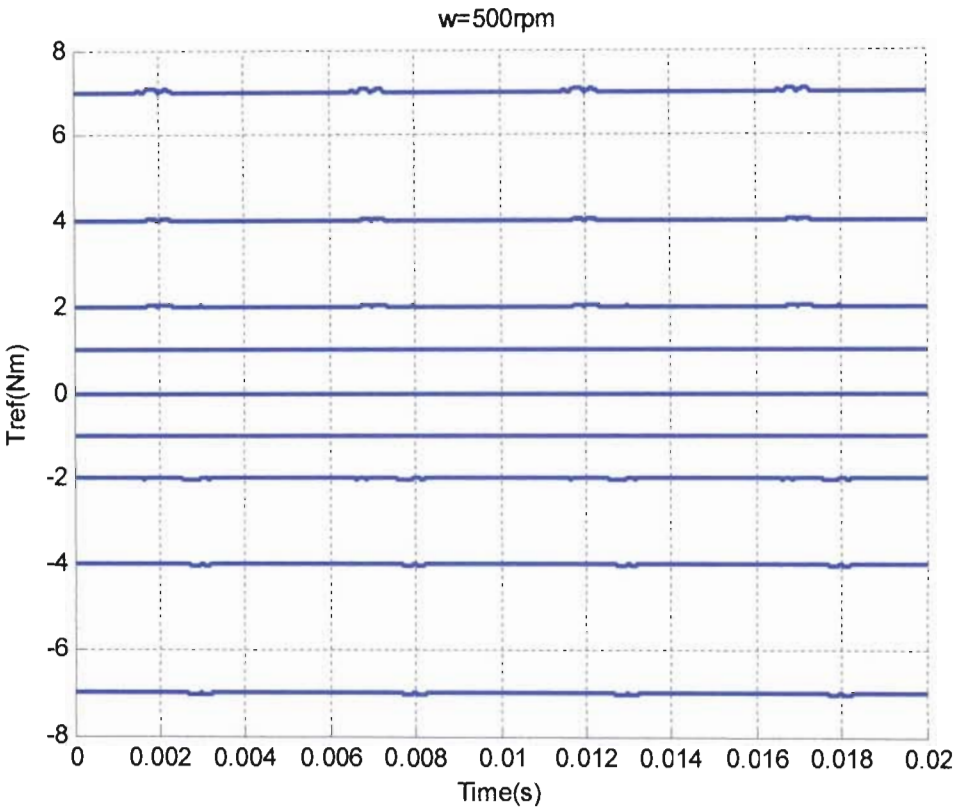

Fig. 4.10 Torque results when speed is 500rpm

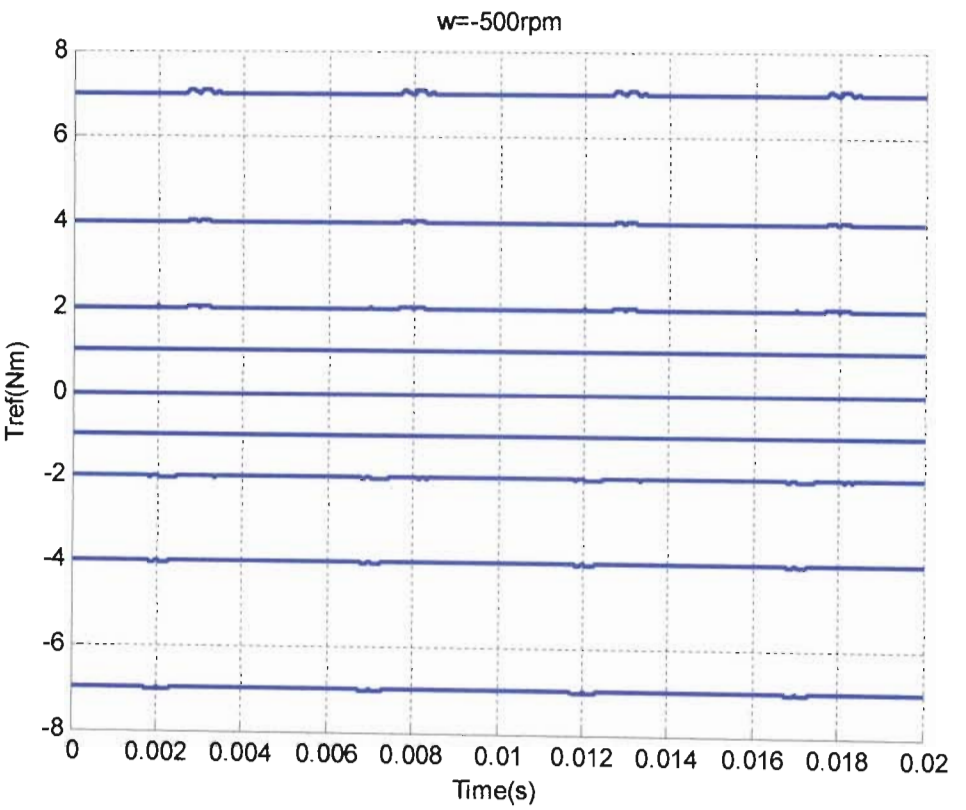

Fig. 4.11 Torque results when speed is -500rpm

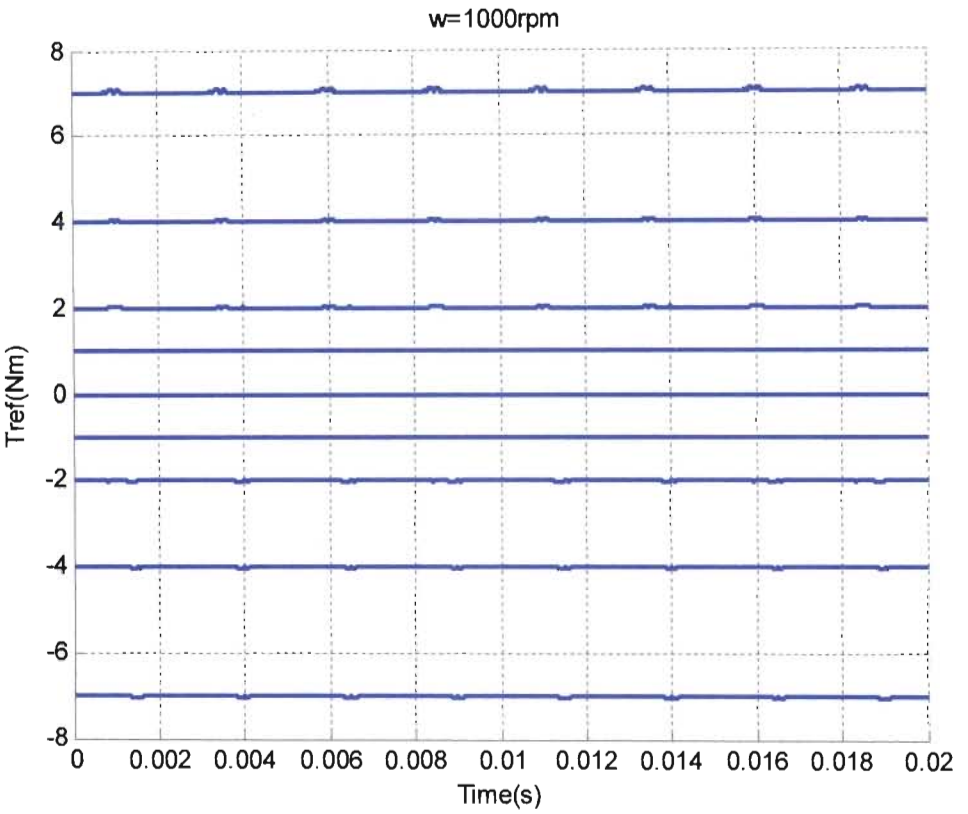

Fig. 4.12 Torque results when speed is 1000rpm

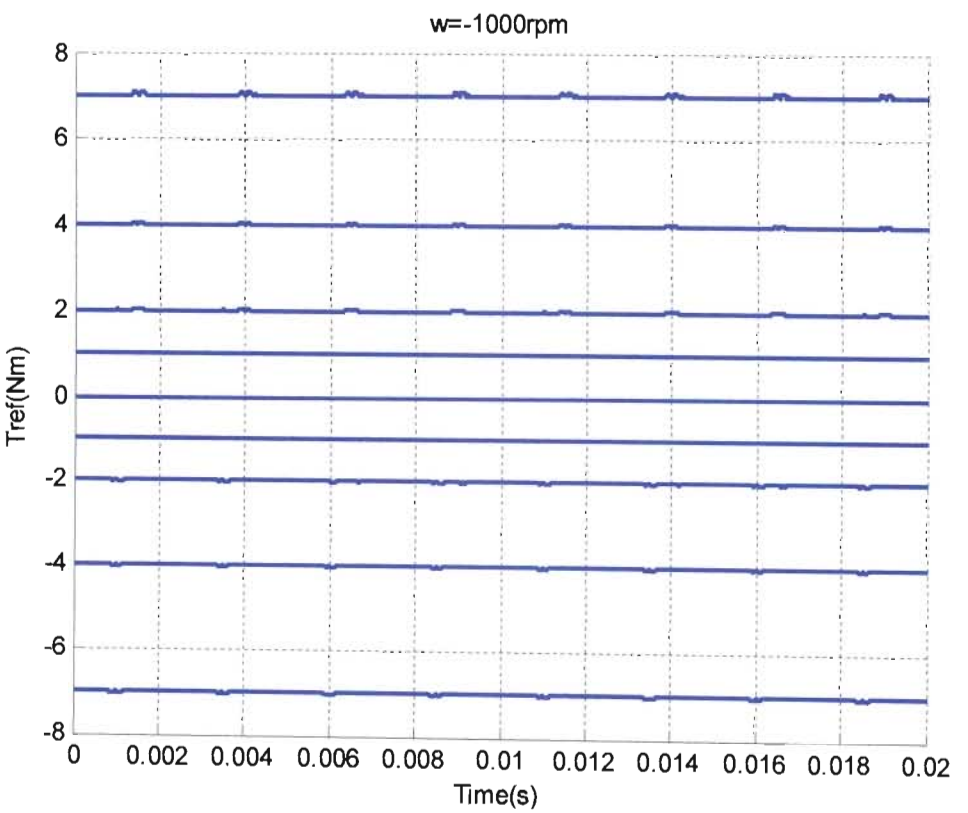

Fig. 4.13 Torque results when speed is -1000rpm

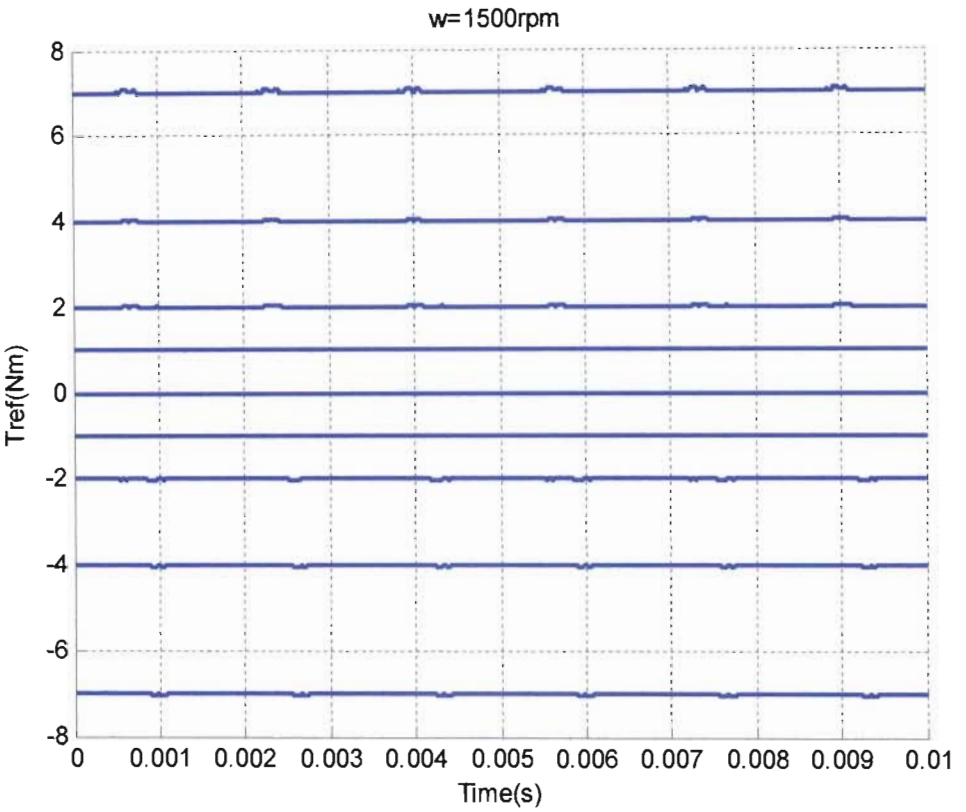

Fig. 4.14 Torque results when speed is 1500rpm

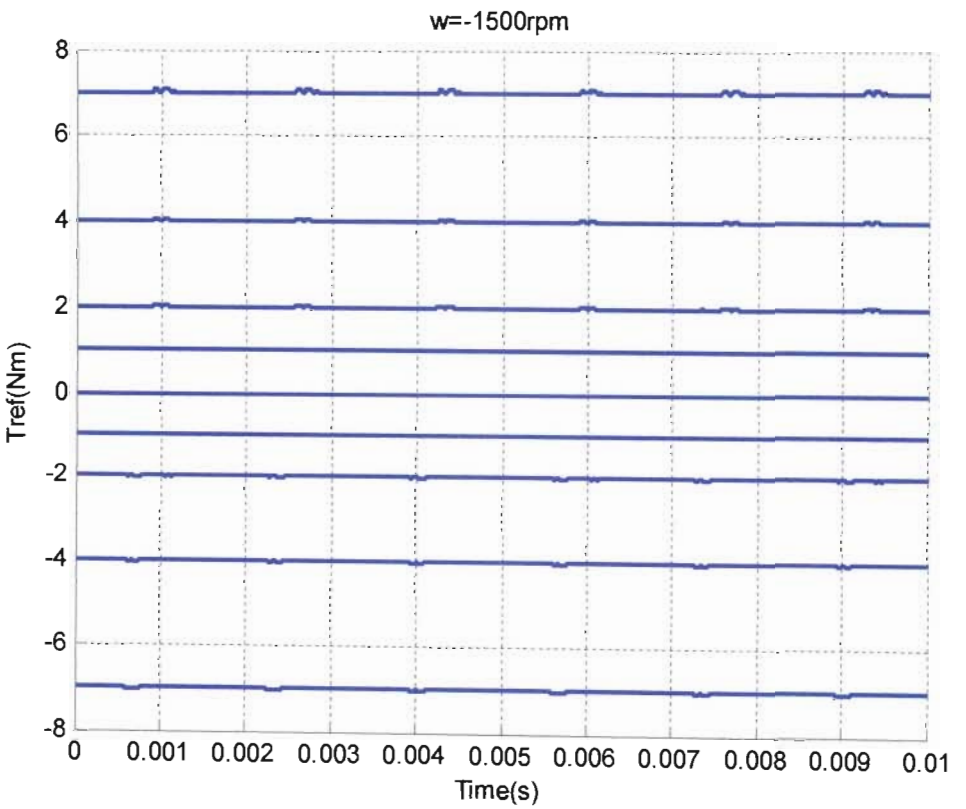

Fig. 4.15 Torque results when speed is -1500rpm

T_{ref} (Nm) → Rotor speed (rpm) ↓	-7	-4	-2	-1	0	1	2	4	7
500rpm	1.01	1.51	1.92	2.83	0	3.32	2.54	1.52	1.74
- 500rpm	1.01	1.51	1.92	2.83	0	3.32	3.1	1.52	1.74
1000rpm	1.01	1.51	1.92	2.72	0	3.23	2.53	1.48	1.72
-1000rpm	1.01	1.51	1.84	2.72	0	3.23	3.1	1.48	1.72
1500rpm	1.02	1.51	1.93	2.82	0	3.34	2.51	1.52	1.76
-1500rpm	1.02	1.51	1.88	2.82	0	3.33	3.07	1.52	1.76

Table 4.2 Free rotor total torque T_{all} % ripple envelope with ideal current control

Fig. 4.10-Fig. 4.15, and Table 4.2 show that the free rotor torque ripple magnitude (due to errors in the inversion of $i-\theta-T$ to obtain $T-\theta-i$, and linear interpolation error) increases with the torque reference magnitude, but that the percentage ripple is lower at higher torque magnitudes.

Table 4.2 shows a worst case torque ripple envelope of 3.34%. This is significantly higher that the envelope of 1% seen in the locked rotor results of Table 4.1. The reason for this is that the free rotor passes through all possible values of rotor angle, whereas only a few discrete values of locked rotor angles are tested.

The Fig. 4.16 shows the PSCAD plots of $T_{all}(t)$, $\theta(t)$ and TSF $f_1(t)$ to $f_4(t)$ for a T_{ref} of 2Nm and rotor speed of 500rpm. These simulation results show periodic deviations from the reference torque, with peaks at rotor angles of $(6.56^\circ, 21.59^\circ, 36.59^\circ, 51.52^\circ)$. It can therefore be concluded that the errors in the inverse interpolation between ($T-\theta-i$ and $i-\theta-T$) exhibit a similar pattern. It is also expected that the worst case error coincides with TSF overlap angles because the inverse table is used twice in these regions. Future work could include a detailed investigation into methods of improving the accuracy of inversion of the $i-\theta-T$ characteristic and possible use of nonlinear interpolation methods.

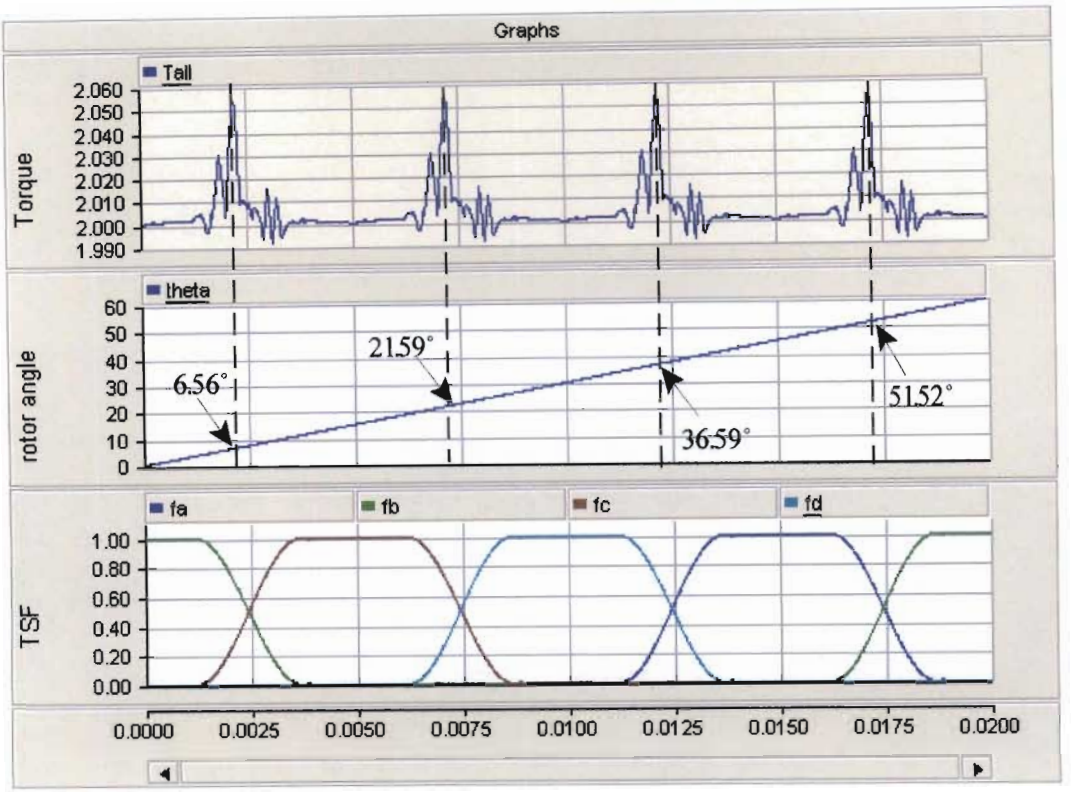

Fig. 4.16 Torque ripple related to rotor position results in PSCAD when speed is 500 rpm and torque reference is 2 Nm with ideal current controller

This section has explained the need for inversion of the SRM $i-\theta-T$ characteristic to obtain the corresponding $T-\theta-i$ characteristic, and how this is used to transform TSF phase torque references into corresponding phase current references. PSCAD simulation results have also been presented for an ideal current control scenario to test the accuracy of the $T-\theta-i$ characteristic for the 8/6 SRM of this thesis. It has been found that small errors in this characteristic produce a worst case torque ripple envelope of 3.34%. The next section investigates the performance of the TSF torque control method in conjunction with non-ideal phase current controllers.

4.4.2 TSF Torque Control with Hysteresis Current Control

Hysteresis current control is adopted in this thesis because of its relatively good performance and simple implementation. PI and PID current controllers with PWM outputs could result in less ripple, but would require extensive commissioning for each operating point, and an

online gain scheduling algorithm [4.11-4.12]. Future work could investigate possible current loop linearization by a combination of feedforward and feedback compensation of back emf and phase inductance variations. Implementation of a nonlinear/intelligent/adaptive current control methods such as Neural Networks [4.13] could also be considered.

Fig. 4.17 shows a PSCAD simulation of the TSF torque control method applied to the four-phase AHB voltage source inverter fed SRM presented in Chapters 2 and 3. Discrete hysteresis current control is achieved by simple comparison of sampled phase current errors with upper and lower threshold values (±0.1A). Each of the four phase currents is sampled via one of the "Sampler" blocks at the lower right hand side of Fig. 4.17. The sample rate is manually adjusted to the same value in the dialogue boxes of each sampler. The maximum hysteresis switching frequency is thus limited to the sampling rate/frequency.

Locked Rotor TSF Torque Control Results with Hysteresis Current Control

Fig 4.18 shows the locked rotor ($\theta = 0^\circ$) T_{all} torque response to a 1Nm step in T_{ref} for different switching frequencies f and dc link voltages Vdc. Fig. 4.18(a) shows the (i) phase 2 reference and simulated current and (ii) reference and simulated T_{all} (note that $f_1(0^\circ)=f_3(0^\circ)=f_4(0^\circ)=0$ and $f_2(0^\circ)=1$, i.e. $T_{all}(0^\circ)=T_2$) for f=2.5 kHz and Vdc=81V. It can be seen that the fixed frequency hysteresis current control exhibits significant current ripple (±37.4%) with the relatively low sample rate of 2.5 kHz. The corresponding torque ripple is seen to be significantly higher (70.0%) due to the strong nonlinearity of the torque characteristic with respect to current.

The hysteresis current control error threshold is only ±0.1A. This corresponds to a ripple of only ±2.09% for the 4.68A reference current in Fig 4.18, but corrective switching at the error threshold crossing instants is not guaranteed due to the fixed sampling rate. The switching frequency will thus generally be lower than the sampling frequency, but significantly higher than the speed dependent commutation frequency. Higher sampling rates, however, will result in less delay from the threshold crossing to the corrective switching action, and therefore reduce the current ripple. Fig. 4.18(b) shows that increasing the hysteresis sampling/switching frequency from 2.5kHz to 10kHz significantly reduces both the current ripple (from ±37.4% to ±12.8%) and torque ripple (from ±70.0% to ±22.5%).

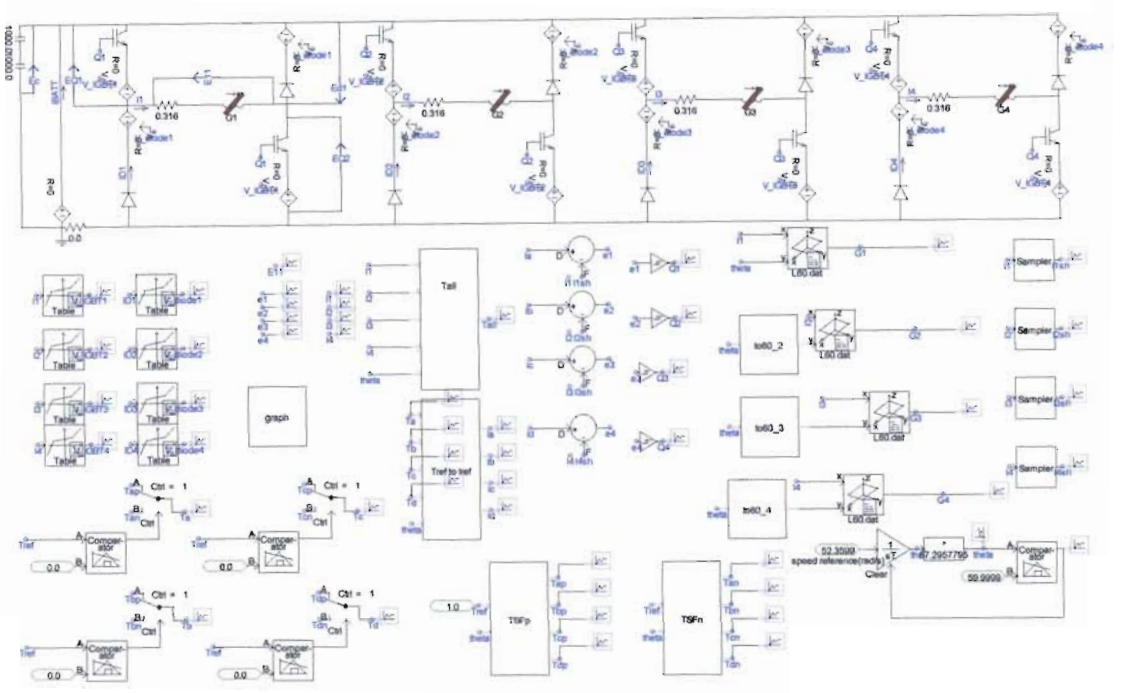

Fig. 4.17 TSF Torque and hysteresis current control diagram for four phase 8/6 SRM

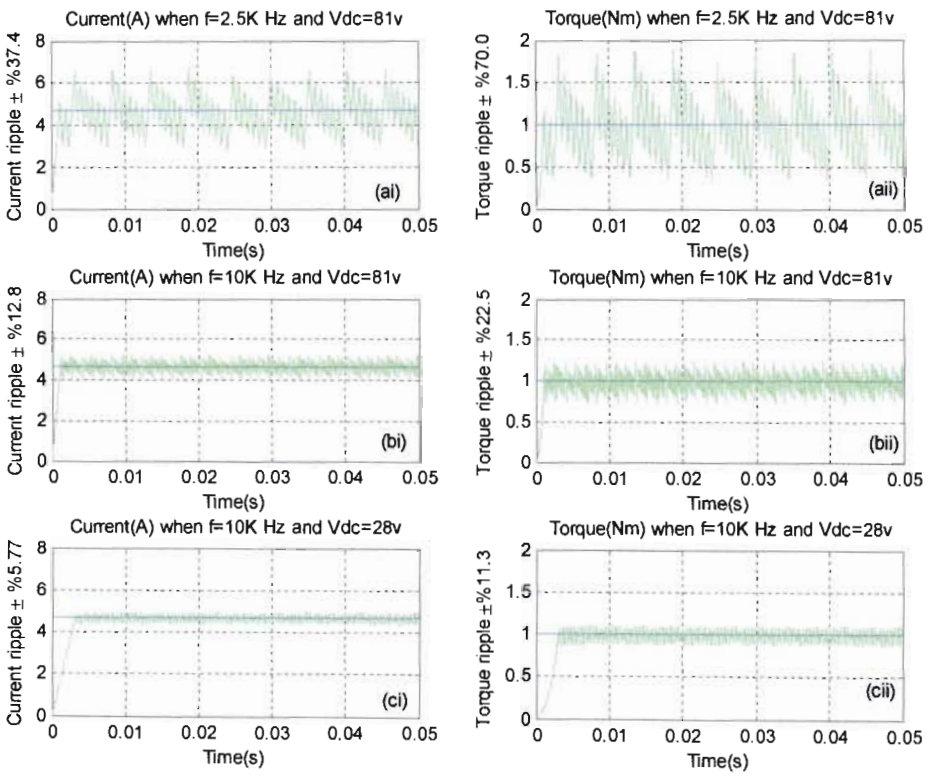

Fig. 4.18 Phase current and torque at 2.5 KHz and 10 KHz switching frequency

The current ripple magnitude for fixed frequency hysteresis current control also depends on the dc link voltage and the rotor speed, because the change in current during the delay between the error threshold crossing and corrective switching action will be proportional to the voltage across the phase inductance. The phase inductance voltage is given by

$$Vp = Vdc - back\_emf - ipRp. \qquad (4.5)$$

where Vdc is the DC link voltage, ip is the phase current, Rp is the phase resistance.

The simulation results in Fig 4.18 are obtained under locked rotor conditions, i.e. at zero speed and hence zero back emf, and fixed current reference (and hence fixed resistive volt drop). Fig 4.18(c) confirms that reducing Vdc from 81V to 28V results in a further reduction in both the current ripple (from ±12.8% to ±5.77%) and torque ripple (from ±22.5% to ±11.3%). This is, however, is not practical due to the significant reduction in maximum speed and torque achievable at this relatively low voltage. A sampling/switching frequency of 10 kHz and dc link voltage of 81V are used for the remainder of the simulation studies in this chapter.

The results of Fig. 4.18 show the effect of sampling frequency and dc link voltage on the hysteresis current control ripple and resultant high frequency torque ripple. These results are obtained for a rotor angle of 0°. In this condition, the TSF allocates full responsibility for torque production to phase 2 of the motor.

Fig. 4.19(a) to (d) shows the locked rotor TSF torque control (Tref=± 1Nm) results with hysteresis current control at rotor angles of (a) 0°, (b) 6°, (c) 7.25° and (d) 9°. It can be seen that at 0°, phase 2 contributes 100% of the torque. At 6°, phase 3 begins to contribute towards the total torque. At 7.25°, phase 2 and phase 3 each contribute about half of the total torque. At 9°, phase 3 contributes more than phase2. The responses for negative torque are similar, except that the varying contributions come from phases 1 and 4 instead of phases 2 and 3. Comparison shows higher torque ripple occurs during phase overlap intervals due to the additive effect of the ripple on each phase.

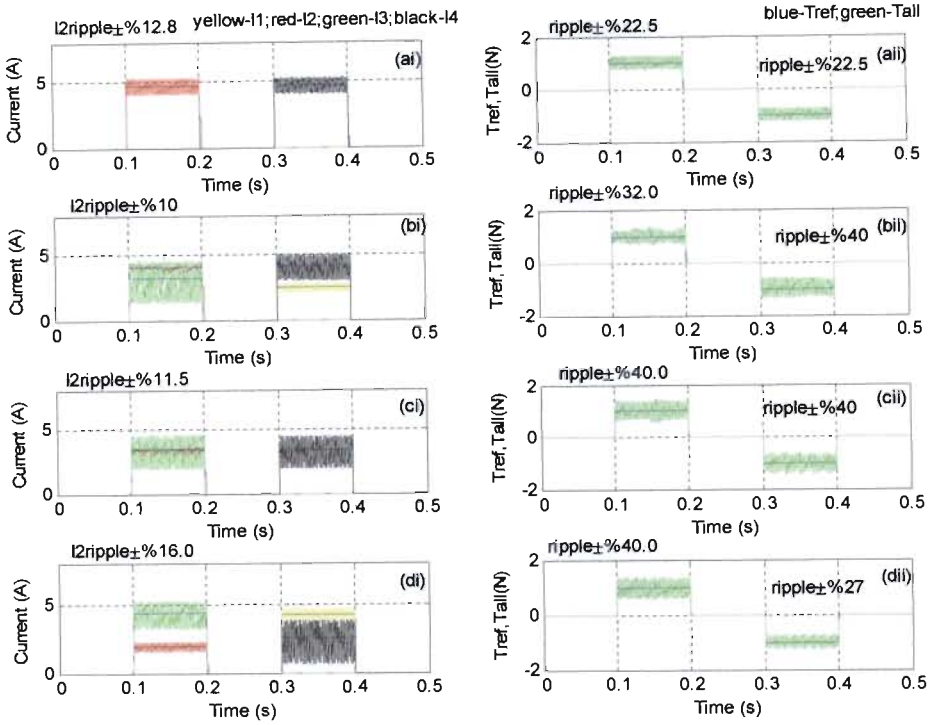

(A) Current and Torque results

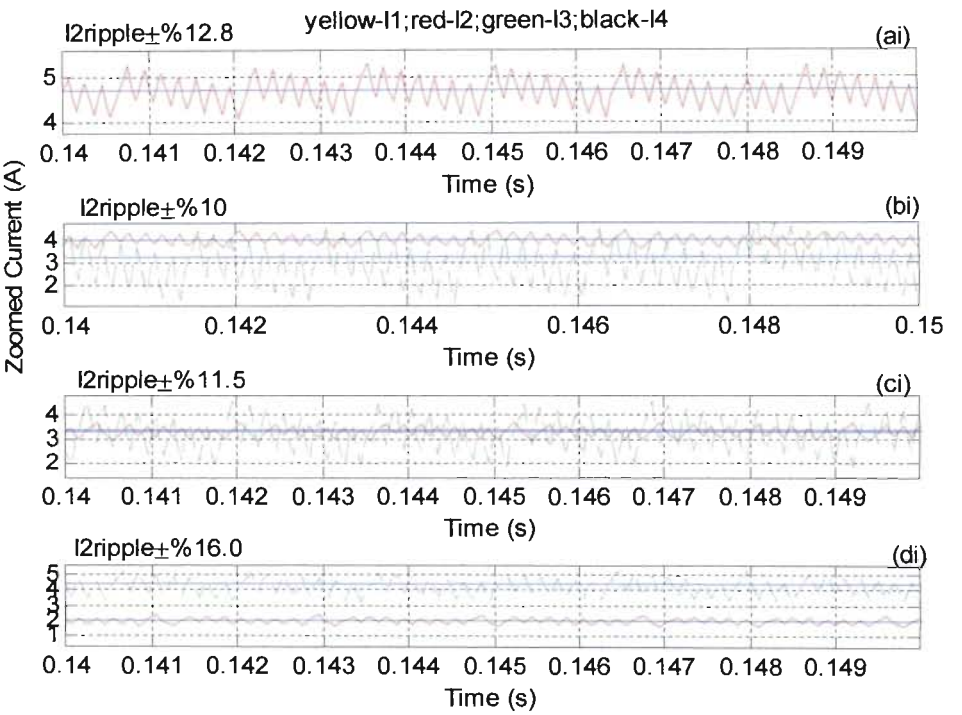

(B) Zoomed Current Results for Positive Torque Reference

Fig. 4.19 Locked Rotor TSF Torque Control Results with Hysteresis Current Control at rotor angle of (a) 0°, *(b)* 6°, *(c)* 7.25° *and (d)* 9°

Free Rotor TSF Torque Control Results with Hysteresis Current Control

Fig. 4.20 to 4.35 show (i) the simulated torque reference and total response T_{all}, (ii) all four phase current references and actual values, and (iii) the phase 1 voltage produced by the corresponding TSF torque and hysteresis current control system for various combinations of torque reference and fixed rotor speeds. The initial rotor angle $\theta(0) = 0^{\circ}$ is in all of these tests. Table 4.3 and Table 4.4 presents the summary of free rotor TSF torque and hysteresis current control simulations in motoring and generating mode at various values of fixed speed (±150rpm and ±500rpm) respectively.

The effect of different free rotor starting angles on the transient total torque step response is investigated in detail in Chapter 5. Chapter 4 focuses on steady state performance. All of these results show a slight dip in the phase voltage magnitude with increasing phase current due to the dc supply resistance. This effect is more evident at higher current magnitudes, corresponding to higher torque reference magnitudes, i.e. in plots (ciii) and (diii) of Fig. 4.20 to 4.35.

All of the phase voltage results, i.e. plots (aiii) to (diii), in these figures also contain a graphical misrepresentation of very small phase inductance voltage Vp values during periods where the phase current is zero. A zoomed version of Fig. 4.20(aiii) is shown in appendices C.11 and C.12 to illustrate this problem, and verify that the "off" phase voltage is in the range expected due to the voltage divider formed by the phase impedance and two reverse biased diodes.

Fig. No.	ω (rpm)	T_{ref} (Nm)	Remarks
4.20	150	1	The torque ripple of ±30% in Fig. 4.20(ai) is lower than the worst case of 40% seen in the (overlapping) locked rotor results of Fig. 4.19(cii) and (dii), despite compounding of the $T-\theta-i$ table errors under free rotor conditions, as discussed in section 4.4.1. This is most likely due to increased back emf, resulting in lower hysteresis current control ripple (due to lower di/dt) and therefore lower torque ripple
		2	Increasing the torque reference in Fig. 4.20 (bi) to (di) results in progressively higher current references and actual currents, and therefore progressively lower phase inductances (as can be seen from the phase inductance characteristic of Fig. 2.12). This in turn results in higher di/dt values, and hence higher current ripple magnitudes and higher torque ripple magnitudes. The overall effect, however, is a decrease in the relative (percentage) torque ripple with increasing torque magnitude.
		4	
		7	
4.21		-1	The difference between the *motoring* mode and *generating* mode torque ripple characteristics at various torque magnitudes is less than 3% at 150 rpm (low speed). The absolute torque ripple magnitude increases but the relative (percentage) torque ripple decreases with increasing torque magnitudes.
		-2	
		-4	
		-7	
4.22	-150	1	Comparison of Fig. 4.21 and 4.22 shows that positive and negative directions of rotation produce symmetrical torque ripple characteristics in *generating* mode at 150 rpm.
		2	
		4	
		7	
4.23		-1	Comparison of Fig. 4.20 and 4.23 shows that positive and negative directions of rotation produce symmetrical torque ripple characteristics in *motoring* mode at 150 rpm.
		-2	
		-4	
		-7	

Table 4.3 Summary of free rotor TSF torque and hysteresis current control simulations in motoring and generating mode at a fixed speed of ±150 rpm

Fig. No.	ω (rpm)	T_{ref} (Nm)	Remarks
4.24	500	1	Comparison of Fig. 4.20(aiii) and 4.24(aiii) shows that increasing the speed from 150rpm to 500rpm results in a continuous period of "off" or negative phase voltage near the end of the phase conduction period. This is due the increase in back emf and corresponding decrease in achievable di/dt. Comparison of Fig. 4.20 (ai) and 4.24(ai) also shows a decrease in the average torque, (as quantified later in Table 4.5).
		2	Comparison of Fig 4.24(aiii) to (diii) show that increasing torque reference magnitudes result in an increase in the continuous period of "off" or negative phase voltage near the end of the phase conduction period. Comparison of Fig 4.24(aii) to (dii) shows a corresponding increase in the lag between the actual phase currents and the phase current references during these periods. Comparison of Fig 4.24(ai) to (di) shows a corresponding increase in the shortfall (error) in the average torque (as quantified later in Table 4.5). The relative torque ripple (%) decreases with increasing torque reference magnitude.
		4	
		7	
4.25		-1	Comparison of Fig. 4.24 and 4.25 shows increasing difference between the *motoring* mode and *generating* mode torque ripple characteristics with increasing torque magnitude (and phase current) at 500rpm. This is because of insufficient voltage across the phase inductance (at higher values of phase current) to compensate for the difference between motoring and generating turn-on and turn-off characteristics (as shown in Fig. 4.36 and 4.37). |Reg.Ripple| and |Comm.Ripple| represent the torque ripple due to the current regulation and commutation respectively. The |Reg.Ripple| decreases and |Comm.Ripple| increases with increasing torque reference magnitude.
		-2	
		-4	
		-7	
4.26	-500	1	Comparison of Fig. 4.25 and 4.26 shows that positive and negative directions of rotation produce symmetrical torque ripple characteristics in *generating* mode at 500 rpm.
		2	
		4	
		7	
4.27		-1	Comparison of Fig. 4.24 and 4.27 shows that positive and negative directions of rotation produce symmetrical torque ripple characteristics in *motoring* mode at 500 rpm.
		-2	
		-4	
		-7	

Table 4.4 Summary of free rotor TSF torque and hysteresis current control simulations in motoring and generating mode at a fixed speed of ±500 rpm

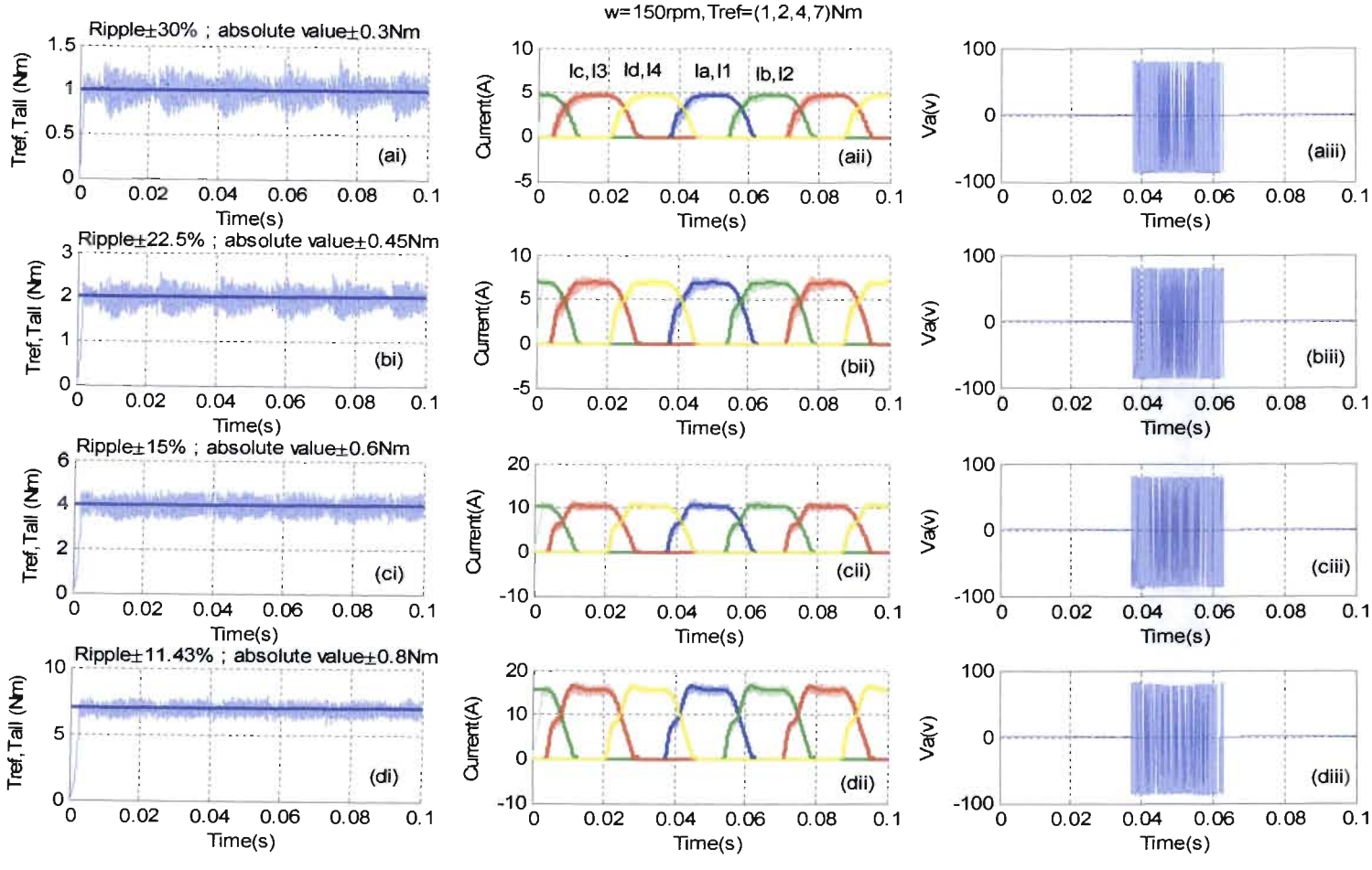

Fig. 4.20 Four phase torque and current control results with speed at 150 rpm and torque reference at 1, 2, 4,7 Nm

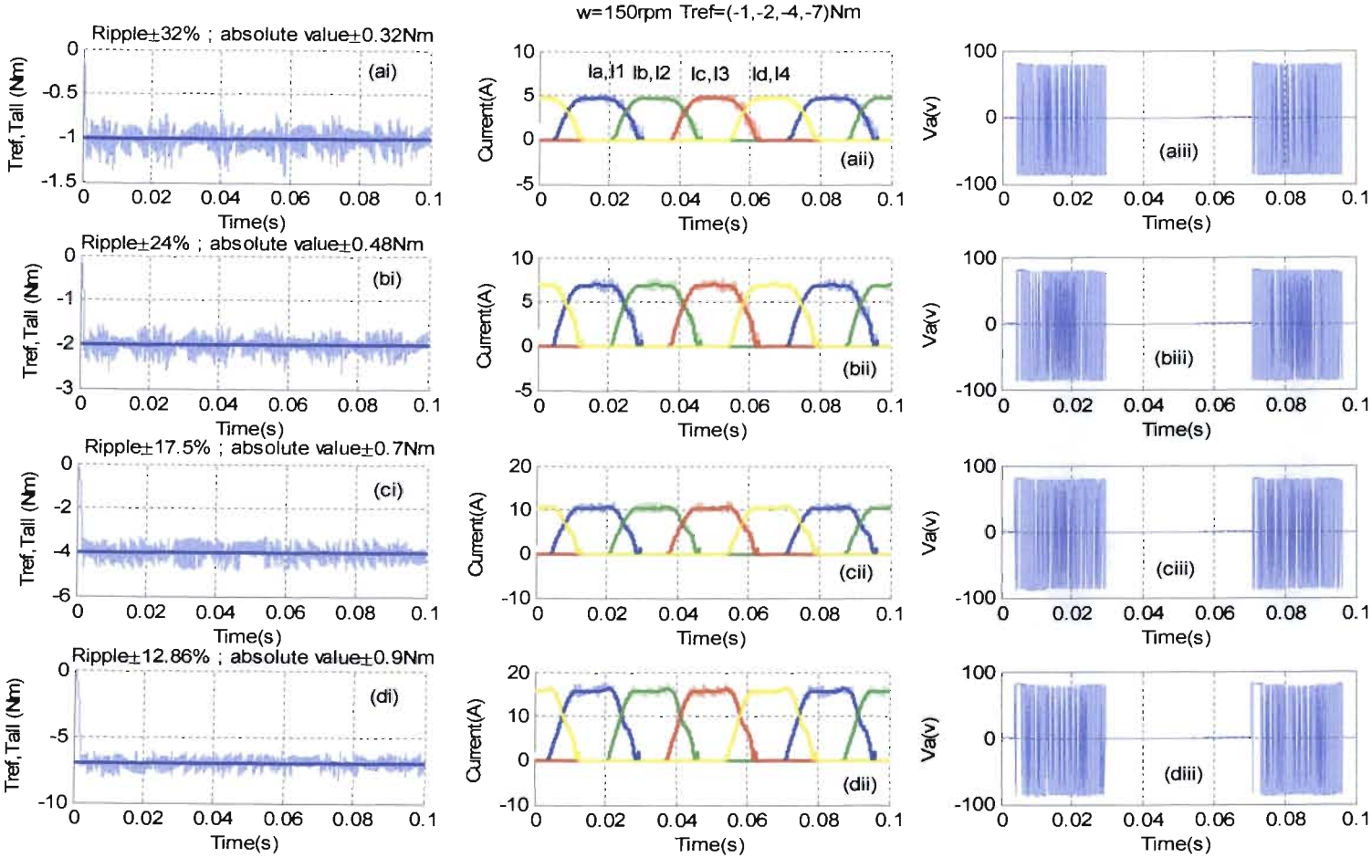

Fig. 4.21 Four phase torque and current control results with speed at 150 rpm and torque reference at -1, -2, -4,-7 Nm

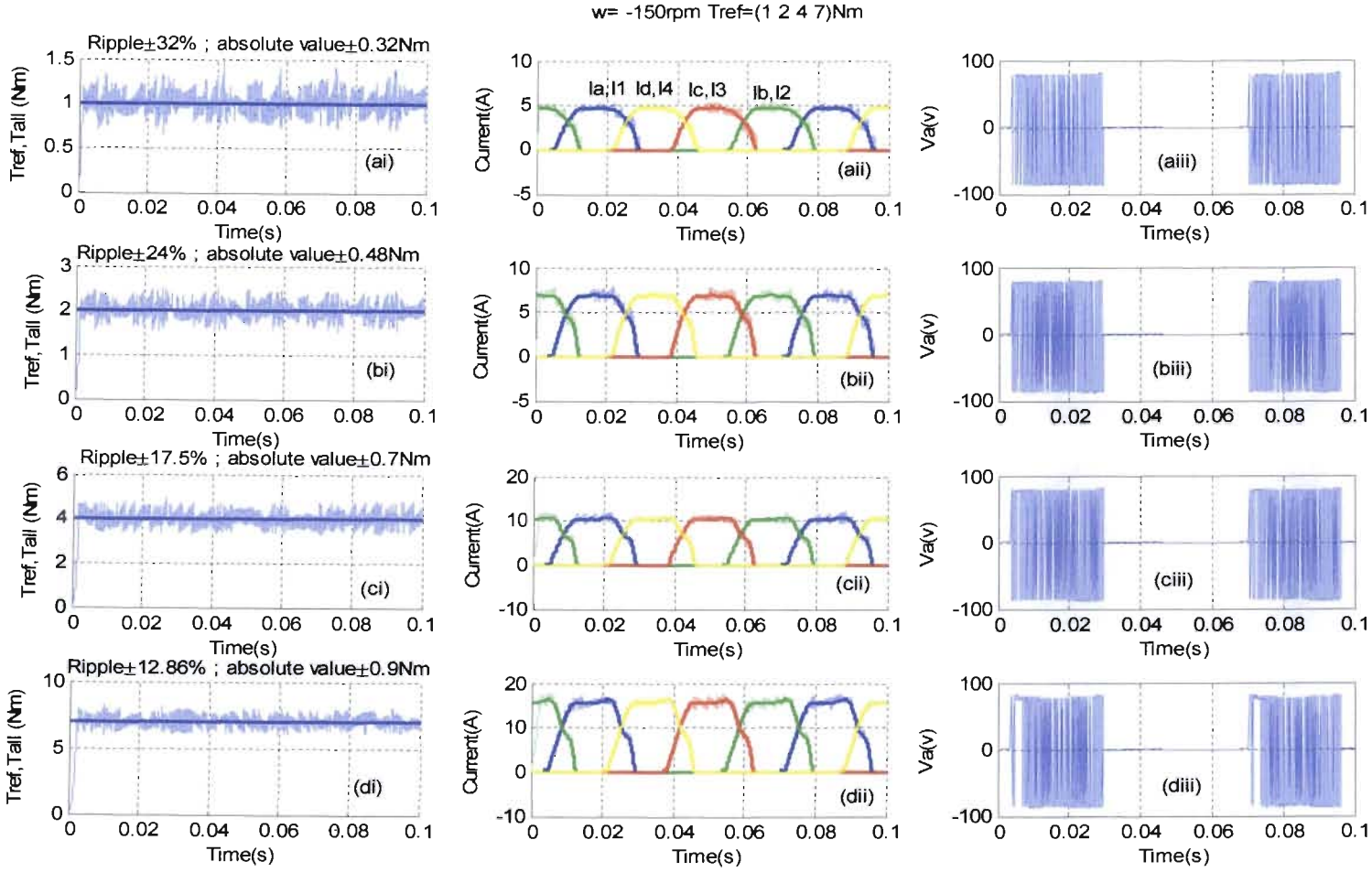

Fig. 4.22 Four phase torque and current control results with speed at -150 rpm and torque reference at 1, 2, 4,7 Nm

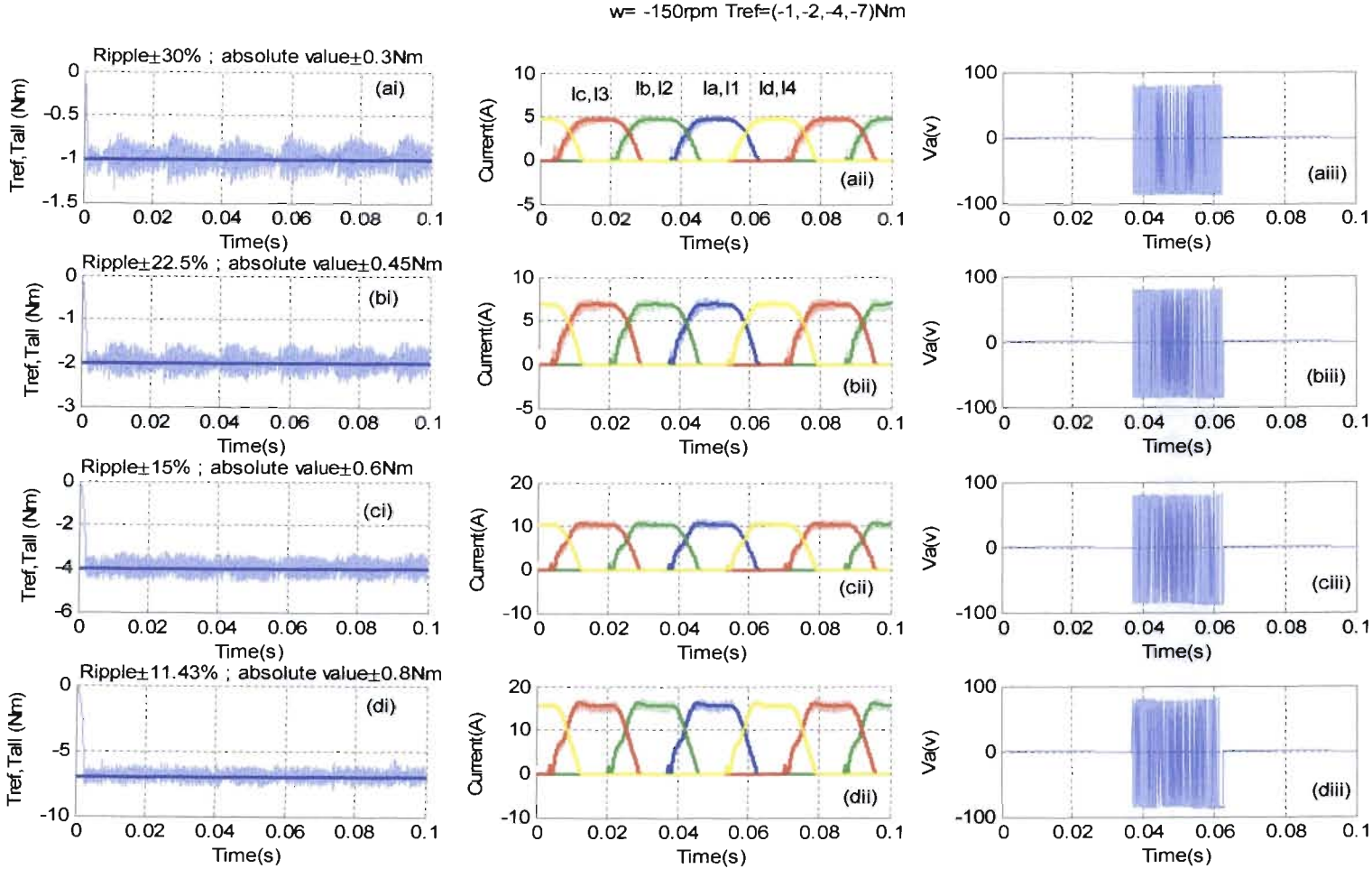

Fig. 4.23 Four phase torque and current control results with speed at -150 rpm and torque reference at -1, -2, -4,-7 Nm

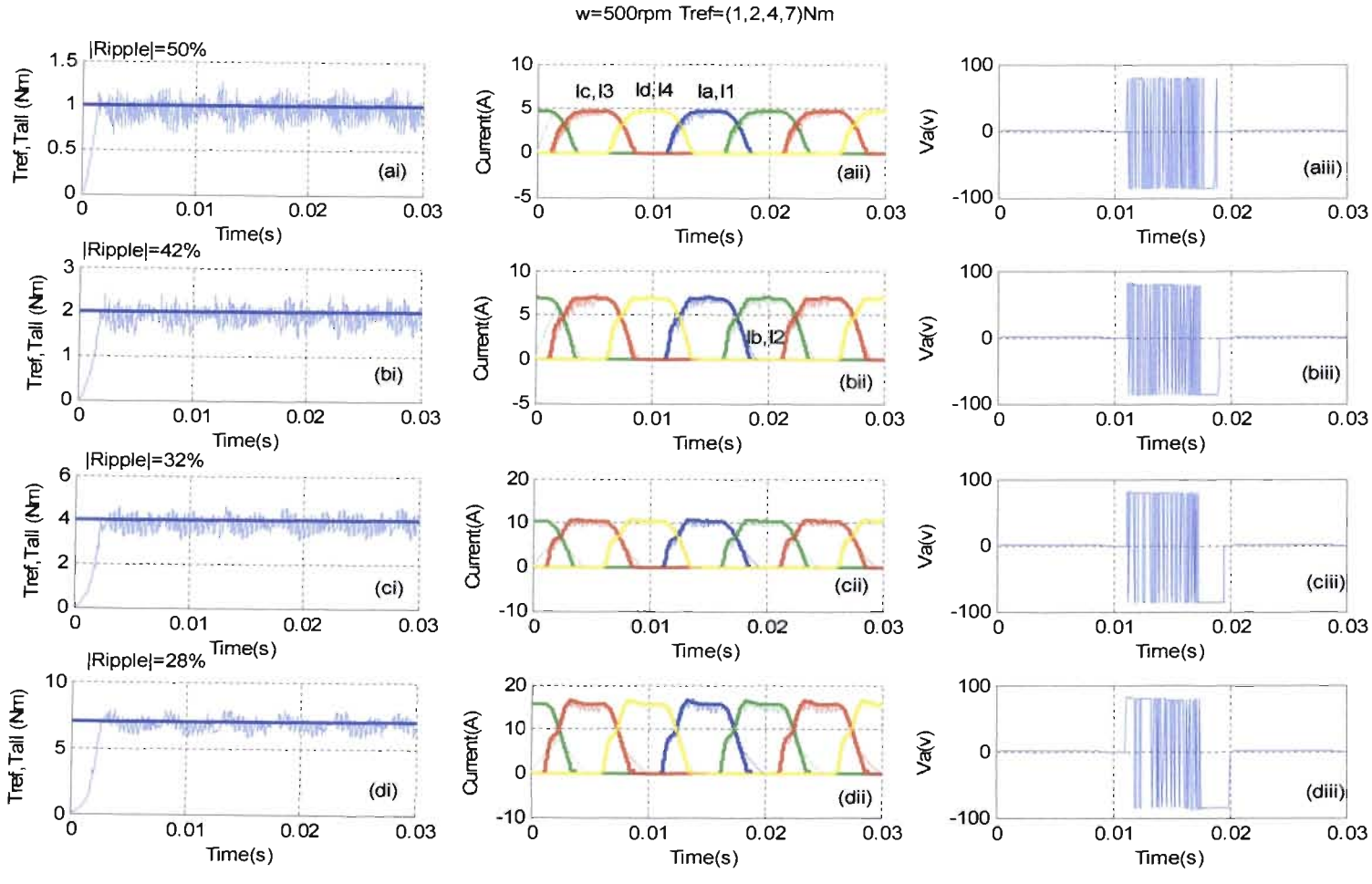

Fig. 4.24 Four phase torque and current control results with speed at 500 rpm and torque reference at 1, 2, 4,7 Nm

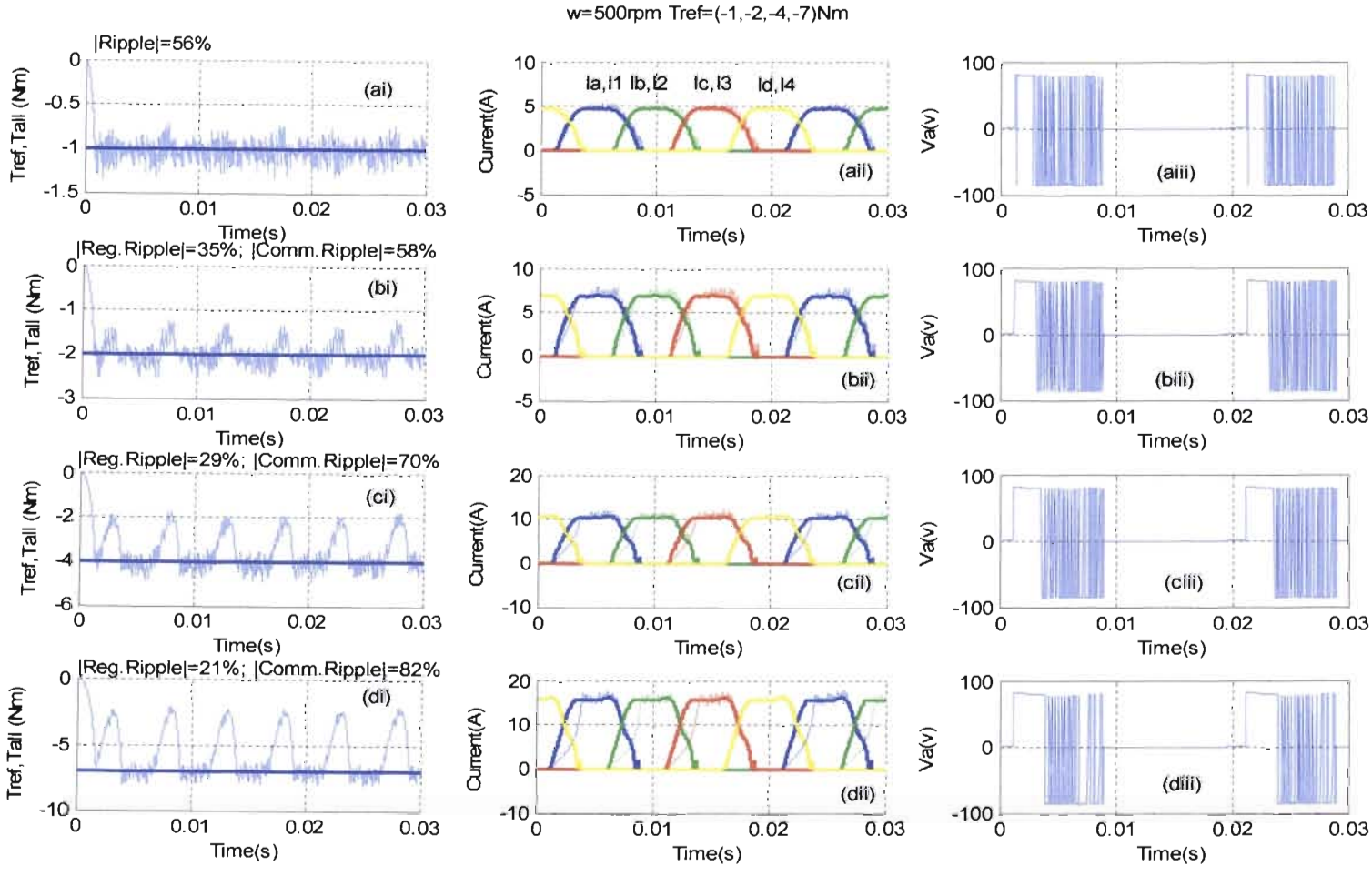

Fig. 4.25 Four phase torque and current control results with speed at 500 rpm and torque reference at -1, -2, -4,-7 Nm

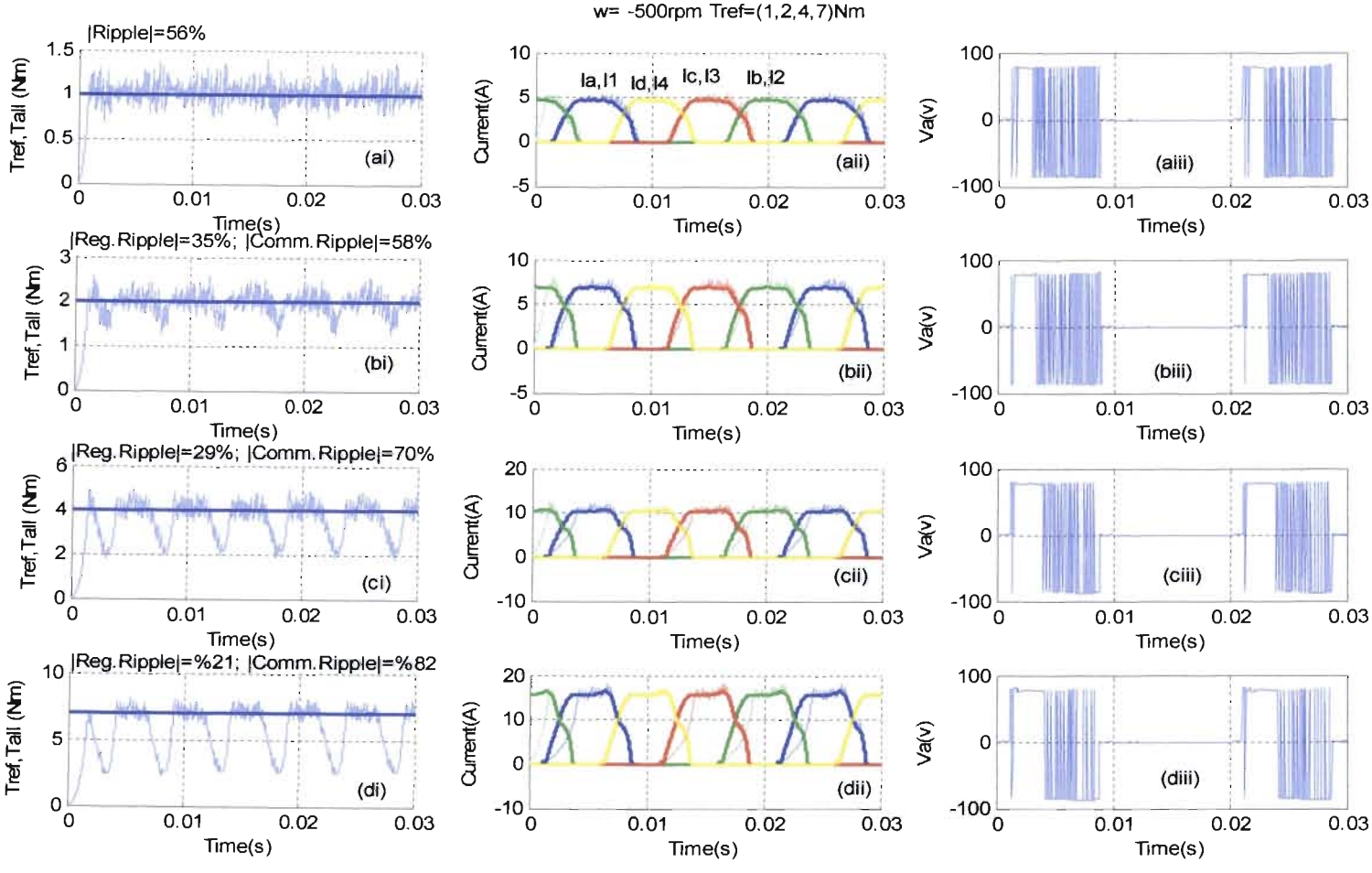

Fig. 4.26Four phase torque and current control results with speed at -500 rpm and torque reference at 1, 2, 4,7 Nm

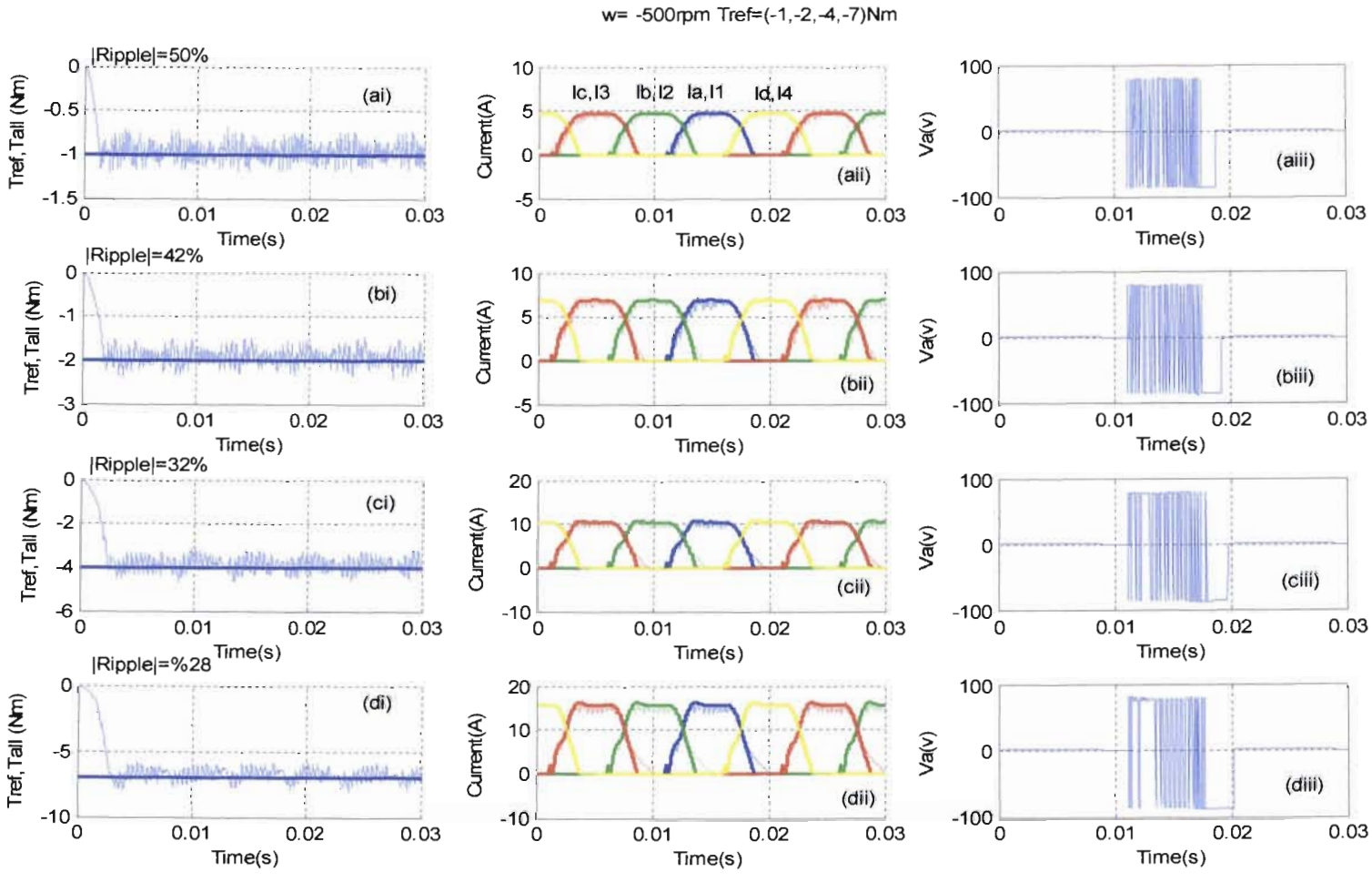

Fig. 4.27 Four phase torque and current control results with speed at -500 rpm and torque reference at -1, -2, -4,-7 Nm

Symmetry with respect to direction of rotation

Figs. 4.20 to 4.27 show that the total torque response is independent of the direction of rotation in both motoring and generating modes for speeds of ±150 rpm and ±500 rpm. Figs. 4.28 to 4.35 show that the same is true at speeds of ±1000 rpm and ±1500 rpm.

Results at ±1000rpm (medium speed)

The continuous on/off periods observed in motoring/generating mode in Fig. 4.28 to Fig. 4.31, at the beginning/end of the conduction period, increase with increasing torque reference magnitude (which produces higher phase current magnitudes, and therefore higher resistive volt drops), and increasing rotor speed.

In *motoring* mode, shown in Fig. 4.28 and Fig. 4.31, there is still reasonably good tracking of low torque reference magnitudes (i.e. ±1 Nm, ±2 Nm), despite relatively large lags or "tails" on the phase current responses at the end of each conduction period. The tracking performance is significantly degraded at higher torque references (i.e. ±4 Nm, ±7 Nm), as the increased back emf and resistive volt drops result not only in larger tails, but also prevent the current controller from achieving the required peak current values. The torque ripple in these cases is calculated by using the average torque value shown in Table 4.5 in both motoring and generating modes at the speed of ±1000 rpm and ±1500 rpm.

In *generating* mode, shown in Fig. 4.29 and Fig. 4.30, there are noticeable drops in the total torque magnitude for all torque reference magnitudes, despite the fact that the required peak current magnitude can now be tracked due to the relative inversion of the back emf (this indicates the extent to which the *motoring* performance can be improved by increasing Vdc). The only reason for the torque drops is thus the disproportionate increase in the turn-on lag. The reason that the turn on-lag in generating mode is significantly higher than the turn-off lag (tail) in motoring mode for a given speed and torque/current reference magnitude is discussed in section 4.4.3, together with possible solutions which could be explored as part of future work. It is also explained there why the |Comm.Ripple| increases to a significantly high value with increasing torque reference magnitude.

Results at ±1500rpm (high speed)

Fig. 3.31 to 3.34 show that all current control (and hence torque response) performance degradations due to increased back emf and resistive volt drops are further exaggerated when speed is further increased from ±1000 rpm to ±1500 rpm. The clear inability of the current controller to track the reference current during commutation periods results in severe commutation torque ripple. The only way to improve the current control performance at higher speeds is to increase the dc link voltage Vdc. This, however, will cause a significant increase in the current ripple (and hence torque ripple) at low speeds unless the sampling frequency (and hence switching frequency) is also increased, as shown in Fig. 4.18. Future work on the use of PWM current control, however, could allow the voltage to be increased without increasing the current ripple.

Summary of Results

Table 4.5 shows a summary of the average torque produced for the various motoring and generating torque and current control simulation results shown in Figs. 4.20 to 4.35. This table shows the following general trends.

- The average torque is relatively independent of the direction of rotation.
- The average torque shortfall increases with increasing torque reference due to the increased resistive voltage drops at the correspondingly higher currents.
- The average torque shortfall increases with increasing speed due to increasing back emf.

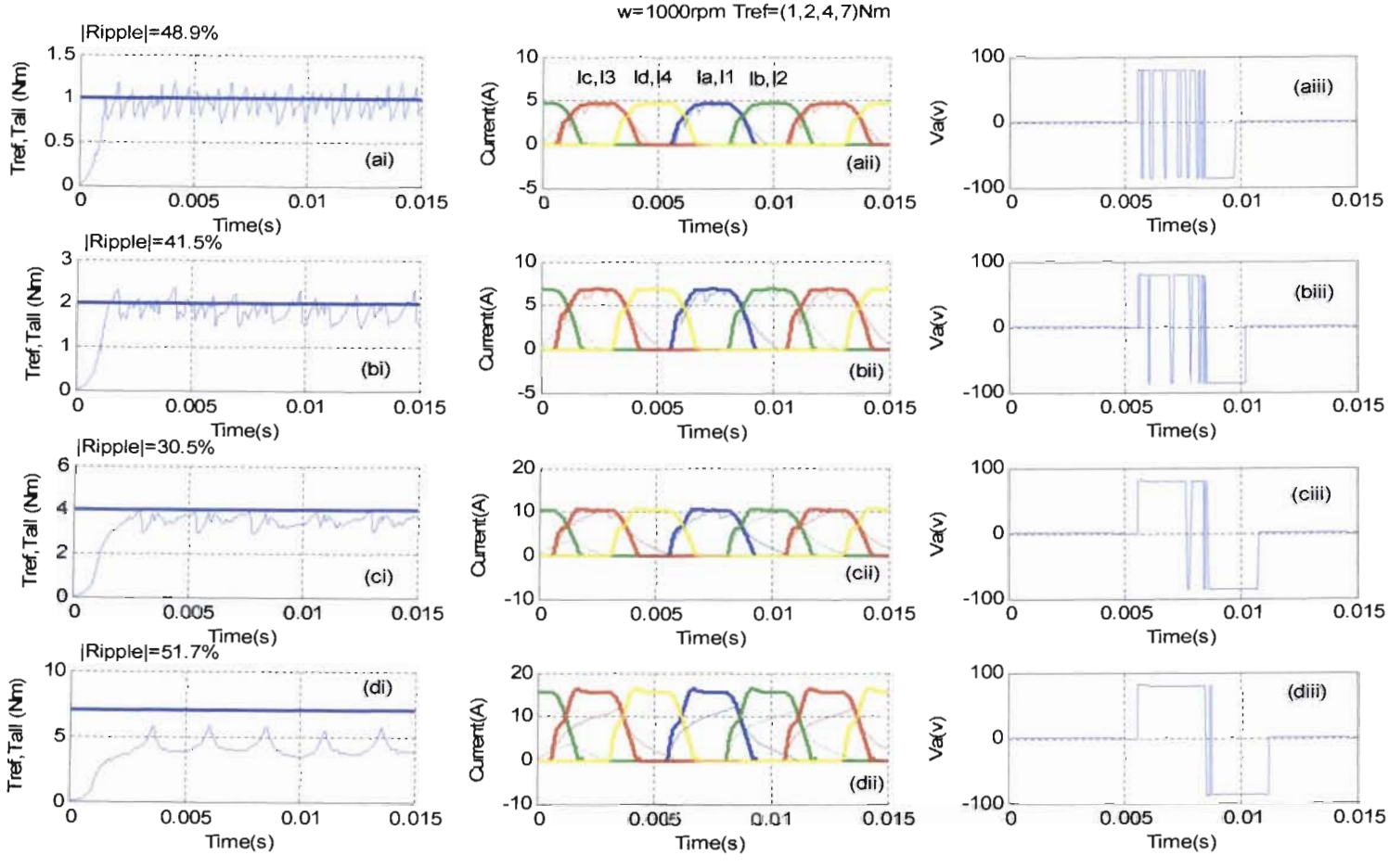

Fig. 4.28 Four phase torque and current control results with speed at 1000 rpm and torque reference at 1, 2, 4,7 Nm

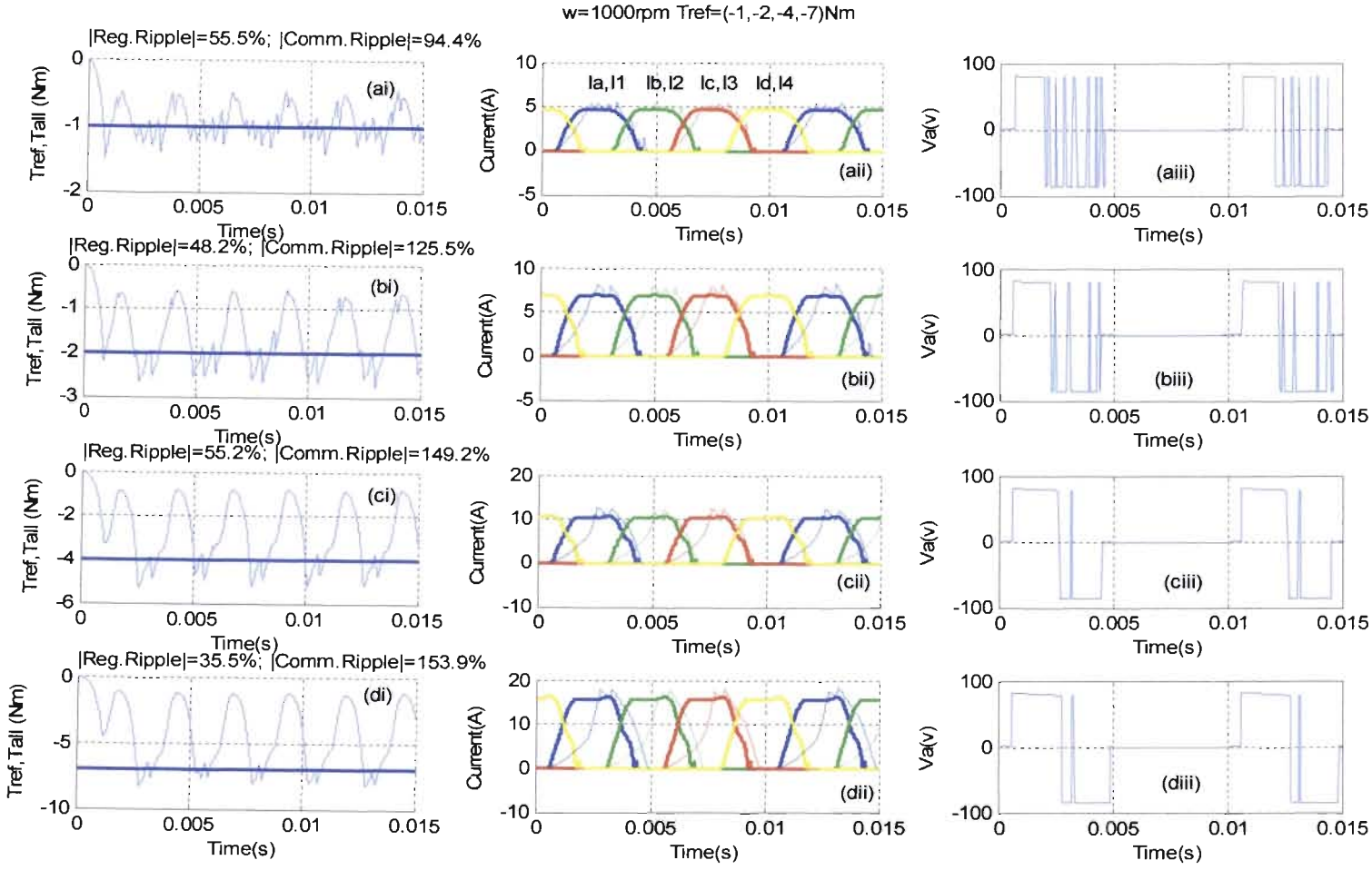

Fig. 4.29 Four phase torque and current control results with speed at 1000 rpm and torque reference at -1, -2, -4,-7 Nm

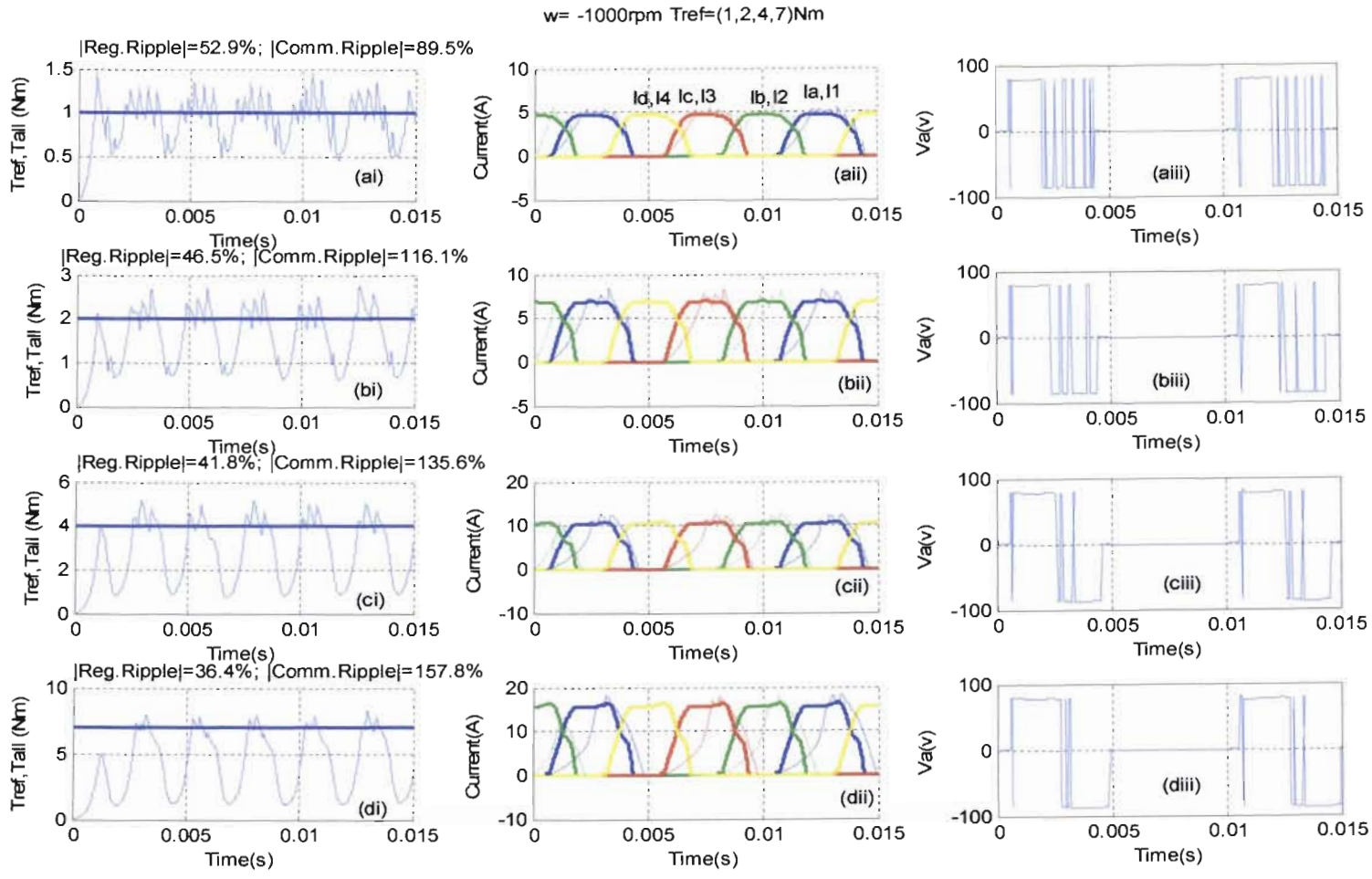

Fig. 4.30 Four phase torque and current control results with speed at -1000 rpm and torque reference at 1, 2, 4,7 Nm

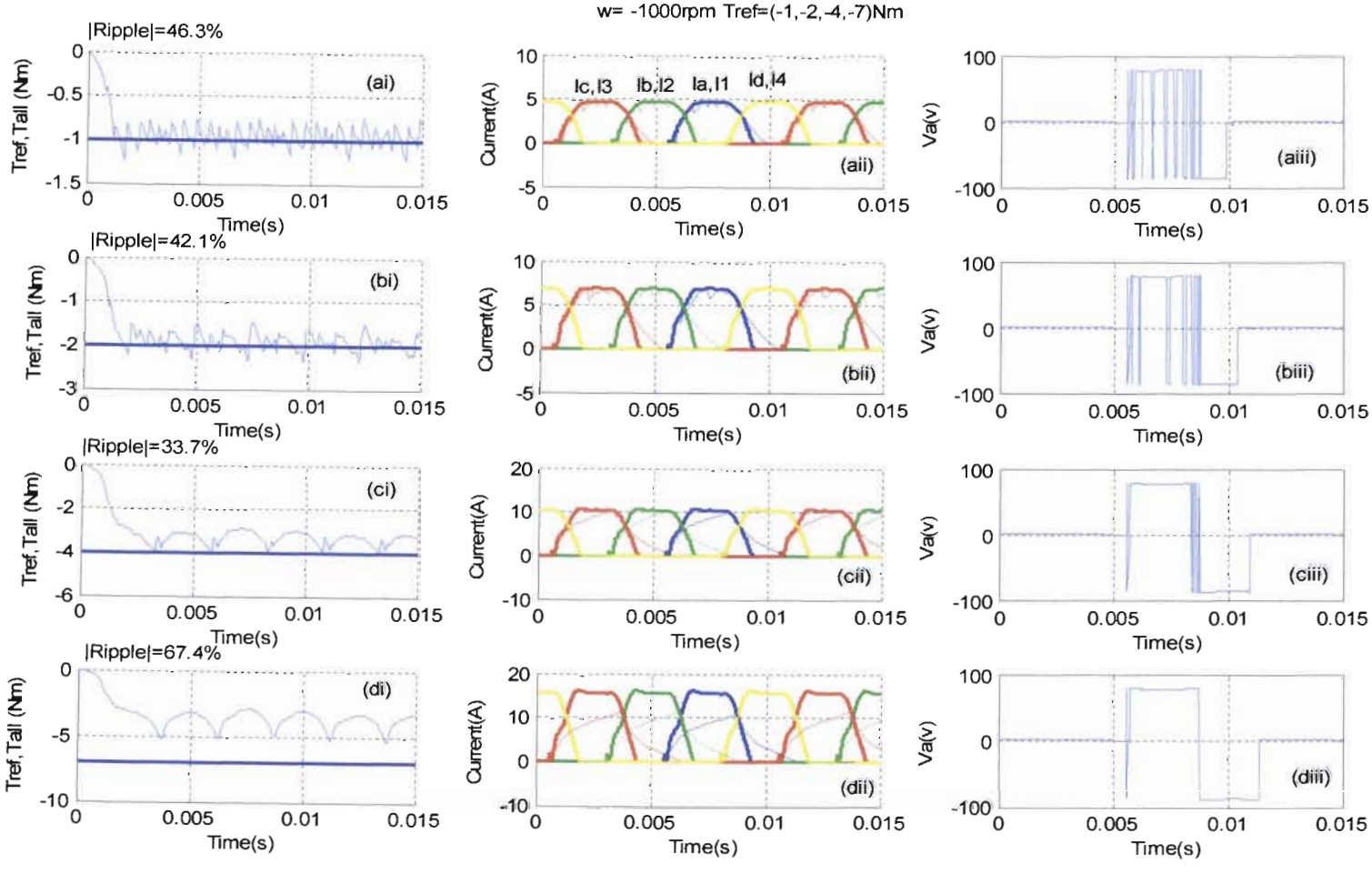

Fig. 4.31 Four phase torque and current control results with speed at -1000 rpm and torque reference at -1, -2, -4,-7 Nm

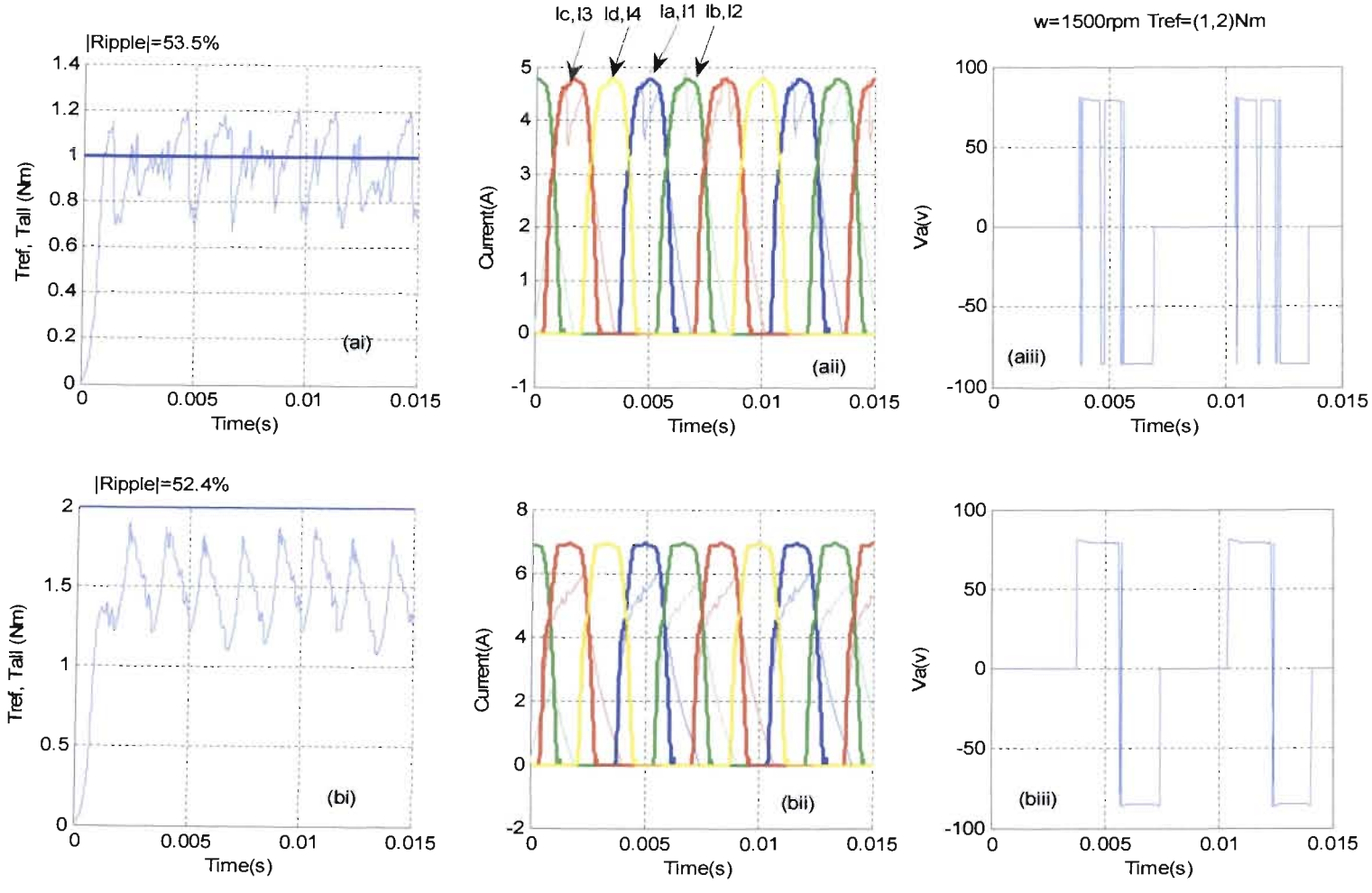

Fig. 4.32 Four phase torque and current control results with speed at 1500 rpm and torque reference at 1, 2 Nm

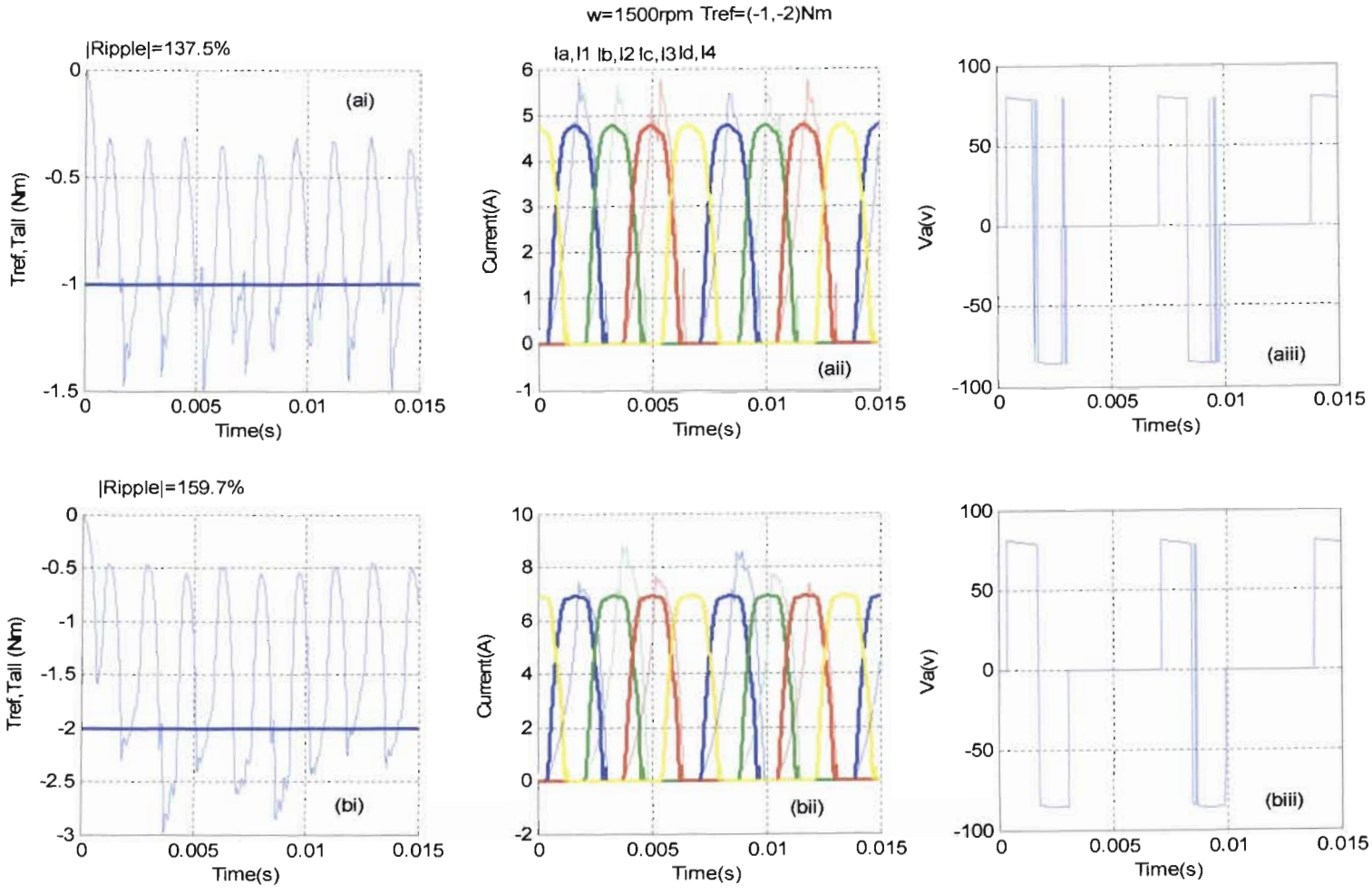

Fig. 4.33 Four phase torque and current control results with speed at 1500 rpm and torque reference at -1, -2 Nm

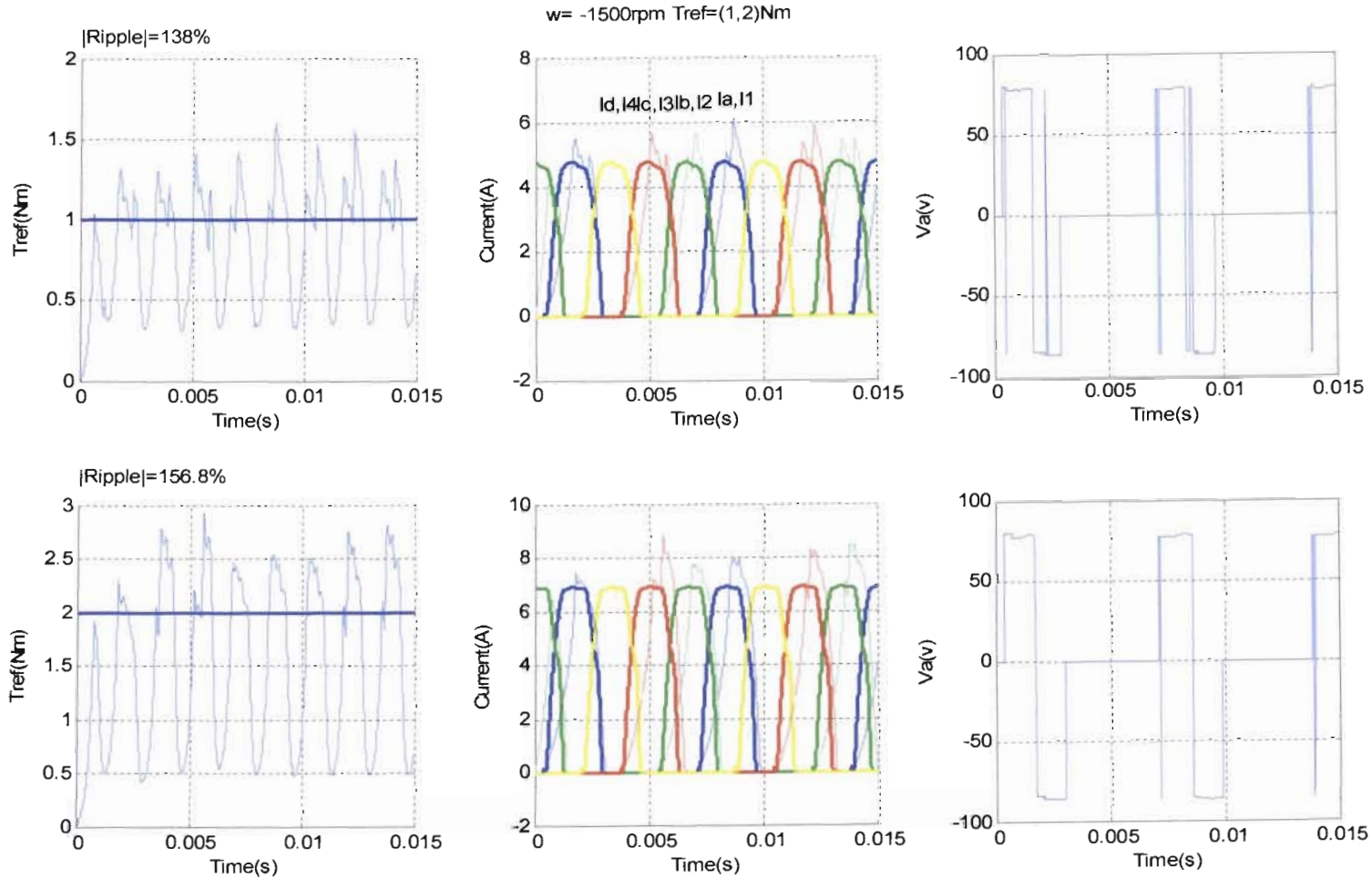

Fig. 4.34 Four phase torque and current control results with speed at -1500 rpm and torque reference at 1, 2 Nm

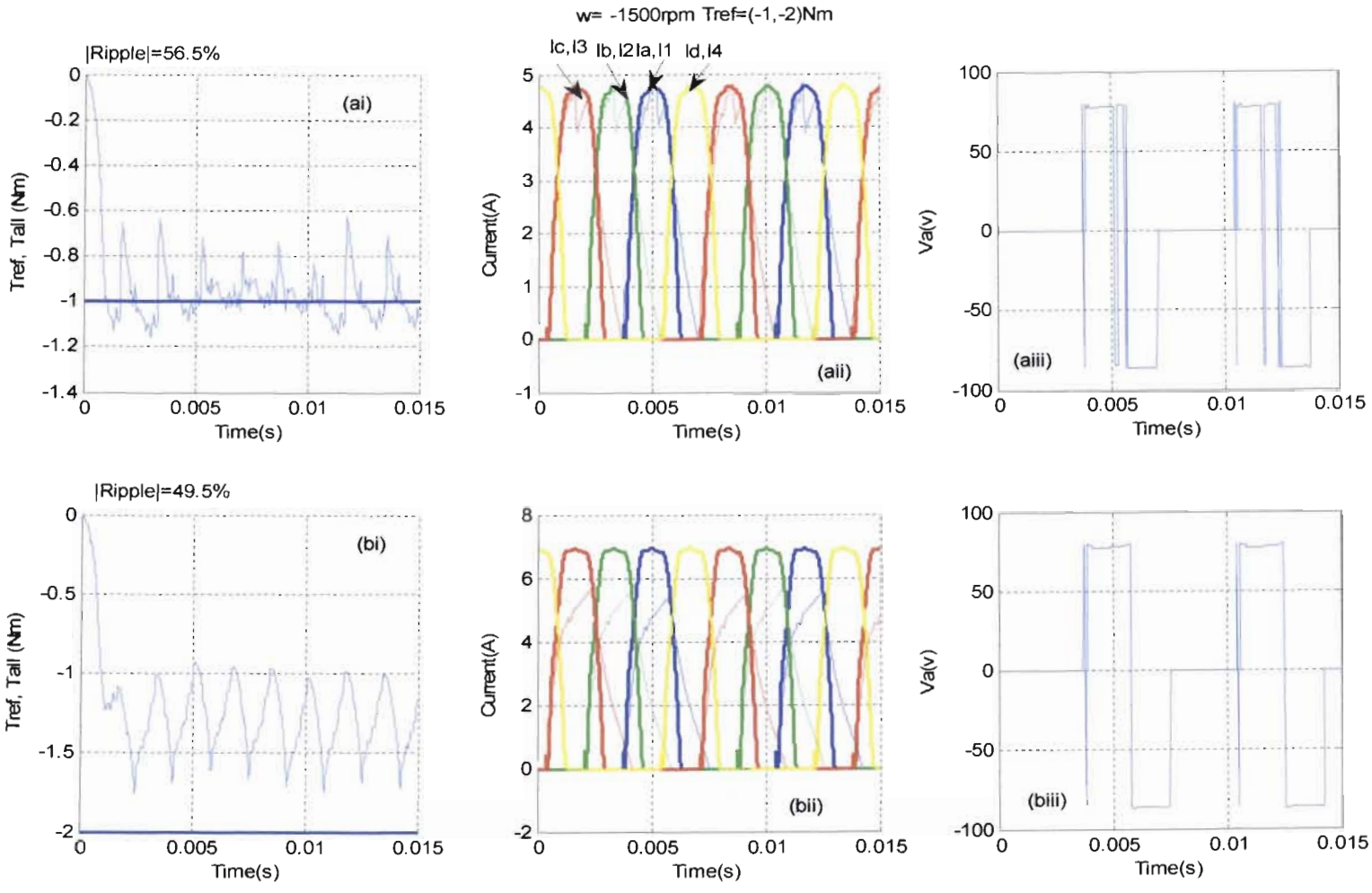

Fig. 4.35 Four phase torque and current control results with speed at-1500 rpm and torque reference at -1, -2 Nm

Tref (Nm) → Rotor speed (rpm)↓	***-7***	***-4***	***-2***	***-1***	***0***	***1***	***2***	***4***	***7***
150rpm	-6.999	-4.0269	-2.0078	-1.0087	0	0.9871	1.9564	3.9201	6.8667
Torque error (%)	.014	-0..67	-0.39	-0.87	-	1.29	2.18	2.00	1.90
- 150rpm	-6.8623	-3.9242	-1.9618	-0.9894	0	1.0114	2.0097	4.0128	7.0205
Torque error (%)	1.97	1.90	1.91	1.06	-	-1.14	-.485	-.320	-.293
500rpm	-5.6614	-3.5484	-1.9729	-1.0237	0	0.9536	1.9075	3.8166	6.799
Torque error (%)	19.1	11.3	1.36	-2.37	-	4.64	4.62	4.58	2.87
- 500rpm	-6.771	-3.8355	-1.9138	-0.9646	0	1.0301	1.9679	3.5826	5.7106
Torque error (%)	3.27	4.11	4.31	3.54	-	-3.01	1.61	10.4	18.4
1000rpm	-4.5475	-2.8937	-1.6568	-0.9477	0	0.943	1.8537	3.5256	4.163
Torque error (%)	35.0	27.7	17.2	5.23	-	5.70	7.32	11.9	40.5
- 1000rpm	-3.7387	-3.3216	-1.8984	-0.9491	0	0.945	1.6557	2.9478	4.4339
Torque error (%)	46.6	17.0	5.08	5.09	-	5.50	17.2	26.3	36.7
1500rpm			-1.5344	-0.8441	0	0.9634	1.4762		
Torque error (%)			23.3	15.6	-	3.66	26.2		
- 1500rpm			-1.2795	-0.9722	0	0.8575	1.5657		
Torque error (%)			36.0	2.78	-	14.3	21.7		

Table 4.5 Average torque and torque error by percentage results derived from Fig. 4.20 to Fig. 4.35

4.4.3 Motoring and Generating Turn-on and Turn-off Asymmetry

The results in Figs. 4.24 to 4.35 show that the torque ripple is significantly higher in generating mode (i.e. when T_{ref} and speed have opposite signs), than in motoring mode (i.e. when T_{ref} and speed have the same sign). This effect is seen to correspond with the fact that the turn-on delay in generating mode is significantly higher than the corresponding turn-off delay in motoring mode. This section shows that this occurs because the turn-on transient occurs at a different point on the phase inductance characteristic that the turn-off transient. Fig. 4.36 shows plots of the steady state phase inductance, phase 1 current, back emf, phase 1 voltage, and total torque in motoring mode, with a torque reference of +7 Nm at a speed of 500rpm. Fig 4.40 shows the same curves in the equivalent generating mode (i.e. with a torque reference of -7 Nm).

Fig. 4.36 shows that, in *motoring* mode, turn-on is initiated when the inductance (G1) is low. The inductance also remains relatively low during the whole turn-on period. The inductance is not significantly higher when turn-off is initiated, but increases significantly during the turn-off period. It is noted that the turn-on and turn-off periods are dictated by the torque sharing function in terms of *angle* intervals. The corresponding *time* periods will therefore depend on speed, but the relationship between the inductance characteristic is fixed both with respect to angle and time.

Fig 4.37 shows that, in *generating* mode, turn-on is initiated when the inductance (G1) is almost at its peak value. The inductance decreases during the turn-on period, but remains relatively high for most of the turn-on period. It can be seen the relatively large drops in the torque magnitude correspond with the resulting turn-on current lag. However, the inductance is relatively low when turn-off is initiated, and remains relatively low during the whole turn-off period. The current tracking performance during the turn-on period is thus much worse in generating mode than in motoring mode, but there is better tracking during the turn-off period in generating mode than in motoring mode.

Figs. 4.36 and 4.37 show plots of the back emf calculated using eq. 2.9a in Chapter 2, as shown in Appendix C.14. It can be seen that the back emf is negative in generating mode and positive in motoring mode with respect to the switched dc link voltage. The peak back emf is also significantly higher in generating mode, and already within 12% of the dc link voltage at this speed of 500 rpm. There is, however, no significant back emf assistance

during turn-on due to the relatively strong dependence at the back emf on phase current magnitude (and the low current magnitudes at the beginning of the turn-on period).

Increasing Vdc will result in higher phase voltages and therefore significantly improve the current tracking (and hence torque control) performance by reducing the current response lag during turn-on in generating mode and turn-off in motoring mode. Fig. 4.38 confirms that the turn-on current lag will be significantly reduced by increasing Vdc from 81v to 200v, and that corresponding drops in the torque magnitude (and shortfall in average torque) will thus also be significantly less than in Fig. 4.37, at the expense of more than twice the high (hysteresis switching) frequency torque ripple. There are, however, no significant dips in the torque response in motoring mode. The increased voltage would therefore only worsen the torque response by significantly increasing the high (hysteresis switching) frequency ripple. It is therefore strongly suggested that future work investigate the use of PWM current control to obtain the full benefit of increased dc link voltage.

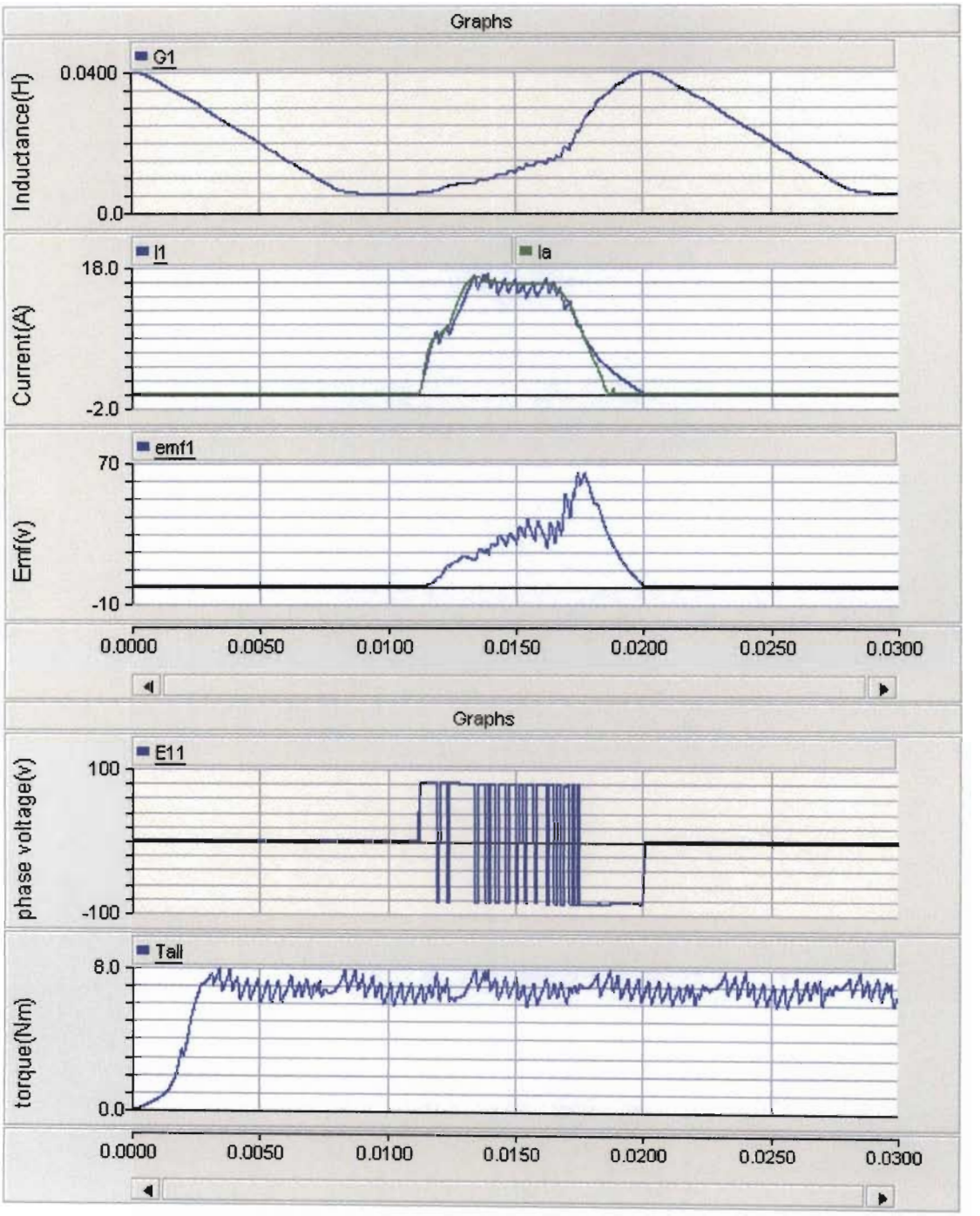

Fig. 4.36 Simulation results when torque reference is 7 Nm, speed is 500 rpm with hysteresis current control

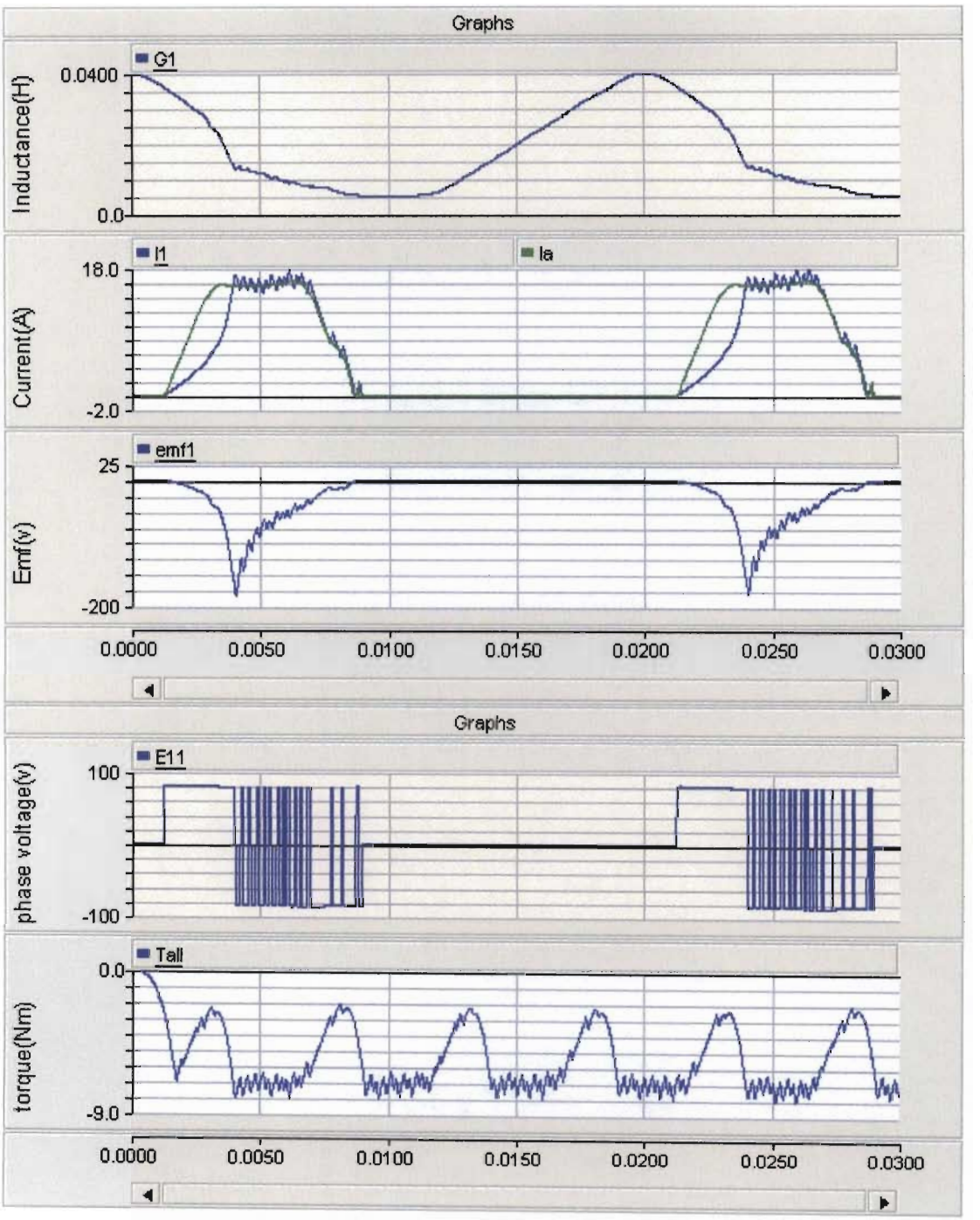

Fig. 4.37 Simulation results when torque reference is -7 Nm, speed is 500 rpm with hysteresis current control

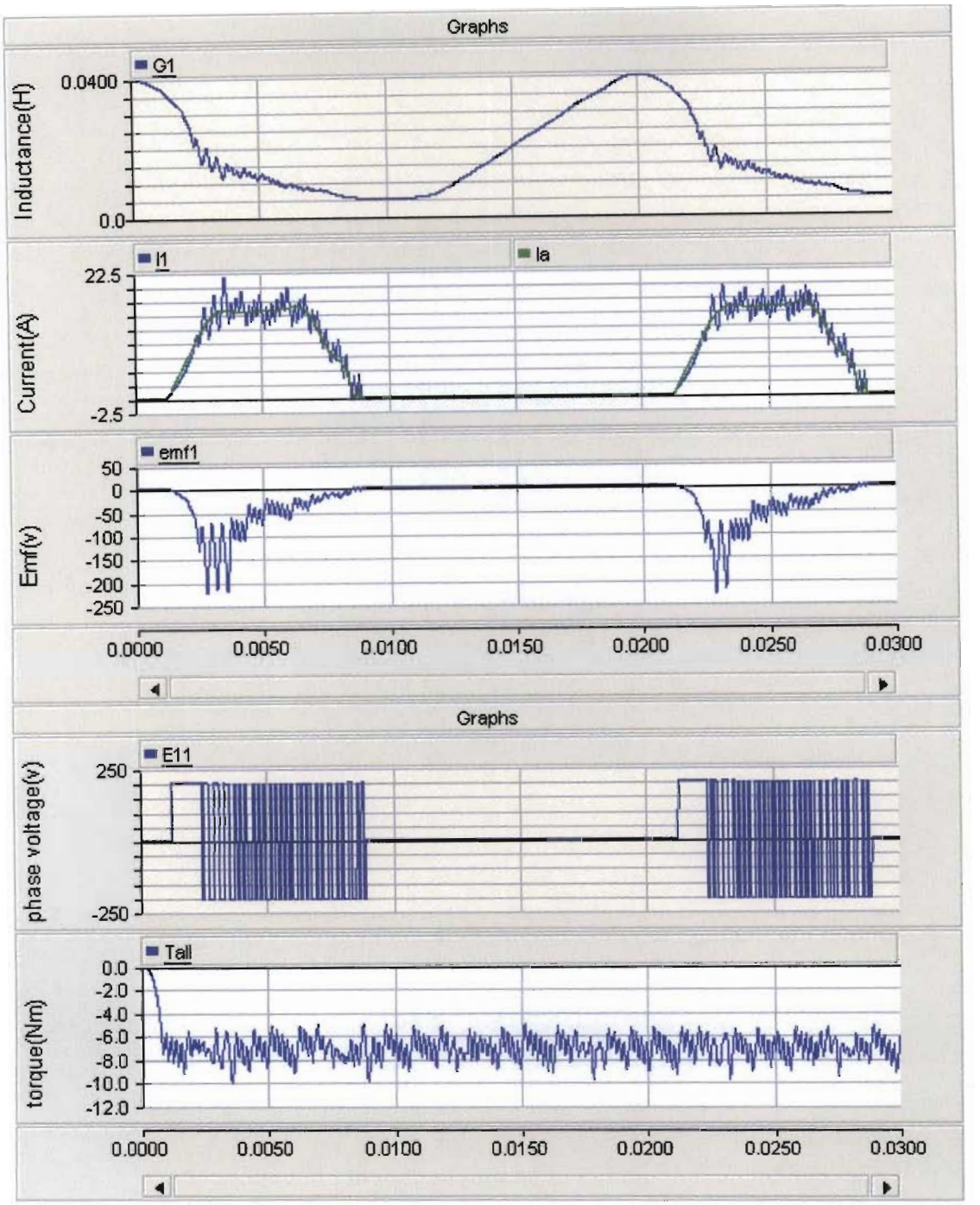

Fig. 4.38 Results of the same test condition show in Fig. 4.40 with higher Vdc (200v instead of 81v)

4.5 Summary

The principle of torque control via direct adjustment of commutation angles has been introduced, and PSCAD simulation results have been presented which predict relatively high commutation torque ripple for several combinations of fixed turn-on and turn-off angles for the 8/6 SRM of this thesis.

An alternative Torque Sharing Function (TSF) strategy for minimizing commutation torque ripple has also been introduced. The corresponding PSCAD torque control model has been presented and tested under several locked and free rotor conditions, assuming ideal current control. The relatively low torque ripple observed in these results is attributed to small errors in the construction of the lookup table required by this method to transform phase torque references into corresponding phase current references.

A PSCAD model for hysteresis current control with a fixed error sampling rate (and hence upwardly bounded switching frequency) has also been combined with the TSF model, and tested under various operating conditions. It has been shown that this hysteresis current control method requires a relatively high sampling rate in order to produce low current (and hence torque) switching ripple at low speeds, with higher values of dc link voltage. Simulation results predict that this method can produce 8/6 SRM torque responses with low commutation ripple in both motoring and generating modes. However, these results also predict significant hysteresis switching induced current ripple (and hence high frequency torque ripple) at the dc voltage levels which would be required to achieve average torque magnitudes higher than 2 Nm at speed s above 500 rpm. It has therefore been suggested that future work investigate PWM current control to reduce voltage switching induced current and torque ripple.

The next chapter presents a practical implementation of the TSF torque and current control strategy, and measured results to confirm the various predictions derived from the simulations of this chapter. This chapter has also focused only on steady state performance. The next chapter presents and analyses simulated and measured results under transient test conditions.

CHAPTER FIVE

PRACTICAL IMPLEMENTATION

5.1 Introduction

Chapter 2 presented measurements and Matlab/Simulink simulation models for an 8/6 SRM. Chapter 3 used PSCAD to compare several power converter topologies for this motor, and validated PSCAD equivalents of the Matlab/Simulink models in conjunction with an AHB converter. Chapter 4 used the PSCAD motor and converter models to develop and test a TSF torque control strategy with regularly sampled hysteresis current control.

This chapter presents a laboratory prototype implementation of this strategy in sections 5.2 and 5.3, and compares measured and simulated results under several operating conditions in section 5.4. The hardware used for this implementation is described in section 5.2. Section 5.3 then presents an overview of the software used to implement a real time version of the controller presented in Chapter 4, and several practical limitations of this software at the time of writing this thesis.

5.2 Prototype 8/6 SRM Drive Hardware

Fig. 5.1 shows a block diagram of the prototype hardware configuration.

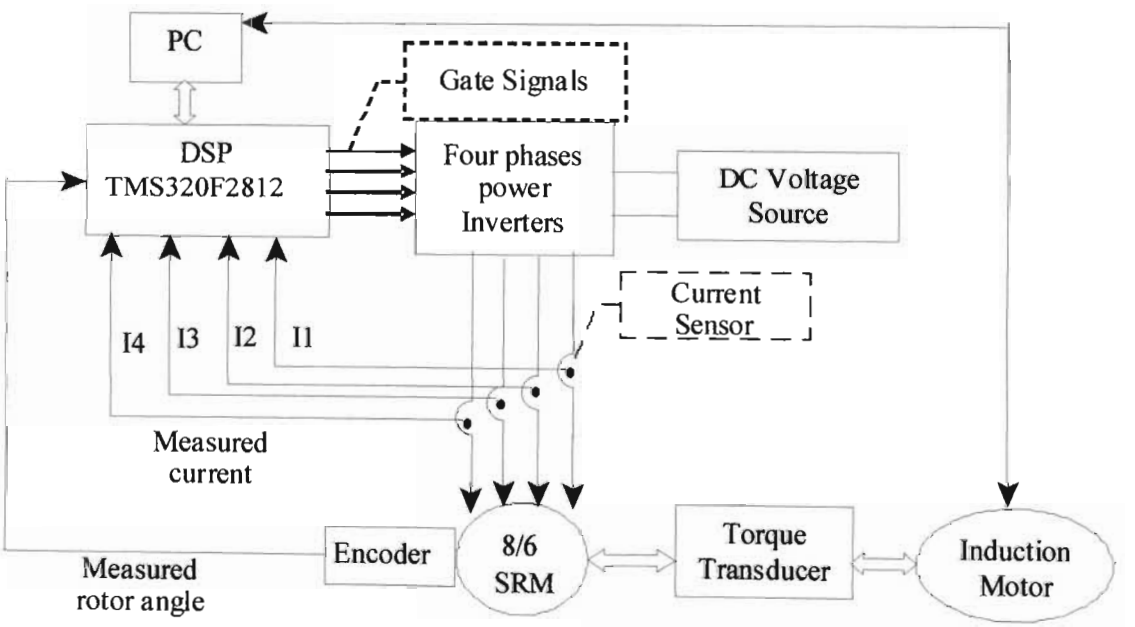

Fig. 5.1 Block diagram of the prototype 8/6 SRM drive hardware configuration

A photograph of the corresponding experimental setup is shown in Fig. 5.2.

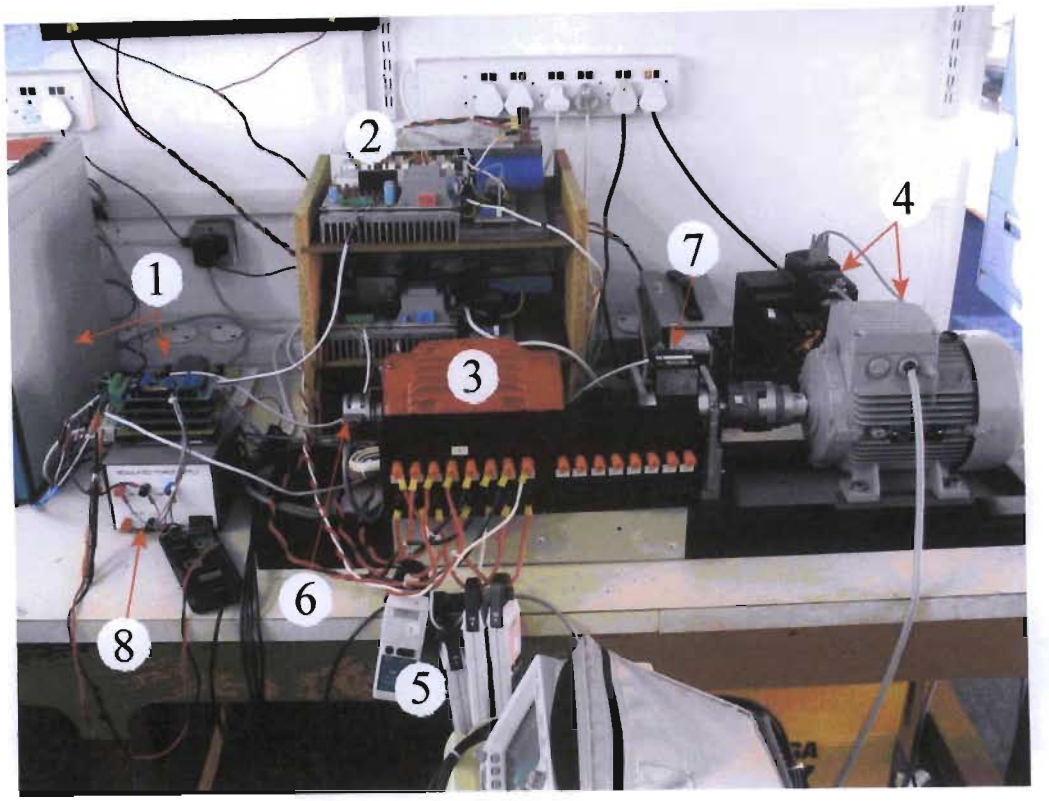

Fig. 5.2 Photograph of the prototype 8/6 SRM drive experimental setup

The laboratory system comprises the following 7 modules.

(1) Controller hardware (PC and DSP)
(2) Power converter
(3) SRM motor
(4) Load (3kW induction motor and commercial vector drive [5.1])
(5) Current sensors
(6) Shaft encoder
(7) Torque transducer
(8) Standalone dc power supply (+5V/2A, +15V/2A, -15V/1A)

The PC is used to develop the real time version of the torque and current control strategy presented in chapter 4. The program is downloaded to the DSP flash ROM via a windows utility. In the laboratory, this program is then interactively controlled (started, stopped, fed references and flags from buttons and sliders etc.) and monitored (with digital displays and/or graphs etc.) by running the corresponding DSP interface block in a VisSim window on the PC

(in an industrial/embedded application, there is no need for the PC: all control signals can be obtained directly from digital or analogue inputs or communication ports, and monitoring signals fed to analogue or digital outputs or communication ports). The DSP then effects torque and current control via gate signals to power inverters, based on phase current and angle measurements from the current sensors and quadrature shaft encoder respectively.

The Induction motor and commercial vector drive are used as a constant speed load for the SRM (as explained in Chapter 4, this type of load provides a consistent basis for comparison of the responses to various torque references in both motoring and generating mode). A high grade torque transducer is coupled between SRM and IM for torque measurement in such a way that the SRM torque can also be directly measured under locked rotor conditions.

The controller hardware is made up of a DSP motherboard, and several in-house developed application specific daughter boards.

DSP Motherboard

The Texas Instruments TMS320F2812 "eZdsp" development "motherboard" is chosen as the core control hardware because of its relatively high speed and relatively large memory, but primarily because of its integrated motion control specific peripheral I/O functions. This eZdsp board is supplied with the Code Composer Studio V2.12 ANSI C compliant IDE [5.2] from Texas Instruments. However, only the compiler was used in the work of this thesis: all development was done in the VisSim graphical programming environment [5.3] from Visual Solutions, as explained in section 5.3.

The F2812 DSP has two event-manager modules, shown as EVA and EVB in Fig. 5.3. It can be seen that these each have their own identical general-purpose (GP) timers, full-compare/PWM units, capture units, and quadrature-encoder pulse (QEP) circuits.

The GP timers can be operated independently, or synchronized with each other in a number of ways. The compare register associated with each GP timer can be used for various general or real time PWM-specific compare functions. The GP timer also provides the time base for the other event-manager sub modules, namely GP timer 1 for all the compares and PWM circuits, and GP timer 2/1 for the capture units and the quadrature-pulse counting operations. There are three full-compare units on each event manger. These compare units use GP timer1 as the time base and generate six independent outputs for general compare or PWM-waveform generation. Each of these six outputs has a complementary output, which can be configured to

implement dead time for control of conventional power converter topologies (e.g. each event manager can control all six devices of a three phase voltage source inverter).

Two capture inputs (CAP1 and CAP2 for EVA, and CAP4 and CAP5 for EVB) can be used to interface the on-chip QEP circuit with an external quadrature encoder. Direction is determined by identifying the leading-quadrature pulse sequence, and GP timer 2/4 is incremented or decremented accordingly at each rising and falling edge of the two input signals (to effectively operate at four times the frequency of either input pulse).

The analogue-to-digital converter (ADC) module in the F2812 also has a flexible interface to EVA and EVB. The ADC interface is built around a fast, 12- bit ADC module with a total conversion time of 200ns. The ADC module has 16 channels, configured as two independent 8-channel modules to service EVA and EVB. The F2812 also includes two serial communications interface (SCI) modules. Daughter boards have been developed in-house to make optimum use of all of the peripheral interfaces incorporated into the F2812 DSP.

DSP Daughter Boards

The following DSP daughter boards have been developed.

General I/O Capture/QEP digital inputs, PWM and digital outputs

Analogue I/O 4 x differential ±10V input amplifiers for input offset/scaling/filtering. Two of these cards are required to interface the four phase current sensor outputs and one torque transducer output.

SCI 2 x RS232 ports (in-house RS485 and USB versions also available). One of these is used to stream up to 5 channels of live data to Matlab at a sample rate of up to 1kHz for plotting and archiving at much higher rates than is possible by running the corresponding DSP interface block in a VisSim window on the PC (which uses a JTAG interface).

Power Supply Various in-house AC/DC and DC/DC versions are available for portable/embedded applications, but a standalone supply is used in this laboratory system.

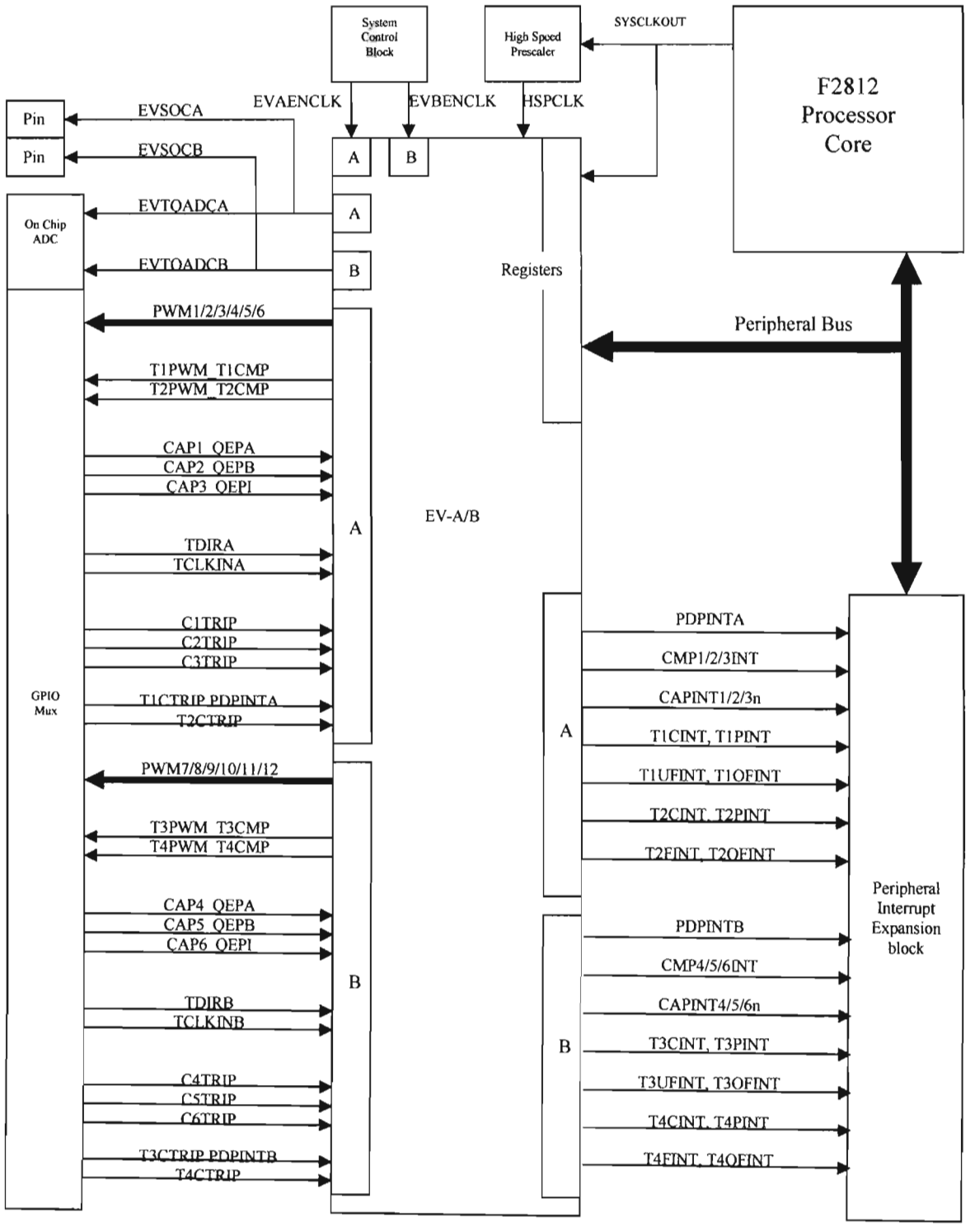

Fig. 5.3 Event manager interfacing in TMS320F2812 DSP system [5.4]

Four Phase AHB Power Converter

Fig. 5.4 shows a conventional three-phase IGBT converter. Three 10kVA converters of this type were configured as shown in Fig. 5.5 to implement an ad-hoc four phase AHB converter (each phase requiring two converter legs). The DC link of all three converters (each with its own 1000μF capacitor) was connected to the same tapping of a 280V battery supply.

In Fig. 5.5, A1 and B1 in converter1 are connected to phase terminals s1 and s1'. The corresponding IGBTs are controlled by feeding a digital output from the General I/O board to the corresponding gate inputs (e.g. Q1 and Q4 in Fig. 5.4). Similarly, A2 and B2 in converter2 are connected to phase terminals s2 and s2', B3 and C3 in converter3 are connected to phase terminal s4 and s4', and C2 and C1 in converters 2 and 1 are connected to phase terminals s3 and s3'. Future work could include the design of an application specific four-phase converter.

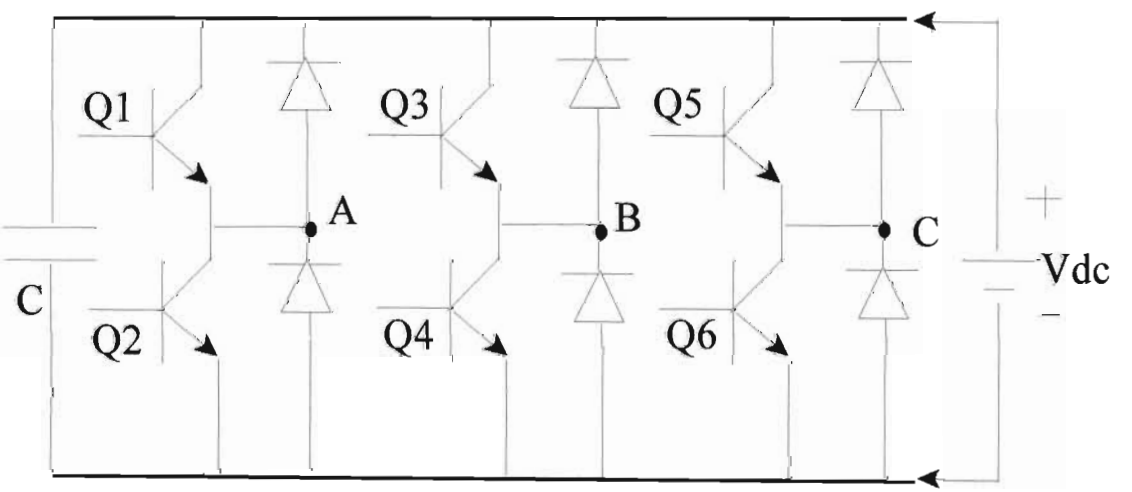

Fig. 5.4 Three phase asymmetrical half bridge (AHB) converter

Load

The 3kW induction motor and commercial vector drive were carefully commissioned to produce speed control with good disturbance regulation response in order to achieve a reasonably good constant speed load. A mechanical clamp was mounted on the induction motor shaft end of the torque transducer to facilitate locked SRM rotor torque response measurements.

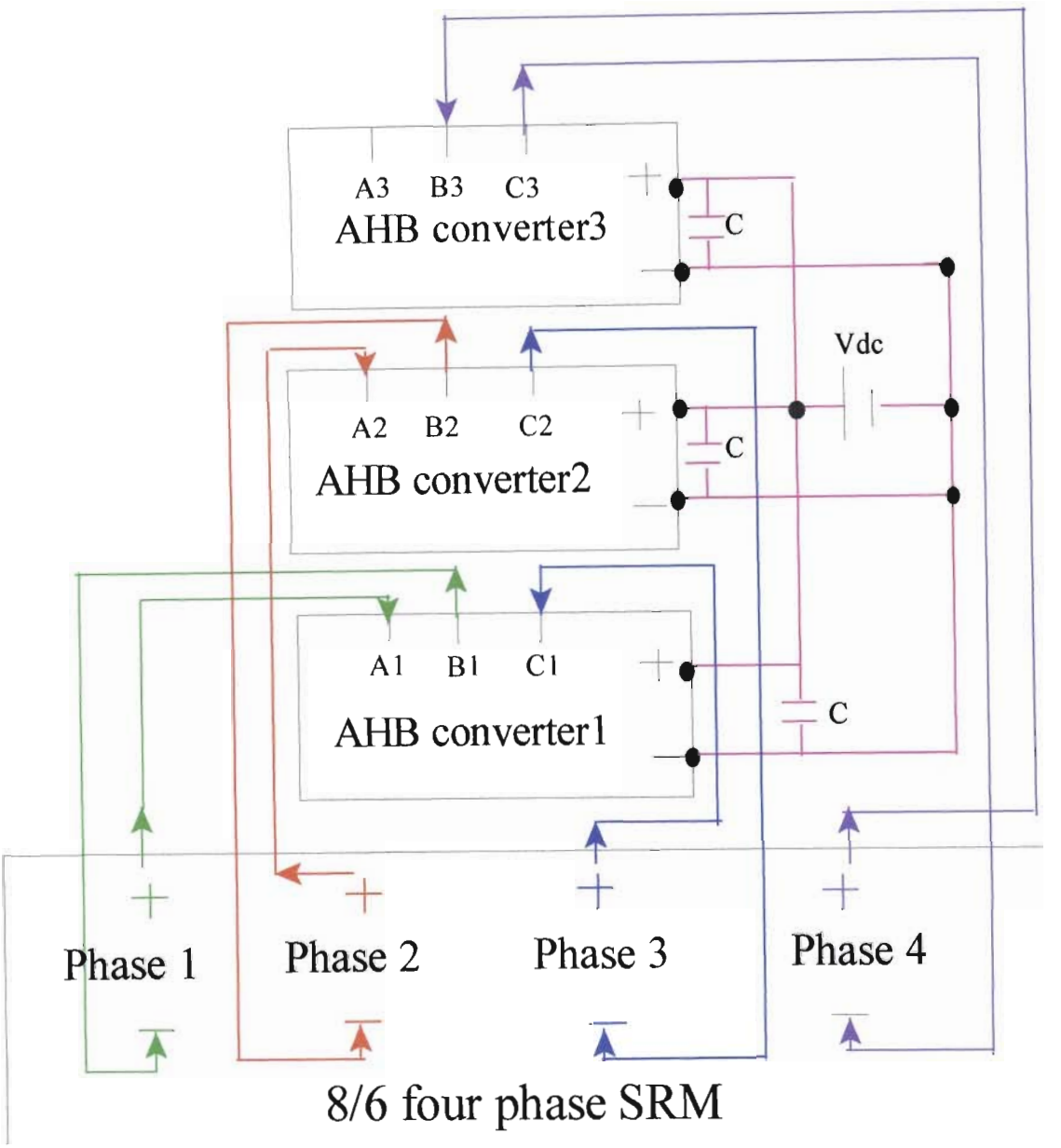

Fig. 5.5 Ad-hoc four phase AHB power converter configuration

Current Sensor

A 100mV/A LEM current probe [5.5] is used to measure each phase current. The signals from these probes are fed to four analogue inputs of the DSP via an analogue I/O daughter card for current control feedback. This feedback data is accessed from the A/D converters inside the DSP by using a built in library function block in the VisSim programming environment. The measured current response results presented in this chapter, however, are captured directly from these probes by means of a two channel Agilent storage oscilloscope [5.6].

Torque Sensor

A 50Nm Magtrol torque transducer [5.7] is mounted with torsionally rigid couplings between the shafts of the SRM and induction motor. The shaft locking mechanism is mounted on the induction motor shaft end of the transducer to allow locked rotor SRM torque response measurements. The ±10V torque sensor output is fed to a fifth analogue input of the DSP via a second Analogue I/O daughter card.

Quadrature Encoder

A quadrature encoder is fitted on the back of the SRM shaft. The two quadrature phase outputs, and index pulse output are connected to the QEP inputs of the DSP via a General I/O daughter card to obtain absolute SRM rotor angle feedback, which is crucial for correct torque and current control, because of the strong dependence of the phase inductance and torque characteristics on rotor position (as explained in Chapter 2). Angle and speed data are also obtained from a library function block in the VisSim programming environment.

5.3 VisSim DSP Programming Environment

VisSim [5.3] provides a fully integrated control system design environment where all design and simulation tasks can be completed without writing a line of code. This tool automatically generates the C code of the required real time control program blocks. This code is then automatically compiled and linked with the required library elements (VisSim supports all embedded F2812 DSP functions in the form of graphical blocks) using the ANSI C compiler provided by Texas Instruments. The resulting executable DSP code is then downloaded to RAM or flash memory. The look and feel of the VisSim programming environment is similar to Simulink.

The three main steps in the development of a DSP algorithm in VisSim are as follows.

1 Create the block diagram to be executed on the target DSP.
2 Generate the C source code.
3 Compile and link the C source code to produce an executable file.

In creating the block diagram, all of the blocks which constitute the required real time function must be entirely encapsulated in one master "compound" block. VisSim then invokes the C compiler included with the corresponding hardware kit to compile the compound block

and link the .C file, support libraries, and header files to create an .OUT file for that block. This file is called the DSP interface for that program, which will actually run in the DSP core. All of the required control hardware and software functionality is then achieved by simply running the executable code via the corresponding DSP interface. It is also possible to generate a bootable version of the executable code, which will automatically load and run out of flash memory for portable or embedded applications where PC control and monitoring functionality is not required.

Fig. 5.6 (a) shows the master compound block, Fig 5.6 (b) shows the main sub-compound blocks, and Fig 5.6 (c) shows the DSP interface of the VisSim implementation of the TSF SRM torque and hysteresis current control strategy presented in Chapter 4. The contents and functions of all sub-compound blocks are presented and explained in Appendix D.3.

Practical hardware/software limitations at the time of writing this thesis

The simulation results in Chapter 4 use a sampling rate of 10 kHz, and a dc link voltage of 81V. However, the DSP interface in Fig. 5.6 (c) (i.e. the executable version of Fig. 5.6 (b)) is too computationally burdensome to execute in real time in the 100μs required in order to achieve a sampling rate of 10 kHz. The main computational load comes from the T-θ-i lookup table used to determine the phase current references as a function of the instantaneous total torque reference and rotor angle (the i-θ-T table is also used in this experimental work to estimate the actual torque produced by each phase and the total torque, for comparison with simulation results). It has been experimentally determined that these blocks can currently only execute at a real time sampling rate of 2.5 kHz.

The hysteresis current control function for each phase, however, comprises only software A/D scaling and offset arithmetic and a comparator. This relatively low computational overhead means that it is possible to run the current control blocks at 10 kHz. A request was therefore made to the suppliers of VisSim to provide a means of executing different blocks at different sampling rates [5.8]. The compound block configuration parameter "Local time step" was thus introduced to allow multi-rate execution. This feature was used to try to execute the current control blocks at 10 kHz, and all other blocks at 2.5 kHz. The torque and current control performance under these conditions was found to be erratic. The actual sampling intervals were therefore measured by toggling one of the digital outputs at each sampling instant, and monitoring the resulting waveform on an oscilloscope. It was found that the only way to achieve regular sampling was to execute all of the blocks at a master "simulation time step" of 1/2.5 kHz. The "local time step" function, therefore, does not appear to work in this

case. No solution to this problem has been found at the time of writing this thesis [5.9]: all results presented in this chapter (measured and simulated) were obtained with a sampling rate of 2.5 kHz.

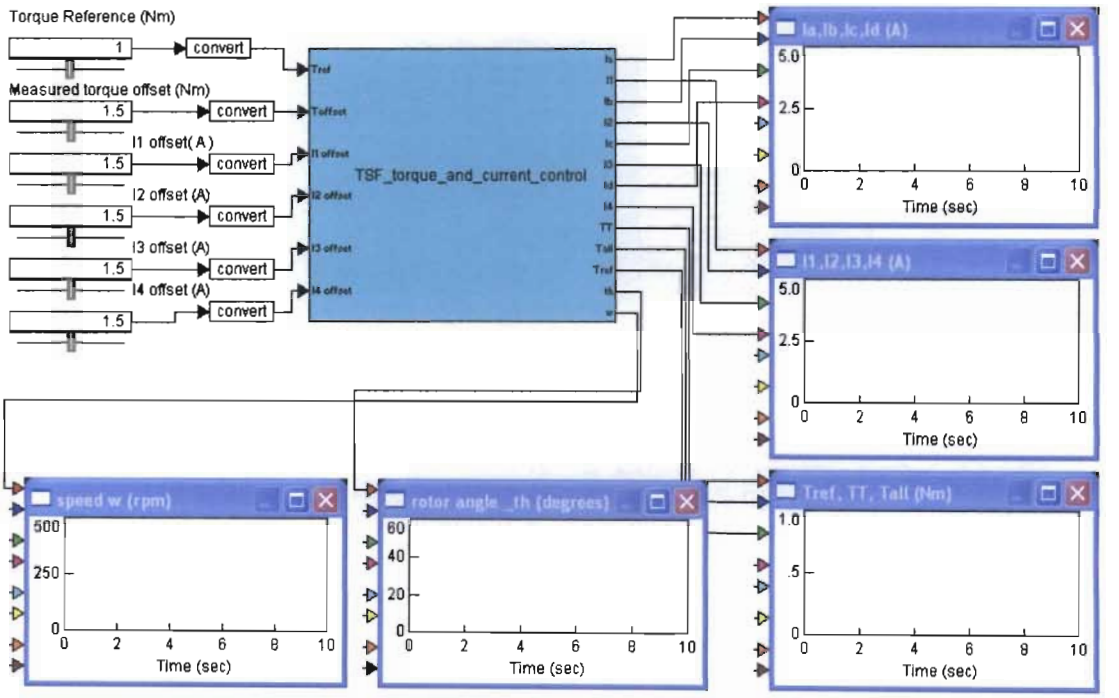

Fig. 5.6 (a) Master compound block

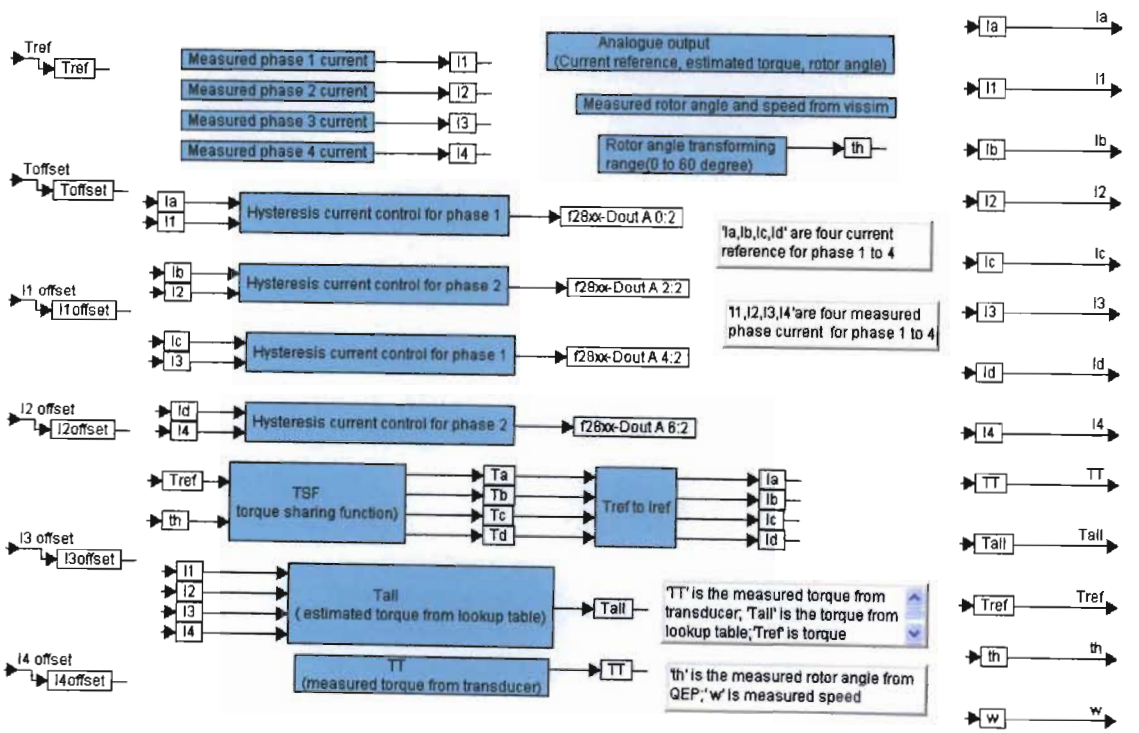

Fig. 5.6 (b) Main sub-compound blocks

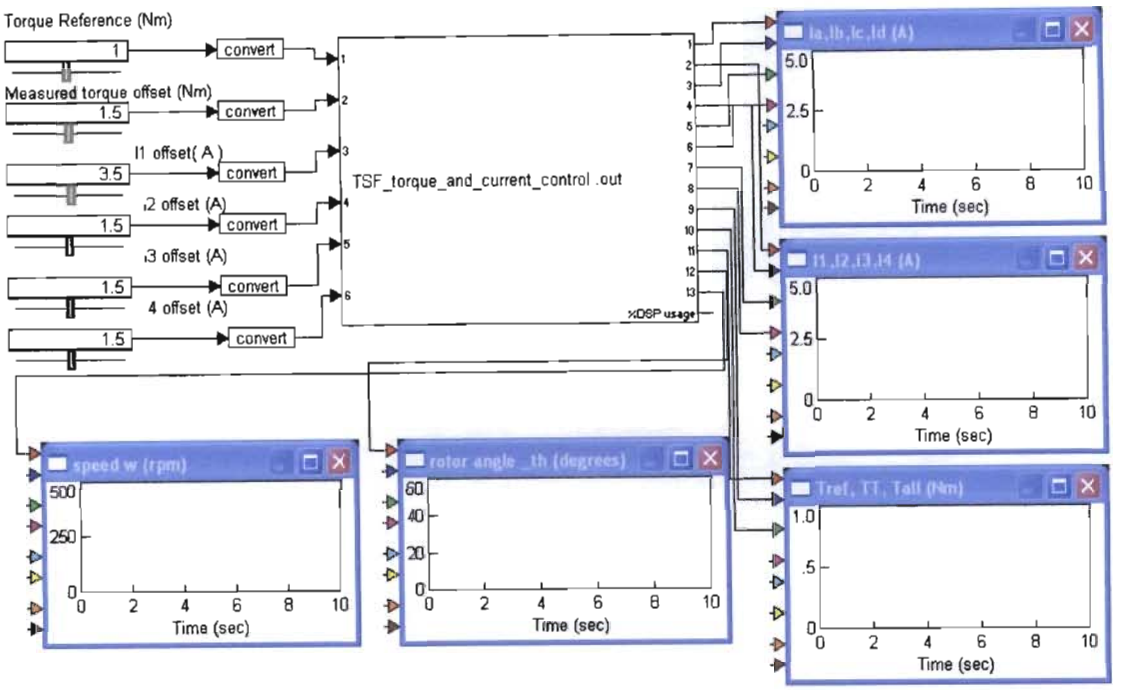

Fig. 5.6 (c) DSP interface of the master compound block

Fig. 5.6 VisSim implementation of the TSF SRM torque and hysteresis current control

The next section compares measured responses obtained from the practical system with corresponding simulation results under several operating conditions.

5.4 Measured vs Simulated Torque and Current Control Responses

This section is divided into three main parts. Section 5.4.1 compares measured torque responses with torque estimates obtained in real time in the DSP with the i-θ-T table. The corresponding measured and simulated current responses are also compared. Section 5.4.2 then compares estimated torque and measured current with simulated torque and current responses under free rotor conditions with no load. Section 5.4.3 presents several transient and steady state torque and current responses obtained in motoring and generating mode under various constant speed load conditions.

5.4.1 Locked Rotor Tests

Fig 5.7 shows the following responses to a 1Nm torque reference pulse at a fixed rotor angle of 0° :

(i) the phase 2 current reference Ib and actual current I2,

(ii) estimated torque, and

(iii) the measured torque

with dc link voltages of

(a) 14V,

(b) 28V, and

(c) 55V.

These results show current ripple of ±(8.6,15,29)% for voltages of (14,28,55) at the maximum sampling rate of 2.5kHz achievable at the time of writing this thesis (in contrast, for example, with the 5.8% ripple predicted in the 10kHz simulation result of Fig 4.18 for a voltage of 28V). The frequency response characteristics of the torque transducer are not published in [5.7], and were not available from the manufacturer at the time of writing this thesis, so it cannot be conclusively explained why the measured torque ripple does not increase with increasing voltage, as do the measured current ripple and estimated torque ripple. It is clear that the actual torque ripple should increase with actual current ripple. It is also interesting to note that, for each dc link voltage, the ripple/noise on the measured torque signal is of approximately the same magnitude for the whole duration of each test (i.e. this noise/ripple appears to be completely independent of the actual current and torque). The measured torque results, however, do closely agree with the estimated torque in terms of average value.

As explained in Chapter 4, higher ripple is expected at higher voltages due to higher di/dt in conjunction with a fixed hysteresis error sampling rate. Fig. 5.8 shows the simulated responses obtained from PSCAD for the same test conditions used to obtain the measured results of Fig. 5.6. Comparison of Fig. 5.7 and Fig. 5.8 shows that the simulation results agree closely with the measurements when the rotor is locked at $0^\bullet$.

At $0^\bullet$, phase 2 is responsible, according to the Torque Sharing Function presented in Chapter 4, for producing all of the desired torque. Fig. 5.9 shows the PSCAD simulated output of the TSF in response to an input angle ramp from $0^\bullet$ to $60^\bullet$ (the horizontal lines at the top and bottom of the function traces are due to wrapping of the angle, i.e. $0^\bullet \equiv 60^\bullet$ - these are not removed from this simulation result because this is not possible in the following measured result). Fig. 5.10 shows the corresponding TSF response measured from the DSP (several plots are superimposed on one another in Fig. 5.10 due to practical difficulties in isolating one $0^\bullet$ to $60^\bullet$ cycle). Appendix D.2 shows that the actual versions of PSCAD TSF used in this thesis [4.6] (prior to this test) have small anomalies in the region of 11.5° and 26.5°, but that these do not have a significant influence on the comparative torque and current responses presented here. It is, however, suggested that these anomalies be avoided in future work.

Figs. 5.7 and 5.8 show that a constant phase 2 current reference of 4.7A is required to track the 1Nm reference torque input pulse with the rotor locked at $0^{\bullet}$. All other current references for this particular angle are at 0A. The measured torque signal appears to comprise a constant amplitude noise signal superimposed on the reference torque. The relatively large ripple on the estimated torque may also be present on the actual torque, but may not be measurable by the torque transducer due to the filtering effect of the SRM rotor inertia.

Figs. 5.9 and 5.10 show the relative TSF weighting of all four phase current references for all angles from $0^{\bullet}$ to $60^{\bullet}$. The current references are obtained by feeding the individual phase torque references from the TSF block into the T-θ-I lookup table. Fig. 5.11 (a) shows the measured current references produced by the DSP implementation of the TSF and T-θ-I blocks when the rotor angle is swept from $0^{\bullet}$ to $60^{\bullet}$, at a relatively low speed of 75 rpm (several measured traces are superimposed due to practical difficulties in capturing only one sweep). Fig. 5.11 (b) shows the corresponding simulated current references produced by the PSCAD versions of these blocks. Fig. 5.11(c) compares the measured and simulated results. The close agreement between these results confirms the validity of the TSF, T-θ-i, and i-θ-T tables in PSCAD and VisSim (small differences are attributable to small errors/noise in the measured angle).

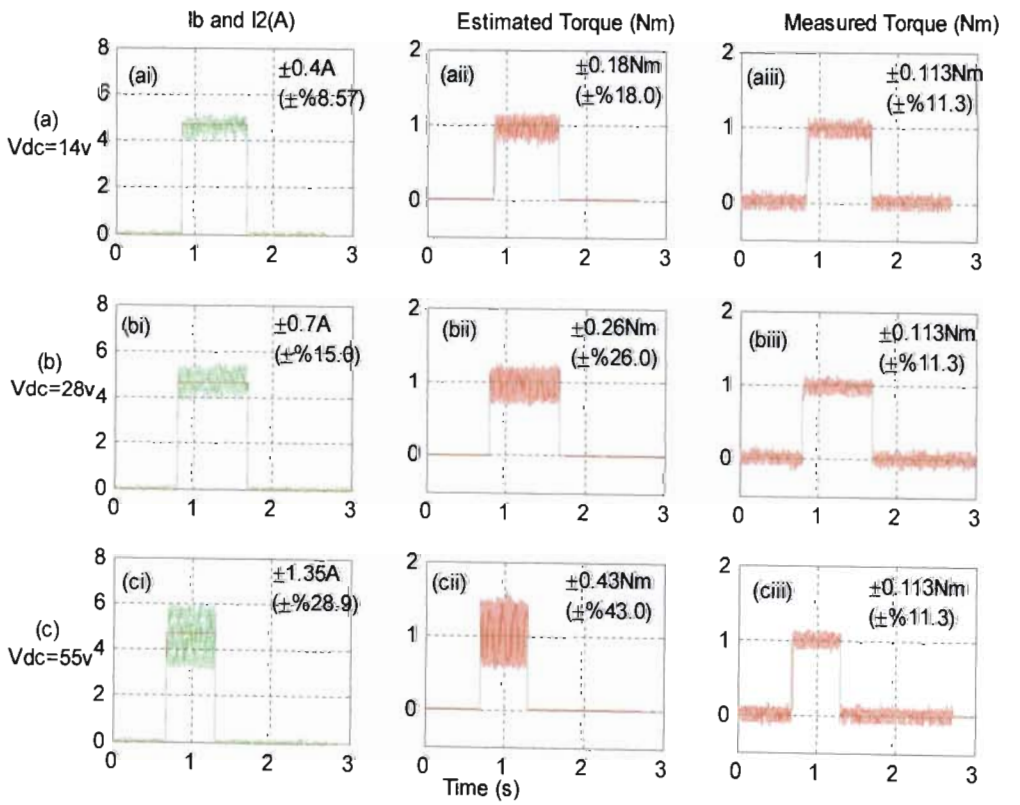

Fig. 5.7 Measured phase 2 current and total torque for Vdc ∈ (14v,28v,55v) and θ= 0°

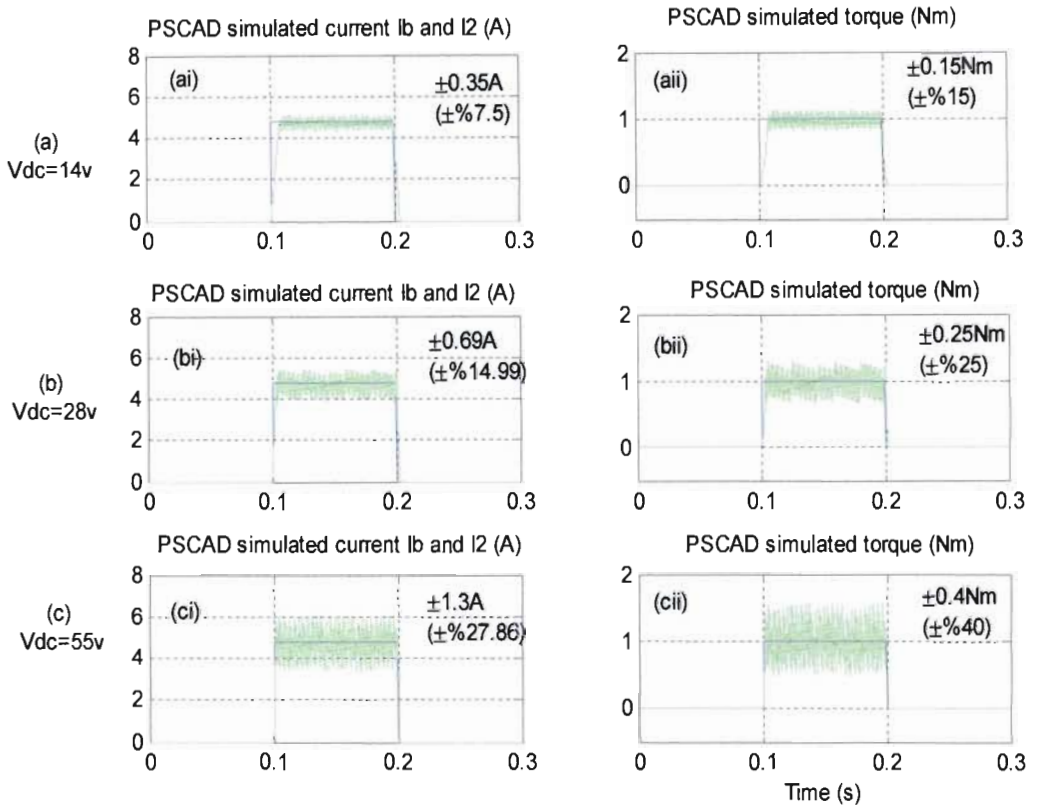

Fig. 5.8 PSCAD simulated current and torque results for Vdc∈ (14v,28v,55v)

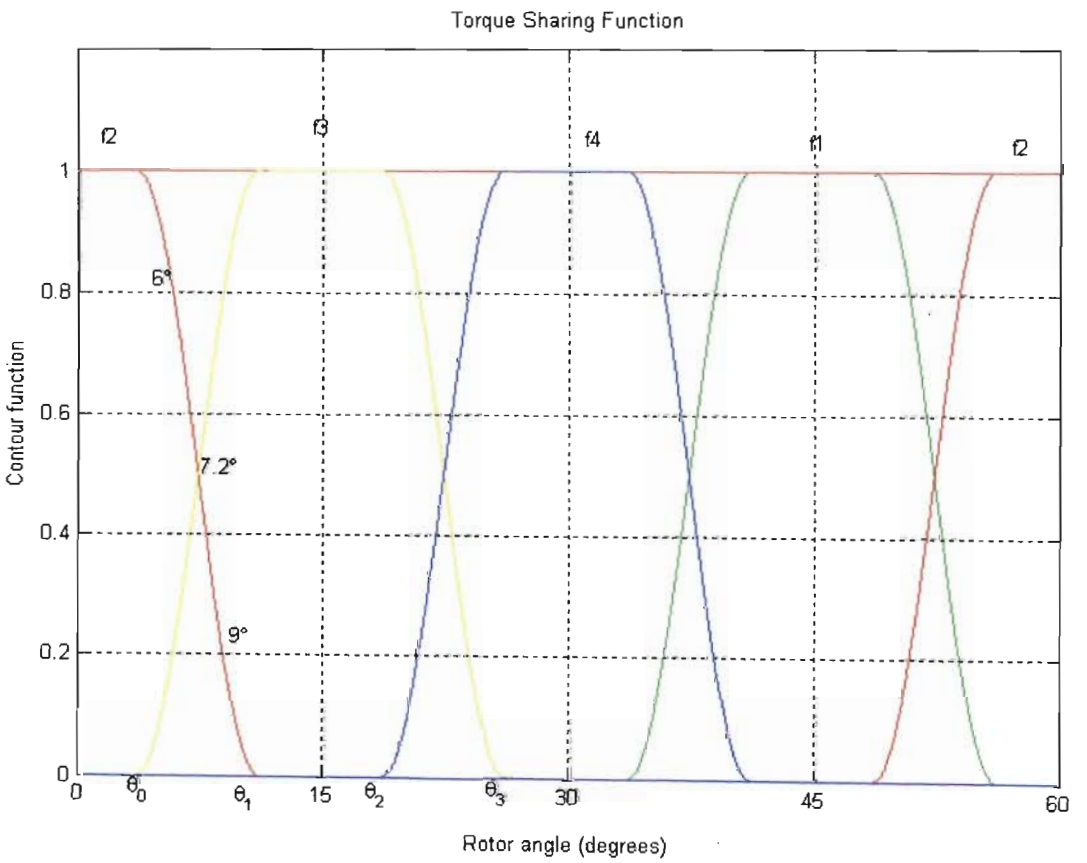

Fig. 5.9 PSCAD torque sharing function diagram

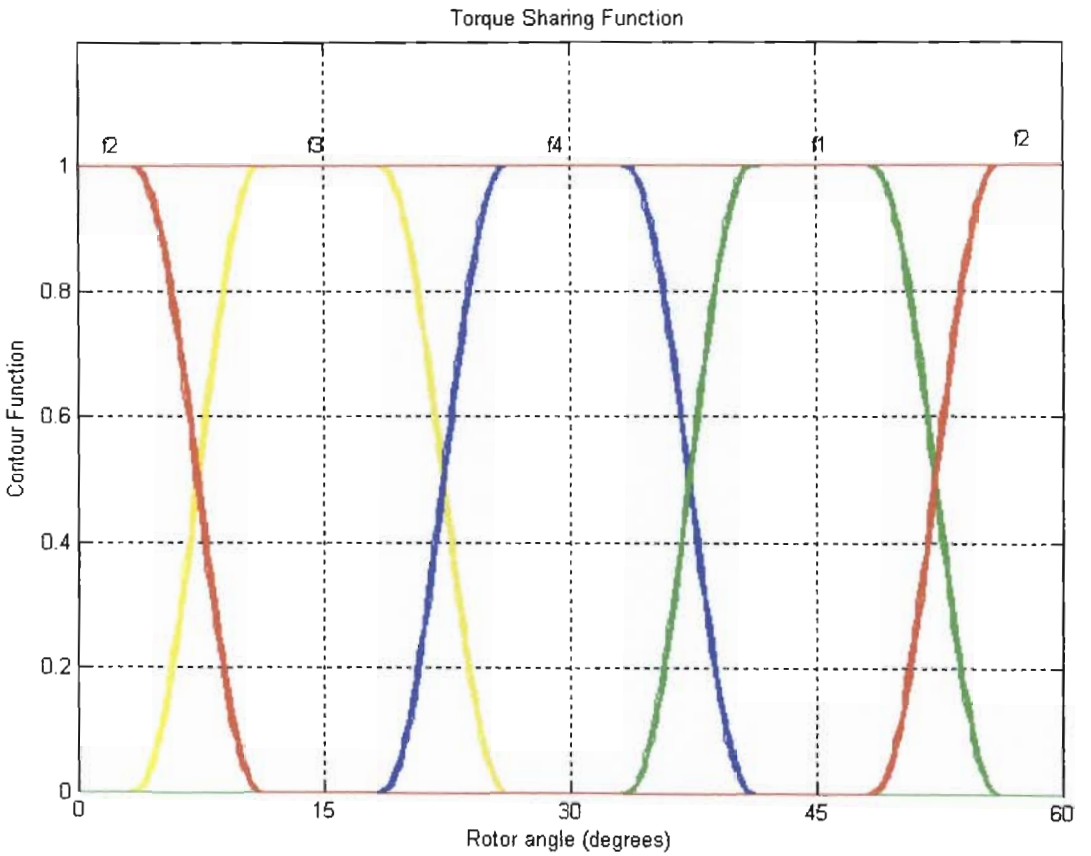

Fig. 5.10 Measured torque sharing function diagram

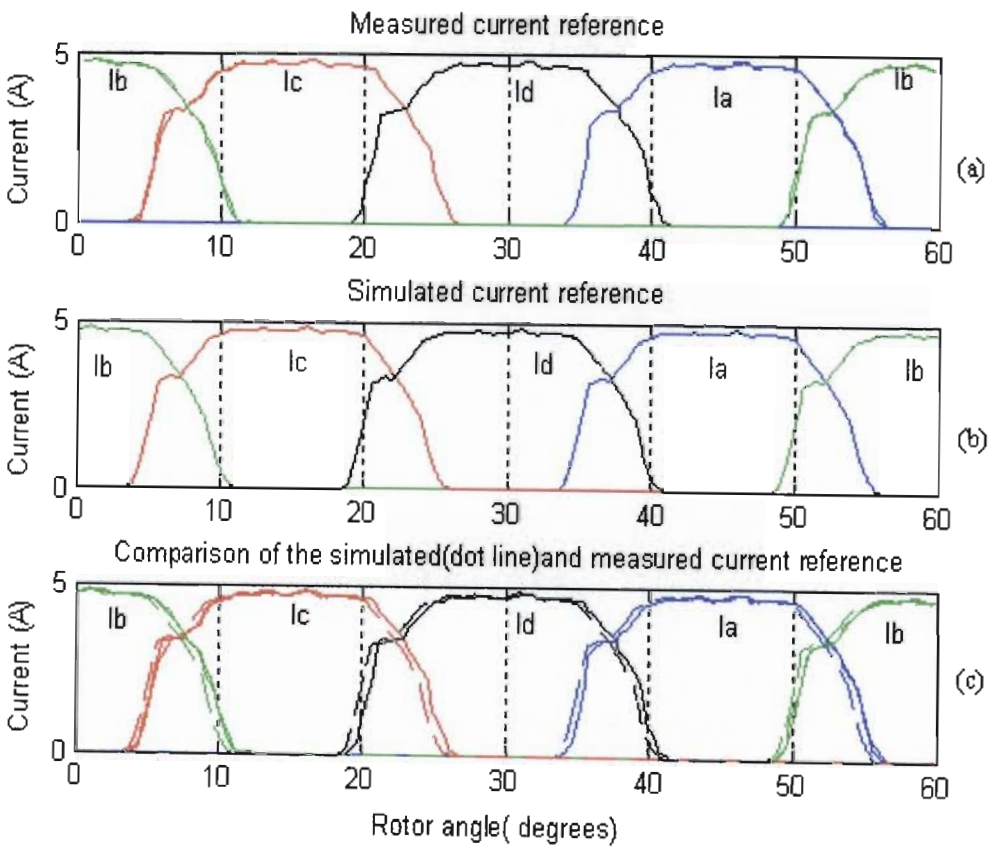

Fig. 5.11 Measured and simulated current reference when the torque reference is 1Nm

Fig. 5.12 and 5.13 compare the measured and simulated (i) phase 2 current and (ii) total torque and current responses to the 1Nm pulse torque reference for the following locked rotor positions.

(a) 0° , where it can be seen that phase 2 produces all of the total torque

(b) 6°, where phase 3 begins to contribute

(c) 7.2°, where phase 2 and phase 3 each contribute about 50%

(d) 9°, where phase 3 contributes more than phase 2

Fig.5.12. (aiii) to (diii) show the measured torque transducer output. The estimated torque ripple is seen to increase with increasing rotor angle for the following two possible reasons.

1. Phase 2 inductance decreases (and hence di/dt increases) with increasing angle.
2. There is an additive effect due to ripple in phase 2 and phase 3 for angles greater than 3.5°.

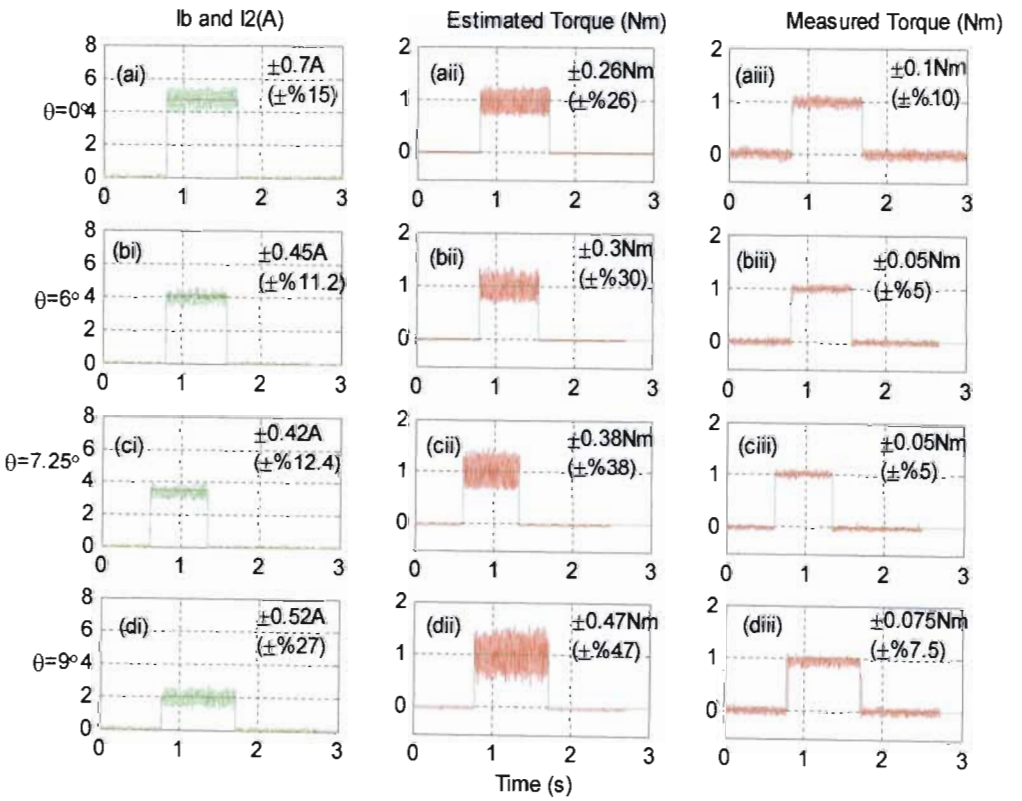

Fig. 5.12 Measured current and torque results when rotor is locked at

$\theta \in (0°, 6°, 7.25°, 9°)$

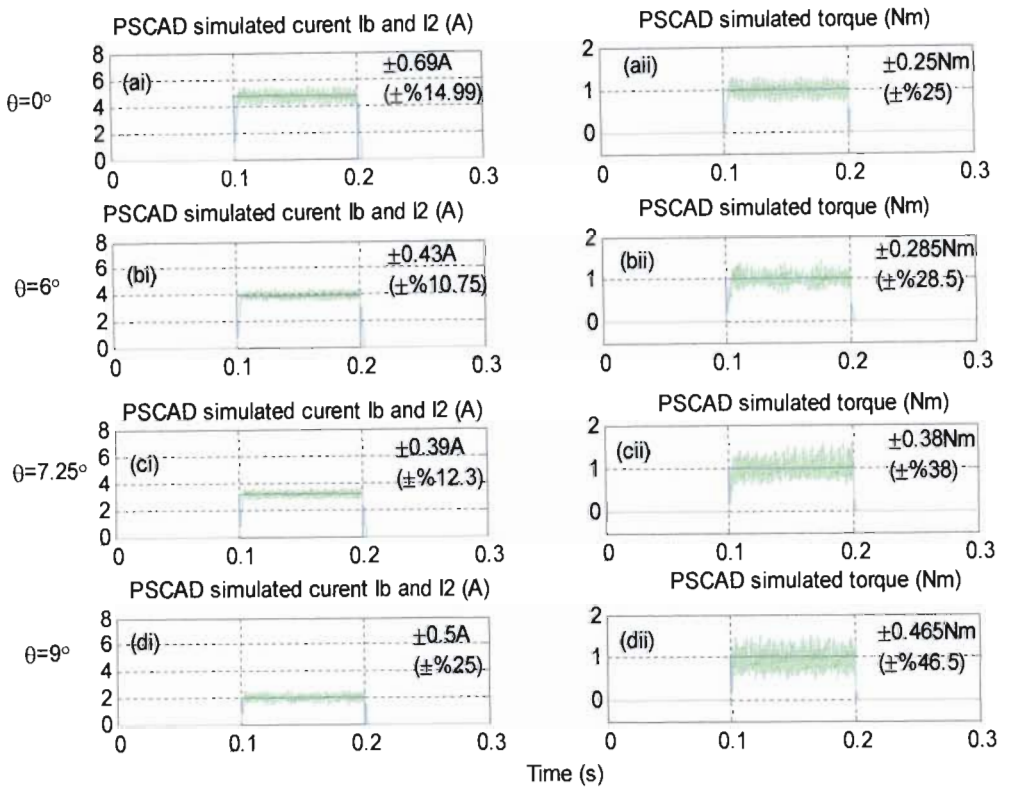

Fig. 5.13 PSCAD Current and torque results when rotor locked at $\theta \in (0^\circ, 6^\circ, 7.25^\circ, 9^\circ)$

Comparison of the measured current responses in Fig. 5.12 with the corresponding estimated torque and measured torque responses shows once more (as seen in Fig. 5.7) that the estimated torque response follows the trend of increasing current ripple with increasing rotor angle, but the measured torque response does not. In addition to the uncertainty with respect to the bandwidth of the torque transducer and its built-in signal processing circuitry under locked rotor conditions (as discussed with respect to Fig. 5.7), there is no way to use it for direct measurement of the electromagnetic torque produced by the SRM under free rotor conditions. This torque can only be estimated under these conditions using the equations presented in Appendix D.4. These equations, however, require accurate determination of the inertia and friction functions of the motor and load rotors, bearings and coupling elements. A second quadrature encoder is also required on the load shaft to measure instantaneous speed of both the motor and load shaft segments, which could differ significantly under transient conditions due to torsional displacements across the couplings. This mechanical setup and calibration exercise is beyond the scope of this thesis, but could form part of future work. Therefore, in the remainder of this chapter, the term "measured torque" refers to the torque estimated in real time in the DSP based on measured phase currents, as would be the case in an industrial SRM drive.

Comparison of Figs. 5.12 and 5.13 shows close agreement between the measured and simulated responses at all of the locked rotor test angles. The next section presents steady state no-load responses to low constant torque references.

5.4.2 Steady State No Load Responses to Low Constant Torque References

Fig. 5.14 and Fig. 5.15 show the measured and simulated steady state phase 1 current, total torque, and speed responses with constant torque references of 0.2Nm and 0.5Nm respectively. Fig. 5.14 shows that the dc link voltage of 28V is sufficient for good tracking of the relatively low magnitude (2A) current reference waveform, and hence produces the required average total torque of 0.2Nm at the corresponding (relatively low) no load speed of approximately 250 rpm. However, Fig. 5.15 shows that 28V is insufficient for good tracking of the larger reference current waveforms (3.2A) required to produce an average total torque of 0.5Nm. The back emf in this case is not only higher due to the approximate doubling in no load speed, but also due to the higher phase currents (which also result in a higher resistive volt drop). There is therefore a significant drop in both the measured and simulated di/dt: there are less than half the switching events *per current pulse* in Fig. 5.15 than in Fig. 5.14 (as would be expected if only the frequency of the current reference pulses were doubled).

The measured speed response in Fig 5.14 (ci) shows high frequency noise and slight ripple which have no obvious correlation with periods of overlap in the reference current pulses or with the hysteresis switching events in the actual phase currents, and are not present in the simulated response shown in Fig. 5.14 (cii). However, the average measured and simulated speeds are both approximately 250 rpm. The back emf, and therefore di/dt, in both cases should thus also be approximately equal (provided that the actual phase currents are also approximately equal). The measured and simulated switching frequency should also be equal under these conditions. Careful comparison and analysis of the measured and simulated current responses in Fig. 5.14(ai) and (aii) confirm that di/dt is approximately equal in both cases, but that the measured current ripple is significantly higher than the simulated current ripple due to "dropped" samples in the practical system. Appendix D.5 shows this analysis in detail. It also shows that the ripple in the simulated current responses attains approximately the same magnitude as the measured current responses when an "average" sampling rate of 1.4kHz is used in PSCAD. However, lower measured torque ripple is observed in Figs. 5.14(bi) and 5.15 (ci) than that observed in the simulated result of Figs 5.14(bii) and 5.15 (cii). The measured torque ripple is expected to be higher if the measured current ripple is higher, as is clearly the case in Fig. 5.14, but the measured torque is actually calculated by feeding the sampled phase current values into the i-θ-T lookup tables and adding the resulting

torque for each phase. Dropped phase current samples would therefore result in dropped measured torque values.

At the time of writing this thesis, it has not been determined why samples are dropped despite indication to the contrary by what should be a robust real time DSP sample rate measuring mechanism, as shown in Appendix D.6. It is also not known why the locked rotor results do not seem to exhibit this problem. Time restrictions also prevent re-measurement and re-simulation of the remainder of the free rotor results presented in this chapter at a practical sampling rate where no samples are dropped, i.e. where close agreement is expected between the measured and simulated current and torque ripple. The value of the following results and analyses, therefore, lies mainly in the identification of trends in the simulation results, and verification that similar trends are observed in the measured results, despite the possibility of larger current ripple in the measured results due to erratic sample dropping. A further problem which has been identified is that insufficient PSCAD time axis plotting resolution causes some simulated hysteresis switching events to appear to occur before the threshold values have been reached, as can be seen in Fig. 5.15(bii). It is also now known that zero threshold values can be used for sampled hysteresis control.

The measured and simulated current switching frequencies in Fig. 5.15(ai) and (aii) appear to be more similar than those in Fig. 5.14(ai) and (aii). This is possibly due to the lower number of samples (and hence possible switching events) per current pulse and the fact that fewer actual switching events occur due to the reduction in achievable di/dt with increasing speed.

No attempt has been made to model the dc supply dynamics. The dc link is fed from a battery supply with many outlets (and corresponding loads/generators), and thus has unpredictable instantaneous internal resistance (state of charge) or internal resistance volt drop (total load current). Small discrepancies could therefore exist between the simulated and measured results due to fluctuations in the dc supply voltage, and possible interaction between phases due to varying supply impedance fluctuations. Fig. 5.16 shows two of the measured current pulses from Fig 5.15 (ai) and the corresponding dc link voltage measurement. It can be seen that the there are slight voltage dips/surges which coincide with increases/decreases in the phase 1 current, but that the total effect of all four phases produces less than ±0.8V (i.e. less than 3%) variation.

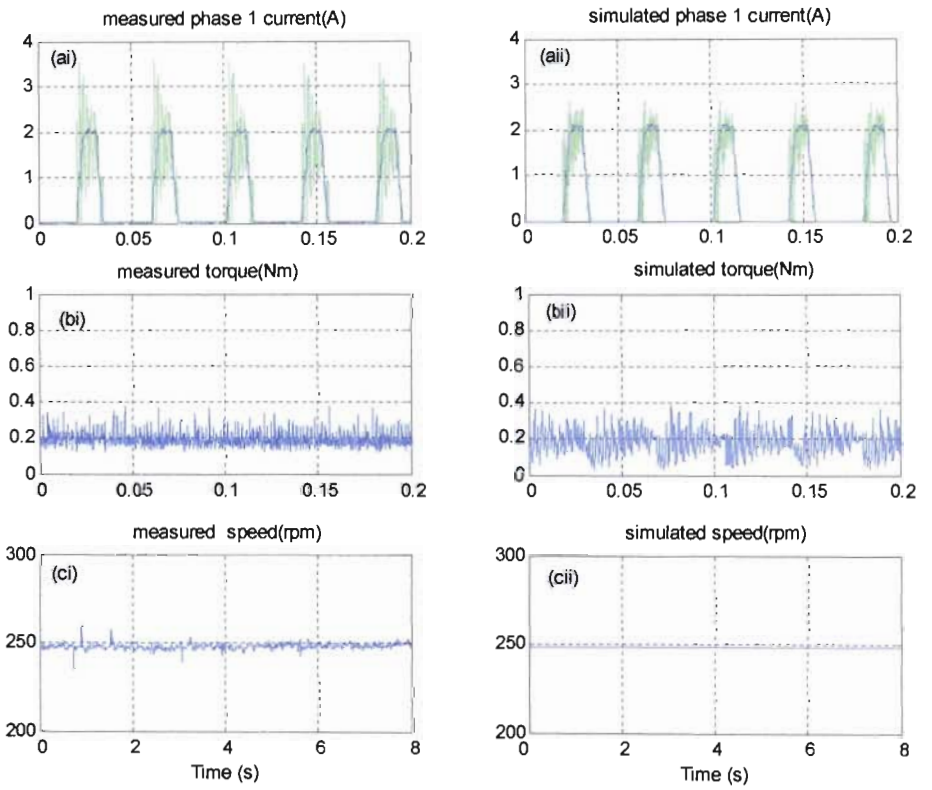

Fig. 5.14 Measured and simulated results when torque reference is 0.2Nm

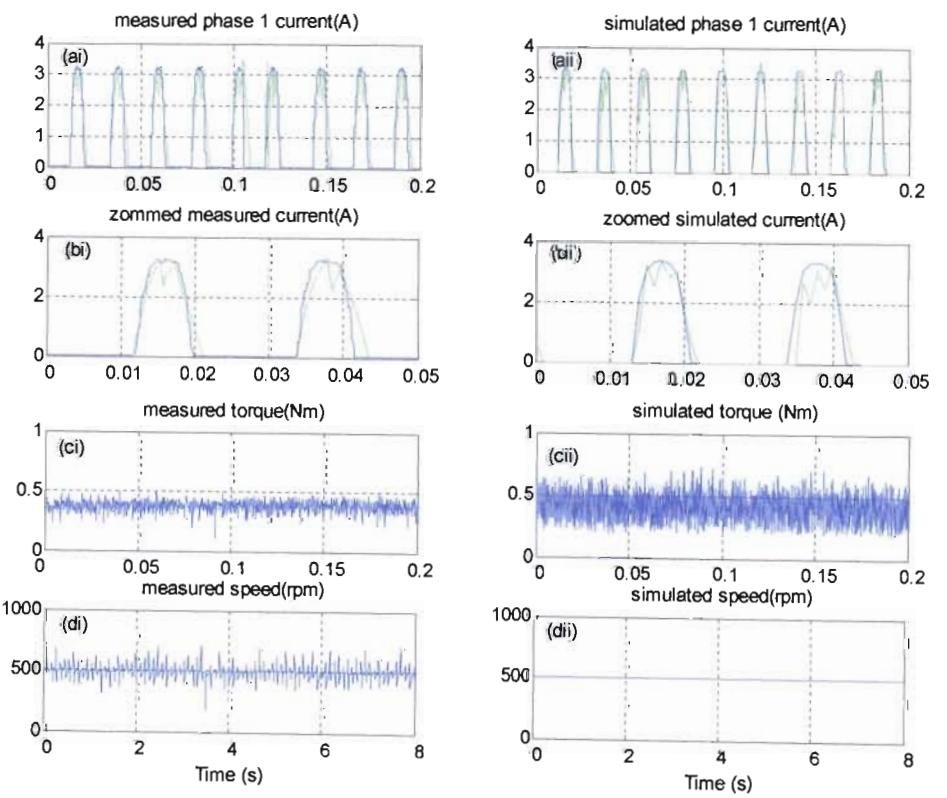

Fig. 5.15 Measured and simulated results when torque reference is 0.5Nm

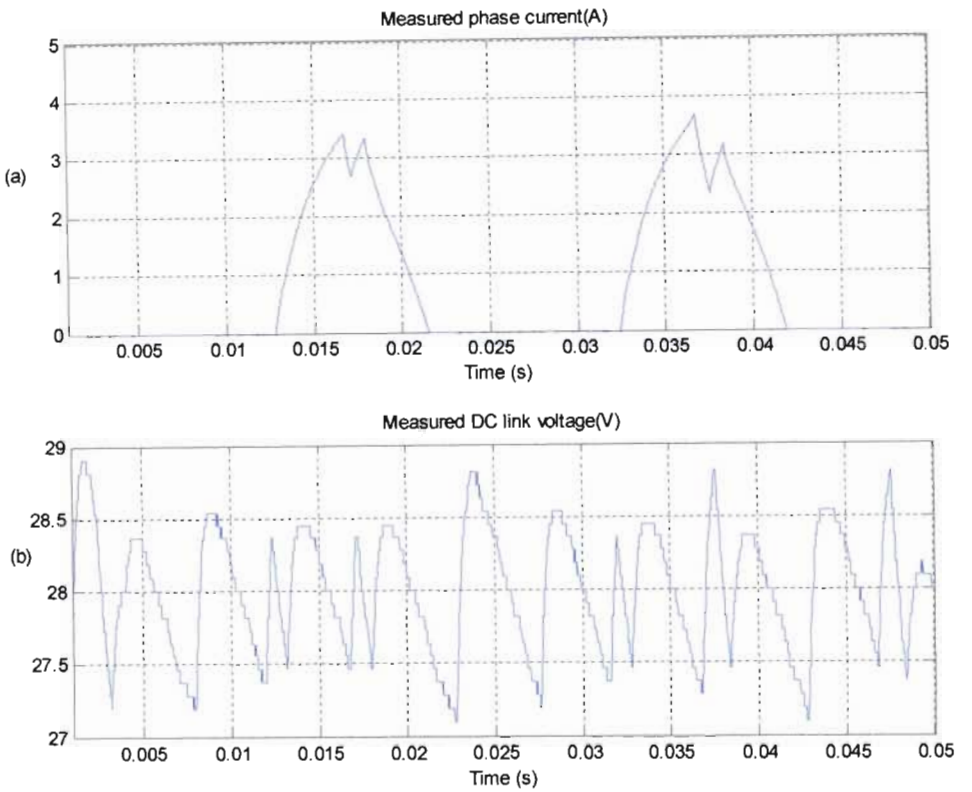

Fig. 5.16 Measured phase1 current (a) and DC link voltage (b) under same test condition shown in Fig. 5.15

The next section compares measured and simulated dynamic torque responses under various constant speed load conditions.

5.4.3 Dynamic Torque and Current Responses With Constant Speed Load

The previous section showed the steady state no load torque, current and speed responses to two low, constant values of torque reference. The SRM can only operate in the motoring mode under these no load conditions. This section presents the following measured and simulated responses in motoring and generating mode.

1. varying torque pulse magnitude with different turn-on and turn-off angles
2. varying torque pulse magnitude at different speeds
3. triangle and sinusoidal torque

Varying Torque Pulse Magnitude with Different Turn-on and Turn-off Angles

The following four modes of operation are possible at constant (non-zero) rotor speed.

$T_{ref} > 0, \omega > 0$ (Motoring in positive direction)

$T_{ref} > 0, \omega < 0$ (Generating in negative direction)

$T_{ref} < 0, \omega > 0$ (Generating in positive direction)

$T_{ref} < 0, \omega < 0$ (Motoring in negative direction)

ON and OFF transient responses are investigated in each of these modes using a torque reference T_{ref} pulse of +1Nm or -1Nm, and a constant speed ω of +150rpm or -150rpm. It is shown that, while the step time (i.e. the time at which the torque reference is changed from zero to +1Nm or -1Nm) is arbitrary, the corresponding instantaneous rotor angle has a significant effect on the transient torque and current responses. This is done by means of the following two tests for each of the above four conditions.

1. The ON test: *changing the turn-on angle* with fixed turn-off angle
2. The OFF test: *changing the turn-off angle* with fixed turn-on angle

Fig. 5.17 shows the torque reference turn-on and turn-off angles used to obtain the measured and simulated current and torque responses of Fig. 5.18 to Fig. 5.33, as summarized in Table 5.1, 5.2 and 5.3.

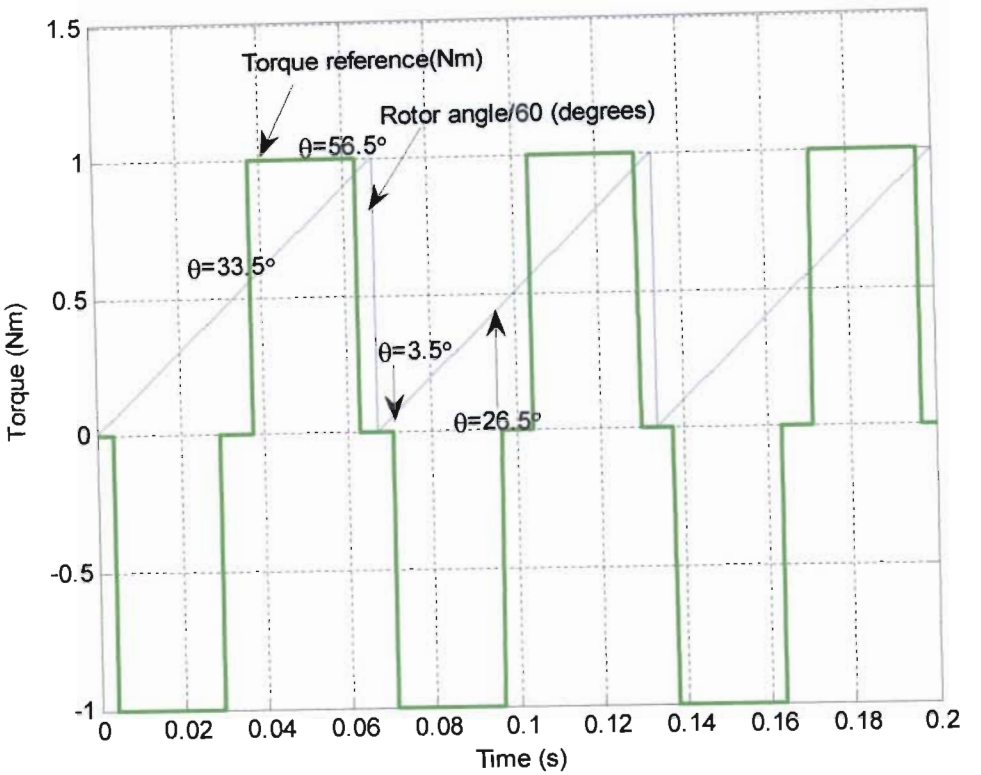

(a)

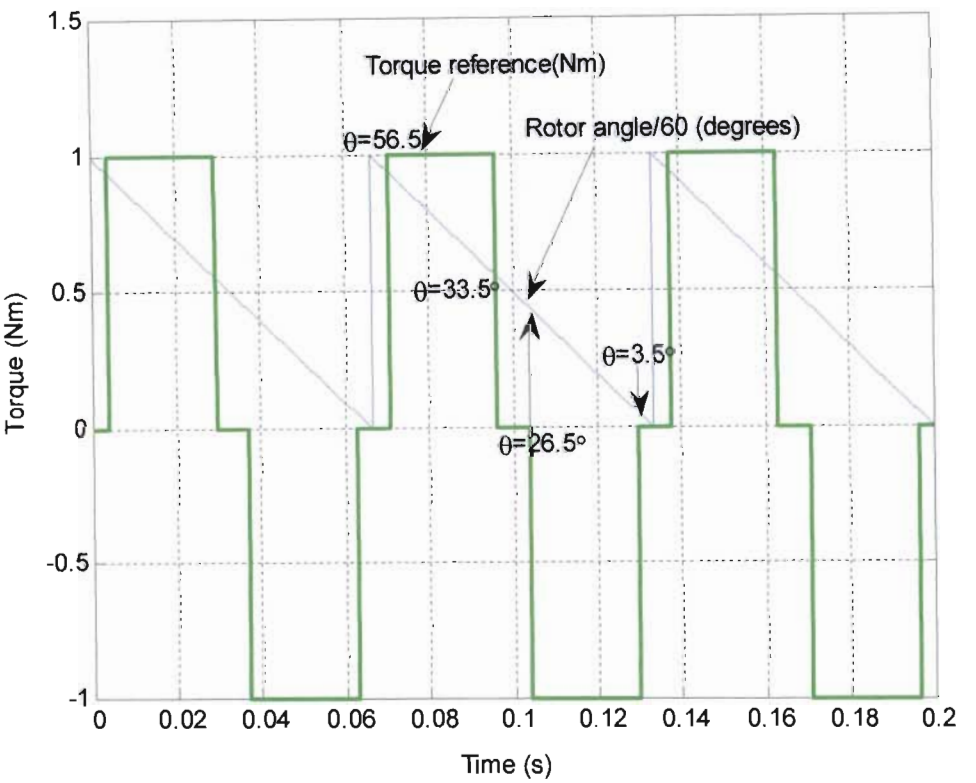

(b)

Fig. 5.17 Turn-on and turn-off angle condition for positive and negative torque reference (± 1Nm) with (a) positive speed and (b) negative speed

Fig.	(A), (B) Meas., Sim. I(A) or T(Nm)	Mode	W (rpm)	T (Nm)	∠ON	∠OFF	Remarks
5.18	I	Mot.	150	1	(i) 33.5° (ii) 37.0° (iii) 45.0° (iv) 50.0°	56.5°	Fig. 5.18(ai) to a(iv) show significantly increasing lag in the measured phase 1 current response as the turn-on angle is increased/retarded beyond 37° , due to increased phase inductance and hence decreased di/dt (as shown in Fig. 4.36). The simulated current responses in Fig. 5.18(bi) to (biv) show the same trend, and agree closely with the measured result in periods where samples are not dropped by the DSP, e.g. during most of the first current pulses in Fig. 5.18(aii) to (aiv). When sample dropping does occur, the measured current ripple is higher. A similar trend is seen in the measured and simulated total torque response lags of Figs. 5.19(A) and (B) respectively, but the lags in the phase 1 current responses cannot be directly compared with those in the total torque responses due to the contribution of other phases during commutation. The same is true with respect to the current ripple and torque ripple during commutation. A further problem is that it was not possible to capture phase current or torque reference simultaneously with total torque from the DSP (i.e. current and torque ripple cannot be directly compared in non-commutation periods, and the exact torque reference turn-on and turn off times are not known)
5.19	T						
5.20	I				33.5°	(i) 56.5° (ii) 53.0° (iii) 45.0° (iv) 40.0°	Figs. 5.20 and 5.21 (aii) to (aiv) show decreasing lag in the measured and simulated current and torque responses as the turn-off angle is decreased/advanced from 53° , due to decreased phase inductance, and hence increased di/dt. There is no appreciable current lag observed in Figs. 5.20 and 5.21 (ai) for a turn off angle of 56.5° (where the peak inductance occurs) because the di/dt response required to track the unswitched reference current waveform is lower than that which is achievable at this particular dc link voltage (28V) and speed (150rpm).
5.21	T						

Table 5.1 Summary of (A) measured and (B) simulated ON and OFF current and torque responses in MOTORING mode with POSITIVE ROTATION

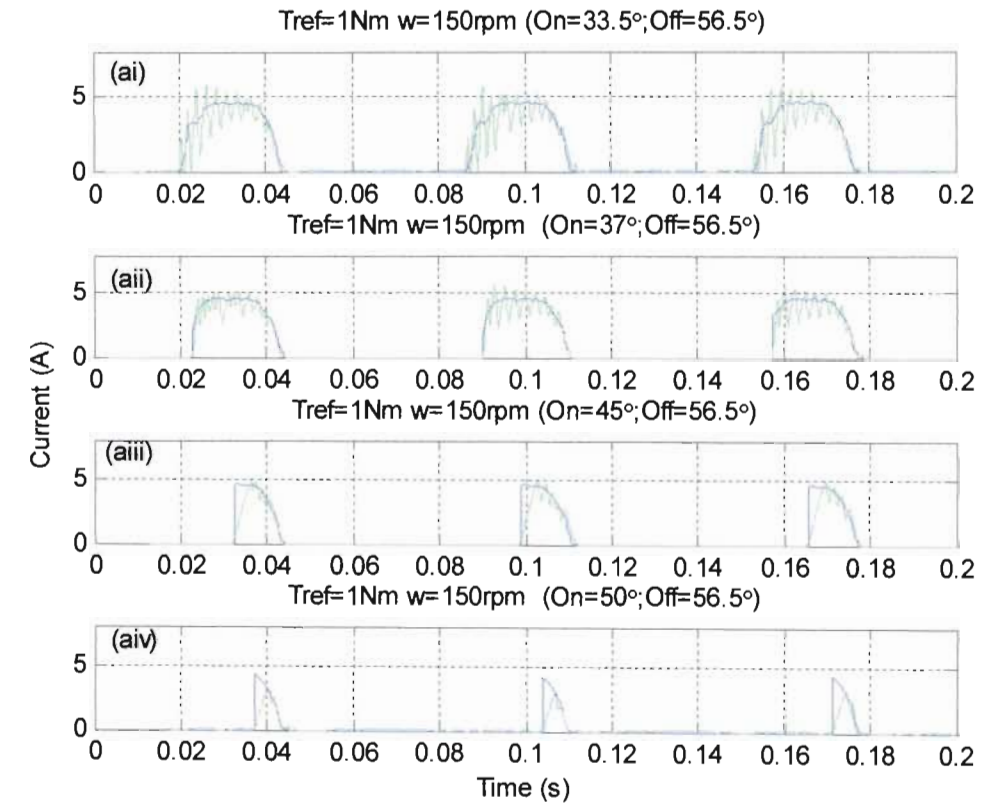

(A)

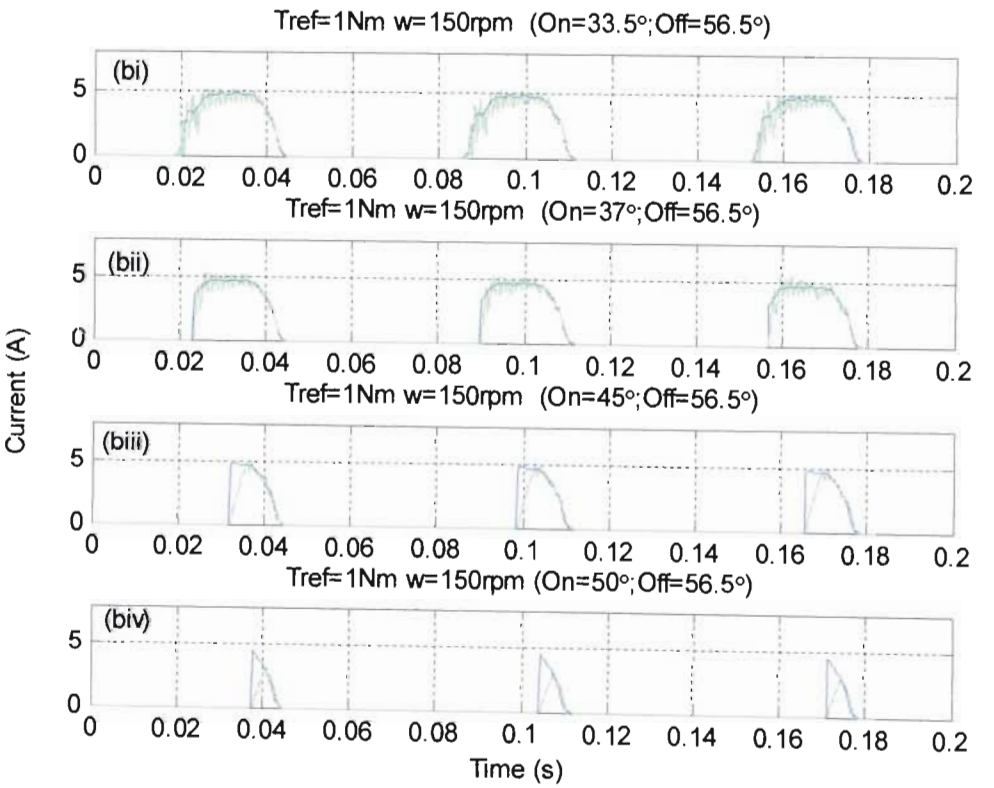

(B)

Fig. 5.18 Measured (A) and simulated (B) phase 1 ***current results*** *with* ***ON*** *test when torque reference is* ***1Nm,*** *speed is* ***150rpm***

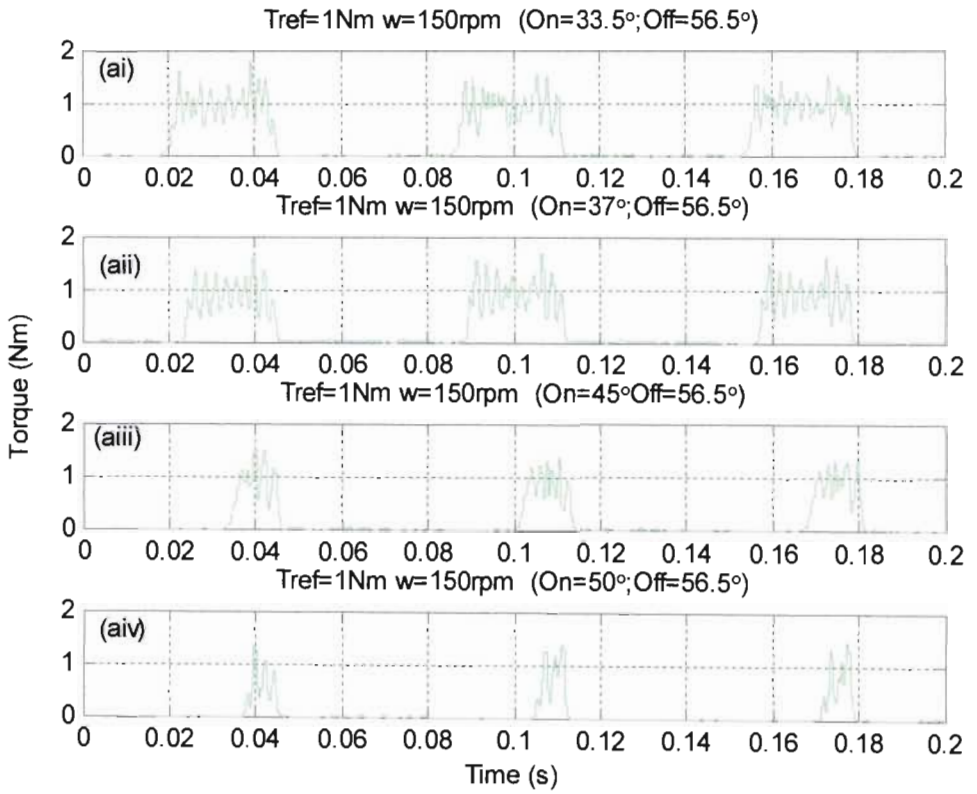

(A)

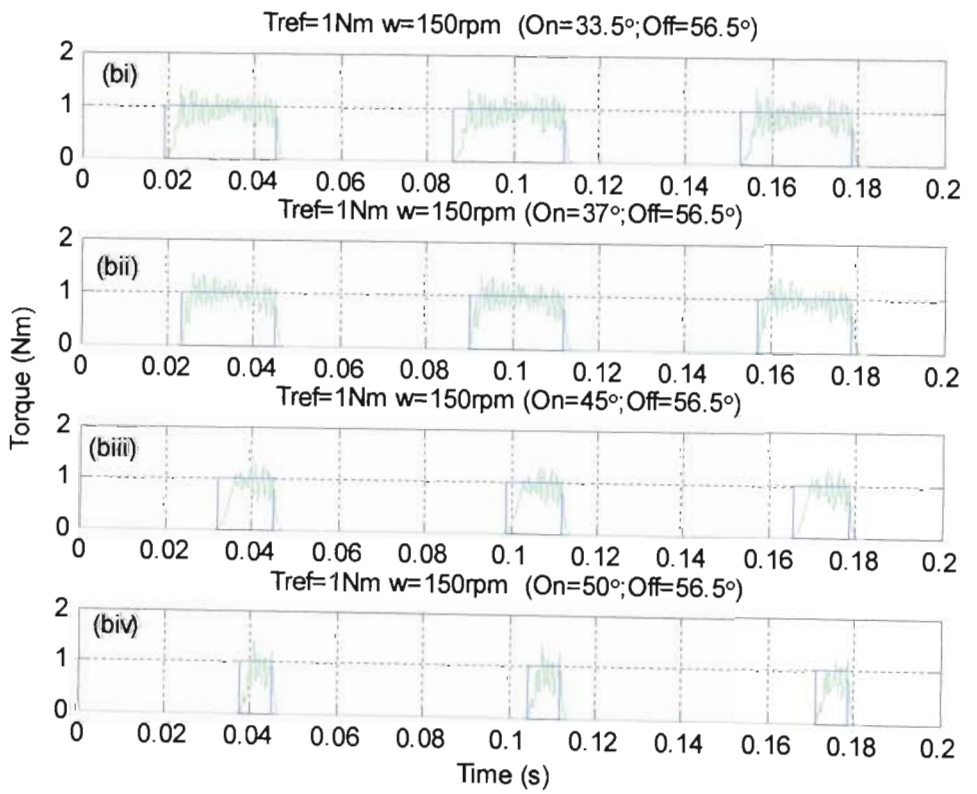

(B)

Fig. 5.19 Measured (A) and simulated (B) ***torque results*** *with* ***ON*** *test when torque reference is* ***1Nm,*** *speed is* ***150rpm***

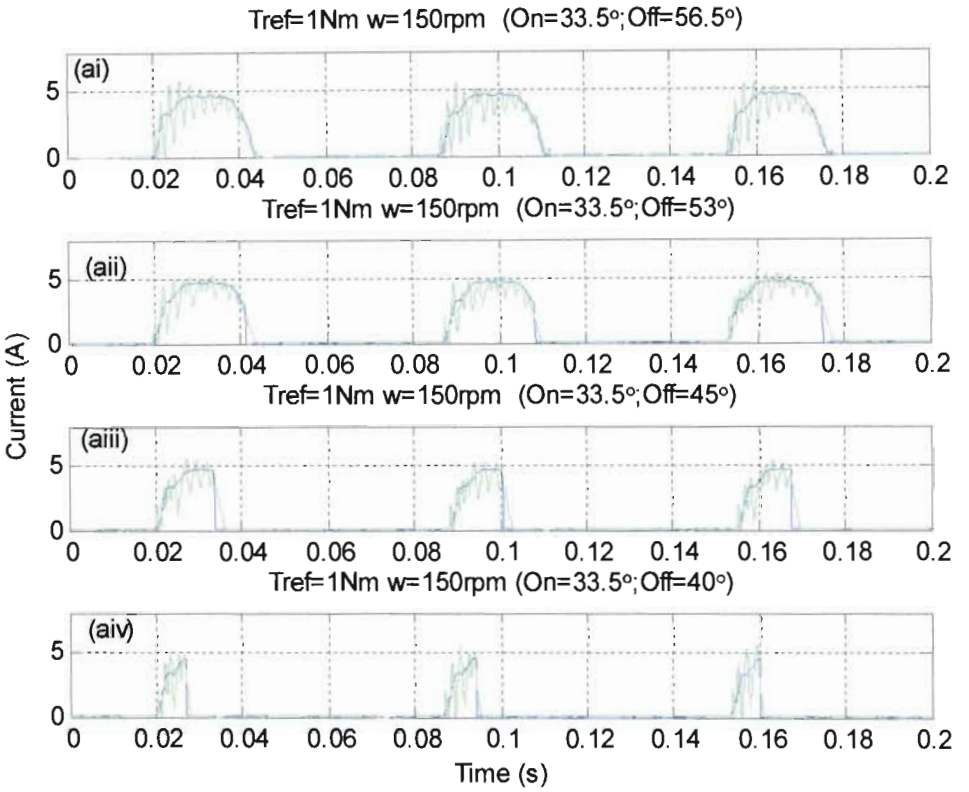

(A)

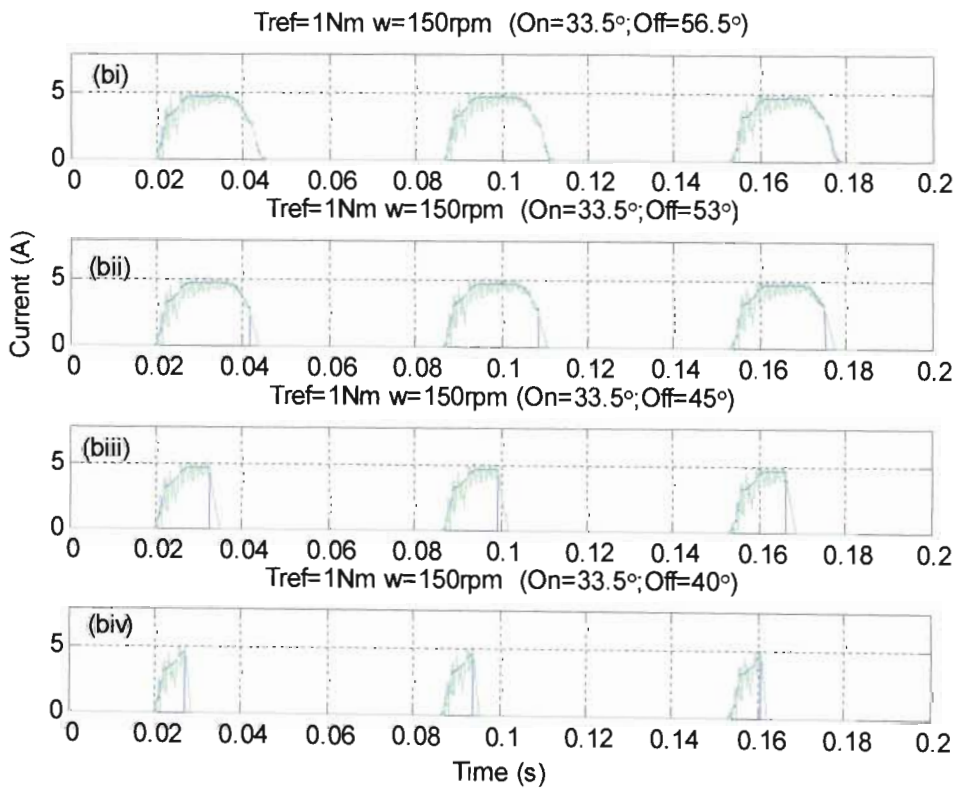

(B)

Fig. 5.20 Measured (A) and simulated (B) phase 1 ***current results*** *with* ***OFF*** *test when torque reference is* ***1Nm,*** *speed is* ***150rpm***

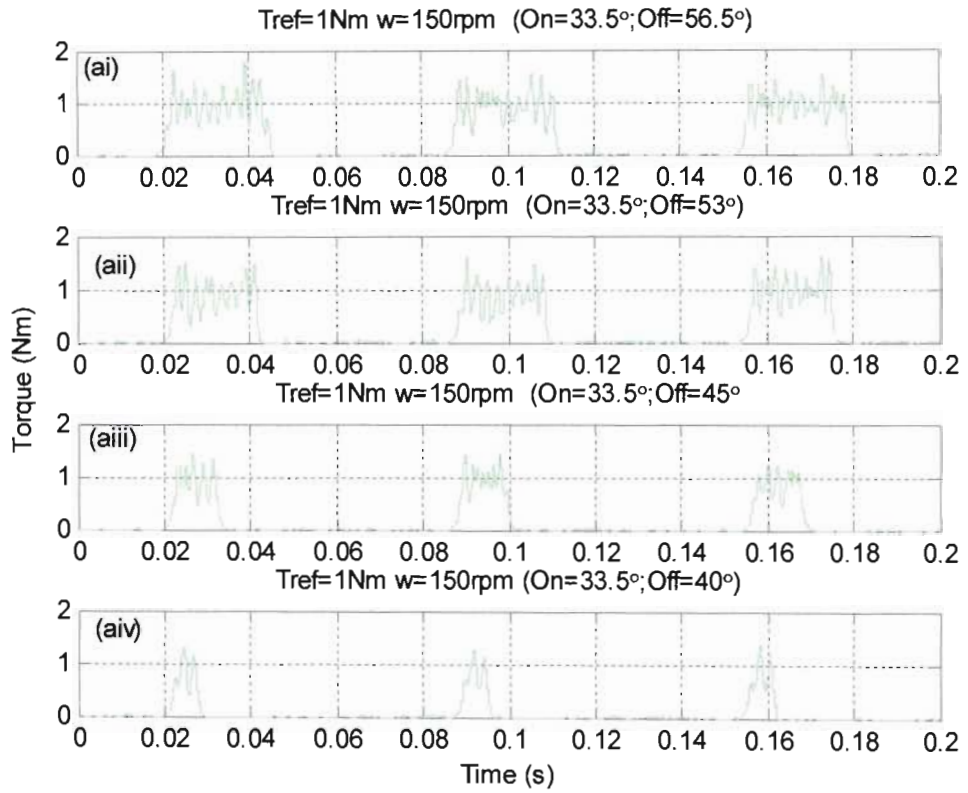

(A)

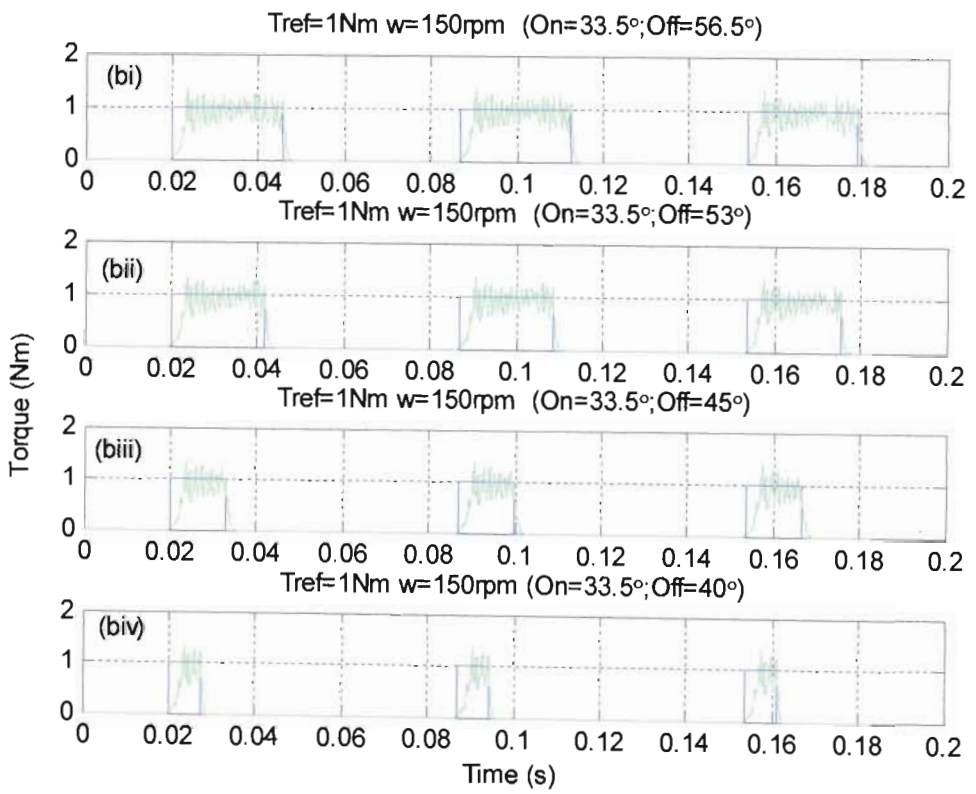

(B)

Fig. 5.21 Measured (A) and simulated (B) ***torque results*** *with* ***OFF*** *test when torque reference is* ***1Nm,*** *speed is* ***150rpm***

Fig.	(A), (B) Meas., Sim. I(A) or T(Nm)	Mode	W (rpm)	T (Nm)	∠ON	∠OFF	Remarks
5.22	I	Gen.	150	-1	(i) 3.50° (ii) 7.00° (iii) 15.0° (iv) 20.0°	26.5°	Figs. 5.22 and 5.23(ai) to (aiv) and (bii) to (biv) show decreasing lag in the measured and simulated current and torque responses as the turn-on angle is increased/retarded from 7°. This decreasing lag is due to decreasing phase inductance, and hence increasing di/dt. (as shown in Fig. 4.37) There is no appreciable current or torque lag observed in Figs. 5.23 and 5.23 (ai) for a turn-on angle of 3.5° (where the peak inductance occurs) because the di/dt response required to track the unswitched reference current waveform is lower than that which is achievable at this particular dc link voltage (28V) and speed (150rpm).
5.23	T						
5.24	I				3.50°	(i) 26.5° (ii) 23.0° (iii) 15.0° (iv) 10.0°	Figs. 5.24 and 5.25 (ai) to (aiv) show significantly increasing lag in the measured and simulated current and torque responses as the turn-off angle is decreased/advanced below 23°. This increasing lag is due to increasing phase inductance, and hence decreasing di/dt. The simulated current responses in Figs. 5.22 and 5.24(bi) to (biv) agree closely with the measured result in periods where samples are not dropped by the DSP, e.g during most of the first current pulses in Fig. 5.22(aii) to (aiv). When sample dropping does occur, the measured current ripple is higher.
5.25	T						

Table 5.2 Summary of (A) measured and (B) simulated ON and OFF current and torque responses in GENERATING mode with POSITIVE ROTATION

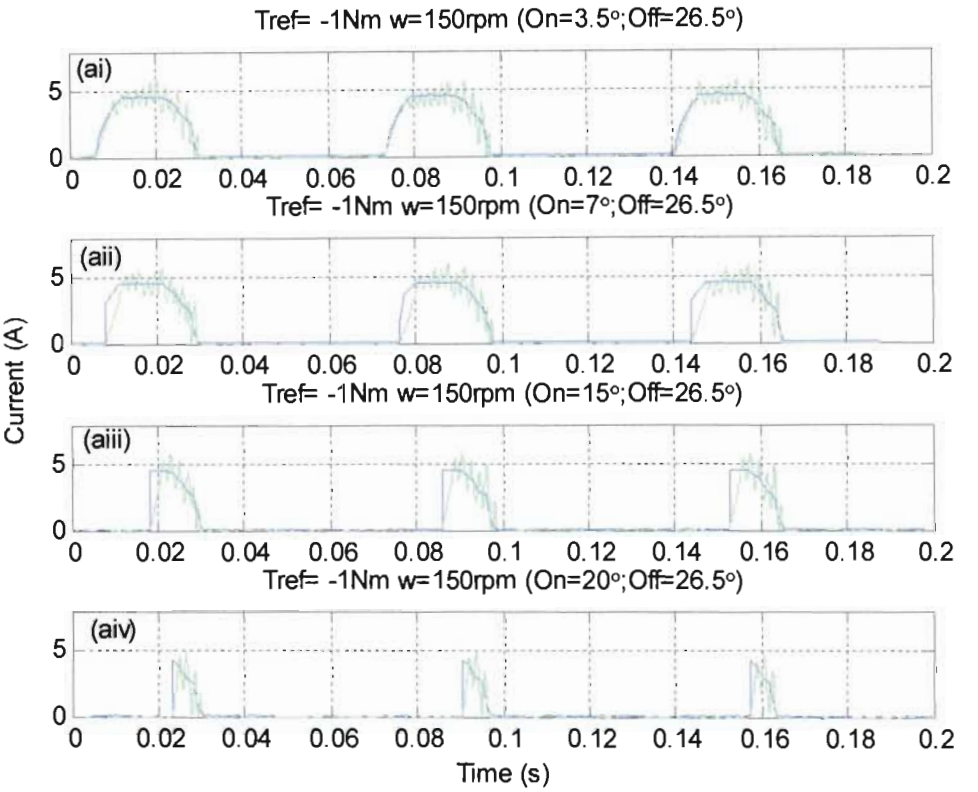

(A)

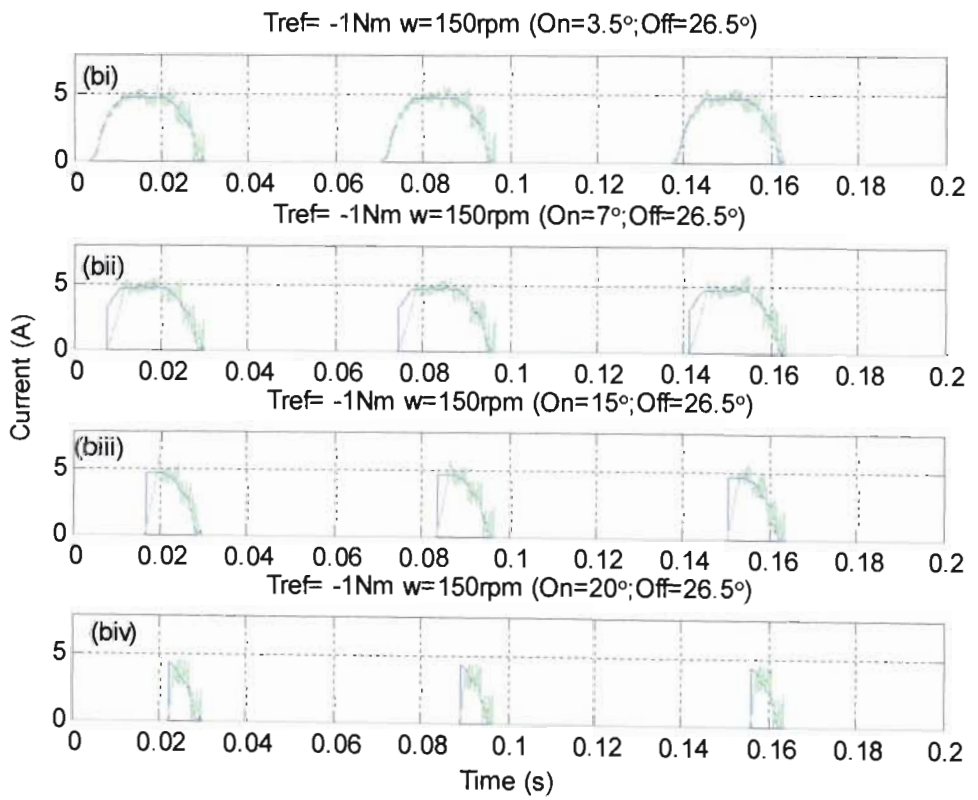

(B)

Fig. 5.22 Measured (A) and simulated (B) phase 1 ***current results*** *with* ***ON*** *test when torque reference is* ***-1Nm,*** *speed is* ***150rpm***

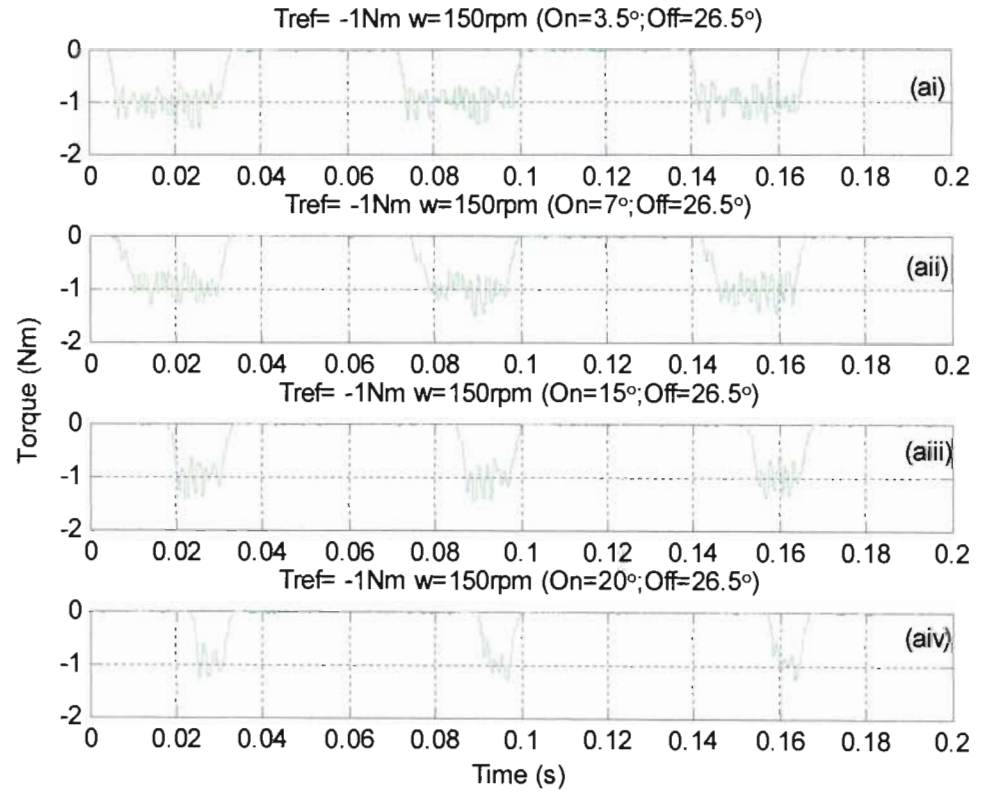

(A)

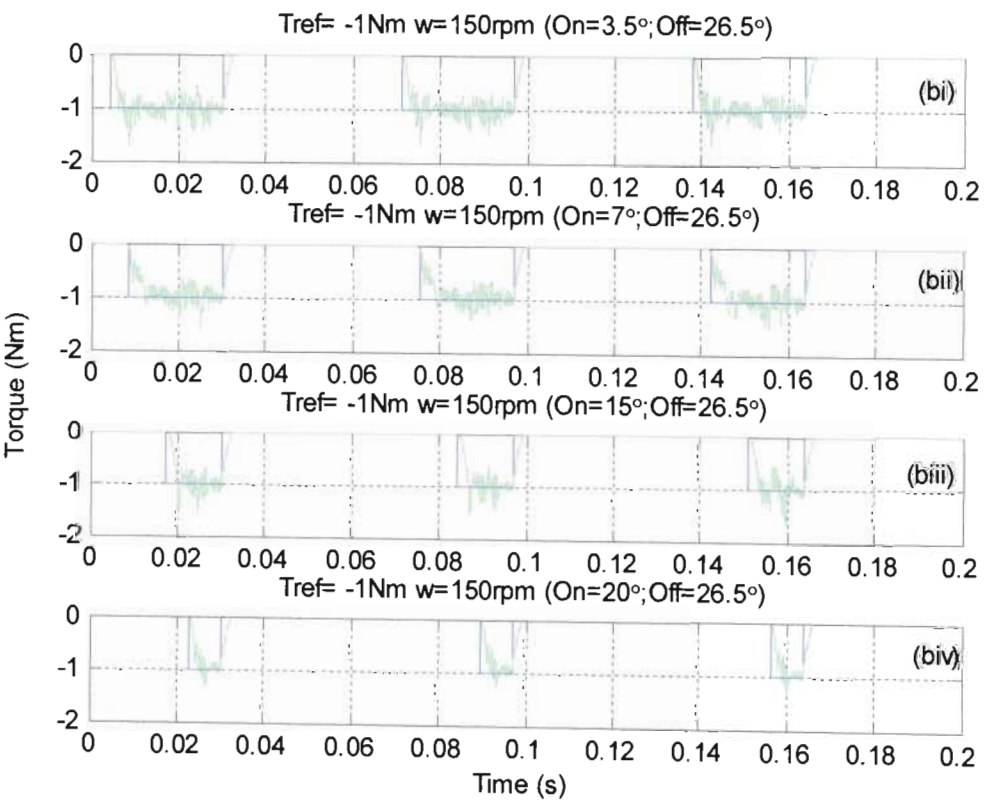

(B)

Fig. 5.23 Measured (A) and simulated (B) ***torque results*** *with* ***ON*** *test when torque reference is* ***-1Nm,*** *speed is* ***150rpm***

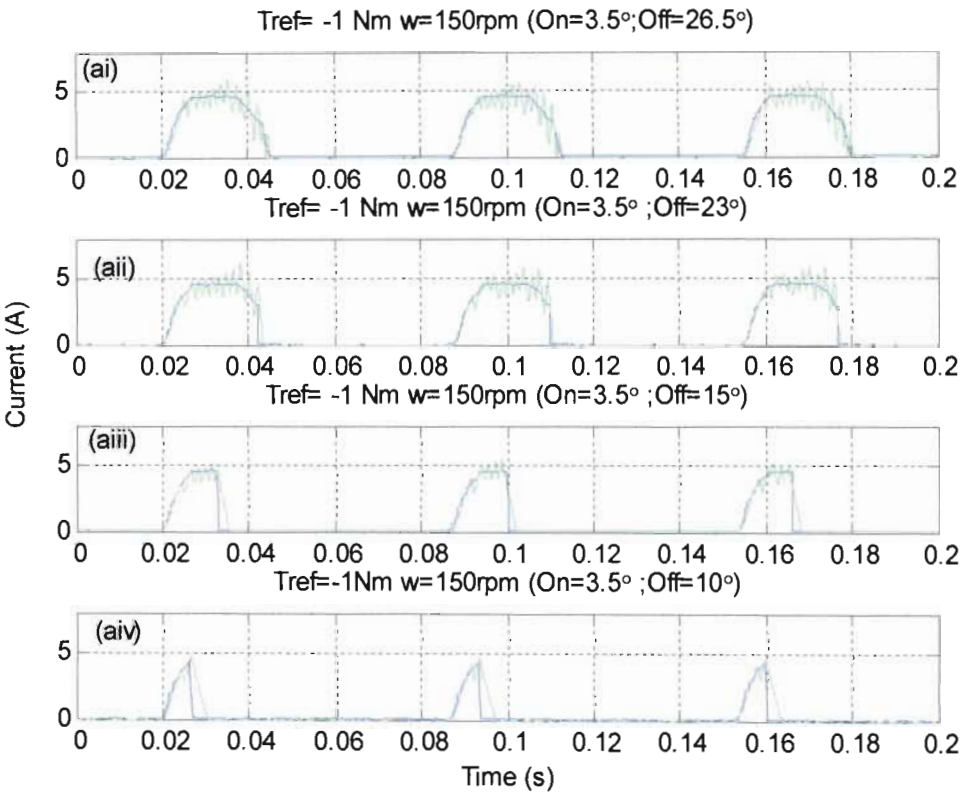

(A)

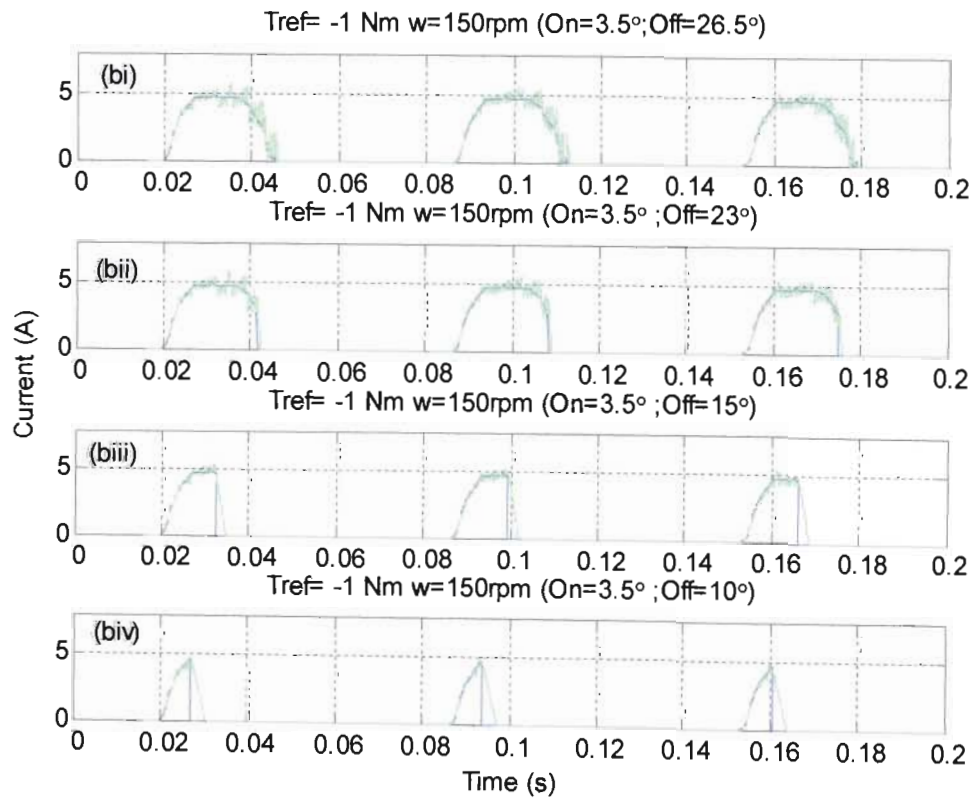

(B)

Fig. 5.24 Measured (A) and simulated (B) phase1 ***current results*** *with* ***OFF*** *test when torque reference is* ***-1Nm,*** *speed is* ***150rpm***

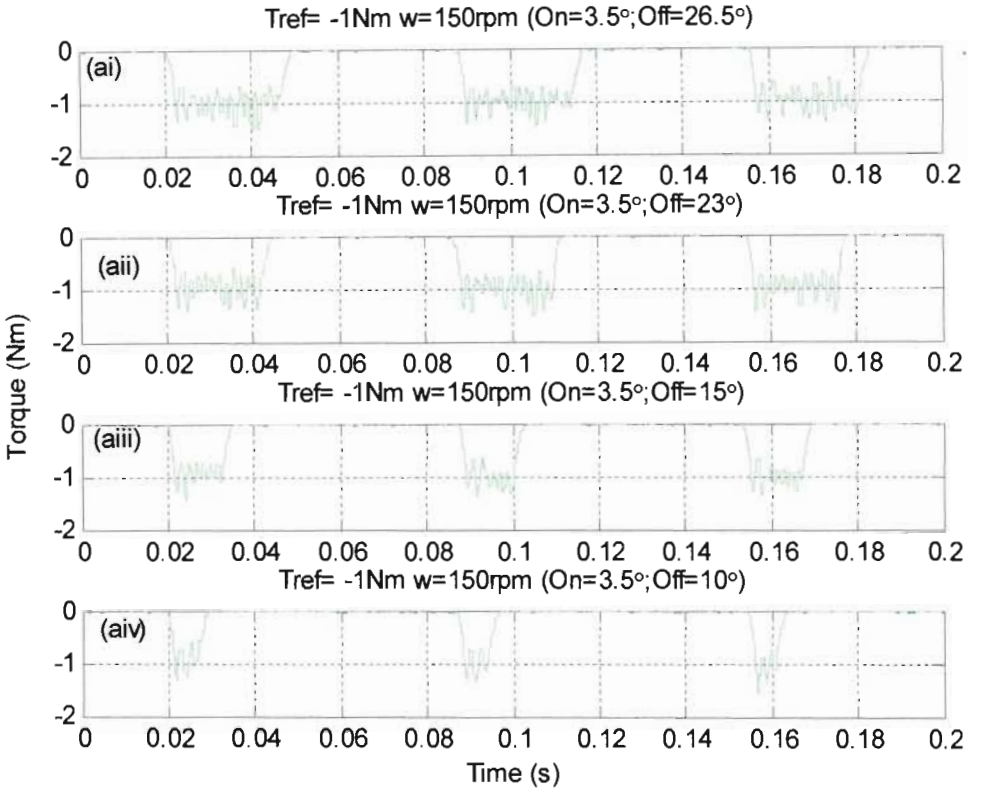

(A)

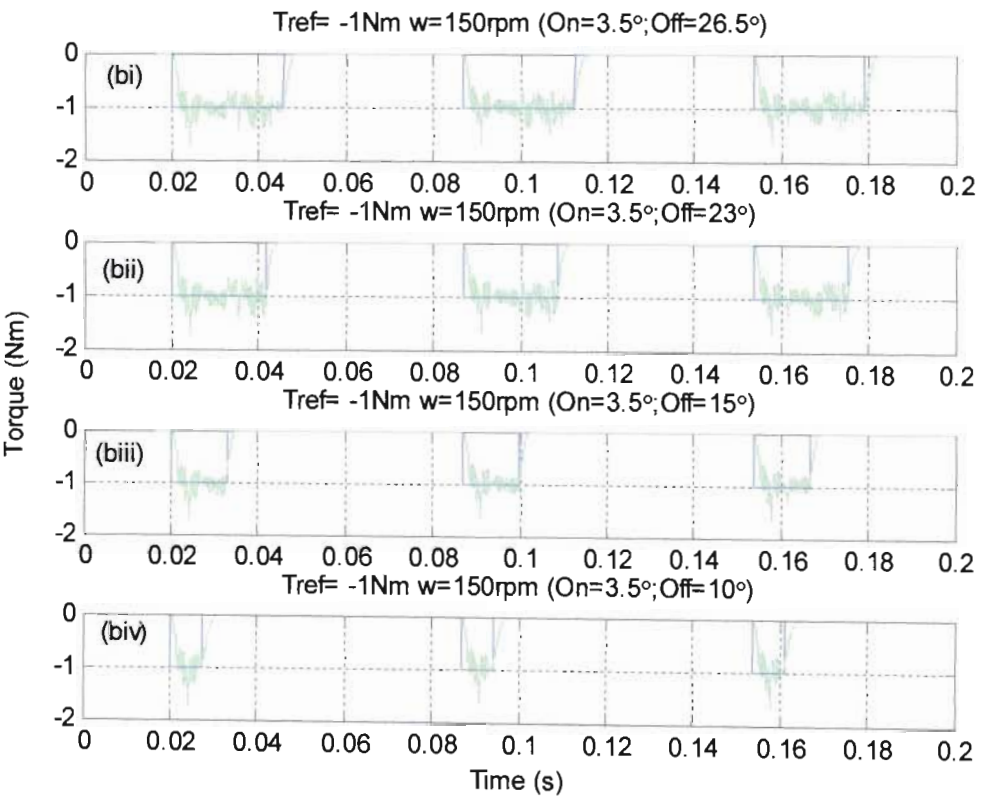

(B)

Fig. 5.25 Measured (A) and simulated (B) ***torque results*** *with* ***OFF*** *test when torque reference is* ***-1Nm,*** *speed is* ***150rpm***

Fig.	(A), (B) Meas., Sim. I(A) or T(Nm)	Mode	W (rpm)	T (Nm)	∠ON	∠OFF	Remarks
5.26	I	Mot.	-150	-1	(i) 26.5° (ii) 23.0° (iii) 15.0° (iv) 10.0	3.50°	The motoring ON test results of Figs. 5.26 and 5.27 agree closely with their positive rotation equivalents shown in Figs. 5.18 and 5.19, as discussed in Table 5.1. The actual turn-on angles differ for negative rotation because the rotor angle is always wrapped to lie between 0° and 60°, as shown in Fig. 5.17(b). Retarding the turn-on time is therefore also achieved by *decreasing* the turn-on angle.
5.27	T						
5.28	I				26.5°	(i) 3.50° (ii) 7.00° (iii) 15.0° (iv) 20.0°	The motoring OFF test results of Figs. 5.28 and 5.29 agree closely with their positive rotation equivalents shown in Figs. 5.20 and 5.21, as discussed in Table 5.1. The actual turn-off angles differ for negative rotation because the rotor angle is always wrapped to lie between 0° and 60°, as shown in Fig. 5.17(b). Advancing the turn-off time is therefore also achieved by *increasing* the turn-off angle.
5.29	T						
5.30	I	Gen.	-150	1	(i) 56.5° (ii) 53.0° (iii) 45.0° (iv) 40.0°	33.5°	The generating ON test results of Figs. 5.30 and 5.31 agree closely with their positive rotation equivalents shown in Figs. 5.22 and 5.23, as discussed in Table 5.2. The actual turn-on angles differ for negative rotation because the rotor angle is always wrapped to lie between 0° and 60°, as shown in Fig. 5.17(b). Retarding the turn-on time is therefore also achieved by *decreasing* the turn-on angle.
5.31	T						
5.32	I				56.5°	(i) 33.5° (ii) 37.0° (iii) 45.0° (iv) 50.0°	The generating OFF test results of Figs. 5.32 and 5.33 agree closely with their positive rotation equivalents shown in Figs. 5.24 and 5.25, as discussed in Table 5.2. The actual turn-off angles differ for negative rotation because the rotor angle is always wrapped to lie between 0° and 60°, as shown in Fig. 5.17(b). Advancing the turn-off time is therefore also achieved by *increasing* the turn-off angle.
5.33	T						

Table 5.3 Summary of (A) measured and (B) simulated ON and OFF current and torque responses for Fig. 5.26 to Fig. 5.33

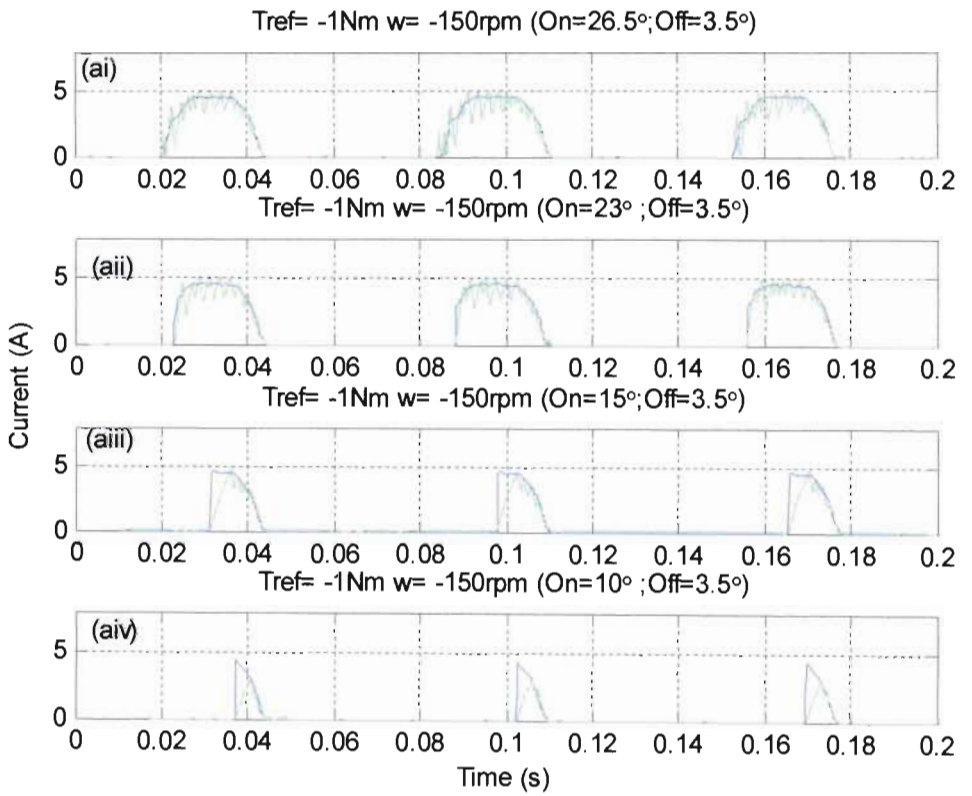

(A)

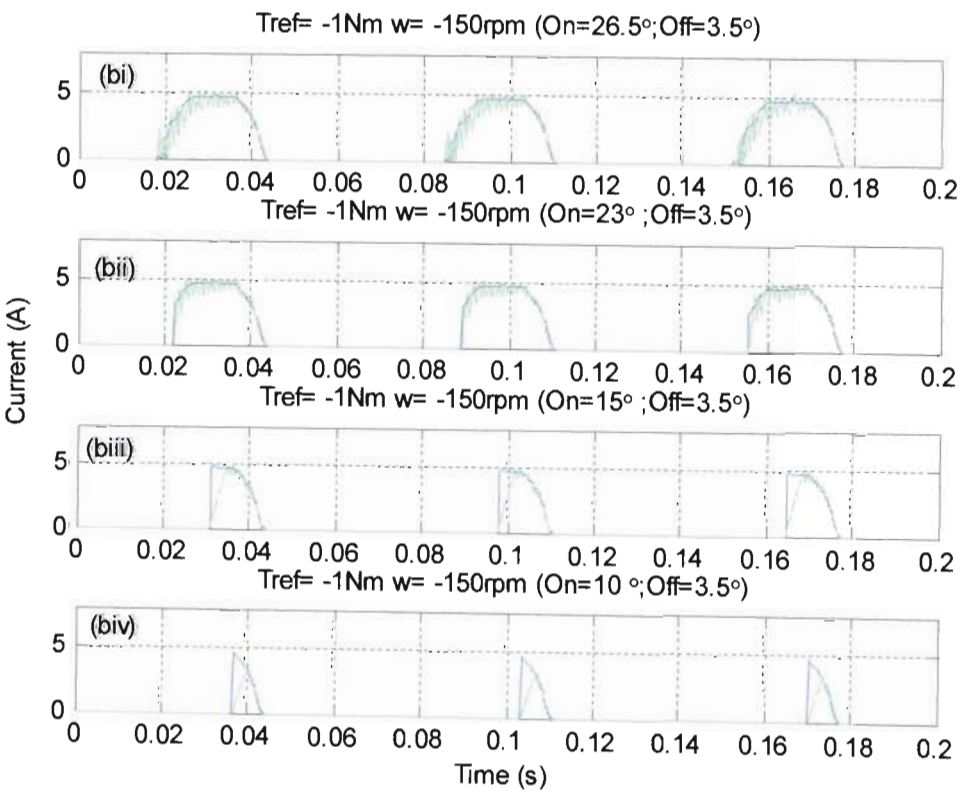

(B)

Fig. 5.26 Measured (A) and simulated (B) phase 1 ***current results*** *with* ***ON*** *test when torque reference is* ***-1Nm,*** *speed is* ***-150rpm***

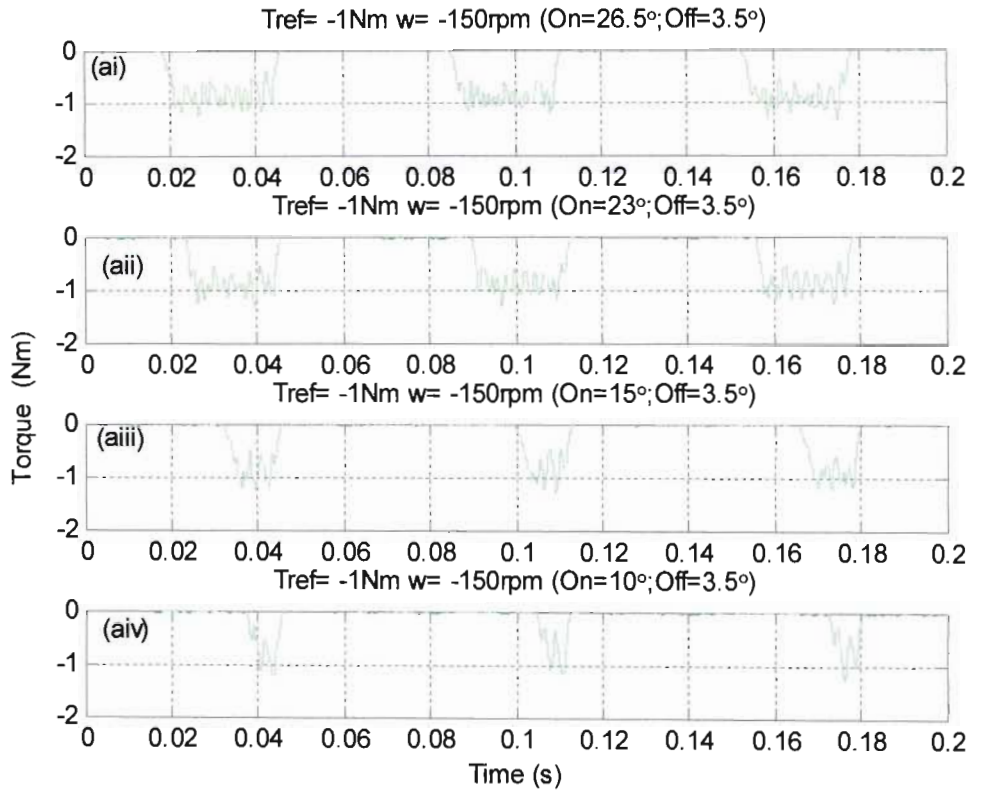

(A)

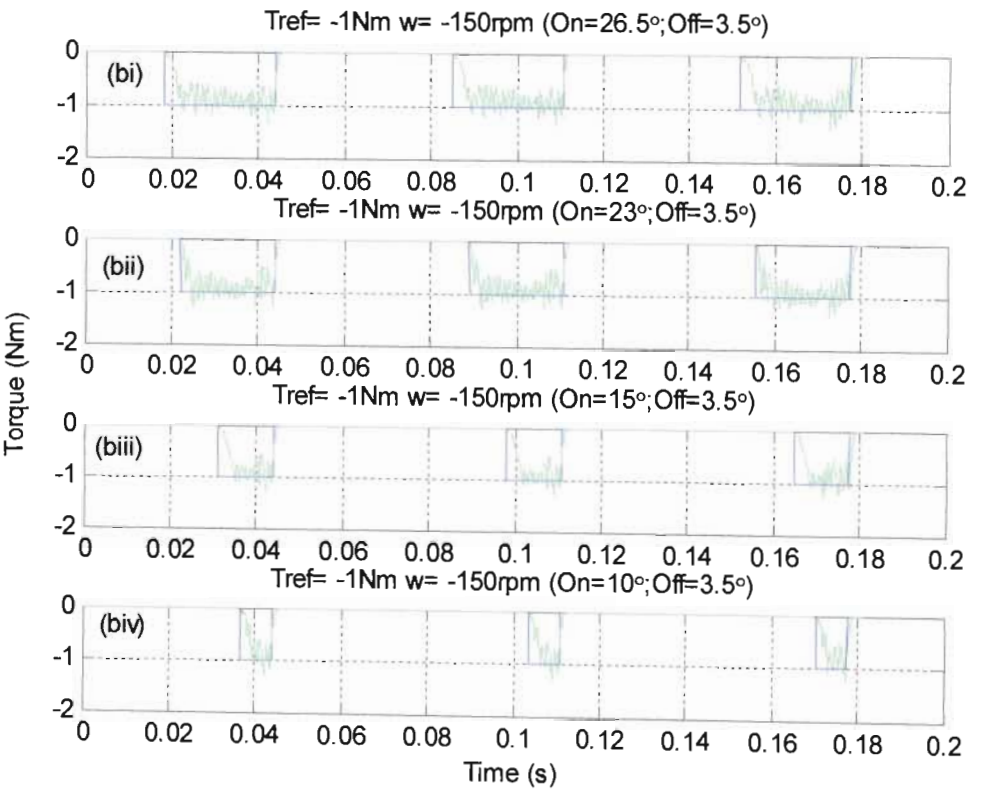

(B)

Fig. 5.27 Measured (A) and simulated (B) ***torque*** *results with* ***ON*** *test when torque reference is* ***-1Nm,*** *speed is* ***-150rpm***

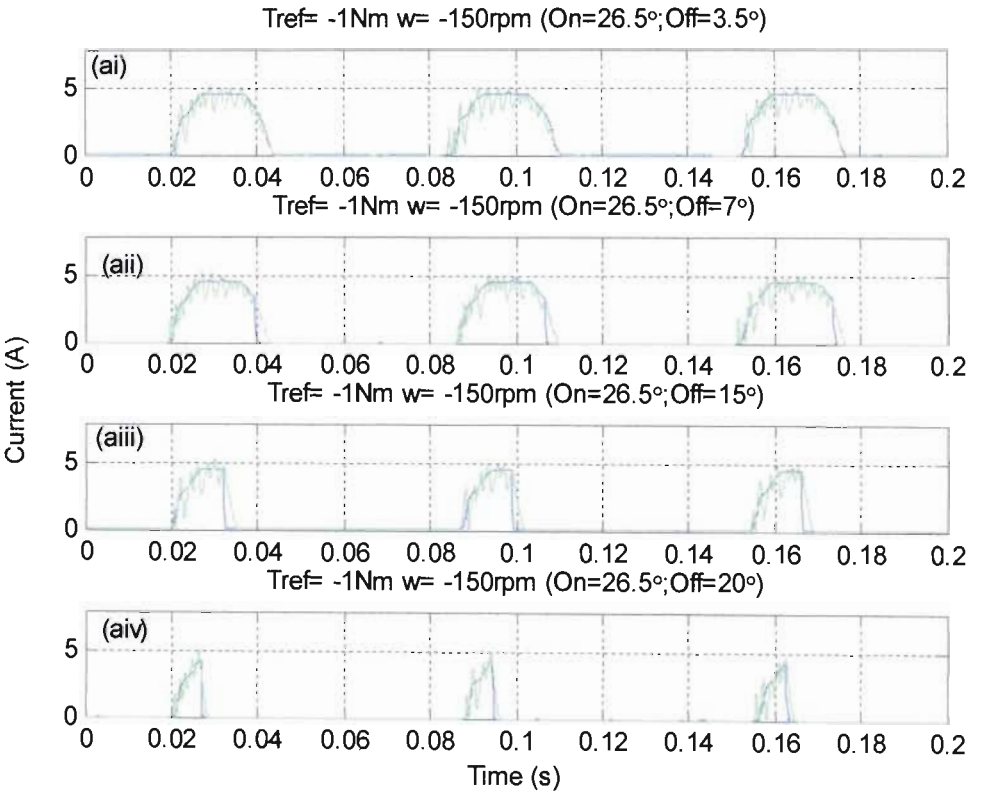

(A)

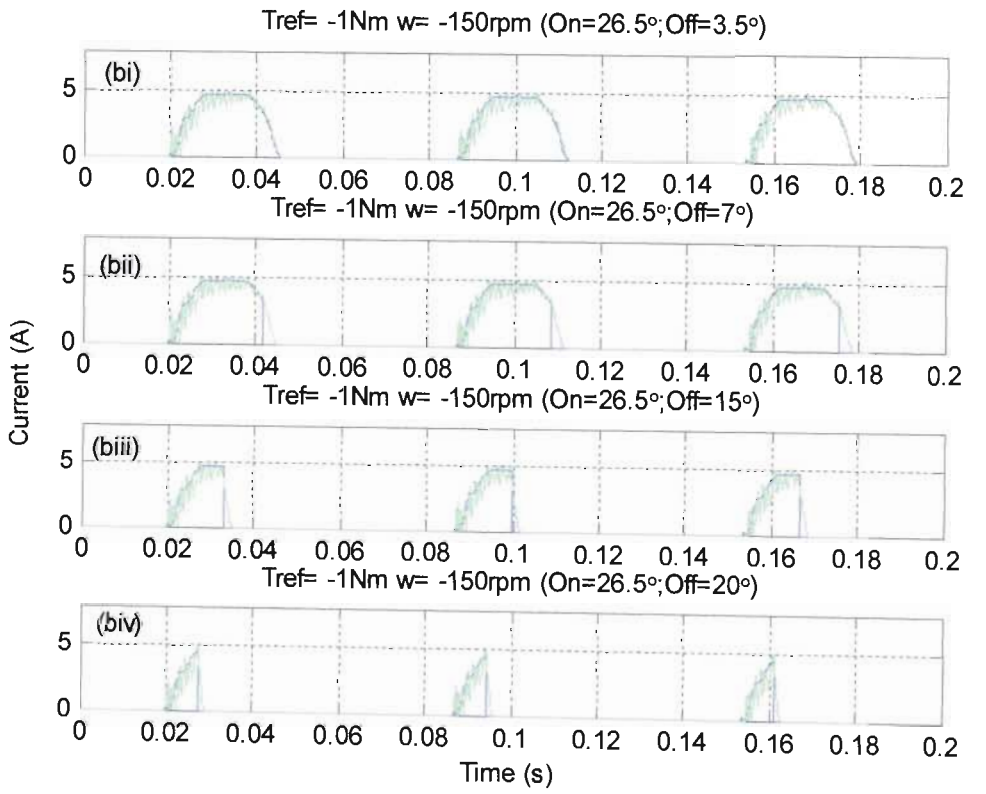

(B)

Fig. 5.28 Measured (A) and simulated (B) phase 1 ***current results*** *with* ***OFF*** *test when torque reference is* ***-1Nm,*** *speed is* ***-150rpm***

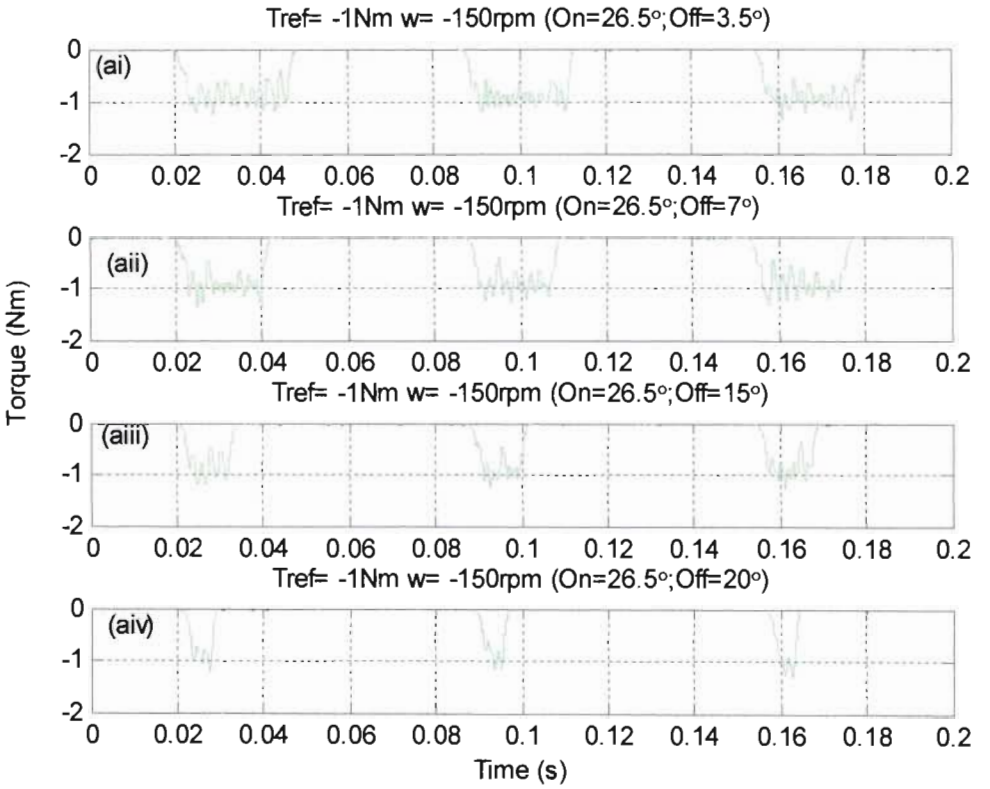

(A)

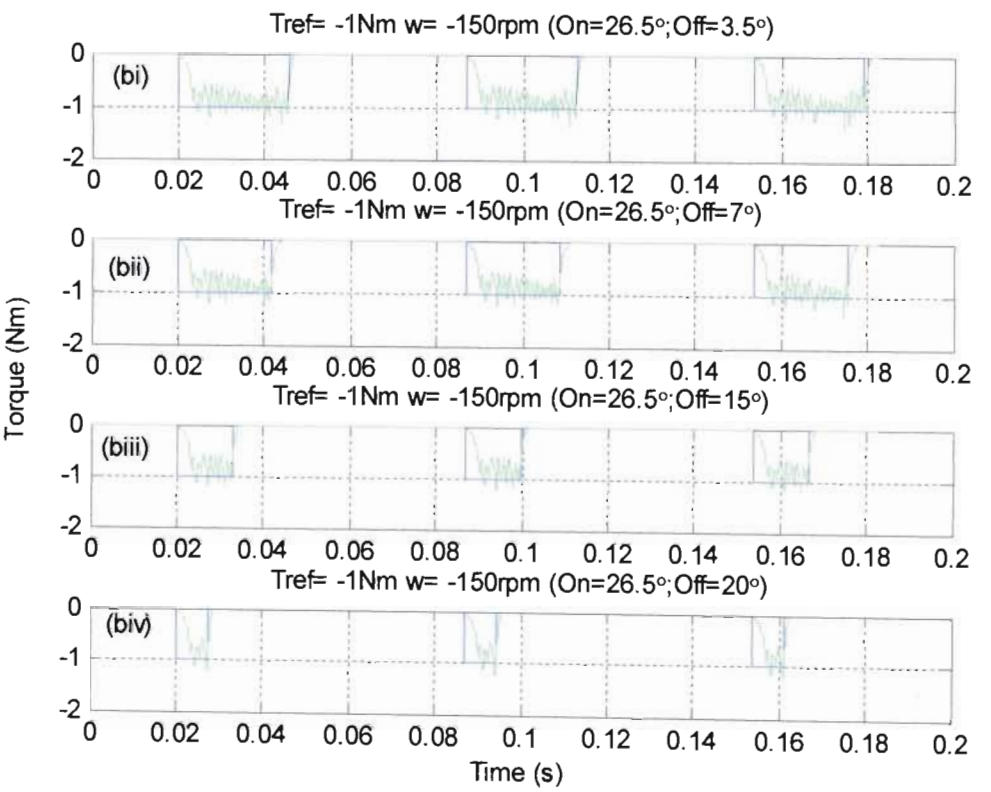

(B)

Fig. 5.29 Measured (A) and simulated (B) ***torque results*** *with* ***OFF*** *test when torque reference is* ***-1Nm,*** *speed is* ***-150rpm***

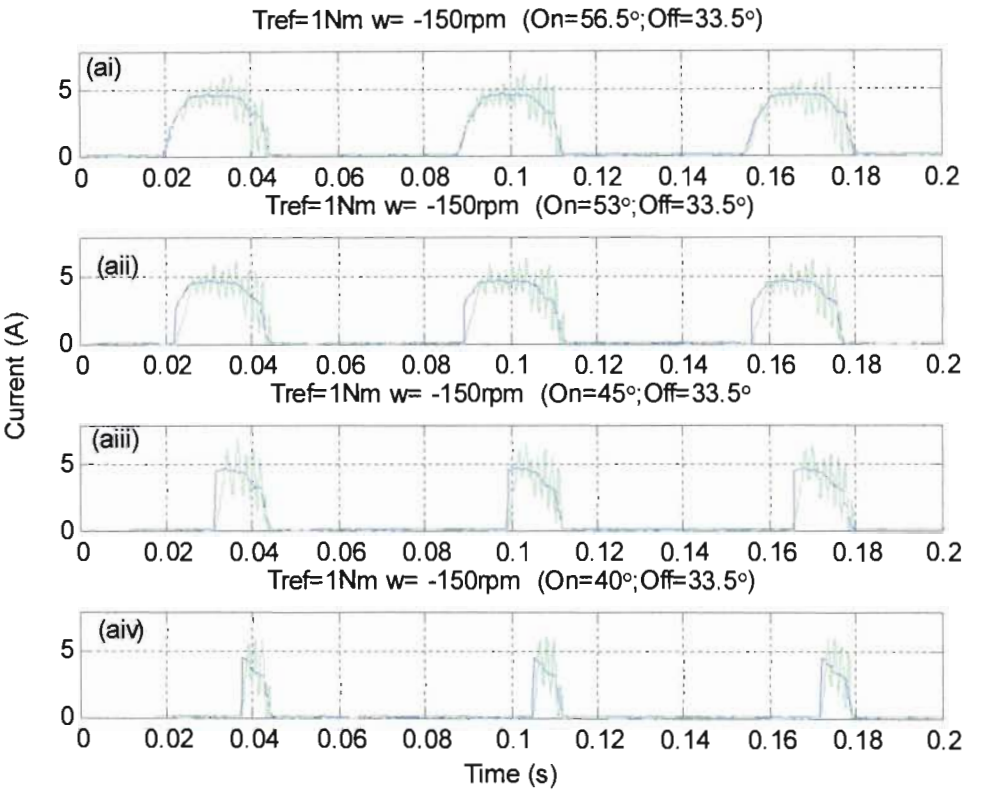

(A)

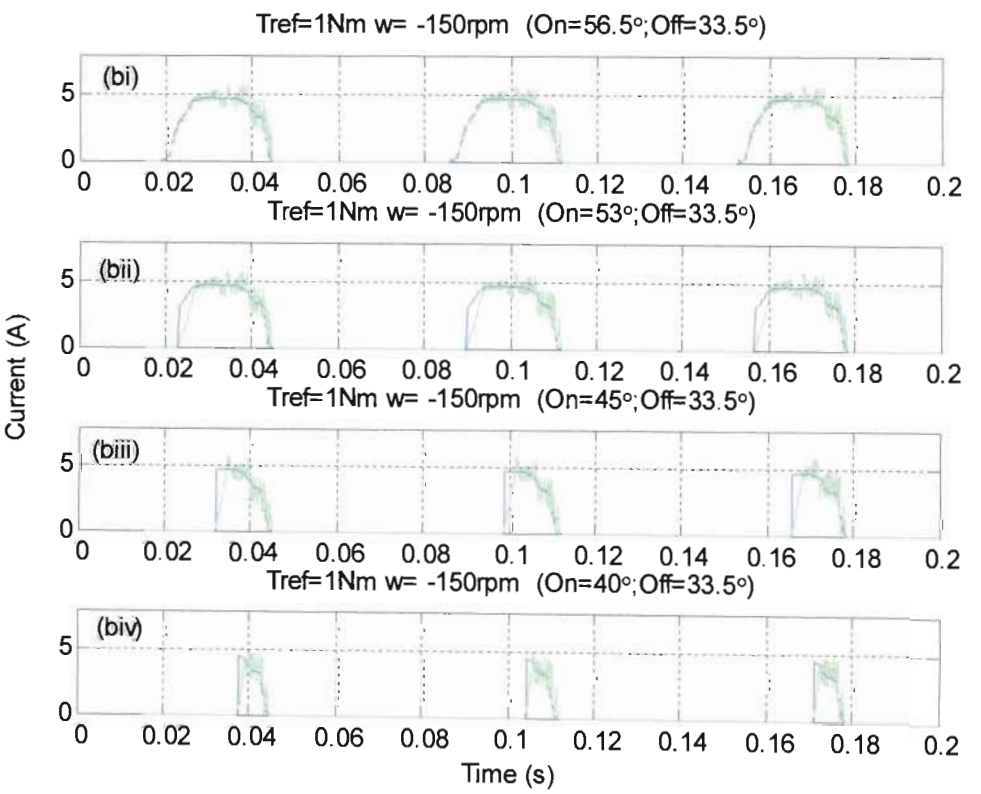

(B)

Fig. 5.30 Measured (A) and simulated (B) phase 1 ***current results*** *with* ***ON*** *test when torque reference is* ***1Nm,*** *speed is* ***-150rpm***

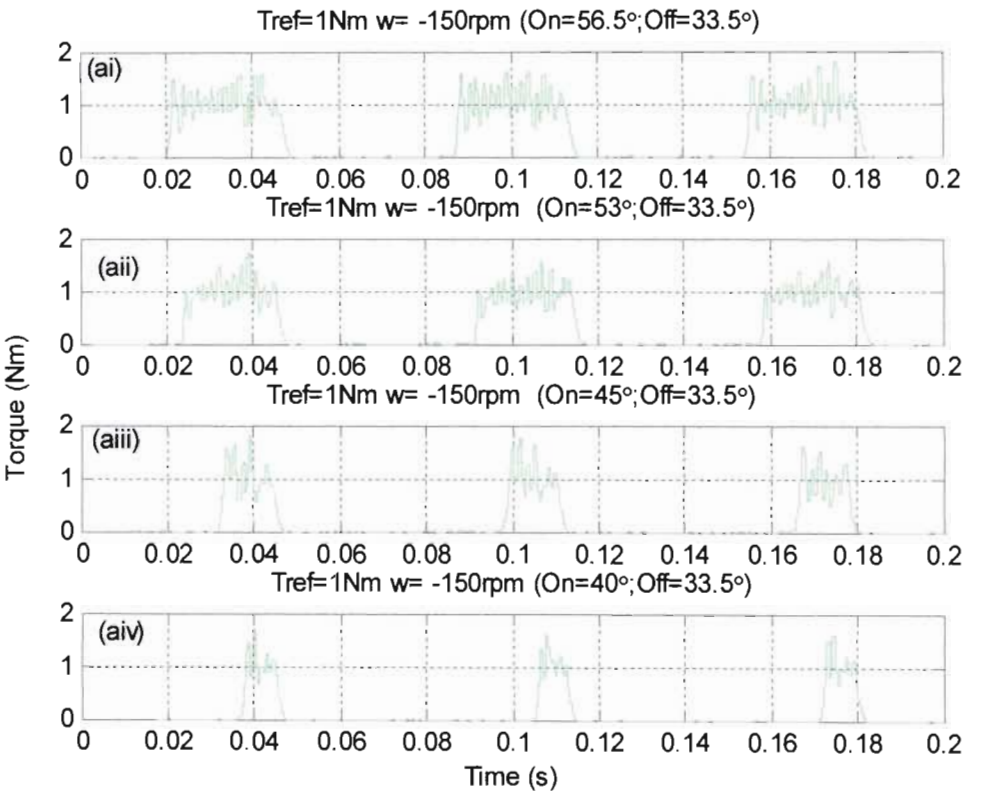

(A)

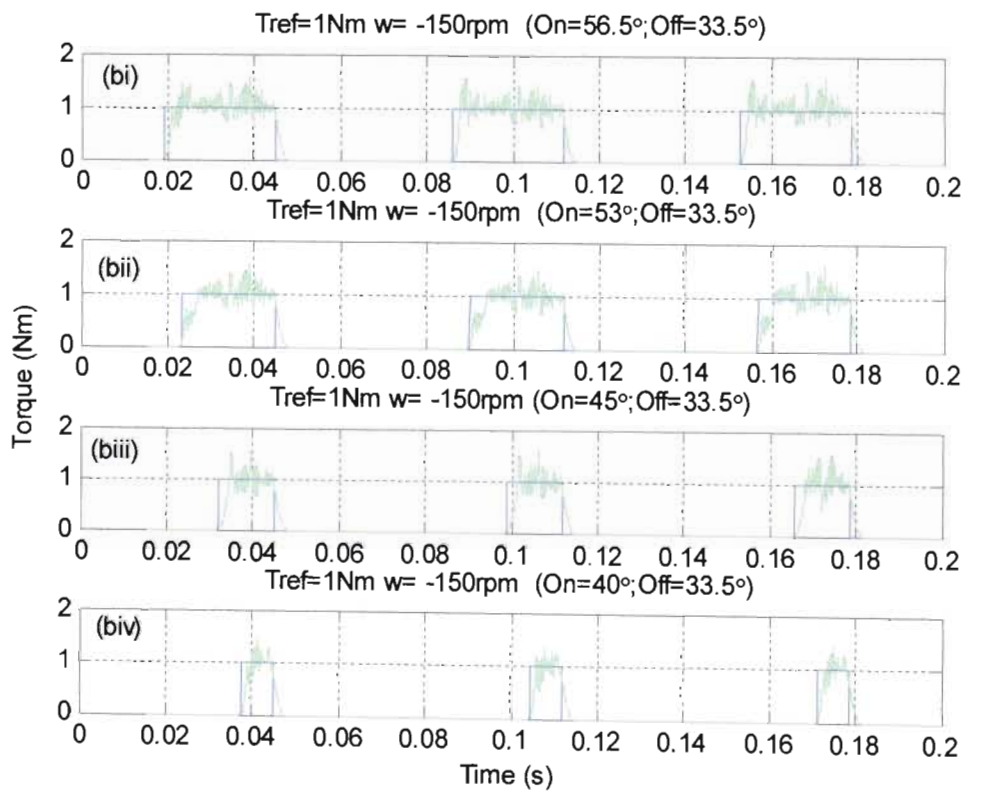

(B)

Fig. 5.31 Measured (A) and simulated (B) ***torque results*** *with* ***ON*** *test when torque reference is* ***1Nm,*** *speed is* ***-150rpm***

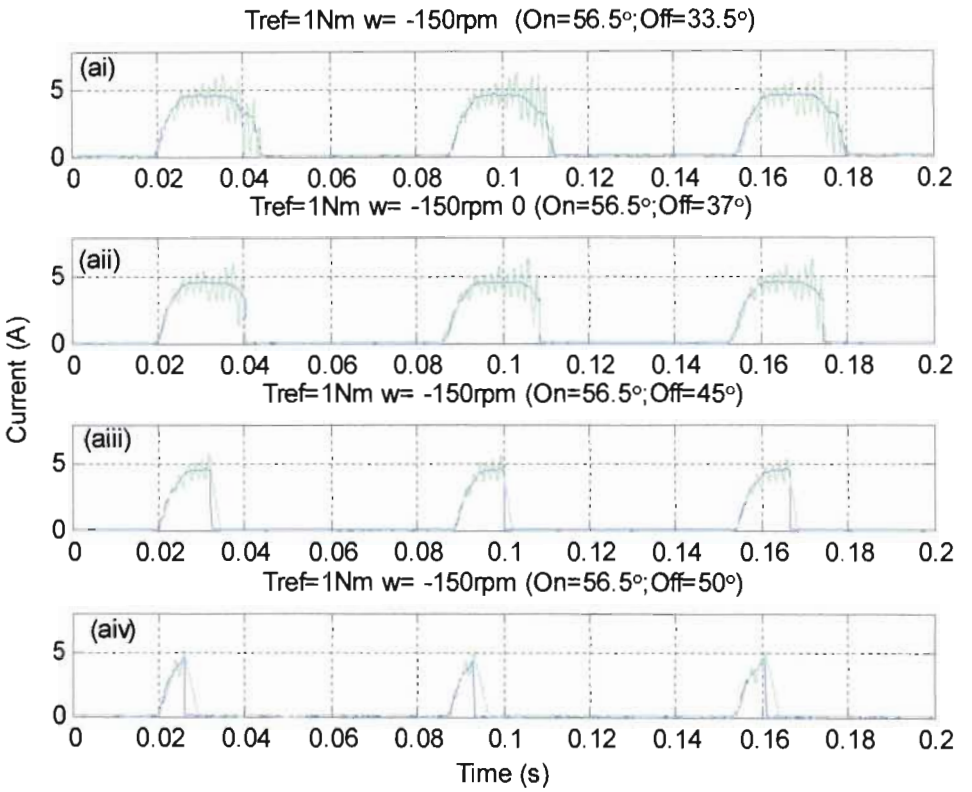

(A)

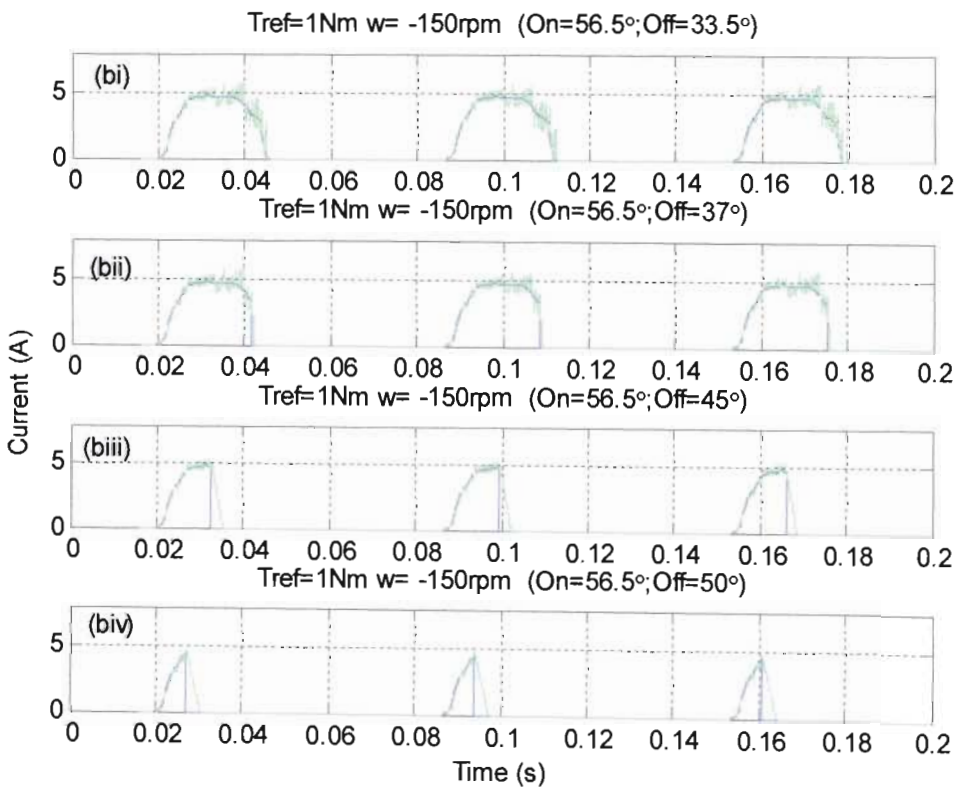

(B)

Fig. 5.32 Measured (A) and simulated (B) phase 1 ***current results*** *with* ***OFF*** *test when torque reference is* ***1Nm,*** *speed is* ***-150rpm***

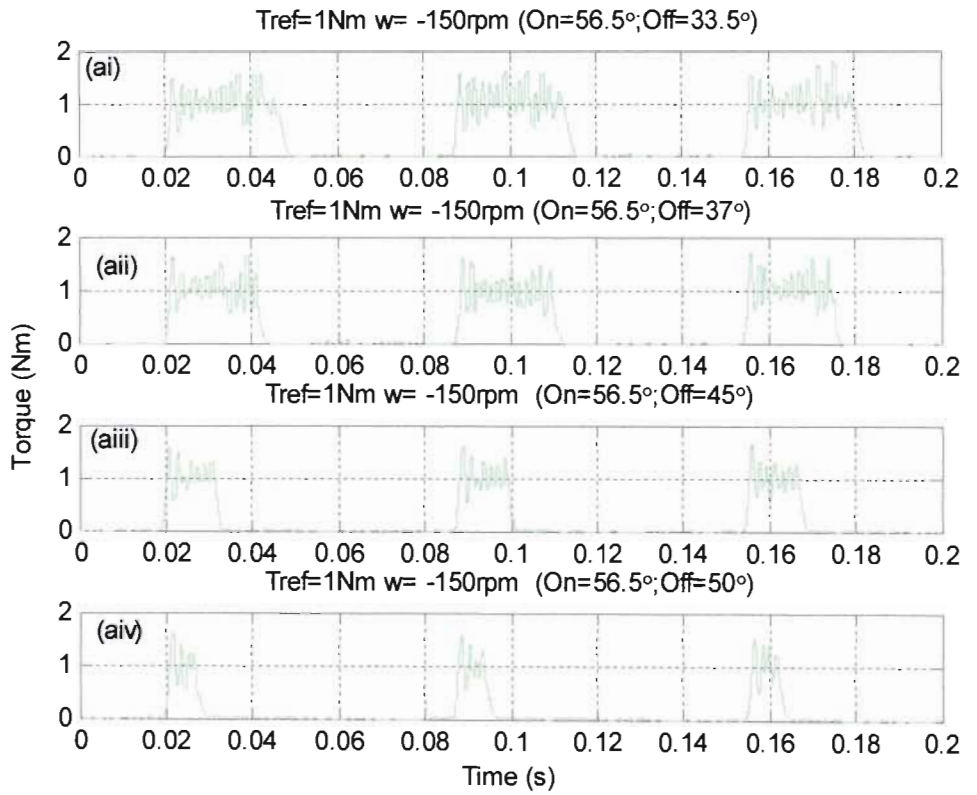

(A)

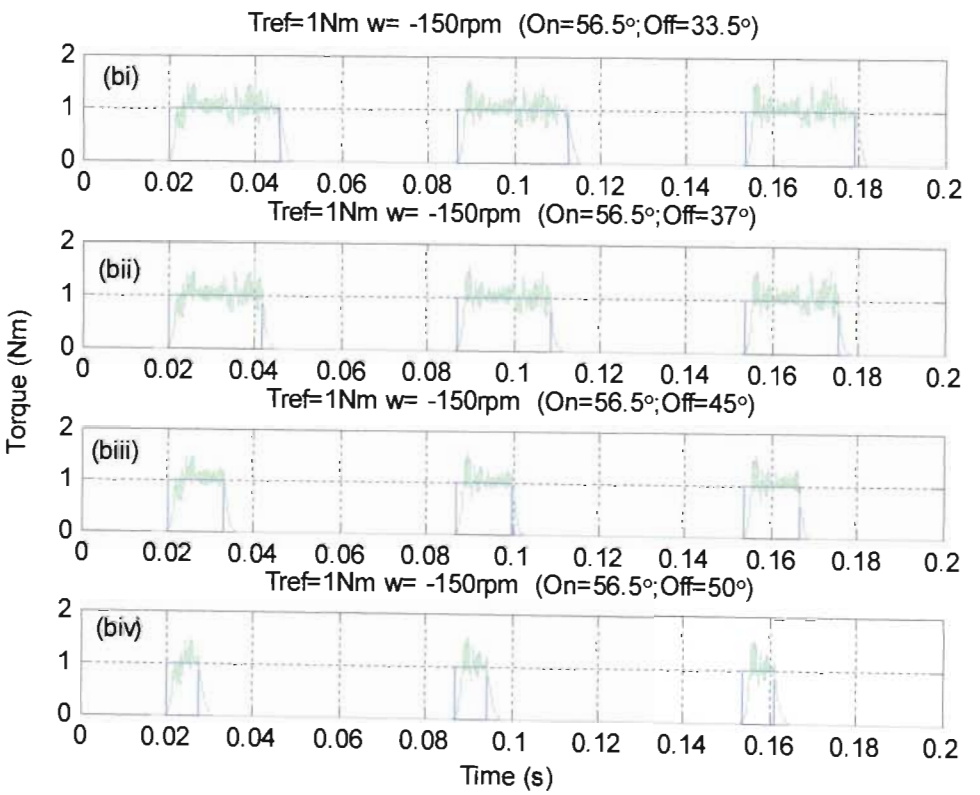

(B)

Fig. 5.33 Measured (A) and simulated (B) ***torque results*** *with* ***OFF*** *test when torque reference is* ***1Nm,*** *speed is* ***-150rpm***

The ON and OFF test results of Figs. 5.18 to 5.33 show the relatively strong rotor angle dependence of the current and torque step response in motoring and generating mode using torque pulses of ±1Nm at constant rotor speeds of ±150rpm. The square-wave torque response for any rotor angle can be inferred by superimposing the corresponding turn-off/turn-on step responses. This angle dependence can only be compensated for by increasing the achievable di/dt. The previously suggested future investigations into C-dump converters, or adaptive/nonlinear PWM current control to achieve low current ripple with higher dc link voltage would therefore also be helpful in this regard.

The next series of tests investigates the speed and current dependence of the current and torque step responses.

Varying Torque Pulse Magnitude at Different Speeds

In this series of tests, the torque reference consists of a positive pulse from 33.5° to 56.5°, followed by a negative pulse of the same magnitude in the next interval from 3.5° to 26.5°. Various constant speed values are once again achieved in practice using a commercial vector drive and 3kW induction motor.

Fig. 5.34 shows the measured and simulated phase 1 current and torque responses to torque reference pulses of ± 1Nm at a speed of (A) 150 rpm, and (B) -150rpm. Fig. 5.35 and Fig. 5.36 shows the results when speed increases to ± 500rpm and 1000rpm respectively. The effect of current magnitude is then investigated by increasing the torque reference magnitude (and hence the reference and actual current magnitude). Fig. 5.37 and Fig. 5.38 show the current and torque responses to torque reference pulses of ± 4 Nm and ± 6Nm respectively. These results are summarized in Table 5.4.

Fig.	W (rpm)	Tref (Nm)	Remarks
5.34(A)	150	± 1	The measured and simulated results of Fig. 5.34 and 5.35 (bi) and (bii) confirm that a dc link voltage of 28V produces good tracking of the reference current in both motoring and generating mode (the current ripple is also observed to be higher in generating mode, as explained in section 4.4.2). Fig. 5.34 and 5.35 (bi) and (bii) show correspondingly good tracking of the ± 1Nm torque reference pulses. The measured torque generally has more ripple, which corresponds to the higher measured current ripple, due to the DSP sample dropping problem discussed in Appendix D.5. Slight variations occur in the measured speed due to the torque steps and ripple (these are more clearly visible at higher torque magnitudes, as shown in Figs.5.37 and 5.38) but these cannot be correlated with the torque or current responses or ripple because it was not possible to capture all of these signals simultaneously from the DSP.
5.34(B)	-150		
5.35(A)	500		Fig. 5.35 shows that increasing the speed from ± 150rpm to ± 500rpm results in more torque and current reference pulses per unit time, but does not affect the magnitude of these reference pulses. As explained in section 4.4.2, the measured and simulated currents lag their references during off commutation in motoring ($T\omega>0$) mode (due to increased back emf) and on commutation in generating ($T\omega<0$) mode (due to significantly higher inductance). The time allowed for the torque response to stabilize is also significantly reduced.
5.35(B)	-500		
5.36	1000		Fig. 5.36 shows the effect of further increasing the speed to +1000rpm in motoring mode only (due to the further reduction in the reference torque pulse width, and hence the time allowed for torque response settling, only +1Nm pulses are used for the torque reference). The measured and simulated phase 1 current responses are in close agreement, but are not able to track the reference waveforms in two respects. The first is that the peak actual current is significantly less that the peak reference current, and the second is that the off commutation lag is very pronounced due to insufficient dc link voltage to overcome the phase inductance and back emf at this speed. The average total torque response is close to the expected value of 0.5 Nm, but does not resemble the discrete train of 1Nm reference pulses corresponding to every phase 1 current pulse at this relatively high frequency.
5.37(A)	150	± 4	The measured and simulated torque and current responses in Fig. 5.37 show that the dc link voltage of 28V is also sufficient to track the ±4Nm total torque reference (and corresponding phase current references) at a speed of ±150rpm, but there are significant commutation lags in the generating modes for both directions of rotation. There is also more phase current and total torque ripple in generating mode because the back emf has the same sign as the dc link voltage. This results in a larger phase voltage than in motoring mode, and therefore higher di/dt in generating mode. The measured speed response in Fig. 5.37(di) shows the relatively limited ability of the commercial vector controlled induction motor drive to regulate the shaft speed under these relatively high dynamic torque disturbance conditions. The correct average speed is nevertheless maintained, and there is reasonably close agreement between the simulated and measured torque and current responses.
5.37(B)			
5.38		6	Fig. 5.38 shows the measured and simulated torque and current responses to a ±6Nm torque reference at a speed of 150rpm. The total torque and phase current are able to reach the peak reference values, but exhibit pronounced commutation lag in generating mode. The measured speed disturbances in Fig. 5.38(di) are also observed to be significantly higher than those produced at ±4Nm in Fig. 5.37 (Adi) and (Bdi).

Table 5.4 Summary of varying torque pulse magnitude at different speeds results

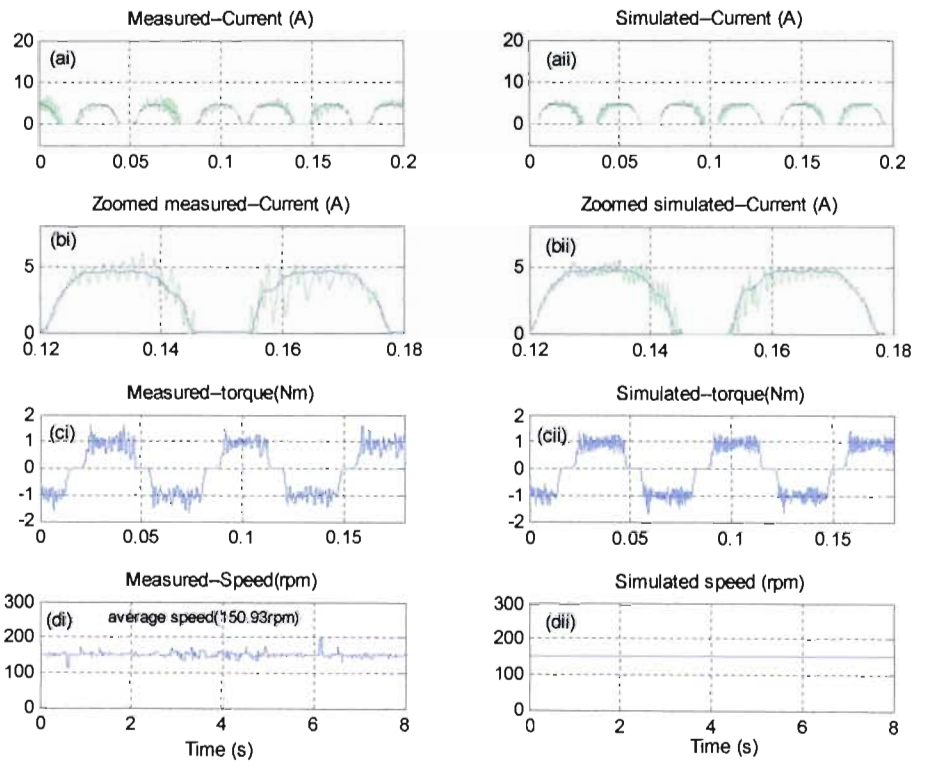

(A)

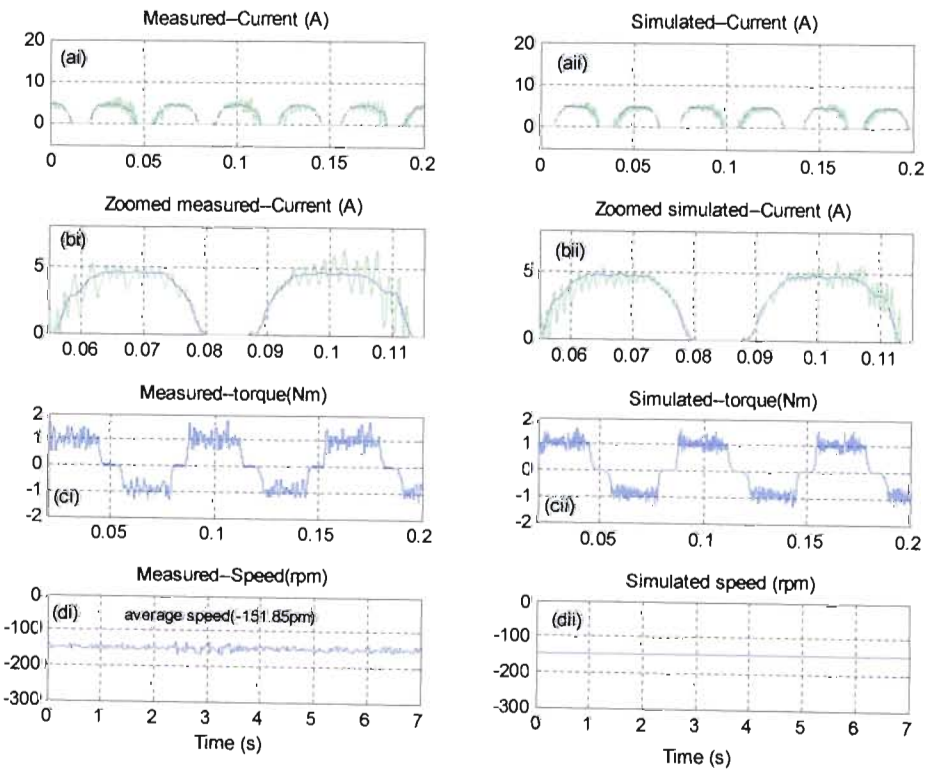

(B)

Fig. 5.34 Measured and simulated results when torque reference is ± 1Nm with constant speed (A) 150rpm and (B) -150rpm

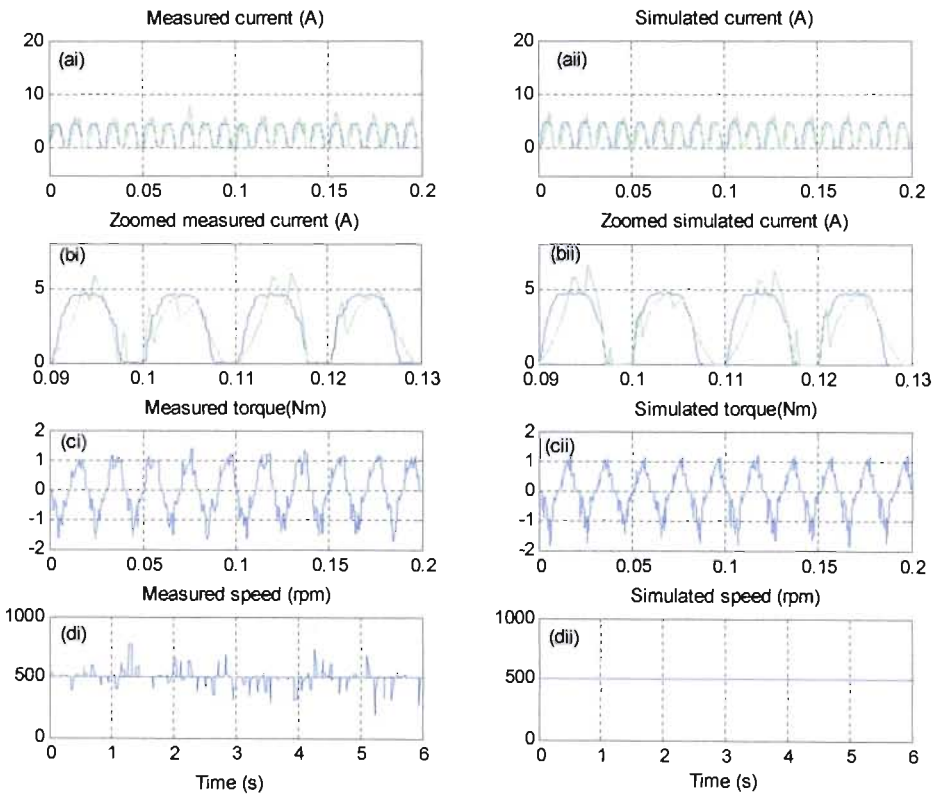

(A)

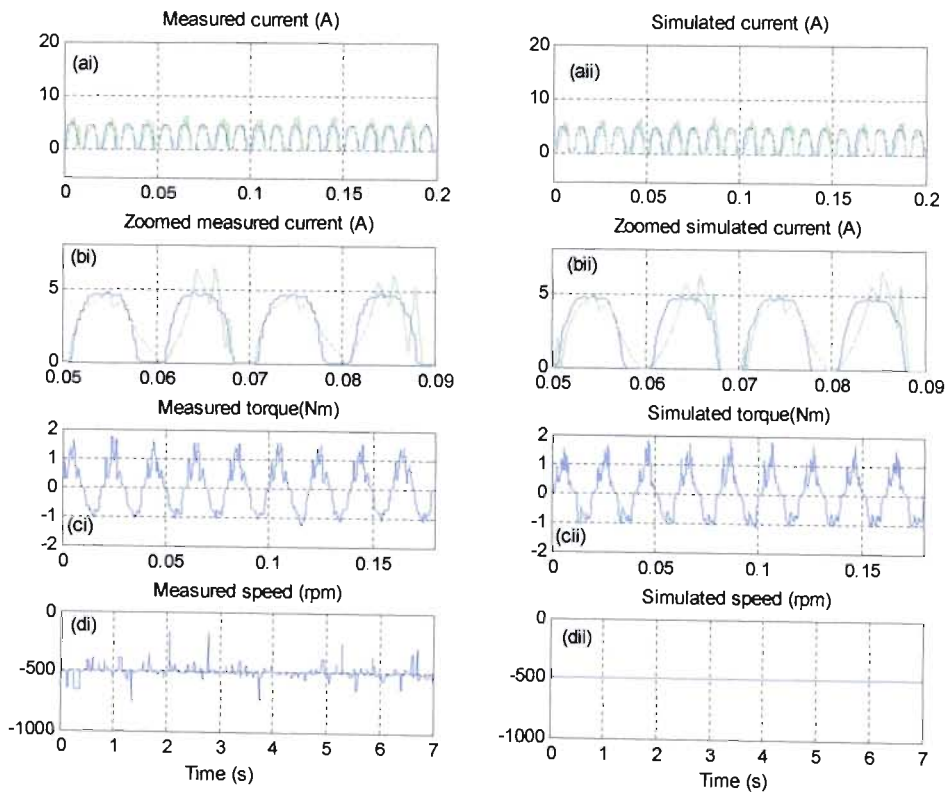

(B)

Fig. 5.35 Measured and simulated results when torque reference is ± 1Nm with constant speed (A) 500rpm and (B) -500rpm

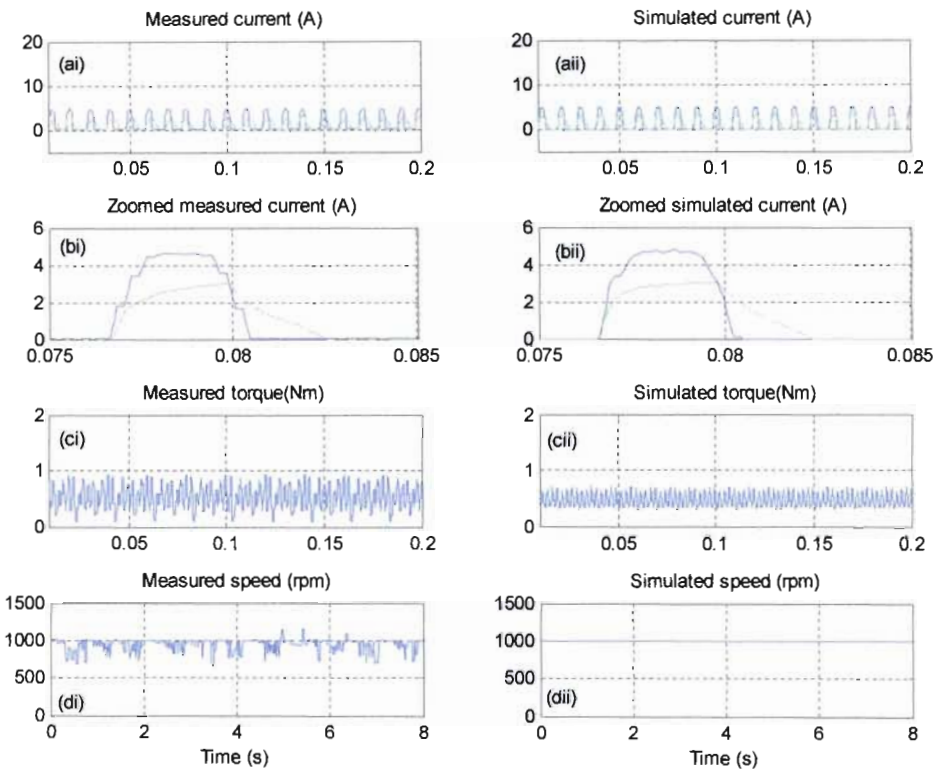

Fig. 5.36 Measured and simulated results when torque reference is 1Nm with constant speed 1000rpm

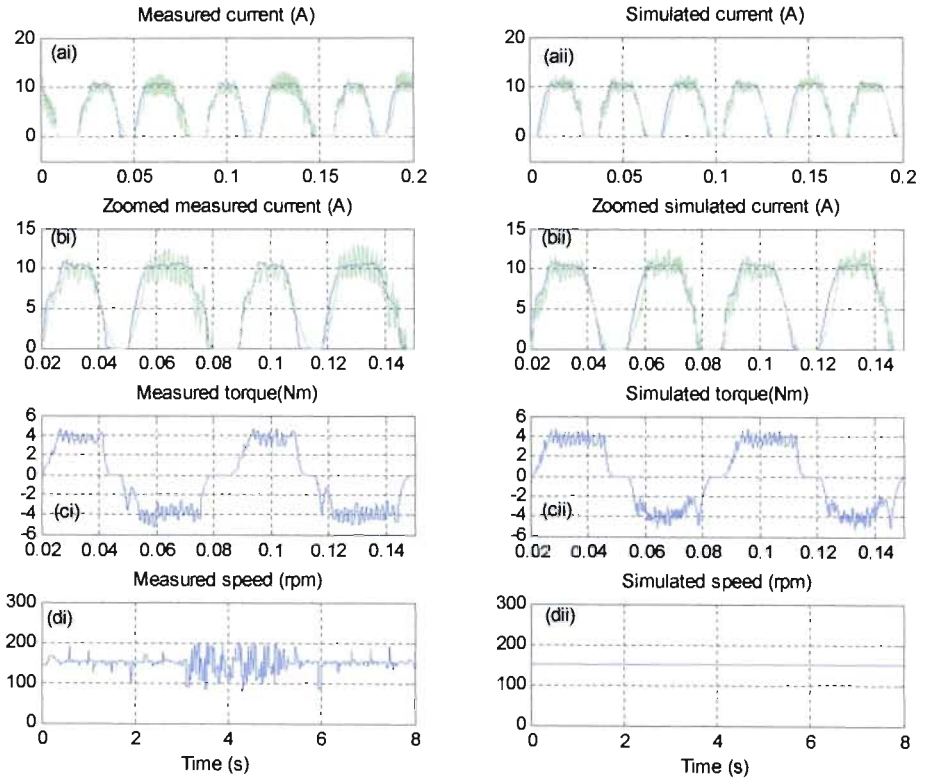

(A)

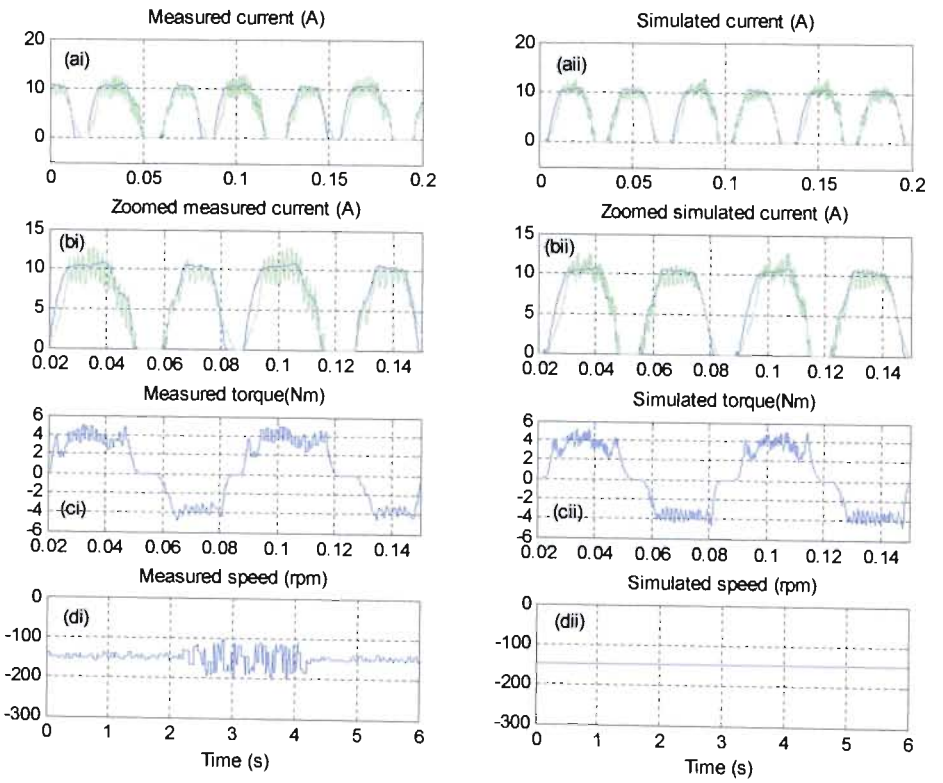

(B)

Fig. 5.37 Measured and simulated results when torque reference is ± 4Nm with constant speed (A) 150rpm and (B) -150rpm

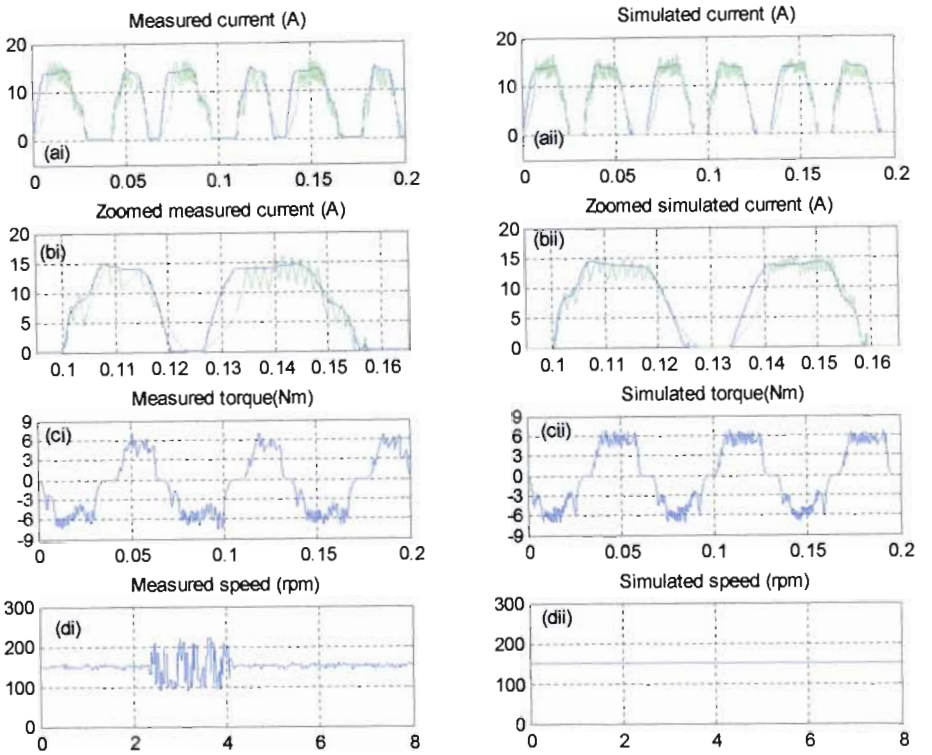

Fig. 5.38 Measured and simulated results when torque reference is ± 6Nm with constant speed 150rpm

Triangle and Sinusoidal Torque Reference

Figs. 5.39 to 5.40 show the current and torque responses to high frequency torque reference pulses. Fig. 5.39 shows the current and torque responses to a ±1Nm, 0.2Hz triangular torque reference waveform. The following observations are made with respect to Fig. 5.39.

- There is reasonably close agreement between all simulated and measured responses, but the measured current and torque ripple are higher due to DSP sample dropping.
- There is very little measured torque ripple in the vicinity of zero crossings due to the absence of current ripple at zero current (as observed in all the simulated and measured torque pulse responses in this thesis).
- Torque ripple increases (due to increased current ripple) with increased current.
- The nonlinear relationship between phase current and torque is evident in the non-triangular envelope of phase current reference pulse magnitudes

Fig. 5.40 shows the current and torque responses to a ±1Nm, 2Hz sinusoidal torque reference waveform. The only significant difference between Figs. 5.39 and 5.40 (apart from the shape of the torque reference waveform) is the number of phase current reference pulses per torque reference cycle.

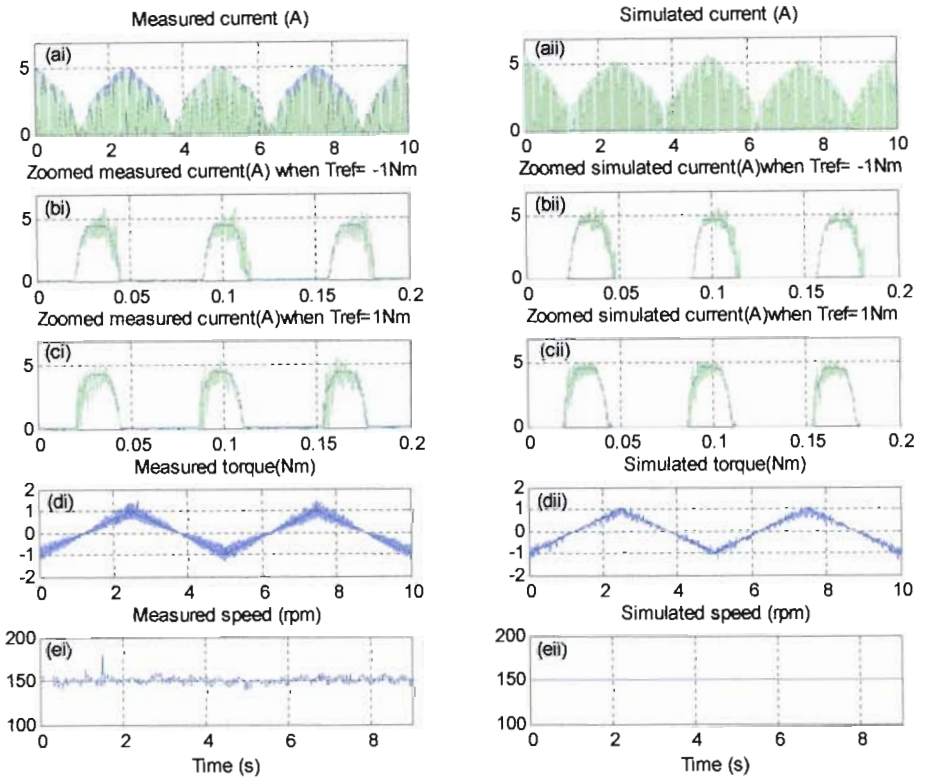

Fig. 5.39 Measured and simulated results when torque reference is triangle ± 1Nm with constant speed 150rpm

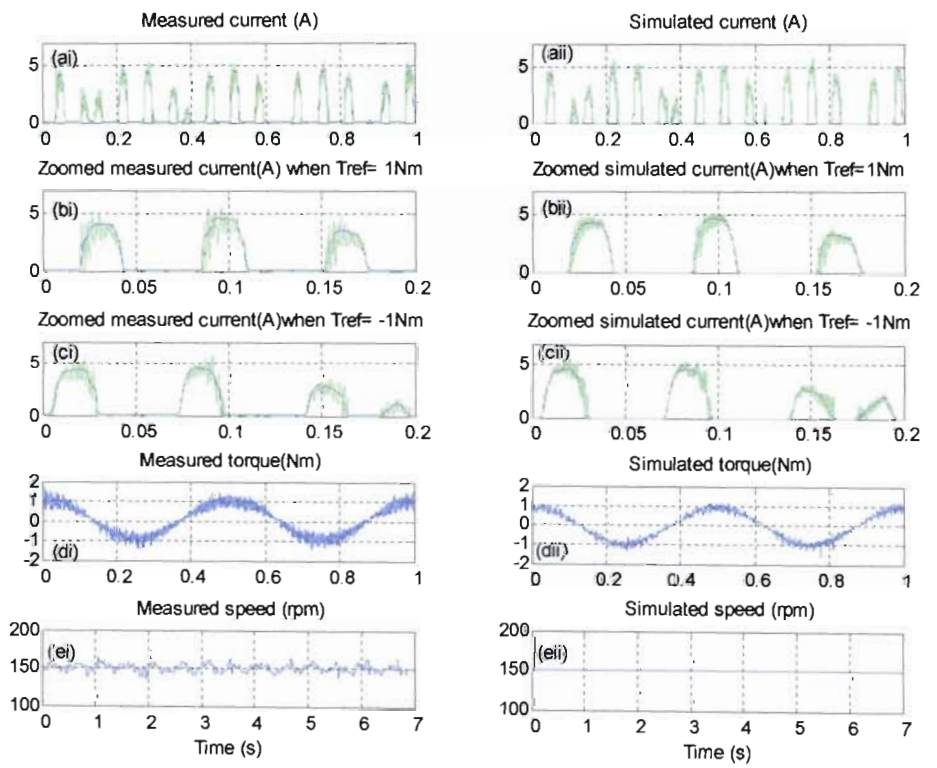

Fig. 5.40 *Measured and simulated results when torque reference is sinusoidal ± 1Nm with constant speed 150rpm*

5.5 Summary

This chapter has presented the hardware setup of a prototype 8/6 four-phase switched reluctance motor drive. This system comprises a TMSF2812 DSP (running real time code developed in the graphical VisSim environment), in-house developed high speed peripheral and I/O interface boards, an 8/6 switched reluctance motor, three three-phase voltage source inverters, four current sensors, a mechanical load (a vector controlled induction motor).

The control performance of the selected TSF torque and hysteresis current control strategy is tested under various locked rotor, motoring and generating conditions. The PSCAD simulation results are compared with the measured results to validate the PSCAD torque and current control strategy models presented in Chapter 4.

Close agreement has been shown between the measured and simulated 8/6 SRM current and torque responses, except for slightly larger ripple in the measured results due to real time pulse dropping in the DSP which had not been resolved at the time of writing this thesis. All of these results show that the selected Torque Sharing Function (TSF) and hysteresis current control strategy performs well under locked rotor and low speed motoring and generating test conditions. The performance at medium and high speeds was seen to be rather limited by the relatively low dc link voltage, which had to be used to limit the relatively large current ripple at the sample rate limitation of 2.5kHz (10kHz should be achievable once outstanding software problems have been resolved with the supplier). This work has focussed on the investigation of transient and steady state torque responses at constant speeds. A detailed study of acceleration effects could form part of future work, once the current ripple has been significantly reduced by increasing the sampling rate or implementing nonlinear/adaptive PWM current control.

The next chapter concludes the main body of this thesis by summarising the main findings and suggestions for future work arising from it.

CHAPTER SIX

CONCLUSION

6.1 General

Switched reluctance motors have been in existence for about as long as induction motors. Their basic principle of operation and physical structure are simple, but they require phase current commutation at precise rotor angles. Their use was fairly limited until the advent of fast and efficient solid state switches, because conventional brush/commutator arrangements (as used in DC machines) cannot be used to vary the commutation angles with speed, as required for efficient torque production. Simple commutation angle adjustment methods are effective in achieving adjustable average torque, but produce levels of torque ripple which are prohibitive in many applications. The relatively low cost, high robustness, and high efficiency of SRMs, therefore continue to drive research into more sophisticated control schemes to minimize torque ripple. To be effective, these schemes must somehow account for the relatively strong nonlinearities due to the doubly salient SRM structure and operation well into magnetic saturation for high power densities. Accurate modeling is therefore an essential tool for the development and optimization of SRM converter topologies and torque ripple minimization strategies.

The main objectives of this thesis are to investigate methods for accurate parameter measurements, modeling, and low ripple torque control of SRMs, and to implement a prototype 8/6 SRM drive. The work performed to achieve these objectives has been presented in Chapters 2 to 5. This chapter presents a summary of the work presented, and conclusions and suggestions for future work made in Chapters 2 to5.

6.2 Switched Reluctance Motor Measurements and Simulation Models

The inductance, flux and torque characteristics of switched reluctance motors are nonlinear, and must usually be numerically determined from real experimental data. Chapter 2 first introduced the fundamental principle of an 8/6 Switched Reluctance Motor and then described the experimental process used to produce a model in Matlab/Simulink for a prototype 8/6 Switched Reluctance Motor, and some methods used to validate this model.

Torque can be measured directly or calculated from measured phase current, rotor position, and numerically determined inductance or indirectly from phase flux. These analytical methods of obtaining torque characteristics were also evaluated by comparison with practical torque measurements, which were also used to determine that the optimal phase winding configuration is inline, not opposing (i.e. common flux).

Chapter 2 also explained how two different lookup tables (for inductance and torque characteristics) were used to simulate the electrical, magnetic and mechanical performance of the motor. Simulation results were shown to closely agree with practical current and rotor position responses under locked and free rotor conditions. It was also explained how the validated simulation models can be used for the torque control design, and importance of power converter topology selection as part of this process.

6.3 Power Converter Strategies for Switched Reluctance Motor

Chapter 3 has explained the principle of operation, and used PSCAD models and simulations to compare the performance of four different SRM power converter topologies under various operating conditions. The AHB converter topology was selected for the experimental work of this thesis due to its relative simplicity with respect to phase commutation and current control, its ability to enable independent phase commutation and current control for torque ripple minimization, and its relatively good phase commutation and current control performance.

It is, however, proposed that future work should aim to minimize the control complexity and exploit the potential advantages of faster independent phase commutation and tighter current control offered by the cost-effective c-dump topology.

Chapter 3 has also presented and validated PSCAD SRM and AHB models by means of locked and free rotor alignment tests, which were then used in Chapter 4 to simulate and analyze two SRM torque control strategies.

6.4 SRM Torque Control

Chapter 4 has introduced the principle of torque control via direct adjustment of commutation angles, and presented PSCAD simulation results which predict relatively high

commutation torque ripple for several combinations of fixed turn-on and turn-off angles for the 8/6 SRM studied in this thesis.

An alternative Torque Sharing Function (TSF) strategy for minimizing commutation torque ripple has also been introduced. The corresponding PSCAD torque control model has been presented and tested under several locked and free rotor conditions, assuming ideal current control. The relatively low torque ripple observed in these results is attributed to small errors in the construction of the lookup table required by this method to transform phase torque references into corresponding phase current references.

A PSCAD model for hysteresis current control with a fixed error sampling rate (and hence upwardly bounded switching frequency) has also been combined with the TSF model, and tested under various operating conditions. It has been shown that this hysteresis current control method requires a relatively high sampling rate in order to produce low current (and hence torque) switching ripple at low speeds, with higher values of dc link voltage. Simulation results predict that this method can produce 8/6 SRM torque responses with low commutation ripple in both motoring and generating modes. However, these results also predict significant hysteresis switching induced current ripple (and hence high frequency torque ripple) at the dc voltage levels required to achieve rated power. It has therefore been suggested that future work investigate PWM current control to reduce voltage switching induced current and torque ripple.

6.5 Practical Implementation

Chapter 5 has presented the hardware setup of a prototype 8/6 four-phase switched reluctance motor drive. This system comprises a TMSF2812 DSP (running real time code developed in the graphical VisSim environment), in-house developed high speed peripheral and I/O interface boards, an 8/6 switched reluctance motor, three three-phase voltage source inverters, four current sensors, a mechanical load (a vector controlled induction motor).

The control performance of the selected TSF torque and hysteresis current control strategy was tested under various locked rotor, motoring and generating conditions. The PSCAD simulation results were compared with the measured results to validate the PSCAD torque and current control strategy models presented in Chapter 4.

Close agreement has been shown between the measured and simulated 8/6 SRM current and torque responses, except for slightly larger ripple in the measured results due to real time pulse dropping in the DSP which had not been resolved at the time of writing this thesis. All of these results show that the selected Torque Sharing Function (TSF) and hysteresis current control strategy perform well under locked rotor and low speed motoring and generating test conditions. The performance at medium and high speeds was seen to be limited by the relatively low dc link voltage, which had to be used to limit the relatively large current ripple at the sample rate limitation of 2.5kHz (10kHz should be achievable once outstanding software problems have been resolved with the supplier). This work has focussed on the investigation of transient and steady state torque responses at constant speeds.

6.6 Suggestions for Further Work

In Chapters 2 to 5, it has been suggested that future work should consider/investigate:

Chapter 2

1. Methods of implementing SRM measurements online, without locking the rotor;
2. A detailed analysis of the assumptions leading to the inductance derived torque curves to determine the causes for their significant deviation from the measured curves and co-energy derived curves (eq. 2.25);
3. A detailed comparison of the simulated and measured results obtained with the co-energy derived torque characteristic, and those obtained using the measured torque characteristic;

Chapter 3

4. The design of an application specific four-phase converter for the 8/6 SRM and optimal use of both hard and soft chopping (and appropriate PWM strategies) to help reduce current and torque ripple;

Chapter 4

5. Possible static and dynamic optimizations of the angles of TSF for the 8/6 four-phase SRM in this thesis;

6. Methods of improving the accuracy of inversion of the $i-\theta-T$ characteristic used in this thesis and possible use of nonlinear interpolation methods;
7. Current loop linearization by a combination of feedforward and feedback compensation of back emf and phase inductance variations;
8. Phase torque tracking error compensating methods to improve torque sharing function control performance;
9. Incorporating mutual inductance effects into TSFs;
10. Solutions for significantly higher turn on-lag in generating mode than the turn-off lag (tail) in motoring mode (such as C-dump action and/or TSF adaptation);
11. PWM current control to enable high dc link voltage operation without excessive current ripple;

Chapter 5

12. Torque regulation performance (e.g. constant torque reference "tracking" with square/ triangle/sinusoidal speed variations) and optimizations;
13. Methods of increasing the sampling frequency (e.g. to 10 KHz) once the "local" sampling rate assignment and pulse dropping problems have been resolved by the DSP software/hardware suppliers;
14. Avoiding the anomalies discovered in popular TSF published for 8/6 SRMs,;
15. Direct (non-locked rotor) torque deduction based on the mechanical parameters of the test rig and online measurements from the induction motor load drive and torque transducer;
16. C-dump converter topologies and/or adaptive/nonlinear PWM current control to achieve low current ripple with higher dc link voltage to minimize the angle dependence of the current and torque step response in motoring and generating modes.

APPENDIX A

8/6 SRM Data and Matlab Code/Models

Table A.1 summarizes the Matlab code used for the 8/6 SRM parameter measurements. These include phase flux, phase inductance and phase torque, as used in the Simulink models for the locked rotor and free rotor alignment tests presented in Chapter 2.

Section	Name	Content Description
A.1	Parameter_ Measurements.m	Measuring 8/6 SRM parameters
A.2	Smoothing_T_L_from_inductance.m	Get the torque from inductance $T(\theta,i)=\frac{1}{2}i^2\frac{dL(\theta,i)}{d\theta}$
A.3	Smoothing_T_L_from_flux.m	Get the torque from flux $T(\theta,i)=\frac{\partial}{\partial\theta}\int\lambda(\theta,i)di$
A.4	Comparing_torque_thesis.m	Plotting the torque results obtained from inductance, flux and direct measurements by transducer
A.5	For_simulink.m	Store the torque characteristic as the lookup table for Simulink model
A.6	freeRotorData.m	Load the measured phase voltage, current and rotor angle tables for free rotor alignment test
A.7	Four_phase_cur_source_trans.m	Plotting of the four phase torque results in section 2.7

Table A.1 Matlab program name and the function description

A.1 Parameter_ Measurements.m

```
%Main program to get 8/6 SRM parameters: Inductance, Torque

clear;clc;close all

%Get the initial value of phase current and phase voltage from static test
by locking rotor at angles from 0 degree (aligned position) to 30
degree(unaligned position)

t=load('oppt.txt');
istore=load('oppI.txt');
istore=(istore-0.0137).*10;
```

```
ustore=load('oppV.txt');ustore=ustore+0.0366;
leng=1500;

for th=0:1:30

first=leng*th+1;
second=first+leng-1;


current(th+1).vector=istore(first:second);
voltage(th+1).vector=ustore(first:second);

%plot phase current and voltage at locked rotor position from 0 to 30 degree
figure(1)
plot(t,current(th+1).vector);grid on;hold on;
figure(2)
plot(t,voltage(th+1).vector);grid on;hold on;
end

for th=0:1:30

A(th+1).item=(current(th+1).vector(1:leng-
1)+current(th+1).vector(2:leng)).*0.00005/2;
JI(th+1).item=cumsum(A(th+1).item);

B(th+1).item=(voltage(th+1).vector(1:leng-
1)+voltage(th+1).vector(2:leng)).*0.00005/2;
JU(th+1).item=cumsum(B(th+1).item);


voltagemean(th+1)=mean(voltage(th+1).vector(1350:leng));
currentmean(th+1)=mean(current(th+1).vector(1350:leng));
R(th+1)=voltagemean(th+1)/currentmean(th+1);

end


Resistance=0.3312; %phase resistance
for th=0:1:30

Flux(th+1).item=JU(th+1).item-(JI(th+1).item.*Resistance);

%disp(th,Flux(th+1).item)
figure(3)
plot(current(th+1).vector(1:leng-1),Flux(th+1).item,'r','LineWidth',2);grid
on;hold on;

%calculate the phase Inductance from equation L=Flux/current
L(th+1).item=Flux(th+1).item./current(th+1).vector(1:leng-1);
B(th+1).item=L(th+1).item;

figure(4)
plot(current(1).vector(50:leng-1),B(th+1).item(50:leng-1));hold on;grid;

%plot rough inductance
 end

%Because of the inductance is so rough that it needs to be smoothed
%smoothing the inductance from angle dimension

for th=0:1:30

Bx(th+1).ITEM=current(th+1).vector(1:leng-1);
By(th+1).ITEM=B(th+1).item;
Bxx=[0.5,1:18];
```

```
dBx(th+1).ITEM=Bx(th+1).ITEM(2:leng-1)-Bx(th+1).ITEM(1:leng-2);
a=find(dBx(th+1).ITEM==0);
Bx_clean(th+1).ITEM=Bx(th+1).ITEM; Bx_clean(th+1).ITEM(a)=[];
By_clean(th+1).ITEM=By(th+1).ITEM; By_clean(th+1).ITEM(a)=[];

ren=[];b=length(Bx_clean(th+1).ITEM);

for i=1:b
   a=find(Bx_clean(th+1).ITEM==Bx_clean(th+1).ITEM(i));
   a(find(a==i))=[];
   ren=[ren,a'];
end

Bx_clean(th+1).ITEM(ren)=[];
By_clean(th+1).ITEM(ren)=[];

poss=find(By_clean(th+1).ITEM==max(By_clean(th+1).ITEM));
By_clean(th+1).ITEM(1:poss)=max(By_clean(th+1).ITEM);

end

%delete some no meaning value of rough inductance
By_clean(9).ITEM(1)=By_clean(9).ITEM(2);
By_clean(14).ITEM(1)=By_clean(14).ITEM(2);
By_clean(15).ITEM(1)=By_clean(15).ITEM(2);
By_clean(16).ITEM(1)=By_clean(16).ITEM(2);

for th=0:1:30

Byy(th+1).ITEM=spline(Bx_clean(th+1).ITEM,By_clean(th+1).ITEM,Bxx);
bYY(th+1).ITEM(19:-1:1)=sort(Byy(th+1).ITEM);

figure(6)
plot(Bxx,bYY(th+1).ITEM);hold on;grid;
Title('newe inductnace');grid on;

%here the L is the New Inductance after spline function of rough inductance
L(th+1).item=bYY(th+1).ITEM;

end


for th=0:1:30

%pos=find(L(th+1).item==max(L(th+1).item));
% L(th+1).item(1:pos)=max(L(th+1).item);
F(th+1).vector=Flux(th+1).item;
LL(th+1).vector=L(th+1).item;
end


% for easy plotting of two dimension of inductance
theta=0:1:30;
cur=0:1:18;
Ivec=linspace(0,18,19);


for j=0:1:30
   for   i=0:1:18
      temp(j+1,i+1)=LL(j+1).vector(i+1);
    end
 end
q=temp';
```

```
%smoothing the inductance from current dimension
for i=0:1:18
lcur(i+1).item=q(i+1,:);
pos=find(lcur(i+1).item==max(lcur(i+1).item));
lcur(i+1).item(1:pos)=max(lcur(i+1).item);
end

for i=0:1:18

figure(8)
plot(theta,lcur(i+1).item);hold on;grid on;

FL030(i+1).item=lcur(i+1).item*i;
FL060(i+1).item=[FL030(i+1).item(31:-1:2),FL030(i+1).item];

figure(1999)
plot(theta,FL030(i+1).item);hold on;grid on;%plot rough flux

figure(2999)
plot([0:60],FL060(i+1).item);hold on;grid on;
end

% for easy plotting of two dimension of inductance

for i=0:1:18
   for j=0:1:30
      tem(i+1,j+1)=lcur(i+1).item(j+1);
  end
end
qq=tem;


% calculating the Torque from inductance
 %-grad1=dl/dtheta; derivative of inductance in respect to theta
for i=0:1:18
grad(i+1).item=gradient(qq(i+1,1:31),theta).*360/2/pi;
end

 for i=0:1:18
   for j=0:1:30
      dldtheta(i+1,j+1)=grad(i+1).item(j+1);
      Torque(i+1,j+1)=(i+1)^2/2.*dldtheta(i+1,j+1);%Torque from inductance
   end
end


%plot torque derived from inductance
for i=0:1:18
figure(9)
plot(theta(1:31),Torque(i+1,:));
H=TITLE('the Torque with different angle');grid on;hold on;
end


%Calculate Torque Using T=d(integrator(Flux)/dtheta;

for th=0:1:30
    m(th+1).item=current(th+1).vector(2:leng-1)-current(th+1).vector(1:leng-
2);
    fi(th+1).item=(Flux(th+1).item(1:leng-2)+Flux(th+1).item(2:leng-
1)).*m(th+1).item/2;
    Jfi(th+1).item=cumsum(fi(th+1).item);%W=integral(flux*i)
end
```

```
theta=0:1:30; CUR=0:1:18;

%Smoothing Jfi
for th=0:1:30
Fx(th+1).ITEM=current(th+1).vector(1:leng-2);%current
Fy(th+1).ITEM=Jfi(th+1).item;  %W
Fxx=[0.5,1:18];

dFx(th+1).ITEM=Fx(th+1).ITEM(2:leng-2)-Fx(th+1).ITEM(1:leng-3);
a=find(dFx(th+1).ITEM==0);
Fx_clean(th+1).ITEM=Fx(th+1).ITEM; Fx_clean(th+1).ITEM(a)=[];
Fy_clean(th+1).ITEM=Fy(th+1).ITEM; Fy_clean(th+1).ITEM(a)=[];

b=length(Fx_clean(th+1).ITEM);
ren=[];

for i=1:b
   a=find(Fx_clean(th+1).ITEM==Fx_clean(th+1).ITEM(i));
   a(find(a==i))=[];
   ren=[ren,a'];
end

Fx_clean(th+1).ITEM(ren)=[];
Fy_clean(th+1).ITEM(ren)=[];

Fyy(th+1).ITEM=spline(Fx_clean(th+1).ITEM,Fy_clean(th+1).ITEM,Fxx);
FYY(th+1).ITEM(1:1:19)=sort(Fyy(th+1).ITEM);

%plot Flux
figure(555)
plot(Fx_clean(th+1).ITEM,Fy_clean(th+1).ITEM,Fxx,FYY(th+1).ITEM,'ro');hold
on;grid;
figure(556)
plot(Fxx,FYY(th+1).ITEM);hold on;grid;
end


for the=0:1:30
for cur=0:1:18
 INT(the+1,cur+1)=FYY(the+1).ITEM(cur+1);%save Flux as INT variable
end
end

%Calculating the Torque from phase Flux
for cur=0:1:18
T_Flux(cur+1).item=gradient(INT(:,cur+1),theta*pi/180);

figure(2001)
plot(theta,T_Flux(cur+1).item,'b');grid on;hold on;
%plot torque derived from flux
end

%plot torque derived from flux at rotor angle range from 0 to 60 degree
for cur=18:-1:0
T_F(cur+1).item=[T_Flux(cur+1).item',-T_Flux(cur+1).item(30:-1:1)'];
figure(2011)
plot([0:60],T_F(cur+1).item,'b');grid on;hold on;
end

% phase voltage and current with rotor locked at 5 degree
%VV=voltage(6).vector;TT=t;II=current(6).vector;
%global VV
%global TT II
```

A.2 Smoothing_T_L_from_inductance.m

```
% second Program to get smoothed phase inductance and smoothed phase torque
derived from inductance
 %smoothing inductance once more

for i=18:-1:0
bbL(i+1).item=lcur(i+1).item;
Th(i+1).item=0:30;
figure(10)
plot(Th(i+1).item,bbL(i+1).item,Th(i+1).item,bbL(i+1).item,'ro');grid
on;hold on;

%Q is used for the position which is not good data for the Inductance and
the data should be deleted for the purpose of smoothing

 Q(19).item=[ ]; Q(18).item=[ ]; Q(17).item=[ ]; Q(16).item=[ ];
 Q(15).item=[ ]; Q(14).item=[ ]; Q(13).item=[ ]; Q(12).item=[ ];
 Q(11).item=[ ]; Q(10).item=[ 21]; Q(9).item=[21]; Q(8).item=[3 5 6 9 17];
 Q(7).item=[[3 5 16 17 18]]; Q(6).item=[13 18]; Q(5).item=[3 12 13];
 Q(4).item=[5 14 18 21]; Q(2).item=[3 12];

Th(i+1).item(Q(i+1).item)=[];
bbL(i+1).item(Q(i+1).item)=[];

x(i+1).item=0:30;
y(i+1).item=spline(Th(i+1).item,bbL(i+1).item,x(i+1).item);

%plot phase inductance which is the final phase inductance variable
figure(121)
plot(x(i+1).item,y(i+1).item);hold on;grid on;
figure(13)
plot((-30:1:0),y(i+1).item(31:-1:1),x(i+1).item,y(i+1).item);hold on;grid
on;

end

% saves inductance as two dimension variable
for mm=0:1:18
    for nn=0:30
   NEWL(mm+1,nn+1)=y(mm+1).item(nn+1);
  end
end

L060=[NEWL NEWL(:,30:-1:1)]';

global NEWL L060

%plot the phase flux from inductance
for hh=0:1:18

figure (14)
plot([0:30],NEWL(hh+1,:));grid on;hold on;%inductance
figure (15)
plot([0:30],NEWL(hh+1,:).*hh);grid on;hold on;%FLUX%
figure(16)
plot([-30:30],[fliplr(NEWL(hh+1,1:30).*hh),NEWL(hh+1,:).*hh]);grid on;hold
on;%FLUX%
FLUX_model3030(hh+1,1:61)=[fliplr(NEWL(hh+1,1:30).*hh),NEWL(hh+1,:).*hh];%-
30 to 30 degree
FLUX_model060(hh+1,1:61)=[NEWL(hh+1,:).*hh,fliplr(NEWL(hh+1,1:30).*hh)]; %0
to 60 degree
figure(500)
plot([0:60],FLUX_model060(hh+1,1:61));grid on;hold on;%FLUX%
```

```
end

% save flux as two dimension variable
for i=1:19
    for j=1:61
        Flux_th_i(i,j)=FLUX_model060(i,j);
    end
end

% get derivatie of DfluxDth;
theta=0:1:60;
for i=1:19
DFlux_th(i).item=gradient(Flux_th_i(i,:),theta*pi/180);
end

for i=1:19
    for j=1:61
       Dflux_th_i(i,j)=DFlux_th(i).item(j);
    end
end


%smoothing the phase torque derived from phase inductance
for i=18:-1:0
xa(i+1).item=0:30;
ya(i+1).item=spline(Th(i+1).item,bbL(i+1).item,xa(i+1).item);
xb(i+1).item=(0:30)+.01;
yb(i+1).item=spline(Th(i+1).item,bbL(i+1).item,xb(i+1).item);
dy(i+1).item=yb(i+1).item-ya(i+1).item;
% Tsen is calculating the torque derived from inductance
Tsen(i+1).item=0.5*i^2*dy(i+1).item/(.01*pi/180);

%plot the torque before smoothing
figure(517)
plot(xa(i+1).item,Tsen(i+1).item);grid on;hold on;

for j=0:30
    T_ind_be(i+1,j+1)=Tsen(i+1).item(j+1);
end
%P is used for the position which are not good data for the torque and
% the data should be deleted for the purpose of smoothing
P(19).item=[3 6:9 11 12 14 15 17 19 20 31];
P(18).item=[3 6:9 11 12 14 15 17 19 20 31];
P(17).item=[3 6:9 11 12 14 15 17 19 20 31];
P(16).item=[3 6:9 11 12 14 15 17 19 20 31];
P(15).item=[3 6:9 11 12 14 15 17 19 20 31];
P(14).item=[3 6:9 11 12 14 15 17 19 20 31];
P(13).item=[2 6 7 8 10 11 12 14 15 17 19 20 22];
P(12).item=[2 6:8 10:12 14 15 17 19:22 31];
P(11).item=[2 6:8 10:12 14 15 17 19:22 31];
P(10).item=[2 6:8 10:12 14 15 16 17 20 22 23 31];
P(9).item=[2 6:8 10:12 14 15 17 19 20 22 23 31];
P(8).item=[6 7 9 10 12 13:17 18 19 21];
P(7).item=[1:3 5 7 8 10:20];
P(6).item=[1 3 5:8 10:12 14 15 17:19 22 23];
P(5).item=[1 3 4 5 6 7 9 10 12 13 15 16 17 19 20 22 23];
P(4).item=[1 3:6 9 10 11 13:22];
P(3).item=[1 2 4 5 7 9 10 12:14 16:20 22 ];
P(2).item=[1 3:7 9 10 12:20 ];

Tsen(i+1).item(1)=0;
Tsen(i+1).item(31)=0;

xa(i+1).item(P(i+1).item)=[];
```

```
Tsen(i+1).item(P(i+1).item)=[];

figure(518)
plot(xa(i+1).item,Tsen(i+1).item,xa(i+1).item,Tsen(i+1).item,'ro');grid
on;hold on;
 Th(i+1).item=0:1:30;
TSE(i+1).item=spline(xa(i+1).item,Tsen(i+1).item,Th(i+1).item);
TSE(i+1).item(2)=-0.1;TSE(i+1).item(31)=0; TSE(i+1).item(1)=0;
TSE(3).item(2)=-0.04;TSE(2).item(2)=-0.01;

figure(519)
plot(Th(i+1).item,TSE(i+1).item,Th(i+1).item,TSE(i+1).item,'ro');grid
on;hold on;

for j=0:30
    T_ind_af(i+1,j+1)=TSE(i+1).item(j+1);
end

T3060(i+1).item=-TSE(i+1).item;
T060(i+1).item=[TSE(i+1).item,T3060(i+1).item(30:-1:1)];

%plot the torque after smoothing
figure(520)
plot([0:60],T060(i+1).item);grid on;hold on;

T3030(i+1).item=[-TSE(i+1).item(31:-1:2),TSE(i+1).item];
figure(530)
plot([-30:1:30],T3030(i+1).item);hold on;grid on;
end
```

A.3 Smoothing_T_L_from_flux.m

```
% Third Program to get smoothed phase torque derived from flux


%smoothing the phase torque derived from phase flux
for i=18:-1:0
xa(i+1).item=0:30;


Tsen(i+1).item=T_Flux(i+1).item;

%plot the torque before smoothing
figure(617)
plot(xa(i+1).item,Tsen(i+1).item,xa(i+1).item,Tsen(i+1).item,'ro');grid
on;hold on;

T_sen060(i+1).item=[Tsen(i+1).item',-Tsen(i+1).item(30:-1:1)'];
%plot the torque after smoothing
figure(627)
plot([0:60],T_sen060(i+1).item,'b');grid on;hold on;
for j=0:30
    T_flux_be(i+1,j+1)=Tsen(i+1).item(j+1);
end
%P is used for the position which are not good data for the torque and
% the data should be deleted for the purpose of smoothing
P(19).item=[];
P(18).item=[];
P(17).item=[];
P(16).item=[];
P(15).item=[];
P(14).item=[];
```

```
P(13).item=[];
P(12).item=[];
P(11).item=[];
P(10).item=[];
P(9).item=[];
P(8).item=[];
P(7).item=[];
P(6).item=[];
P(5).item=[];
P(4).item=[];
P(3).item=[ ];
P(2).item=[ ];

Tsen(i+1).item(1)=0;
Tsen(i+1).item(31)=0;

xa(i+1).item(P(i+1).item)=[];
Tsen(i+1).item(P(i+1).item)=[];

figure(618)
plot(xa(i+1).item,Tsen(i+1).item,xa(i+1).item,Tsen(i+1).item,'ro');grid
on;hold on;

Th(i+1).item=0:1:30;
TSE(i+1).item=spline(xa(i+1).item,Tsen(i+1).item,Th(i+1).item);
TSE(i+1).item(2)=-0.1;TSE(i+1).item(31)=0; TSE(i+1).item(1)=0;
TSE(3).item(2)=-0.04;TSE(2).item(2)=-0.01;

figure(619)
plot(Th(i+1).item,TSE(i+1).item,Th(i+1).item,TSE(i+1).item,'ro');grid
on;hold on;

T3060(i+1).item=-TSE(i+1).item;
T060(i+1).item=[TSE(i+1).item,T3060(i+1).item(30:-1:1)];

%plot the torque after smoothing
figure(620)
plot([0:60],T060(i+1).item);grid on;hold on;

end
% Third Program get smoothed phase torque derived from flux
for i=18:-1:0
xa(i+1).item=0:30;


Tsen(i+1).item=T_Flux(i+1).item;

%plot the torque before smoothing
figure(717)
plot(xa(i+1).item,Tsen(i+1).item,xa(i+1).item,Tsen(i+1).item,'ro');grid
on;hold on;


%P is used for the position which are not good data for the torque and
% the data should be deleted for the purpose of smoothing
P(19).item=[4 5 9 10 13 16 18:20];
P(18).item=[4 5 9 10 13 16 18:20];
P(17).item=[4 5 9 10 13 16 18:20];
P(16).item=[4 5 9 10 13 16 18:20];
P(15).item=[4 5 9 10 13 16 18:20];
P(14).item=[4 5 9 10 13 16 18:20];
P(13).item=[4 5 9 10 13 16 18:20];
P(12).item=[4 5 9 10 13 16 18:20];
P(11).item=[4 5 9 10 13 16 18:20];
P(10).item=[4 5 9 10 13 16 18:20];
```

```
P(9).item=[4 5 9 10 13 16 18:20];
P(8).item=[4 5 9 10 13 16 18:20];
P(7).item=[4 5 9 10 13 16 18:20];
P(6).item=[4 5 9 10 13 16 18:20];
P(5).item=[4 5 9 10 13 16 18:20];
P(4).item=[4 5 9 10 13 16 18:20];
P(3).item=[ 4 5 9 10 13 16 18:20];
P(2).item=[ 4 5 9 10 13 16 18:20];

Tsen(i+1).item(1)=0;
Tsen(i+1).item(31)=0;

xa(i+1).item(P(i+1).item)=[];
Tsen(i+1).item(P(i+1).item)=[];

figure(718)
plot(xa(i+1).item,Tsen(i+1).item,xa(i+1).item,Tsen(i+1).item,'ro');grid
on;hold on;

Th(i+1).item=0:1:30;
TSE(i+1).item=spline(xa(i+1).item,Tsen(i+1).item,Th(i+1).item);
%TSE(i+1).item(2)=-0.1;
TSE(i+1).item(31)=0; TSE(i+1).item(1)=0;

figure(719)
plot(Th(i+1).item,TSE(i+1).item,Th(i+1).item,TSE(i+1).item,'ro');grid
on;hold on;

for j=0:30
    T_flux_af(i+1,j+1)=TSE(i+1).item(j+1);
end
T3060(i+1).item=-TSE(i+1).item;
T060(i+1).item=[TSE(i+1).item,T3060(i+1).item(30:-1:1)];

%plot the torque after smoothing
figure(720)
plot([0:60],T060(i+1).item);grid on;hold on;

T3030(i+1).item=[-TSE(i+1).item(31:-1:2),TSE(i+1).item];
figure(730)
plot([-30:1:30],T3030(i+1).item);hold on;grid on;
end
```

A.4 Comparing_torque_thesis.m

```
%  this program is for plotting the torque curves from different approaches
%  and compare them  with each other
load T_ind_be.mat
load T_ind_af.mat
load T_transducer.mat
load T_flux_be.mat
load T_flux_af.mat
load T_transducer0.mat
%plot Torque from inductance before smoothing and after smoothing
figure(800)
for i=0:18
        Tor_ind_be(i+1).item=T_ind_be(i+1,:);
        Tor_ind_af(i+1).item=T_ind_af(i+1,:);

plot([0:30],Tor_ind_be(i+1).item,'b',[0:30],Tor_ind_af(i+1).item,'r','LineWi
dth',2);grid on;
```

```
        hold on;
end

%plot Torque from inductance after smoothing and transducer
figure(801)
for i=0:1:18;
    T_transducer(1,1:31)=0;
theta=[0:30];
plot([0:30],Tor_ind_af(i+1).item,'b',theta,T_transducer(i+1,1:31),'r','LineW
idth',2);grid on;hold on;

end

%plot Torque from flux before smoothing and after smoothing
figure(802)
for i=0:18
        Tor_flux_be(i+1).item=T_flux_be(i+1,:);
        Tor_flux_af(i+1).item=T_flux_af(i+1,:);

plot([0:30],Tor_flux_be(i+1).item,'b',[0:30],Tor_flux_af(i+1).item,'r','Line
Width',2);grid on;
        hold on;
end

%plot Torque from flux after smoothing and transducer
figure(803)
for i=0:1:18;
    T_transducer(1,1:31)=0;
    TSE(i+1).item=T_transducer0(i+1,:);
theta=[0:30];
plot([0:30],Tor_flux_af(i+1).item,'b',theta,T_transducer(i+1,1:31),'r','Line
Width',2);grid on;hold on;
end
```

A.5 For_simulink.m

```
load T_ind_be.mat
load T_ind_af.mat
load T_transducer.mat
load T_flux_be.mat
load T_flux_af.mat
% For the purpose of lookup table in simulink
% Torque frm inductance
for i=0:1:18
for j=0:1:30
         OO(i+1,j+1)= Tor_ind_af(i+1).item(j+1);
    end
end

OOO=[-fliplr(OO(:,2:31)),OO];
OOOO=[OO,-fliplr(OO(:,1:30))];

%plot the Torque
 %figure(21);
 %mesh([0:30],[0:18],OO);grid on;
% figure(22)
% mesh([-30:30],[0:18],OOO);grid on;Title('Torque for 0---30  postion and 0-
17A current')
% figure(23)
%mesh([0:60],[0:18],OOOO);grid on;Title('Torque for 0--60  postion and 0-17A
current')
```

```
% Torque from flux

for i=0:1:18
for j=0:1:30
          FF(i+1,j+1)= Tor_flux_af(i+1).item(j+1);
    end
end

FFF=[-fliplr(FF(:,2:31)),FF];
FFFF=[FF,-fliplr(FF(:,1:30))];

% Torque from transducer


for i=0:1:18
    for j=0:1:30
        DD(i+1,j+1)=T_transducer(i+1,j+1);
    end
end

DDD=[-fliplr(DD(:,2:31)),DD];
DDDD=[DD,-fliplr(DD(:,1:30))];
for i=0:1:18
    figure(1000)
    plot([-30:30],DDDD(i+1,:));grid on;hold on;
end
```

A.6 freeRotorData.m

```
% loading the measurements results for free rotor alignment test

load July5Vp0to15.dat
 V015=July5Vp0to15(:,2);

t015=July5Vp0to15(:,1);

figure(1)
plot(t015,V015);
 load July5I0to15.dat
 I015=July5I0to15(:,2);

 %rotor angle is not right because of two oscillocope catching
 %load July5th0to15.dat
 %th015=July5th0to15(:,2);

 load July20th0to15.dat
 t2=July20th0to15(:,1);
th2015=July20th0to15(:,2);
figure(3)
plot(t2,th2015);hold on;grid on;
th3015=spline(t2,th2015,t015);
 figure(2)
plot(t015,I015);hold on;grid on;
```

A.7 Four_phase_cur_source_trans.m

```
% for plotting the torque characteristics of four phases in Matlab
% the torque characteristic for one phase is using the torque transducer
% measured result
% need to run 'Comparing_torque_thesis.m' first

close all

%--------------------------used for plot 4 phases torque
%
plot([0:60],T060(i+1).item,[60:120],T060(i+1).item,[120:180],T060(i+1).item,
[180:240],T060(i+1).item,[240:300],T060(i+1).item,[300:360],T060(i+1).item);
 % grid on;Title('one phase for SRM 8/6 current=19A Torque curve theta=0--
360');hold on;

  for i=18:-1:0

 T015=TSE(i+1).item(1:16);T030(i+1).item=TSE(i+1).item(1:31);
 T060(i+1).item=TSE(i+1).item;
 T0120(i+1).item=[T060(i+1).item,T060(i+1).item(2:61)];
 T0240(i+1).item=[T0120(i+1).item,T0120(i+1).item(2:121)];
 T0360(i+1).item=[T0240(i+1).item,T0120(i+1).item(2:121)];

 figure(101)
 subplot(611)
 plot([0:360],T0360(19).item);grid on;hold on;


 subplot(612);
 Tb015(i+1).item=T060(i+1).item(46:61);
 Tb0360(i+1).item=[Tb015(i+1).item,T0360(i+1).item(2:346)];
 plot([0:360],Tb0360(19).item);grid on;hold on;

subplot(613)
Tc030(i+1).item=T060(i+1).item(31:61);
Tc0360(i+1).item=[Tc030(i+1).item,T0360(i+1).item(2:331)];
 plot([0:360],Tc0360(19).item);grid on;hold on;

subplot(614)

Td030(i+1).item=T060(i+1).item(16:61);
Td0360(i+1).item=[Td030(i+1).item,T0360(i+1).item(2:316)];
 plot([0:360],Td0360(19).item);grid on;hold on;

jjj=[0:360];
Tall0360(i+1).item=T0360(i+1).item+Tb0360(i+1).item;Tall2(i+1).item=T0360(i+
1).item+Tc0360(i+1).item;Tall3(i+1).item=T0360(i+1).item+Td0360(i+1).item;
Tall4(i+1).item=Tb0360(i+1).item+Tc0360(i+1).item;Tall5(i+1).item=Tb0360(i+1
).item+Td0360(i+1).item;Tall6(i+1).item=Td0360(i+1).item+Tc0360(i+1).item;

subplot(615)
plot(jjj,Tall0360(19).item,jjj,Tall2(19).item,jjj,Tall3(19).item,jjj,Tall4(1
9).item,jjj,Tall5(19).item,jjj,Tall6(19).item);grid on;hold on;

subplot(616)
plot(jjj,Tall0360(i+1).item,jjj,Tall2(i+1).item,jjj,Tall3(i+1).item,jjj,Tall
4(i+1).item,jjj,Tall5(i+1).item,jjj,Tall6(i+1).item);grid on;hold on;
end

for i=18:-1:0

 figure (102)
```

```
TT0360(18).item=T0360(18).item+Tb0360(18).item+Tc0360(18).item+Td0360(18).it
em;
plot(jjj,TT0360(18).item);grid on;

figure(103)
f=T0360(18).item(46:61);e=T0360(18).item(46:60);
Tcom0360(18).item=[e,e,e,e,e,e,e,e,e,e,e,e,e,e,e,e,e,e,e,e,e,e,e,e,e,e,e];
plot([1:360],Tcom0360(18).item);grid on;hold on;

figure(104)
 subplot(511)
 plot([0:360],T0360(i+1).item);grid on;hold on;
 subplot(512)
 plot([0:360],Tb0360(i+1).item);grid on;hold on;
subplot(513)
plot([0:360],Tc0360(i+1).item);grid on;hold on;
subplot(514)
plot([0:360],Td0360(i+1).item);grid on;hold on;
subplot(515)
plot(jjj,Tall0360(18).item,jjj,Tall2(18).item,jjj,Tall3(18).item,jjj,Tall4(1
8).item,jjj,Tall5(18).item,jjj,Tall6(18).item);grid on;hold on;
%subplot(616)
%plot(jjj,Tall0360(i+1).item,jjj,Tall2(i+1).item,jjj,Tall3(i+1).item,jjj,Tal
l4(i+1).item,jjj,Tall5(i+1).item,jjj,Tall6(i+1).item);grid on;hold on;

  figure(105)
plot([0:360],T0360(i+1).item);grid on;hold on;


figure(106)
jjjj=[0:60];
plot(jjjj,Tall0360(i+1).item(1:61),jjjj,Tall2(i+1).item(1:61),jjjj,Tall3(i+1
).item(1:61),jjjj,Tall4(i+1).item(1:61),jjjj,Tall5(i+1).item(1:61),jjjj,Tall
6(i+1).item(1:61));grid on;hold on;


figure(107)
subplot(211)
plot(jjj,Tall0360(18).item,jjj,Tall2(18).item,jjj,Tall3(18).item,jjj,Tall4(1
8).item,jjj,Tall5(18).item,jjj,Tall6(18).item);grid on;hold on;
subplot(212)
plot(jjj,Tall0360(18).item,jjj,Tall2(18).item,jjj,Tall3(18).item,jjj,Tall4(1
8).item,jjj,Tall5(18).item,jjj,Tall6(18).item);grid on;hold on;

figure(108)
plot(jjj,Tall0360(i+1).item,jjj,Tall2(i+1).item,jjj,Tall3(i+1).item,jjj,Tall
4(i+1).item,jjj,Tall5(i+1).item,jjj,Tall6(i+1).item);grid on;hold on;
plot(8.435,'r--');

end
```

APPENDIX B

Power Converter Details and Lookup Tables

This appendix presents technical details and data (as summarized in Table B.1) relating to the AHB soft and hard chopping control circuit and the lookup tables used with the PSCAD SRM model in Chapter 3

Section	Name	Content Description
B.1	AHB Soft and Hard Chopping Control Circuit	AHB Hysteresis control, hard and soft chopping control circuit
B.2	Parameter lookup tables used in PSCAD	Torque and phase inductance look up tables used in PSCAD simulation models
B.3	Power Converter Measurements	IGBT and Diode measurements of the real converters for the purpose of simulation model of power components in PSCAD

Table B.1 Appendix B contents

B.1. AHB Soft and Hard Chopping Control Circuit

Hysteresis current control circuit

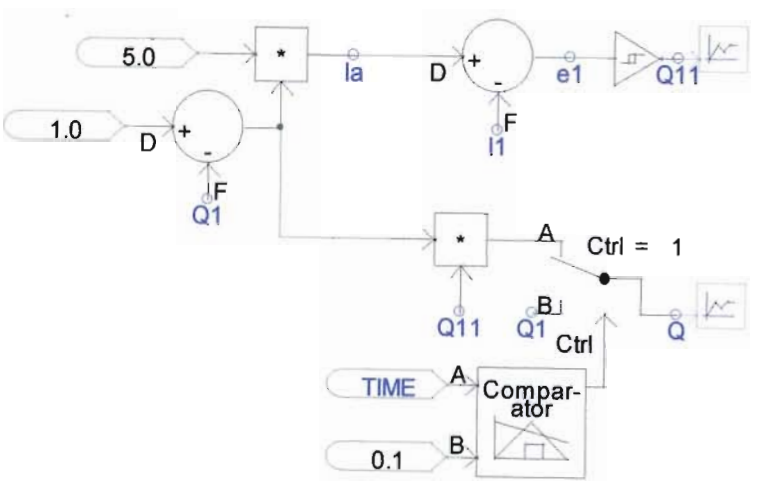

Fig.B.1 Hysteresis current control circuit

Soft chopping current control circuit

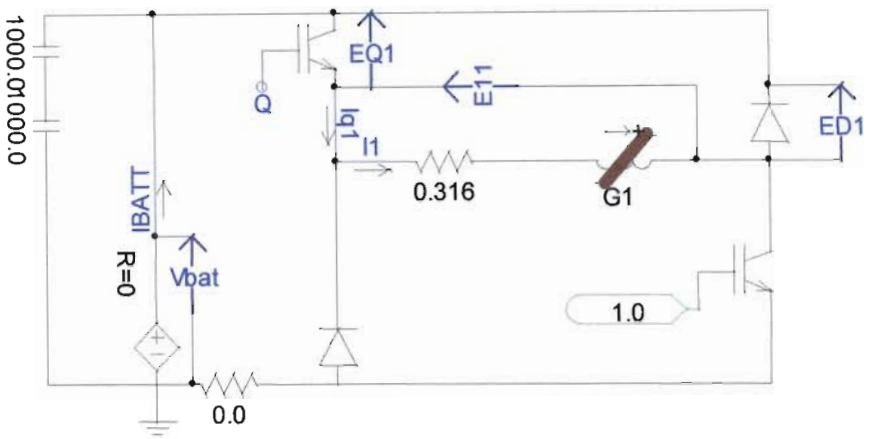

Fig.B.2 Soft chopping current control circuit

Hard chopping current control circuit

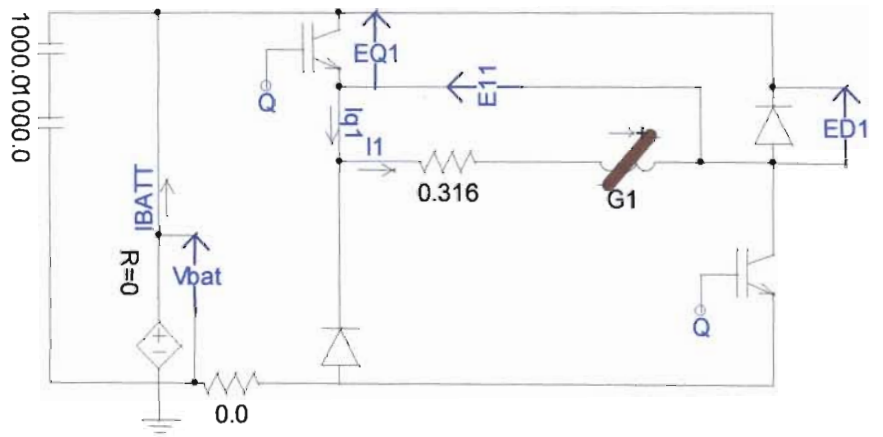

Fig.B.3 Hard chopping current control circuit

B.2 Parameter Lookup Tables Used in PSCAD

Inductance lookup tables

Inductance (i=0:18A, theta= 0° *to* 60°) lookup table L60.dat is shown as follows.

L060 =

Columns 1 through 7

0.0049	0.0050	0.0050	0.0051	0.0054	0.0057	0.0063
0.0049	0.0050	0.0050	0.0051	0.0054	0.0057	0.0063
0.0049	0.0050	0.0050	0.0051	0.0054	0.0057	0.0063
0.0049	0.0049	0.0050	0.0051	0.0053	0.0057	0.0063
0.0049	0.0049	0.0050	0.0051	0.0053	0.0057	0.0063
0.0049	0.0049	0.0050	0.0051	0.0053	0.0057	0.0062
0.0049	0.0049	0.0050	0.0051	0.0053	0.0056	0.0062
0.0049	0.0049	0.0050	0.0051	0.0053	0.0056	0.0062
0.0049	0.0049	0.0050	0.0051	0.0053	0.0056	0.0062
0.0049	0.0049	0.0050	0.0051	0.0053	0.0056	0.0062
0.0049	0.0049	0.0050	0.0051	0.0053	0.0056	0.0062
0.0049	0.0049	0.0050	0.0051	0.0053	0.0056	0.0062
0.0049	0.0049	0.0050	0.0051	0.0053	0.0056	0.0061
0.0049	0.0049	0.0050	0.0051	0.0053	0.0056	0.0061
0.0049	0.0049	0.0050	0.0051	0.0053	0.0056	0.0061
0.0049	0.0049	0.0049	0.0051	0.0053	0.0056	0.0061
0.0048	0.0049	0.0049	0.0051	0.0053	0.0056	0.0061
0.0048	0.0049	0.0049	0.0050	0.0053	0.0056	0.0060

Columns 8 through 14

0.0077	0.0089	0.0106	0.0119	0.0136	0.0147	0.0166
0.0076	0.0089	0.0105	0.0119	0.0135	0.0146	0.0166
0.0076	0.0088	0.0105	0.0117	0.0134	0.0145	0.0166
0.0076	0.0088	0.0104	0.0114	0.0130	0.0141	0.0164
0.0075	0.0085	0.0103	0.0113	0.0130	0.0140	0.0163
0.0074	0.0085	0.0102	0.0112	0.0129	0.0140	0.0161
0.0074	0.0085	0.0098	0.0109	0.0122	0.0131	0.0155
0.0073	0.0083	0.0096	0.0104	0.0118	0.0129	0.0146
0.0072	0.0081	0.0095	0.0100	0.0116	0.0125	0.0139
0.0072	0.0079	0.0091	0.0097	0.0111	0.0119	0.0131
0.0072	0.0077	0.0089	0.0096	0.0106	0.0114	0.0125
0.0071	0.0076	0.0086	0.0093	0.0102	0.0109	0.0120
0.0070	0.0075	0.0083	0.0090	0.0099	0.0105	0.0115
0.0069	0.0074	0.0081	0.0088	0.0095	0.0101	0.0110
0.0068	0.0073	0.0079	0.0085	0.0093	0.0098	0.0106
0.0067	0.0072	0.0078	0.0083	0.0090	0.0095	0.0103
0.0066	0.0070	0.0076	0.0081	0.0088	0.0093	0.0100
0.0066	0.0069	0.0075	0.0080	0.0086	0.0090	0.0097
0.0065	0.0068	0.0073	0.0078	0.0084	0.0088	0.0095

Columns 15 through 21

0.0178	0.0197	0.0212	0.0227	0.0240	0.0256	0.0270
0.0177	0.0194	0.0210	0.0225	0.0239	0.0253	0.0267
0.0175	0.0191	0.0206	0.0221	0.0236	0.0250	0.0263
0.0170	0.0190	0.0205	0.0220	0.0233	0.0246	0.0258
0.0169	0.0189	0.0203	0.0217	0.0231	0.0243	0.0256
0.0168	0.0183	0.0197	0.0211	0.0224	0.0238	0.0252
0.0157	0.0182	0.0193	0.0202	0.0213	0.0224	0.0235
0.0150	0.0172	0.0185	0.0198	0.0206	0.0217	0.0235
0.0149	0.0162	0.0175	0.0187	0.0199	0.0212	0.0222
0.0141	0.0153	0.0165	0.0176	0.0187	0.0199	0.0208
0.0134	0.0145	0.0156	0.0166	0.0177	0.0188	0.0196
0.0128	0.0138	0.0148	0.0157	0.0167	0.0177	0.0185
0.0122	0.0132	0.0141	0.0149	0.0158	0.0168	0.0175
0.0117	0.0126	0.0135	0.0143	0.0151	0.0160	0.0166
0.0113	0.0121	0.0129	0.0136	0.0144	0.0152	0.0158
0.0109	0.0117	0.0124	0.0131	0.0139	0.0146	0.0151

0.0106	0.0113	0.0120	0.0126	0.0133	0.0140	0.0145
0.0103	0.0109	0.0116	0.0122	0.0128	0.0135	0.0139
0.0100	0.0106	0.0112	0.0118	0.0124	0.0129	0.0134

Columns 22 through 28

0.0286	0.0305	0.0319	0.0330	0.0344	0.0357	0.0373
0.0283	0.0300	0.0313	0.0327	0.0339	0.0352	0.0369
0.0278	0.0295	0.0308	0.0322	0.0334	0.0345	0.0360
0.0273	0.0289	0.0303	0.0315	0.0327	0.0341	0.0355
0.0271	0.0287	0.0297	0.0313	0.0322	0.0333	0.0354
0.0267	0.0283	0.0295	0.0307	0.0318	0.0327	0.0338
0.0249	0.0263	0.0275	0.0285	0.0295	0.0308	0.0320
0.0244	0.0254	0.0266	0.0279	0.0293	0.0305	0.0310
0.0234	0.0248	0.0258	0.0267	0.0274	0.0280	0.0286
0.0219	0.0232	0.0241	0.0248	0.0254	0.0258	0.0263
0.0207	0.0218	0.0226	0.0232	0.0236	0.0240	0.0244
0.0195	0.0204	0.0211	0.0216	0.0220	0.0224	0.0228
0.0184	0.0192	0.0198	0.0203	0.0207	0.0210	0.0213
0.0174	0.0182	0.0187	0.0191	0.0195	0.0198	0.0201
0.0165	0.0172	0.0177	0.0181	0.0184	0.0187	0.0190
0.0158	0.0164	0.0168	0.0172	0.0175	0.0177	0.0180
0.0151	0.0156	0.0160	0.0164	0.0167	0.0169	0.0171
0.0144	0.0149	0.0153	0.0156	0.0159	0.0161	0.0164
0.0138	0.0143	0.0147	0.0150	0.0152	0.0154	0.0157

Columns 29 through 35

0.0386	0.0395	0.0395	0.0395	0.0386	0.0373	0.0357
0.0382	0.0388	0.0388	0.0388	0.0382	0.0369	0.0352
0.0368	0.0375	0.0379	0.0375	0.0368	0.0360	0.0345
0.0367	0.0375	0.0376	0.0375	0.0367	0.0355	0.0341
0.0368	0.0375	0.0375	0.0375	0.0368	0.0354	0.0333
0.0346	0.0348	0.0349	0.0348	0.0346	0.0338	0.0327
0.0324	0.0324	0.0324	0.0324	0.0324	0.0320	0.0308
0.0310	0.0317	0.0317	0.0317	0.0310	0.0310	0.0305
0.0289	0.0291	0.0291	0.0291	0.0289	0.0286	0.0280
0.0265	0.0267	0.0267	0.0267	0.0265	0.0263	0.0258
0.0246	0.0247	0.0247	0.0247	0.0246	0.0244	0.0240
0.0229	0.0230	0.0230	0.0230	0.0229	0.0228	0.0224
0.0214	0.0216	0.0216	0.0216	0.0214	0.0213	0.0210
0.0202	0.0203	0.0203	0.0203	0.0202	0.0201	0.0198
0.0191	0.0192	0.0192	0.0192	0.0191	0.0190	0.0187
0.0181	0.0182	0.0182	0.0182	0.0181	0.0180	0.0177
0.0172	0.0173	0.0173	0.0173	0.0172	0.0171	0.0169
0.0164	0.0165	0.0165	0.0165	0.0164	0.0164	0.0161
0.0157	0.0158	0.0158	0.0158	0.0157	0.0157	0.0154

Columns 36 through 42

0.0344	0.0330	0.0319	0.0305	0.0286	0.0270	0.0256
0.0339	0.0327	0.0313	0.0300	0.0283	0.0267	0.0253
0.0334	0.0322	0.0308	0.0295	0.0278	0.0263	0.0250
0.0327	0.0315	0.0303	0.0289	0.0273	0.0258	0.0246
0.0322	0.0313	0.0297	0.0287	0.0271	0.0256	0.0243
0.0318	0.0307	0.0295	0.0283	0.0267	0.0252	0.0238
0.0295	0.0285	0.0275	0.0263	0.0249	0.0235	0.0224
0.0293	0.0279	0.0266	0.0254	0.0244	0.0235	0.0217
0.0274	0.0267	0.0258	0.0248	0.0234	0.0222	0.0212
0.0254	0.0248	0.0241	0.0232	0.0219	0.0208	0.0199
0.0236	0.0232	0.0226	0.0218	0.0207	0.0196	0.0188
0.0220	0.0216	0.0211	0.0204	0.0195	0.0185	0.0177
0.0207	0.0203	0.0198	0.0192	0.0184	0.0175	0.0168
0.0195	0.0191	0.0187	0.0182	0.0174	0.0166	0.0160
0.0184	0.0181	0.0177	0.0172	0.0165	0.0158	0.0152
0.0175	0.0172	0.0168	0.0164	0.0158	0.0151	0.0146
0.0167	0.0164	0.0160	0.0156	0.0151	0.0145	0.0140
0.0159	0.0156	0.0153	0.0149	0.0144	0.0139	0.0135
0.0152	0.0150	0.0147	0.0143	0.0138	0.0134	0.0129

Columns 43 through 49

0.0240	0.0227	0.0212	0.0197	0.0178	0.0166	0.0147

0.0239	0.0225	0.0210	0.0194	0.0177	0.0166	0.0146
0.0236	0.0221	0.0206	0.0191	0.0175	0.0166	0.0145
0.0233	0.0220	0.0205	0.0190	0.0170	0.0164	0.0141
0.0231	0.0217	0.0203	0.0189	0.0169	0.0163	0.0140
0.0224	0.0211	0.0197	0.0183	0.0168	0.0161	0.0140
0.0213	0.0202	0.0193	0.0182	0.0157	0.0155	0.0131
0.0206	0.0198	0.0185	0.0172	0.0150	0.0146	0.0129
0.0199	0.0187	0.0175	0.0162	0.0149	0.0139	0.0125
0.0187	0.0176	0.0165	0.0153	0.0141	0.0131	0.0119
0.0177	0.0166	0.0156	0.0145	0.0134	0.0125	0.0114
0.0167	0.0157	0.0148	0.0138	0.0128	0.0120	0.0109
0.0158	0.0149	0.0141	0.0132	0.0122	0.0115	0.0105
0.0151	0.0143	0.0135	0.0126	0.0117	0.0110	0.0101
0.0144	0.0136	0.0129	0.0121	0.0113	0.0106	0.0098
0.0139	0.0131	0.0124	0.0117	0.0109	0.0103	0.0095
0.0133	0.0126	0.0120	0.0113	0.0106	0.0100	0.0093
0.0128	0.0122	0.0116	0.0109	0.0103	0.0097	0.0090
0.0124	0.0118	0.0112	0.0106	0.0100	0.0095	0.0088

Columns 50 through 56

0.0136	0.0119	0.0106	0.0089	0.0077	0.0063	0.0057
0.0135	0.0119	0.0105	0.0089	0.0076	0.0063	0.0057
0.0134	0.0117	0.0105	0.0088	0.0076	0.0063	0.0057
0.0130	0.0114	0.0104	0.0088	0.0076	0.0063	0.0057
0.0130	0.0113	0.0103	0.0085	0.0075	0.0063	0.0057
0.0129	0.0112	0.0102	0.0085	0.0074	0.0062	0.0057
0.0122	0.0109	0.0098	0.0085	0.0074	0.0062	0.0056
0.0118	0.0104	0.0096	0.0083	0.0073	0.0062	0.0056
0.0116	0.0100	0.0095	0.0081	0.0072	0.0062	0.0056
0.0111	0.0097	0.0091	0.0079	0.0072	0.0062	0.0056
0.0106	0.0096	0.0089	0.0077	0.0072	0.0062	0.0056
0.0102	0.0093	0.0086	0.0076	0.0071	0.0062	0.0056
0.0099	0.0090	0.0083	0.0075	0.0070	0.0062	0.0056
0.0095	0.0088	0.0081	0.0074	0.0069	0.0061	0.0056
0.0093	0.0085	0.0079	0.0073	0.0068	0.0061	0.0056
0.0090	0.0083	0.0078	0.0072	0.0067	0.0061	0.0056
0.0088	0.0081	0.0076	0.0070	0.0066	0.0061	0.0056
0.0086	0.0080	0.0075	0.0069	0.0066	0.0061	0.0056
0.0084	0.0078	0.0073	0.0068	0.0065	0.0060	0.0056

Columns 57 through 61

0.0054	0.0051	0.0050	0.0050	0.0049
0.0054	0.0051	0.0050	0.0050	0.0049
0.0054	0.0051	0.0050	0.0050	0.0049
0.0053	0.0051	0.0050	0.0049	0.0049
0.0053	0.0051	0.0050	0.0049	0.0049
0.0053	0.0051	0.0050	0.0049	0.0049
0.0053	0.0051	0.0050	0.0049	0.0049
0.0053	0.0051	0.0050	0.0049	0.0049
0.0053	0.0051	0.0050	0.0049	0.0049
0.0053	0.0051	0.0050	0.0049	0.0049
0.0053	0.0051	0.0050	0.0049	0.0049
0.0053	0.0051	0.0050	0.0049	0.0049
0.0053	0.0051	0.0050	0.0049	0.0049
0.0053	0.0051	0.0050	0.0049	0.0049
0.0053	0.0051	0.0050	0.0049	0.0049
0.0053	0.0051	0.0049	0.0049	0.0049
0.0053	0.0051	0.0049	0.0049	0.0048
0.0053	0.0050	0.0049	0.0049	0.0048

Torque lookup tables:

TORQUE60yx4.dat
TORQUE60yx4 =

Columns 1 through 7

0	0	0	0	0	0	0
-0.0391	-0.0879	-0.0931	-0.1197	-0.1088	-0.0962	-0.1239
-0.0370	-0.1221	-0.1858	-0.2437	-0.2253	-0.2325	-0.2266
-0.0107	-0.1705	-0.3517	-0.4120	-0.4345	-0.4250	-0.4445
-0.0087	-0.2522	-0.5611	-0.6696	-0.6943	-0.7135	-0.7277
0.0261	-0.3486	-0.7877	-0.9868	-1.0320	-1.0678	-1.0844
0.0350	-0.4259	-0.9714	-1.2453	-1.3568	-1.4440	-1.4978
0.0062	-0.4765	-1.1231	-1.4809	-1.6596	-1.8025	-1.9178
0.0188	-0.5164	-1.2449	-1.6895	-1.9157	-2.1453	-2.3242
0.0431	-0.5686	-1.3468	-1.8316	-2.1457	-2.4201	-2.6888
0.0192	-0.5957	-1.4391	-1.9813	-2.3224	-2.6803	-2.9986
0.0444	-0.6245	-1.5148	-2.1174	-2.5028	-2.9181	-3.3101
0.0404	-0.6609	-1.6036	-2.2694	-2.6836	-3.1556	-3.6071
0.0561	-0.7129	-1.6890	-2.3849	-2.8419	-3.3909	-3.8942
0.0346	-0.7413	-1.7673	-2.5112	-3.0359	-3.6362	-4.2129
0.0221	-0.7754	-1.8518	-2.6437	-3.2026	-3.8841	-4.5056
0.0756	-0.8102	-1.9329	-2.7847	-3.3844	-4.1154	-4.8100
0.0151	-0.8445	-2.0049	-2.9095	-3.5489	-4.3546	-5.1196
0.0532	-0.8735	-2.0605	-3.0353	-3.7338	-4.5994	-5.4222

Columns 8 through 14

0	0	0	0	0	0	0
-0.0684	-0.1264	-0.1324	-0.1289	-0.1134	-0.0736	-0.0665
-0.0699	-0.2525	-0.2664	-0.2665	-0.2510	-0.2195	-0.1992
-0.4461	-0.4718	-0.4766	-0.4798	-0.4745	-0.4305	-0.4334
-0.7398	-0.7622	-0.7795	-0.7682	-0.7651	-0.7318	-0.7347
-1.1022	-1.1363	-1.1497	-1.1561	-1.1437	-1.1212	-1.1062
-1.5359	-1.5651	-1.5907	-1.6175	-1.6019	-1.5809	-1.5671
-1.9892	-2.0481	-2.0702	-2.0959	-2.0969	-2.0833	-2.0716
-2.4442	-2.5522	-2.5819	-2.6152	-2.6200	-2.6024	-2.6023
-2.8819	-3.0210	-3.1074	-3.1642	-3.1617	-3.1576	-3.1581
-3.2841	-3.5104	-3.6477	-3.7247	-3.7354	-3.7383	-3.7458
-3.6633	-3.9694	-4.1762	-4.2871	-4.3108	-4.3337	-4.3407
-4.0239	-4.4046	-4.7018	-4.8452	-4.9001	-4.9298	-4.9101
-4.3617	-4.8177	-5.1587	-5.3917	-5.4765	-5.5284	-5.5121
-4.7301	-5.2373	-5.6768	-5.9263	-6.0695	-6.1369	-6.1336
-5.0719	-5.6452	-6.1246	-6.4480	-6.6429	-6.7152	-6.7246
-5.4220	-6.0305	-6.5708	-6.9231	-7.2264	-7.3365	-7.3355
-5.7760	-6.4227	-7.0097	-7.4410	-7.7078	-7.9024	-7.9648
-6.1076	-6.8012	-7.4596	-7.9177	-8.2417	-8.4875	-8.5130

Columns 15 through 21

0	0	0	0	0	0	0
-0.0392	-0.0294	-0.0545	-0.0931	-0.0992	-0.1100	-0.1040
-0.1766	-0.1627	-0.1981	-0.2299	-0.2381	-0.2481	-0.2391
-0.3912	-0.3901	-0.4136	-0.4542	-0.4781	-0.4730	-0.4600
-0.7019	-0.7003	-0.7212	-0.7600	-0.7600	-0.7766	-0.7828
-1.0939	-1.0884	-1.1008	-1.1351	-1.1524	-1.1532	-1.1410
-1.5440	-1.5366	-1.5465	-1.5899	-1.5778	-1.5943	-1.5591
-2.0571	-2.0188	-2.0476	-2.0690	-2.0555	-2.0609	-2.0065
-2.5856	-2.5626	-2.5848	-2.5725	-2.5727	-2.5600	-2.4693
-3.1506	-3.1346	-3.1221	-3.1249	-3.1011	-3.0631	-2.9668
-3.7096	-3.6529	-3.7109	-3.6806	-3.6505	-3.5956	-3.4473
-4.3108	-4.2816	-4.2936	-4.2667	-4.2059	-4.1287	-3.9584
-4.8983	-4.8683	-4.8741	-4.8283	-4.7748	-4.6692	-4.4705
-5.5121	-5.4545	-5.4484	-5.3964	-5.3197	-5.2114	-4.9986
-6.1176	-6.0567	-6.0572	-5.9877	-5.9118	-5.7558	-5.4921
-6.7245	-6.6947	-6.6446	-6.5660	-6.4531	-6.2775	-6.0149
-7.3333	-7.2708	-7.2353	-7.1501	-7.0186	-6.8251	-6.5151
-7.9807	-7.9089	-7.8576	-7.7501	-7.6186	-7.3948	-7.0722
-8.5130	-8.5130	-8.5053	-8.3445	-8.2067	-7.9677	-7.5994

Columns 22 through 28

0	0	0	0	0	0	0
-0.1195	-0.0505	-0.0998	-0.0762	-0.0530	-0.0459	-0.0645
-0.2699	-0.2210	-0.2237	-0.1631	-0.1003	-0.0879	-0.0861
-0.4700	-0.4332	-0.4233	-0.2902	-0.1706	-0.1050	-0.1019
-0.7718	-0.7387	-0.7193	-0.4697	-0.2685	-0.1714	-0.1401
-1.1418	-1.1083	-1.0998	-0.7036	-0.3766	-0.2432	-0.1718
-1.5732	-1.5394	-1.5052	-0.9498	-0.5318	-0.3327	-0.2393
-2.0078	-2.0094	-1.9863	-1.2880	-0.6834	-0.4302	-0.2752
-2.4609	-2.4943	-2.4778	-1.6942	-0.8783	-0.5488	-0.3555
-2.8893	-2.9971	-3.0434	-2.1058	-1.1166	-0.6861	-0.4497
-3.3595	-3.4521	-3.5684	-2.5146	-1.3609	-0.8315	-0.5425
-3.8305	-3.9193	-4.0789	-2.9747	-1.6280	-1.0179	-0.6259
-4.3190	-4.3955	-4.5773	-3.4437	-1.9321	-1.1862	-0.7475
-4.7889	-4.8478	-5.0620	-3.8899	-2.2540	-1.4002	-0.8645
-5.2910	-5.3319	-5.5192	-4.3883	-2.5925	-1.5707	-0.9846
-5.7765	-5.7797	-5.9648	-4.8500	-2.9468	-1.8249	-1.1227
-6.2522	-6.2403	-6.3685	-5.3175	-3.2954	-2.0899	-1.2304
-6.7728	-6.7125	-6.8047	-5.7912	-3.6827	-2.3563	-1.4060
-7.2676	-7.1590	-7.2449	-6.2427	-4.0528	-2.6507	-1.5904

Columns 29 through 35

0	0	0	0	0	0	0
0.0041	-0.0486	-0.0626	0.0486	-0.0041	0.0645	0.0459
-0.0356	-0.0469	-0.0562	0.0469	0.0356	0.0861	0.0879
-0.0582	-0.0562	-0.0689	0.0562	0.0582	0.1019	0.1050
-0.0968	-0.0802	-0.0550	0.0802	0.0968	0.1401	0.1714
-0.1127	-0.0831	-0.0398	0.0831	0.1127	0.1718	0.2432
-0.1465	-0.1026	-0.0448	0.1026	0.1465	0.2393	0.3327
-0.1811	-0.1272	-0.0464	0.1272	0.1811	0.2752	0.4302
-0.2343	-0.1482	-0.0740	0.1482	0.2343	0.3555	0.5488
-0.2805	-0.1567	-0.0790	0.1567	0.2805	0.4497	0.6861
-0.3420	-0.1843	-0.0724	0.1843	0.3420	0.5425	0.8315
-0.4006	-0.2128	-0.0705	0.2128	0.4006	0.6259	1.0179
-0.4533	-0.2608	-0.0741	0.2608	0.4533	0.7475	1.1862
-0.5306	-0.3042	-0.0719	0.3042	0.5306	0.8645	1.4002
-0.6099	-0.3382	-0.0683	0.3382	0.6099	0.9846	1.5707
-0.7051	-0.3741	-0.0673	0.3741	0.7051	1.1227	1.8249
-0.7916	-0.4019	-0.0837	0.4019	0.7916	1.2304	2.0899
-0.8777	-0.4380	-0.0724	0.4380	0.8777	1.4060	2.3563
-0.9866	-0.5348	-0.0973	0.5348	0.9866	1.5904	2.6507

Columns 36 through 42

0	0	0	0	0	0	0
0.0530	0.0762	0.0998	0.0505	0.1195	0.1040	0.1100
0.1003	0.1631	0.2237	0.2210	0.2699	0.2391	0.2481
0.1706	0.2902	0.4233	0.4332	0.4700	0.4600	0.4730
0.2685	0.4697	0.7193	0.7387	0.7718	0.7828	0.7766
0.3766	0.7036	1.0998	1.1083	1.1418	1.1410	1.1532
0.5318	0.9498	1.5052	1.5394	1.5732	1.5591	1.5943
0.6834	1.2880	1.9863	2.0094	2.0078	2.0065	2.0609
0.8783	1.6942	2.4778	2.4943	2.4609	2.4693	2.5600
1.1166	2.1058	3.0434	2.9971	2.8893	2.9668	3.0631
1.3609	2.5146	3.5684	3.4521	3.3595	3.4473	3.5956
1.6280	2.9747	4.0789	3.9193	3.8305	3.9584	4.1287
1.9321	3.4437	4.5773	4.3955	4.3190	4.4705	4.6692
2.2540	3.8899	5.0620	4.8478	4.7889	4.9986	5.2114
2.5925	4.3883	5.5192	5.3319	5.2910	5.4921	5.7558
2.9468	4.8500	5.9648	5.7797	5.7765	6.0149	6.2775
3.2954	5.3175	6.3685	6.2403	6.2522	6.5151	6.8251
3.6827	5.7912	6.8047	6.7125	6.7728	7.0722	7.3948
4.0528	6.2427	7.2449	7.1590	7.2676	7.5994	7.9677

Columns 43 through 49

0	0	0	0	0	0	0
0.0992	0.0931	0.0545	0.0294	0.0392	0.0665	0.0736
0.2381	0.2299	0.1981	0.1627	0.1766	0.1992	0.2195
0.4781	0.4542	0.4136	0.3901	0.3912	0.4334	0.4305
0.7600	0.7600	0.7212	0.7003	0.7019	0.7347	0.7318
1.1524	1.1351	1.1008	1.0884	1.0939	1.1062	1.1212

1.5778	1.5899	1.5465	1.5366	1.5440	1.5671	1.5809
2.0555	2.0690	2.0476	2.0188	2.0571	2.0716	2.0833
2.5727	2.5725	2.5848	2.5626	2.5856	2.6023	2.6024
3.1011	3.1249	3.1221	3.1346	3.1506	3.1581	3.1576
3.6505	3.6806	3.7109	3.6529	3.7096	3.7458	3.7383
4.2059	4.2667	4.2936	4.2816	4.3108	4.3407	4.3337
4.7748	4.8283	4.8741	4.8683	4.8983	4.9101	4.9298
5.3197	5.3964	5.4484	5.4545	5.5121	5.5121	5.5284
5.9118	5.9877	6.0572	6.0567	6.1176	6.1336	6.1369
6.4531	6.5660	6.6446	6.6947	6.7245	6.7246	6.7152
7.0186	7.1501	7.2353	7.2708	7.3333	7.3355	7.3365
7.6186	7.7501	7.8576	7.9089	7.9807	7.9648	7.9024
8.2067	8.3445	8.5053	8.5130	8.5130	8.5130	8.4875

Columns 50 through 56

0	0	0	0	0	0	0
0.1134	0.1289	0.1324	0.1264	0.0684	0.1239	0.0962
0.2510	0.2665	0.2664	0.2525	0.0699	0.2266	0.2325
0.4745	0.4798	0.4766	0.4718	0.4461	0.4445	0.4250
0.7651	0.7682	0.7795	0.7622	0.7398	0.7277	0.7135
1.1437	1.1561	1.1497	1.1363	1.1022	1.0844	1.0678
1.6019	1.6175	1.5907	1.5651	1.5359	1.4978	1.4440
2.0969	2.0959	2.0702	2.0481	1.9892	1.9178	1.8025
2.6200	2.6152	2.5819	2.5522	2.4442	2.3242	2.1453
3.1617	3.1642	3.1074	3.0210	2.8819	2.6888	2.4201
3.7354	3.7247	3.6477	3.5104	3.2841	2.9986	2.6803
4.3108	4.2871	4.1762	3.9694	3.6633	3.3101	2.9181
4.9001	4.8452	4.7018	4.4046	4.0239	3.6071	3.1556
5.4765	5.3917	5.1587	4.8177	4.3617	3.8942	3.3909
6.0695	5.9263	5.6768	5.2373	4.7301	4.2129	3.6362
6.6429	6.4480	6.1246	5.6452	5.0719	4.5056	3.8841
7.2264	6.9231	6.5708	6.0305	5.4220	4.8100	4.1154
7.7078	7.4410	7.0097	6.4227	5.7760	5.1196	4.3546
8.2417	7.9177	7.4596	6.8012	6.1076	5.4222	4.5994

Columns 57 through 61

0	0	0	0	0
0.1088	0.1197	0.0931	0.0879	0.0391
0.2253	0.2437	0.1858	0.1221	0.0370
0.4345	0.4120	0.3517	0.1705	0.0107
0.6943	0.6696	0.5611	0.2522	0.0087
1.0320	0.9868	0.7877	0.3486	-0.0261
1.3568	1.2453	0.9714	0.4259	-0.0350
1.6596	1.4809	1.1231	0.4765	-0.0062
1.9157	1.6895	1.2449	0.5164	-0.0188
2.1457	1.8316	1.3468	0.5686	-0.0431
2.3224	1.9813	1.4391	0.5957	-0.0192
2.5028	2.1174	1.5148	0.6245	-0.0444
2.6836	2.2694	1.6036	0.6609	-0.0404
2.8419	2.3849	1.6890	0.7129	-0.0561
3.0359	2.5112	1.7673	0.7413	-0.0346
3.2026	2.6437	1.8518	0.7754	-0.0221
3.3844	2.7847	1.9329	0.8102	-0.0756
3.5489	2.9095	2.0049	0.8445	-0.0151
3.7338	3.0353	2.0605	0.8735	-0.0532

B.3 Power Converter Measurements

The IGBT and Diode characteristics are measured several times offline and there are slight differences between these results because of the temperature effects and measurement errors. The royal blue traces in Fig, B.4 show the measured IGBT and Diode characteristics stored as PSCAD lookup tables, and used for all simulation studies in this thesis. The Matlab programs for plotting the measured IGBT and Diode characteristics are shown below.

IGBT characteristic (IGBT.m)

```
%IGBT characteristic
%measured at 2, Aug, 2005
%V1-I1--IGBT1
%V2-I2---IGBT2
 I2=[0.25 0.5 1 1.5 2 3 4 5 6 7 8 9 10 11 12 13 14 15 16];
 V2=[0.6438 0.725 0.8563 0.9375 1.013 1.169 1.275 1.369 1.462 1.531
1.606 1.688 1.775 1.844 1.931 1.994 2.063 2.125 2.188];
 I1=[0.25 0.5 1 1.5 2 3 4 5 6 7 8 9 10 11 12 13 14 15 16];
 V1=[0.766 0.797 0.9688 1.019 1.125 1.288 1.375 1.55 1.6 1.694 1.825
1.862 1.969 2.05 2.119 2.219 2.325 2.363 2.438];

 %I3-V3 measured (adopted group data for IGBT characteristic)
 I3=[0.5 1.5 2.5 3.5 5 7 9 11 13 15];
 V3=[0.625 0.913 1.031 1.188 1.313 1.563 1.656 1.859 1.938 2.109];

 figure(2)

 plot(V1,I1,'r+-',V2,I2,'g--');grid on;
 hold on;
 plot(V3,I3);hold on;

Title('IGBT');

%V4-I4 measured at 1, Aug, 2005
V4=[2.281 2.25 2.2 2.125 2 1.875 1.859 1.813 1.75 1.625 1.531 1.406
1.294 1.237 1.044 0.8688 0.844 0.828 0.656 0.516 0.475];
I4=[16.56 16 15 14 13 12 11 10 9 8 7 6 5 4 3 2 1.5 1 0.5 0.25 0.15];

plot(V4,I4,'c--');
```

Diode characteristic (Diode.m)

```
%diode characteristic
%measured at 2, Aug, 2005
%V1-I1--D1
%V2-I2---D2
V2=[1.756 1.775 1.794 1.781 1.775 1.753 1.725 1.669 1.6 1.559 1.462
1.384 1.266 1.206 1.14 1.1 0.9938 0.93 0.8188];
 I2=[15 14 13 12 11 10 9 8 7 6 5 4 3 2.5 2 1.5 1 0.5 0.25];
 V1=[1.581 1.65 1.68 1.688 1.669 1.619 1.55 1.531 1.506 1.425 1.309
1.278 1.163 1.084 1.056 0.9469 0.8594 0.7562 0.6094];
```

```
I1=[15 14 13 12 11 10 9 8 7 6 5 4 3 2.5 2 1.5 1 0.5 0.3];

%V3-I3-meausred again same day
V3=[1.862 1.812 1.713 1.525 1.325 1.13];
I3=[11 10 8 5 3 1.5];

%V4-I4 measured (adopted group data for Diode characteristic)
V4=[1 1.063 1.313 1.594 1.75];
I4=[1.25 2.5 5 10 15];

figure(1)
plot(V1,I1,'r+-',V2,I2,'g--');grid on;
Title('Diode');
hold on;
plot(V3,I3,'m');

hold on;
plot(V4,I4)

%V6-I6 measured at 1, Aug, 2005
V6=[1.5 1.531 1.563 1.578 1.563 1.531 1.5 1.438 1.344 1.297 1.219
1.141 1.031 0.938 0.875 0.781 0.672 0.531 0.438];
I6=[15.5 15 14 13 12 11 10 9 8 7 6 5 4 3 2 1.5 1 0.5 .25 0.15];
plot(V6,I6,'k--');
```

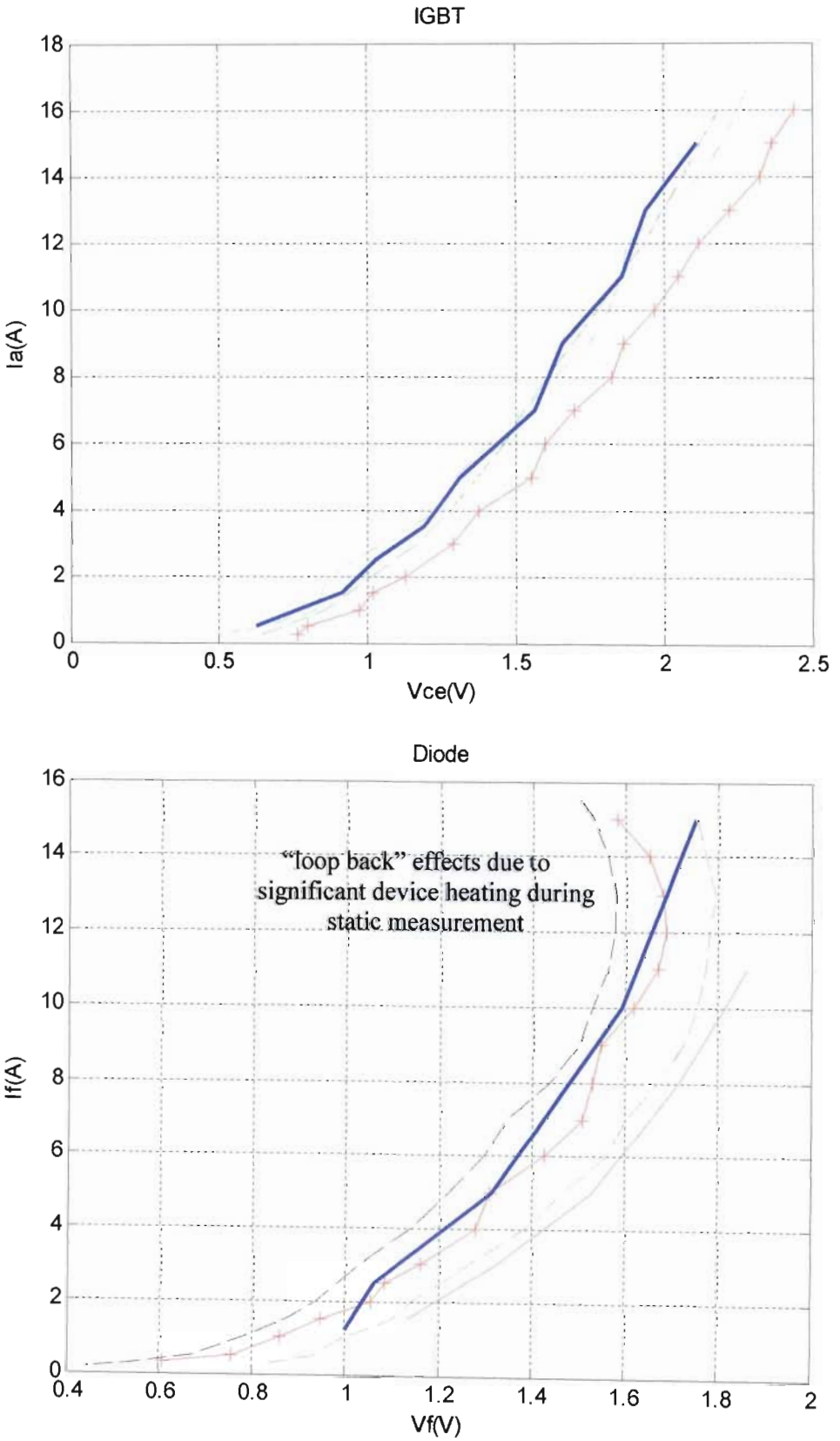

Fig.B.4 Measured IGBT and Diode Characteristics

APPENDIX C

PSCAD Diagram Details for 8/6 SRM Current and Torque Control

Appendix C presents the details of the PSCAD blocks used in Chapter 4, as shown in Table.C.1.

Fig. No.	Name	Content Description
Fig.C.1	IGBT and Diode Characteristics	PSCAD lookup tables
Fig.C.2	Phase Inductance Blocks	Phase 1 to 4 inductance blocks
Fig.C.3	Phase B, C and D rotor angle blocks	phase 1 to 4 rotor angle diagrams
Fig.C.4	Rotor angle curve for phase S1-S1' (phase A)	phase 1 rotor position
Fig.C.5	Phase A, B, C and D rotor angles	rotor angles for phase 1 to 4
Fig.C.6	Torque sharing function (TSF) diagram	Torque sharing function block
Fig.C.7	Torque reference to current reference for each phase $T-\theta-i$	PSCAD lookup table
Fig.C.8	Torque model for four phases SRM $i-\theta-T$	PSCAD lookup table
Fig. C.9	Four phase SRM and AHB converter diagram with and without the 0 ohm resistor	PSCAD diagram with and without 0Ω resistance component
Fig.C.10	voltage results when 0 Ω resistor is in the circuit	Demonstration of 0 Ω resistor error in PSCAD
Fig.C.11	voltage results when 0 Ω resistor is not in the circuit	
Fig.C.12	Four-phase torque and current response with and without source resistance	Influence of 0Ω resistor error on PSCAD torque and current control performance
Fig.C.13	PSCAD plot (a) of phase 1 voltage shown in Matlab plot (b) of Fig.4.23	Matlab plotting problem for small values of phase 1 voltage
Fig.C.14	PSCAD back emf diagram	PSCAD phase 1 back emf

Table C.1 Appendix Contents

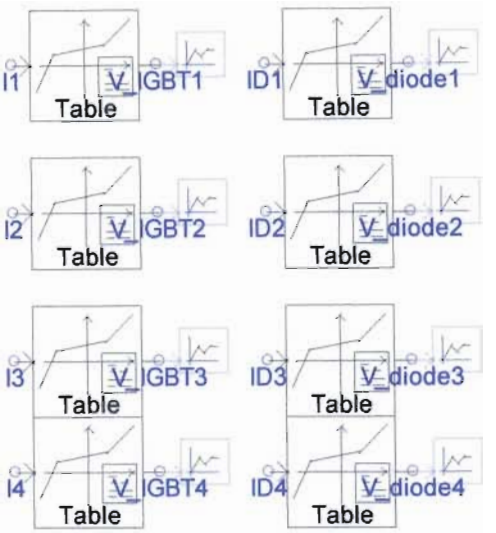

Fig.C.1 IGBT and Diodes Characteristics

IGBT Lookup table

Ia(A)	0.5	1.5	2.5	3.5	5	7	9	11	13	15
Vce(V)	0.625	0.913	1.031	1.188	1.313	1.563	1.656	1.859	1.938	2.109

Diode Lookup table

If (A)	1.25	2.5	5	10	15
Vf (V)	1	1.063	1.313	1.594	1.75

G1, G2, G3, G4 represents the phase inductance for phase 1 to 4.

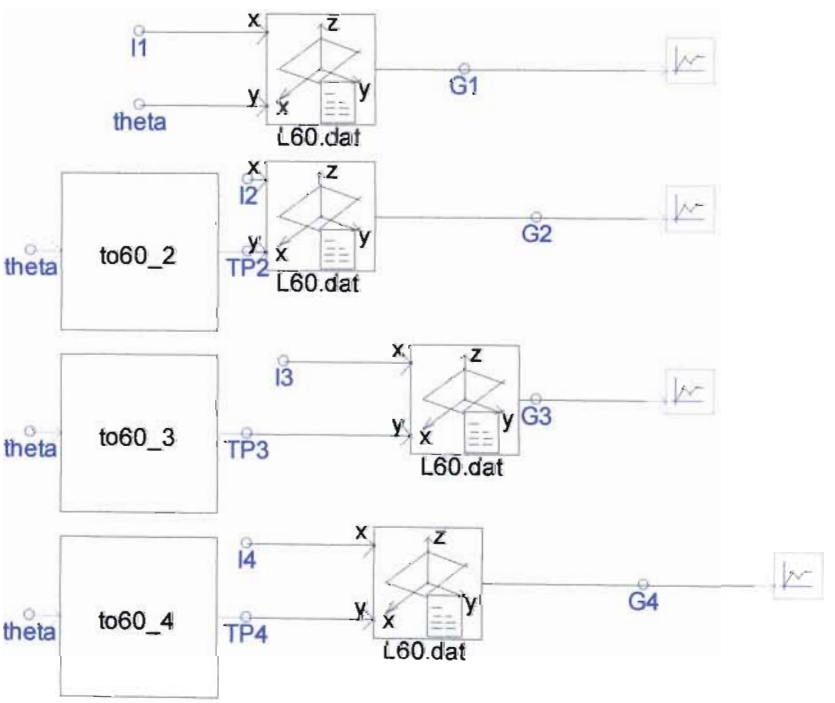

Fig.C.2 Phase Inductance Blocks

L60.dat (as shown in Appendix B.2) is the lookup table for phase 1 inductance. "to60_2, to60_3 and to60_4" are three blocks which function as transferring the rotor angle (theta) for phase 1 to the corresponding rotor angles for phase2, 3 and 4 angle (phase2, phase 3, phase 4 shown in Fig.C.3).

Phase 2 (phaseB)

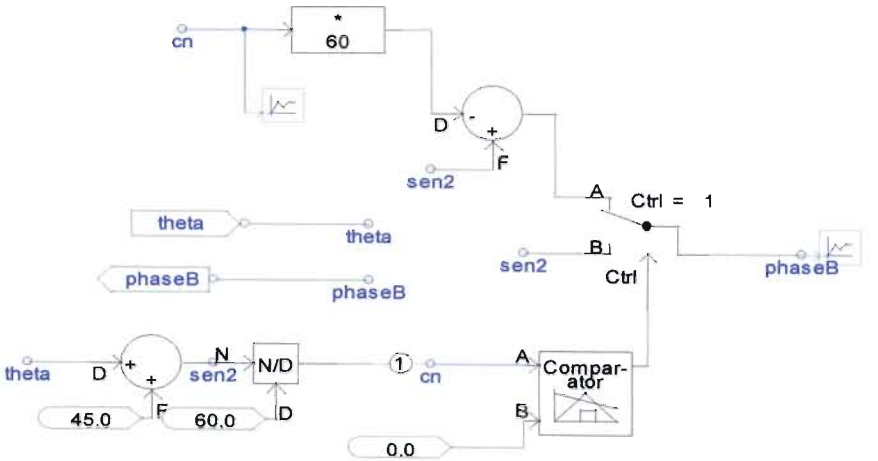

Phase 3(phaseC)

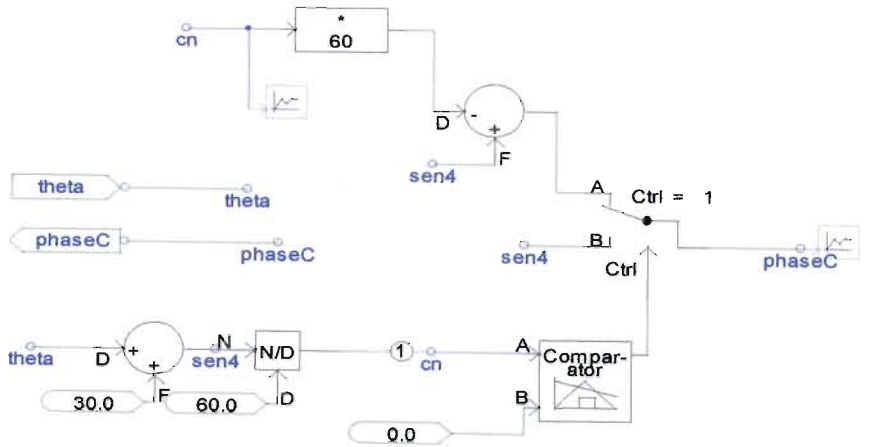

Phase 4(phaseD)

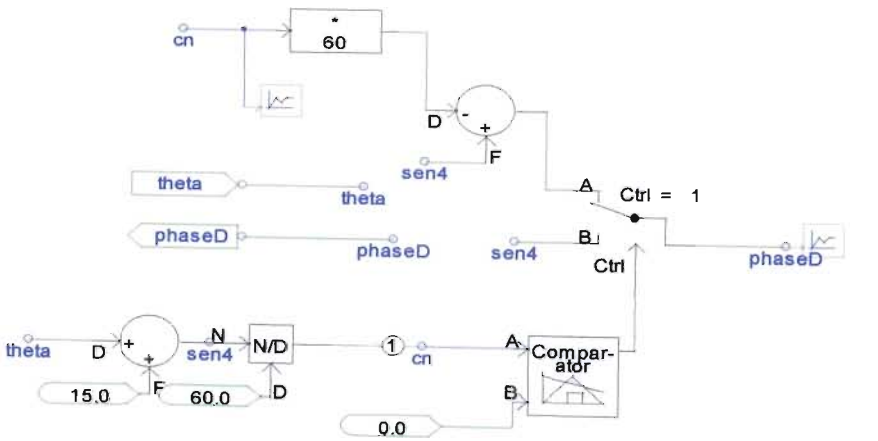

Fig.C.3 Phase 2, 3 and 4 rotor angle transforming blocks

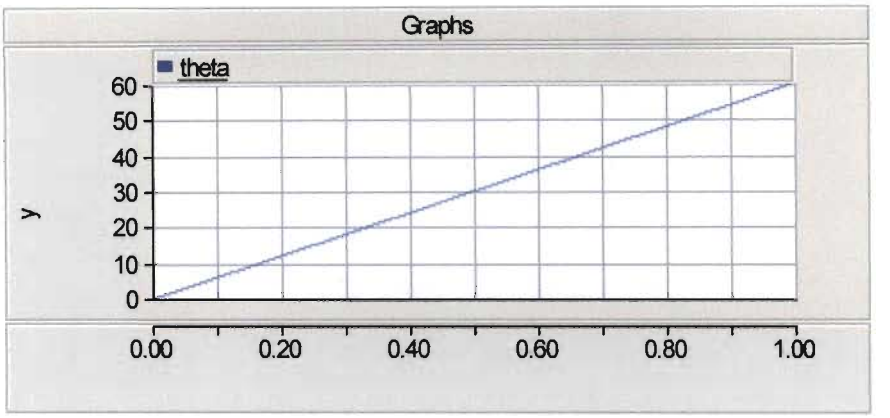

Fig.C.4 Rotor angle curve for phase 1 (phaseA)

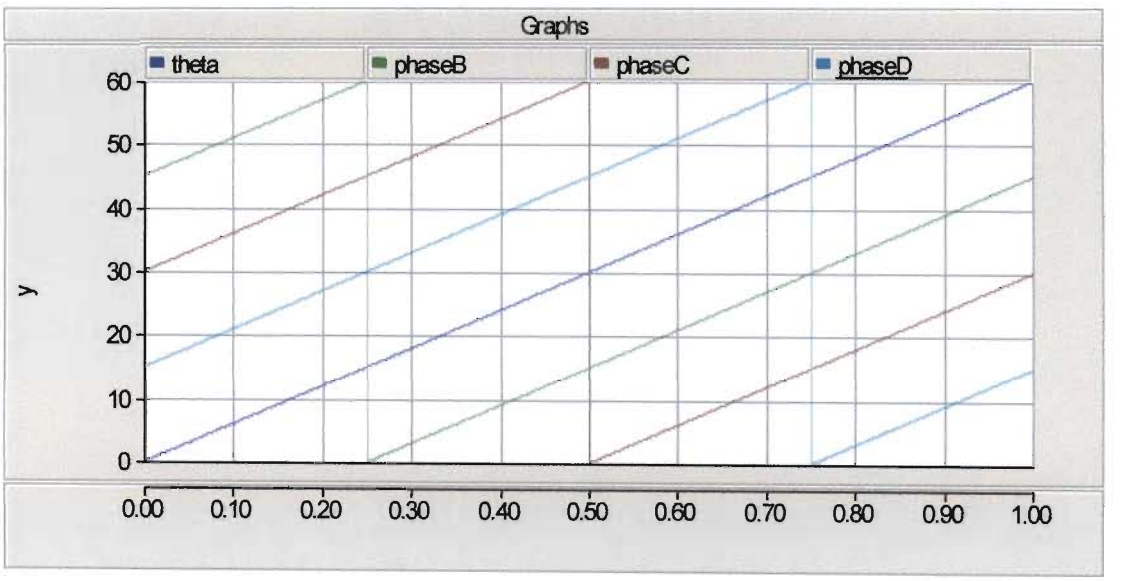

Fig.C.5 Phase 1, 2, 3 and 4 rotor angles (theta, phaseB, phaseC and phaseD)

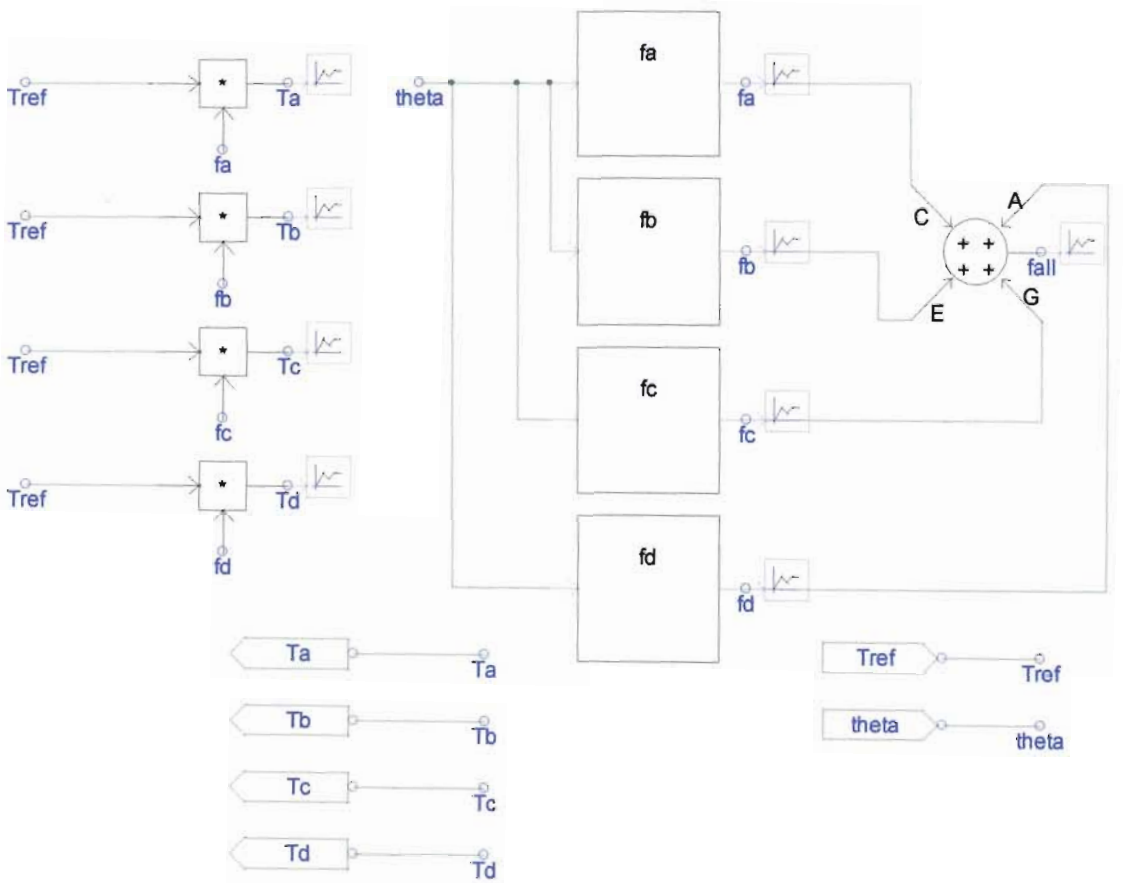

Fig.C.6 Torque sharing function (TSF) diagram

Signals fa, fb, fc and fd are derived from four contour function blocks (with the same name) for phase1, 2, 3and 4 in TSF. The sum of fa, fb, fc and fd is 1.

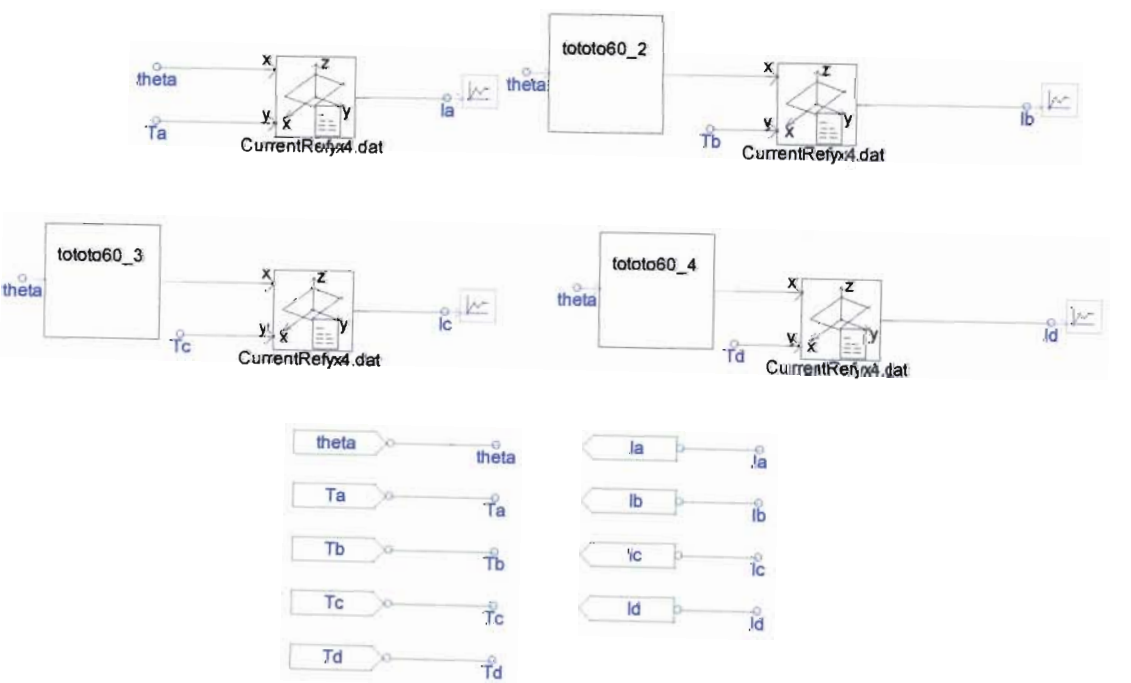

Fig.C.7 Torque reference to current reference for each phase $T-\theta-i$

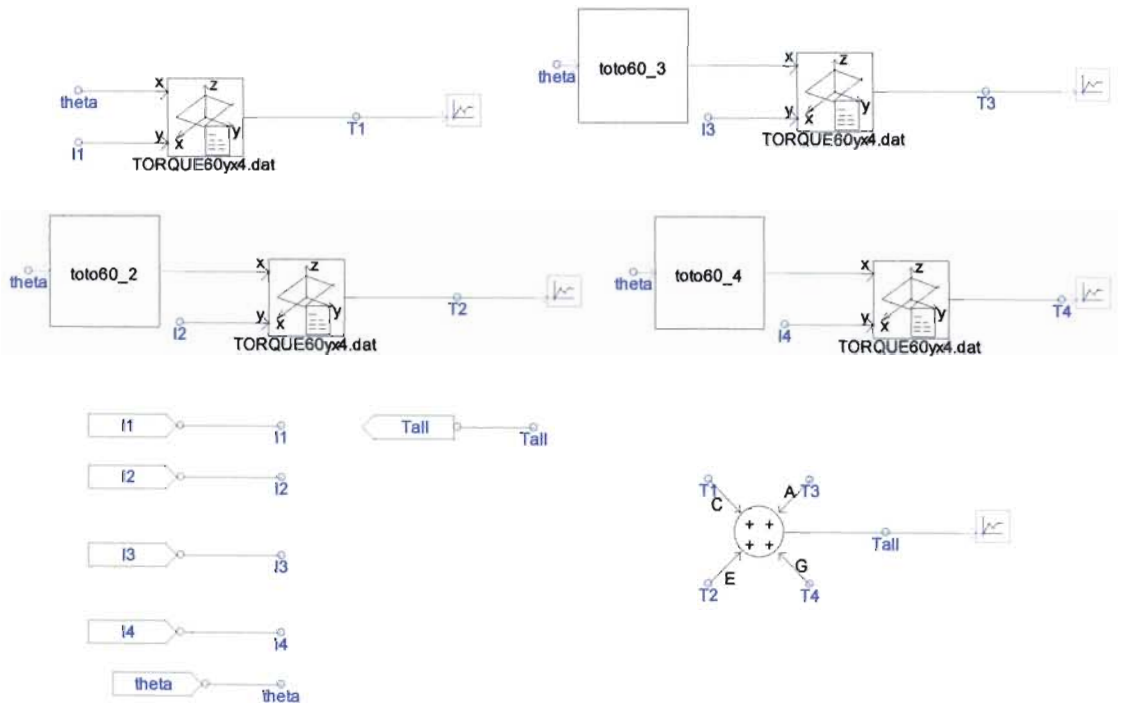

Fig.C.8 Torque model for four phases SRM $i-\theta-T$

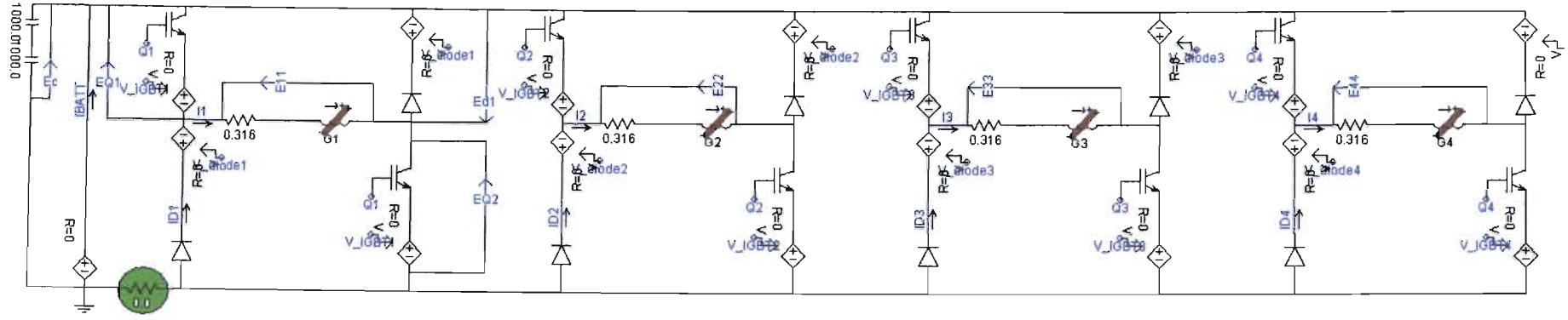

(a)

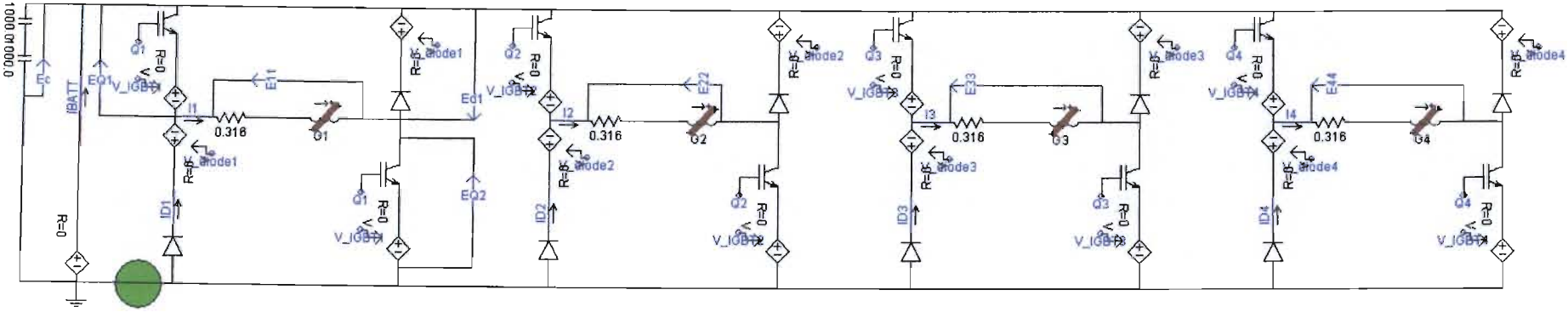

(b)

Fig.C.9 Four phase SRM and AHB converter diagram (a) with and without (b) the 0 ohm resistor

One speed controlled test (w=150rpm, Tref= ± 1Nm) is used to show the influence of the 0 Ω resistance in the circuit. Fig.C.10 shows that the voltage (VR) across the 0 Ω resistor is not zero, and definitely not small enough to be considered zero, and should hence be avoided in PSCAD to eliminate possible errors of this type. Fig.C.11 confirms that VR is zero when the 0 Ω component is removed from the circuit (or bridged out with a wire).

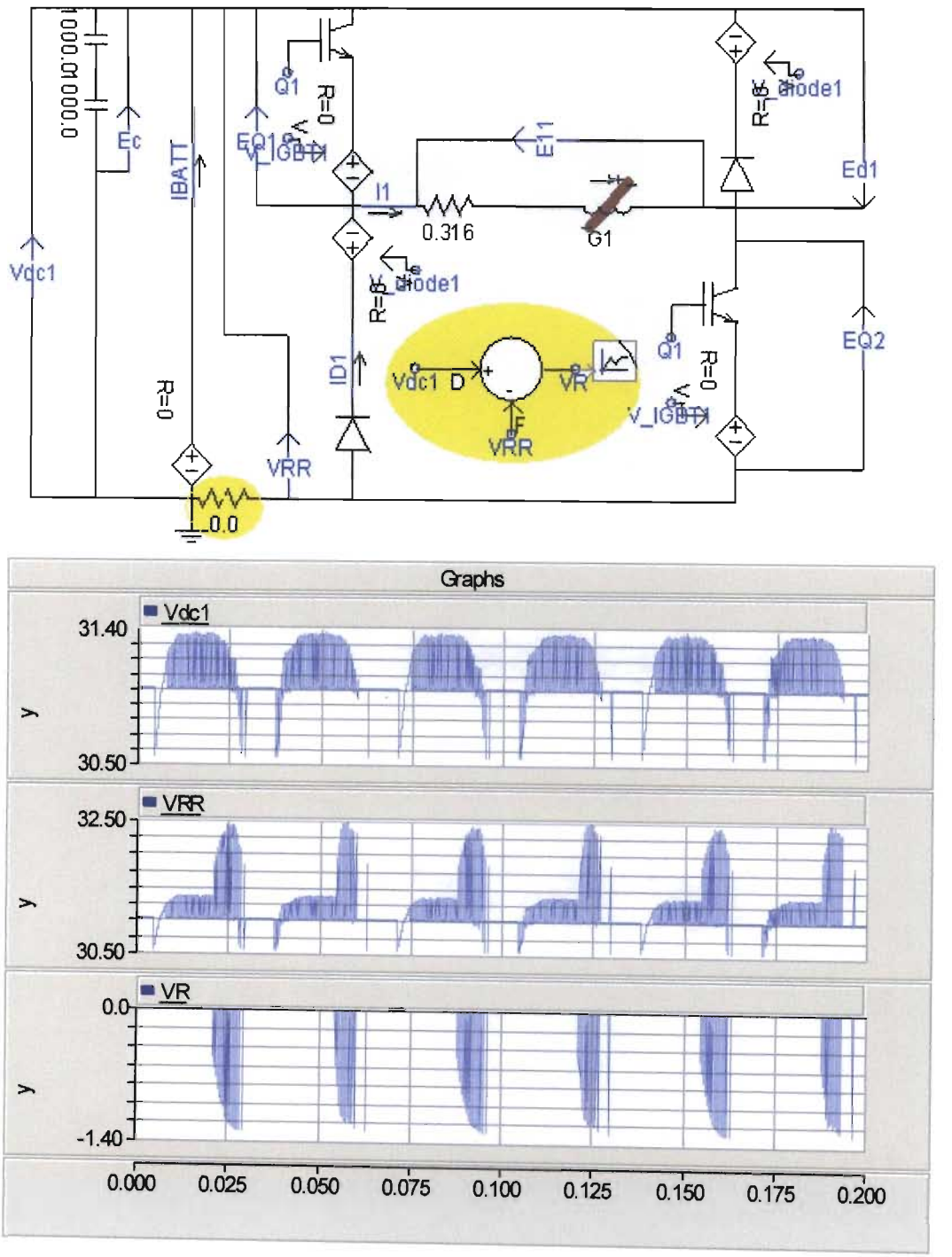

Fig.C.10 voltage results when 0 Ω resistor in the circuit

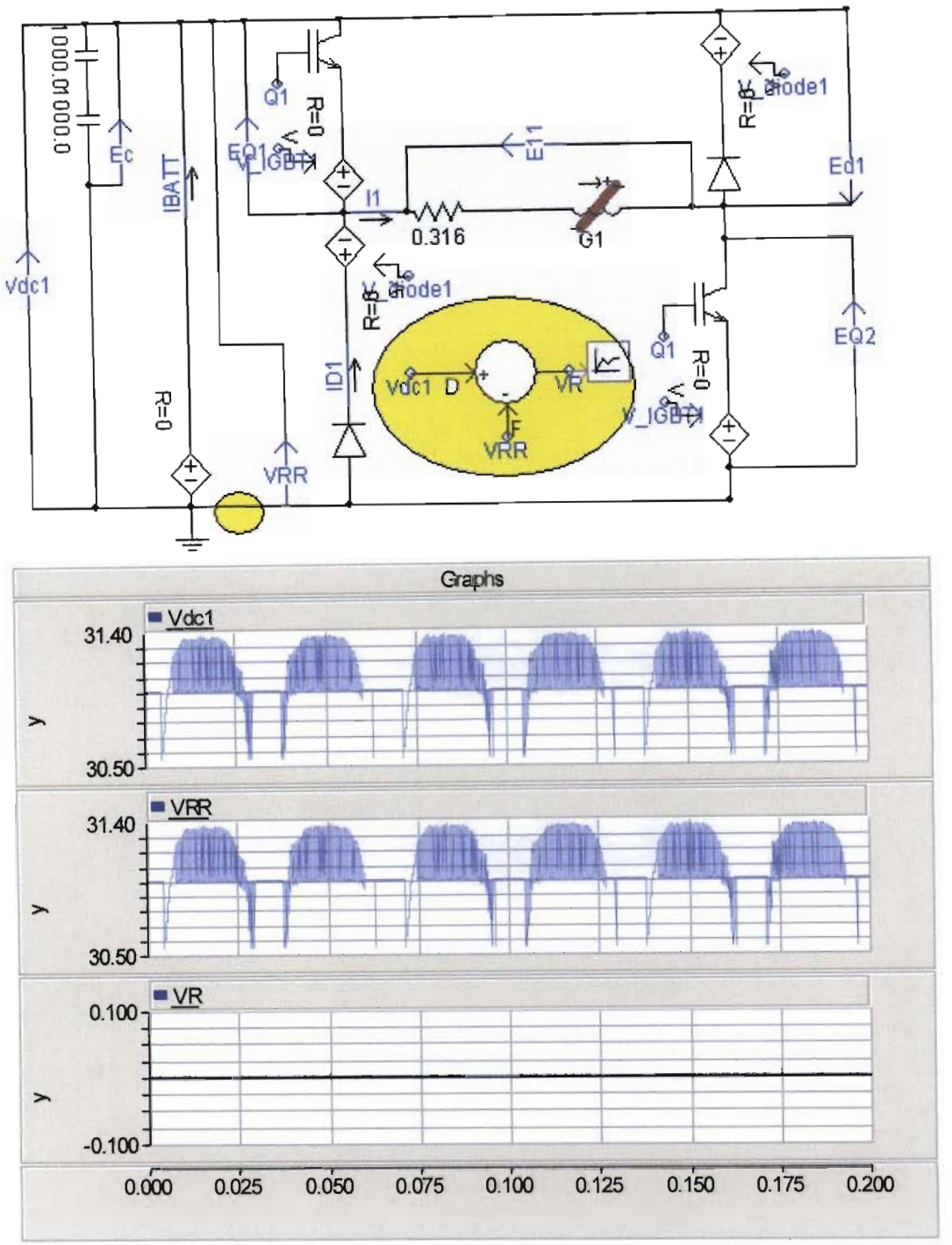

Fig.C.11 voltage results when 0 Ω resistor not in the circuit

There is no indication of any documentation of the observed error. PSCAD does not generate any compilation or run time errors for resistances of zero ohms, as is the case for negative resistances (which produce run time errors). This bug was also only found in the latter stages of writing this thesis (as a result of very detailed analysis and comparison of measured and simulated results) and there was insufficient time to redo all of the simulations

in chapter 4 and 5. However, close agreement between the simulated results in Fig.C.12 (with and without the 0Ω resistor) shows that it's influence is relatively small in these studies.

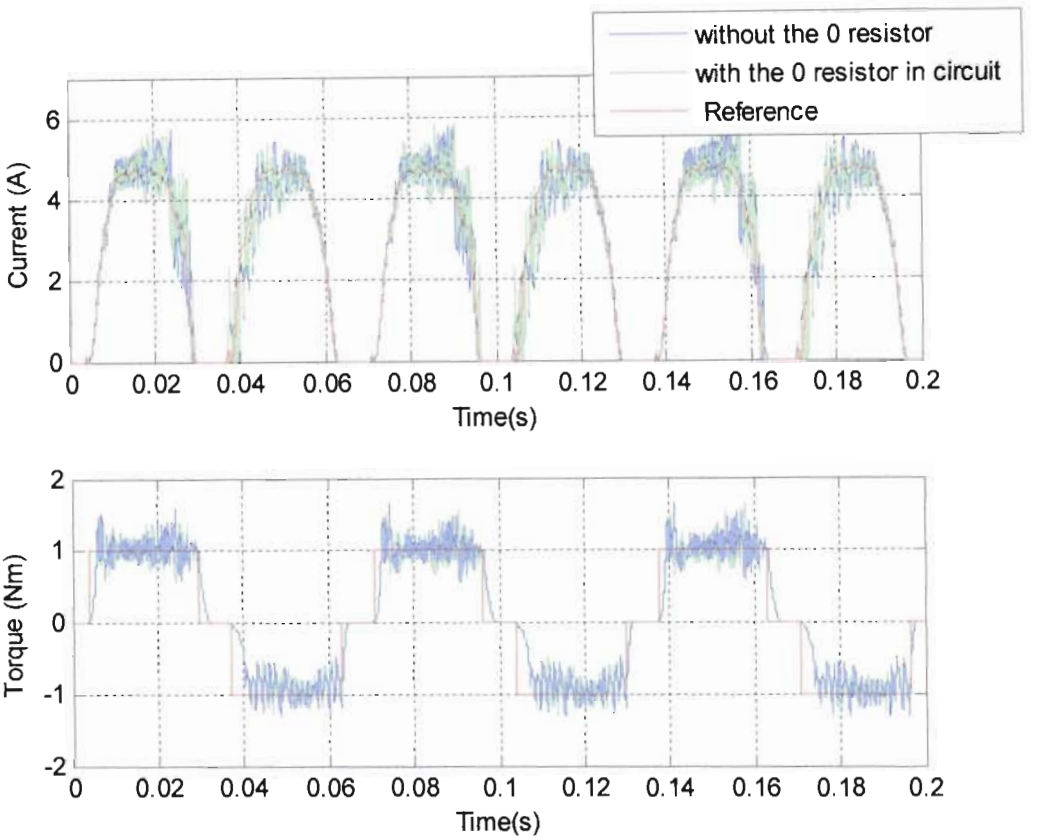

Fig.C.12 Four-phase torque and current response with and without source resistance

Fig.C.13 (a) shows the orginal PSCAD plot of phase 1 voltage shown in Fig.4.23. Fig.C.13(b) shows the same result which is sent to Matlab for plotting. It can be seen that the voltage is not zero before 0.03s and after 0.07s, is it is supposed to be, according to the PSCAD data and PSCAD plot shown in Fig. C.13(a). It is deduced that this error comes from a Matlab graphics scaling problem.

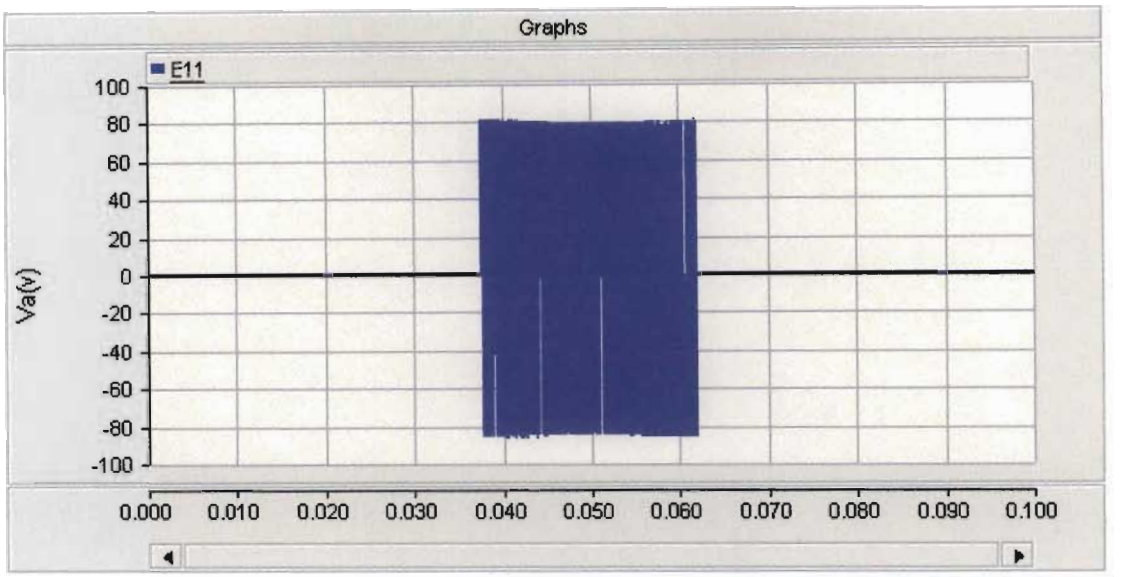

(a)

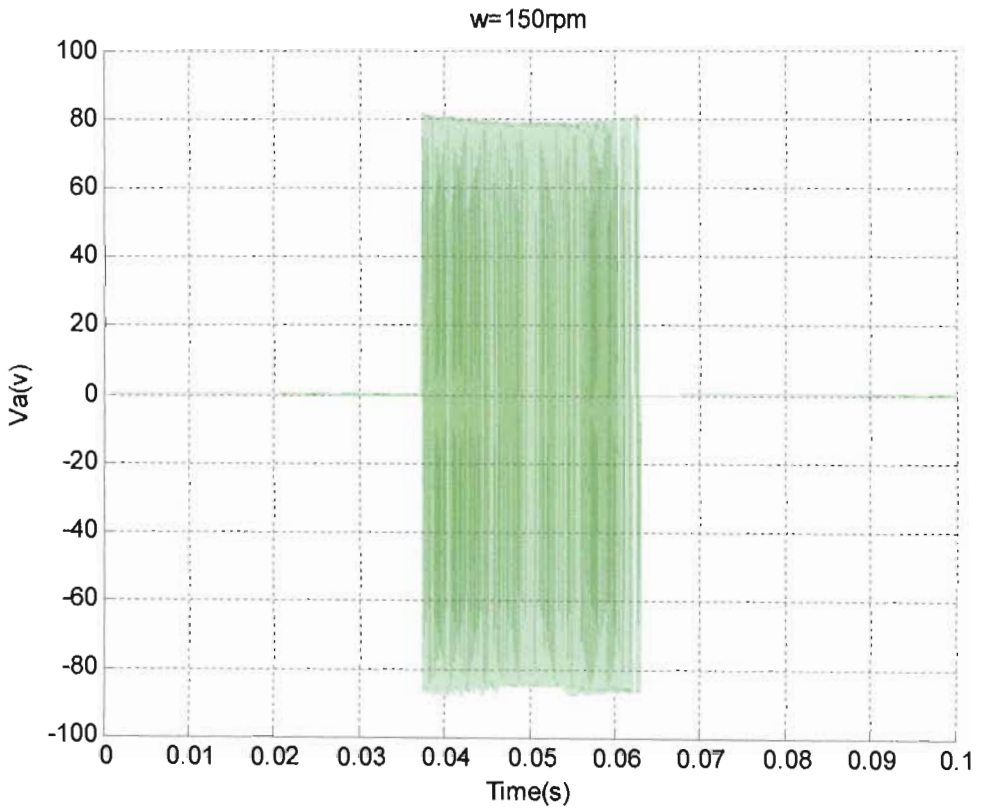

(b)

Fig.C.13 PSCAD plot (a) of phase 1 voltage shown in Matlab plot (b) of Fig.4.23

Fig.C.14 shows the PSCAD phase 1 emf diagram, in which the emf comes from $E=i\frac{d(L(\theta,i))}{dt}$. G1 is the phase 1 inductance; I1 is the phase 1 current.

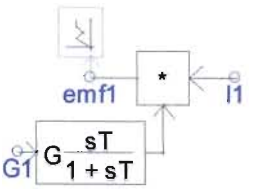

Fig.C.14 PSCAD back emf diagram

APPENDIX D

Practical Implementation Details

This appendix presents technical details (as summarized in table D.1) relating to the practical work and results presented in Chapter 5.

Section	Name	Content Description
D.1	PSCAD diagrams for four phase 8/6 SRM TSF torque and current control	The two PSCAD diagrams used in this chapter for (i) no load free rotor and (ii) speed controlled load simulations
D.2	Comparison of original TSF and corrected TSF	Small anomalies in a published TSF, and effects of removing these anomalies
D.3	VisSim block details	VisSim program details for Fig.5.6
D.4	Mathematical approach to transducer measurement of SRM free rotor torque	Derivation of the SRM torque from the whole system (torque transducer, Induction motor, shaft and coupling)
D.5	Analysis of free rotor test with no load	Estimation of di/dt and sample clock using the ginput () function in Matlab, at no load, with Tref of 0.2Nm. 1.4K Hz PSCAD simulation yields currents very close to the measured responses. Dropped samples in the measured current results are also highlighted.
D.6	Real time DSP sample rate measuring method and results	Measuring diagram and its responses with a sample rate at (a) 1.25K and (b) 2.5K Hz under free rotor test with no load at Tref of 0.2Nm

Table D.1 Appendix D contents

D.1 PSCAD 8/6 SRM TSF Torque and Current Control Diagram

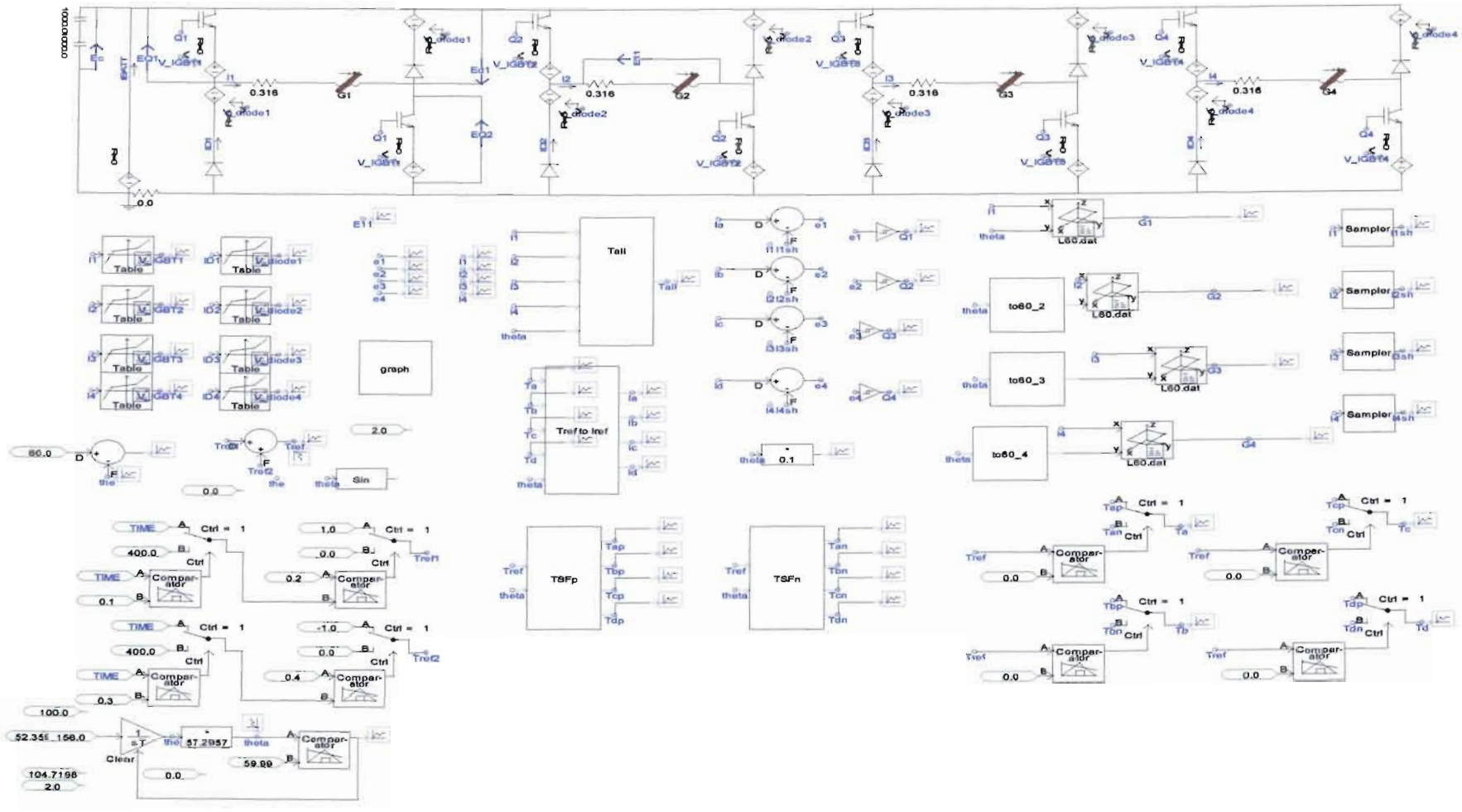

Fig.D.1 Four phase 8/6 SRM torque and current control diagram with speed controlled load

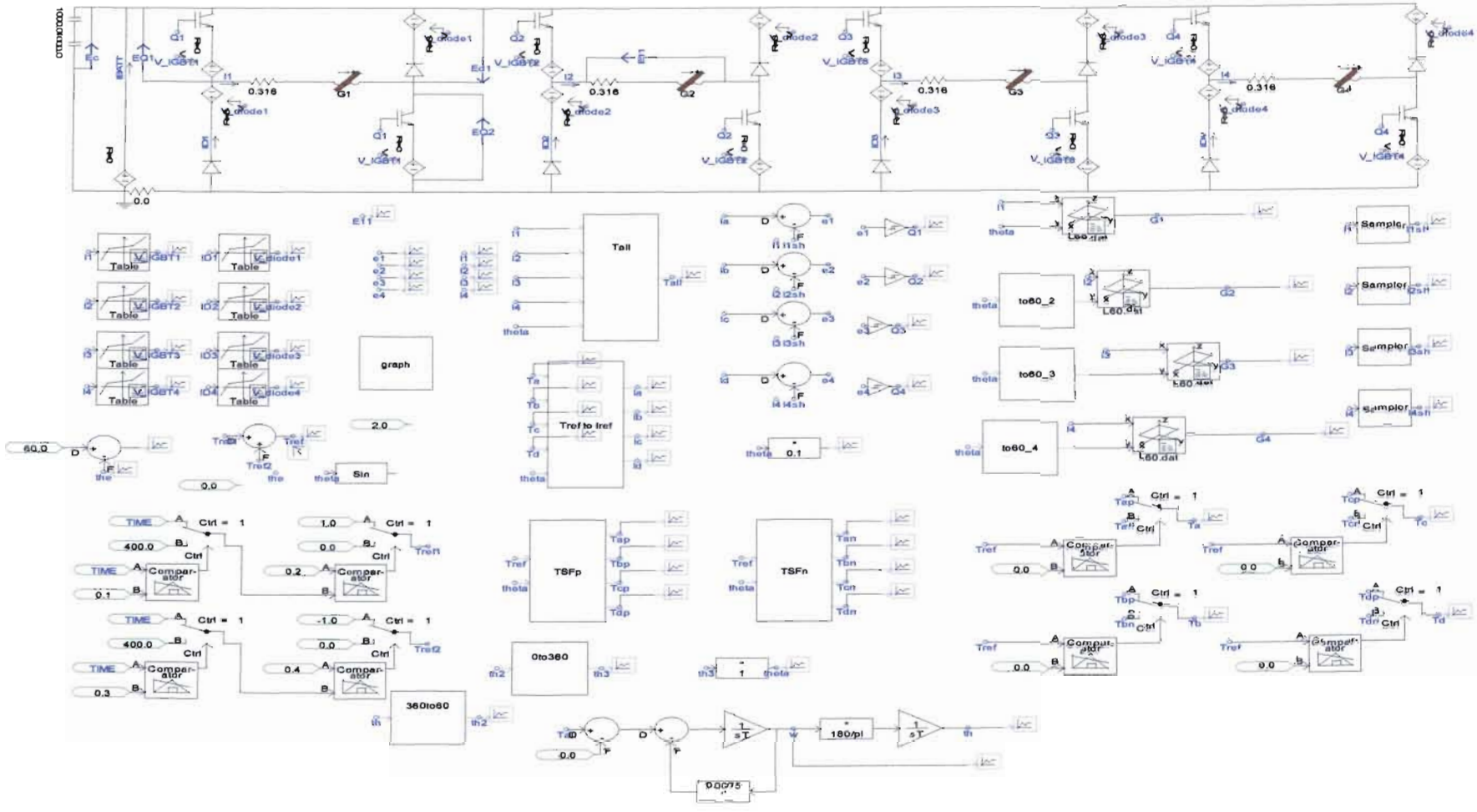

Fig.D.2 Four phase 8/6 SRM torque and current control diagram with no load

D.2 Comparison of Original TSF and Corrected TSF

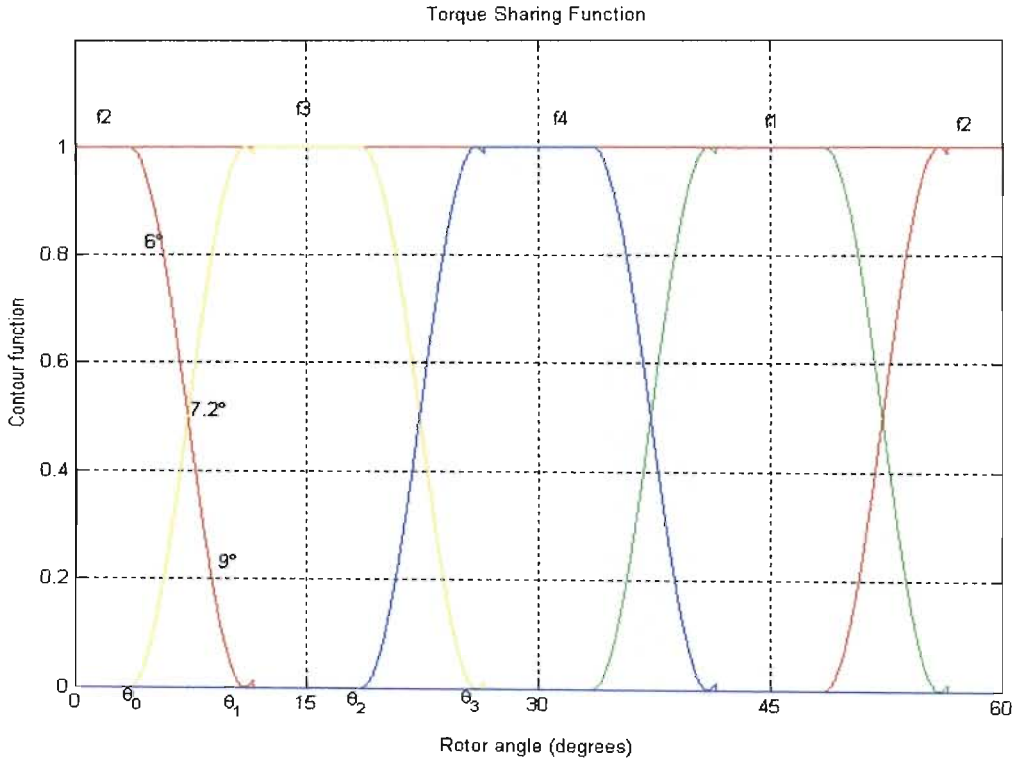

(a)

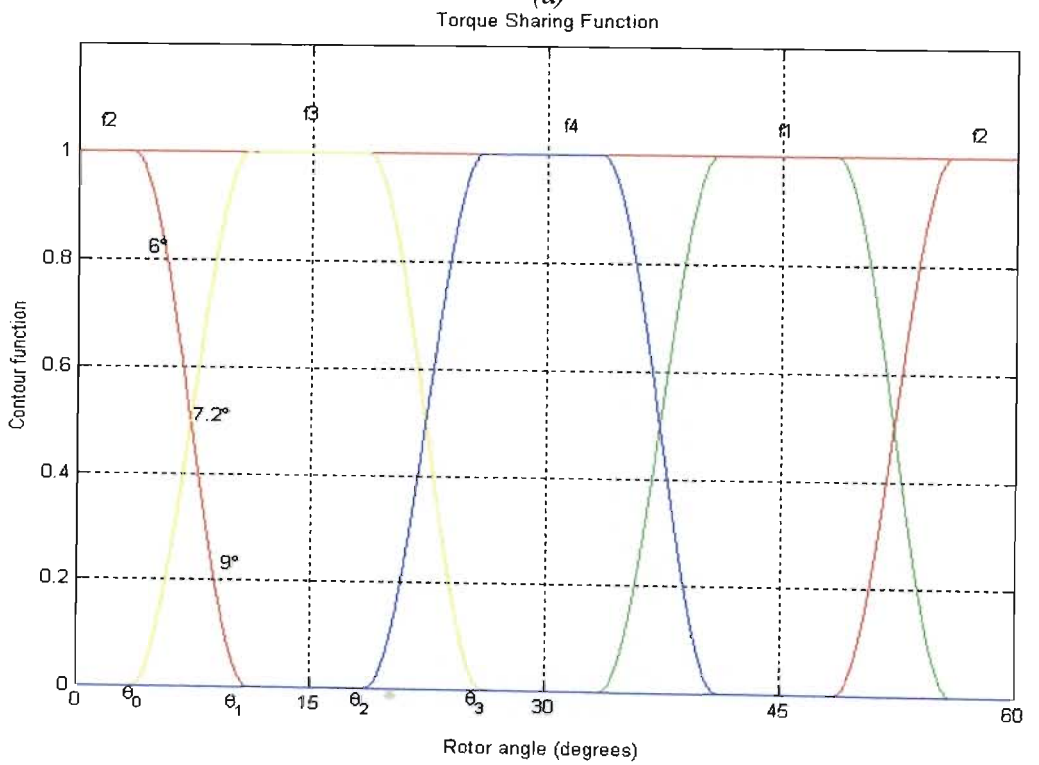

(b)

*Fig.D.3 (a) Original TSF published in [4.6] (*3.5°,11.5°,18.5°,26.5°*), and (b) corrected TSF (*3.5°,11°,18.5°,26°*)*

In Fig.D.4, Tall and I1 are the original responses (obtained with the TSF published in [4.6]) to the 1Nm torque reference (Tref) and corresponding phase 1 current reference (Ia) when the rotor angle is in $(33.5^\circ, 56.5^\circ)$ at a constant speed of 150rpm. Traces "torque of new TSF" and "I1 of the new TSF" are the responses obtained after correcting the TSF commutation angles from $3.5^\circ, 11.5^\circ, 18.5^\circ, 26.5^\circ$ to $3.5^\circ, 11^\circ, 18.5^\circ, 26^\circ$. It can be seen that there are only minor differences between the two sets of current and torque responses.

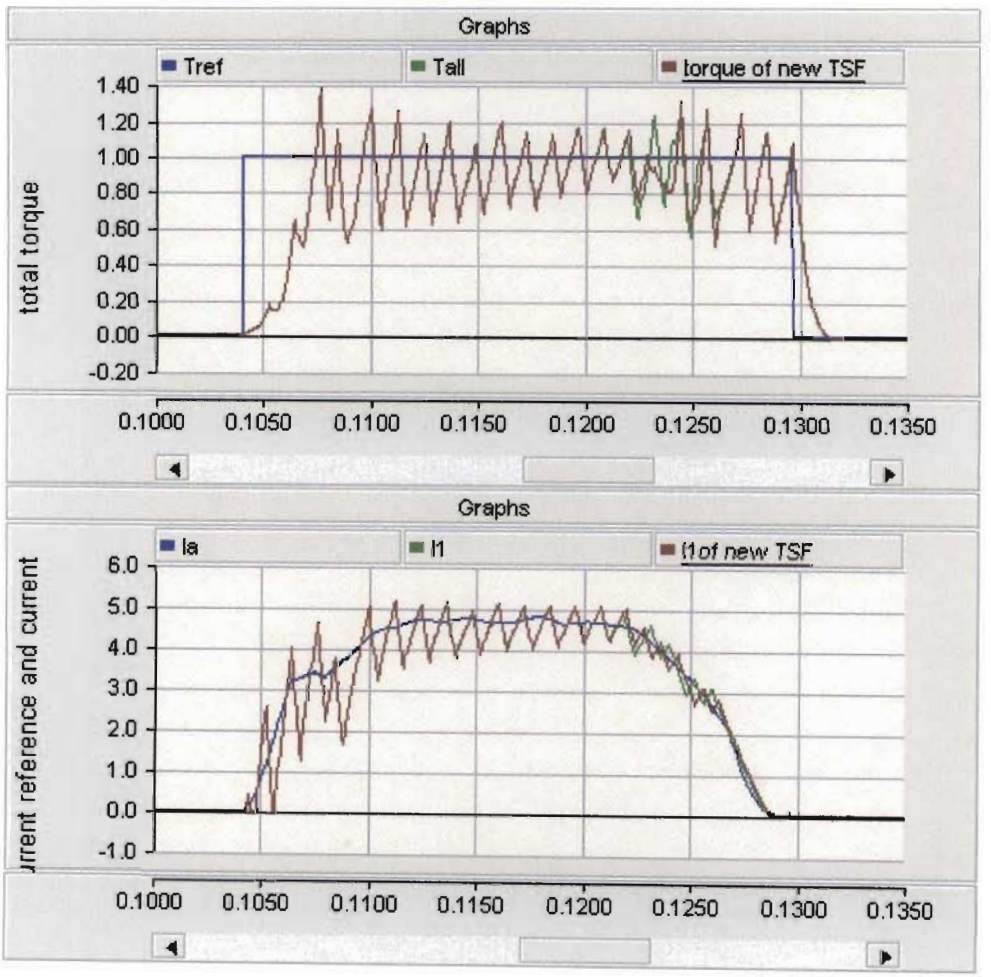

Fig.D.4 Current and torque results

Fig D.5 shows the corresponding responses for a constant torque reference of 7Nm at a speed of 150rpm. Once again there are only slight differences between these results. Therefore, the remainder of the results presented in Chapter 4 (using the TSF of [4.6]) is not re-obtained using the new TSF, but it is suggested that the new, corrected TSF be used in future work.

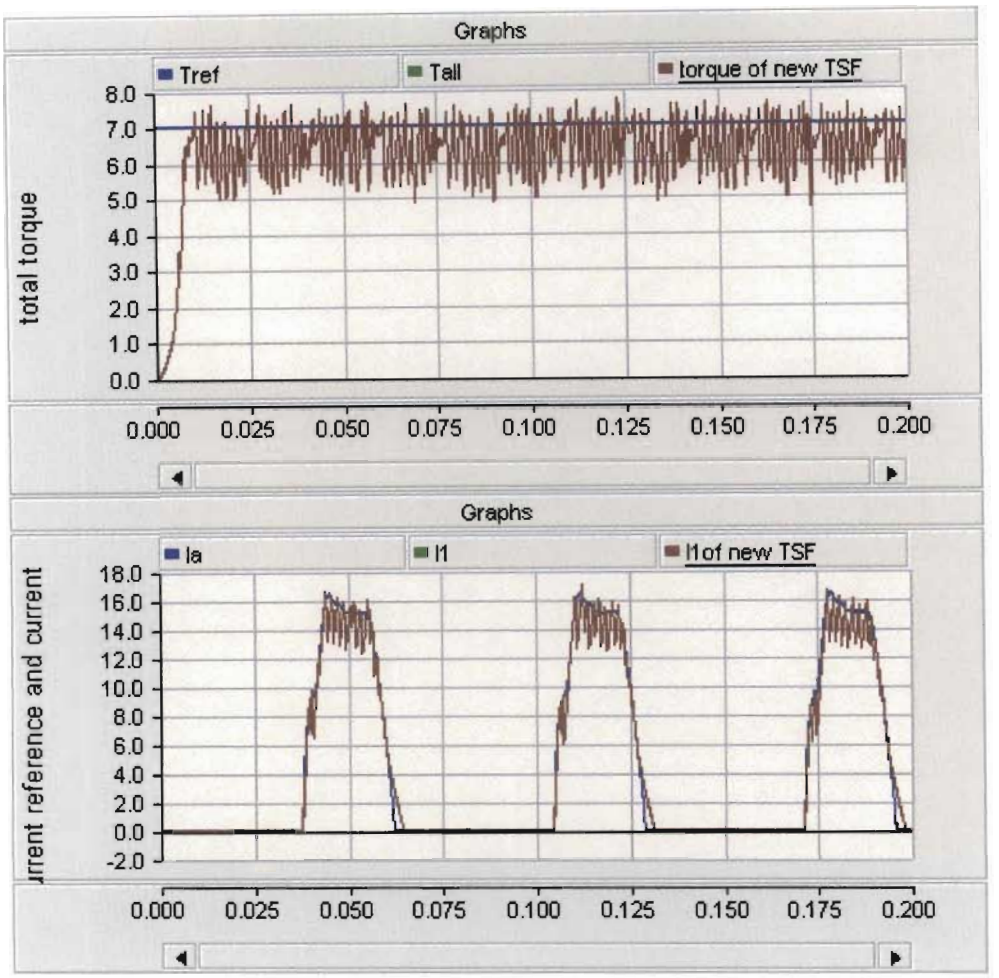

Fig.D.5 Current and torque results

D.3 VisSim Block Details

The contents and functions of the compound block in Fig.5.6 (b) are as follows.

1) ***Measure phase current*** *(use phase 1 as an example)*

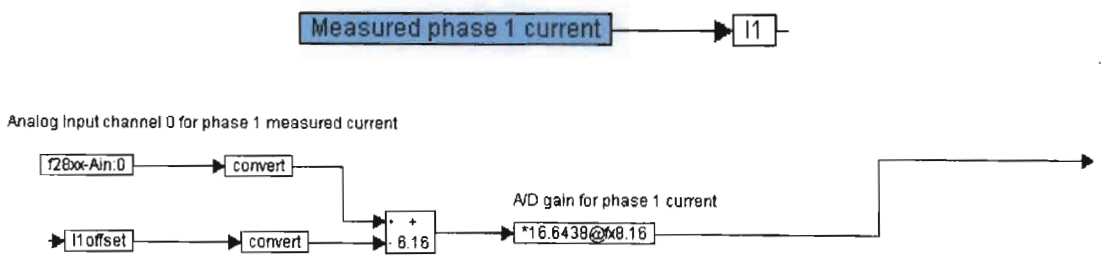

Fig.D.6 Measure phase current

"f28xx-Ain: 0" is the analogue input function block, which outputs a value from 0 to 3 in proportion to the voltages received from the current sensors via one of the Analogue I/O daughter cards described in section 5.2.

2) *Hysteresis current control*

"F28xx-Dout A 0:2" is the digital output block, which sends gate signals to the power converters.

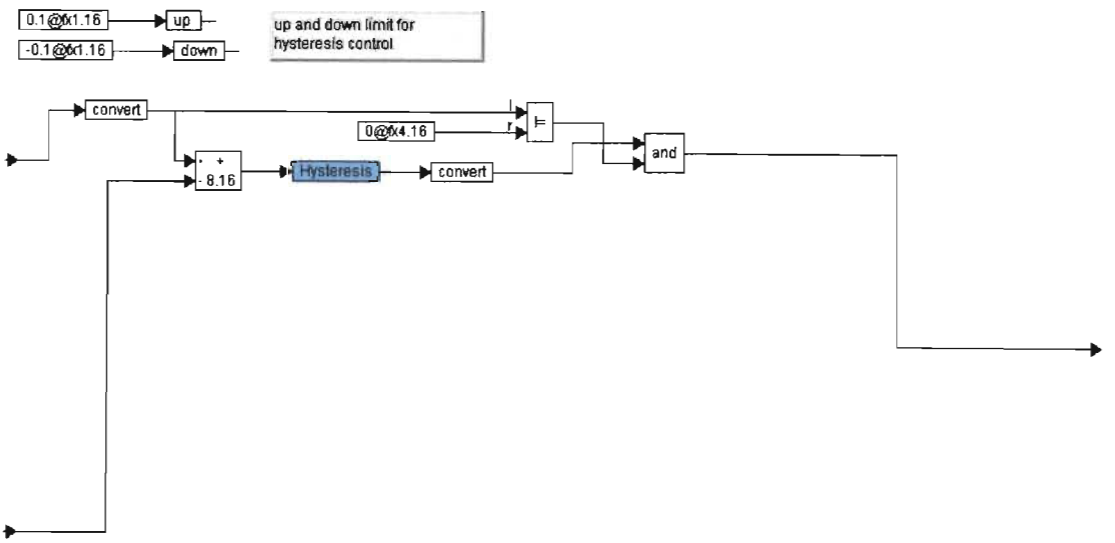

(a) "Hysteresis current control for phase 1" block

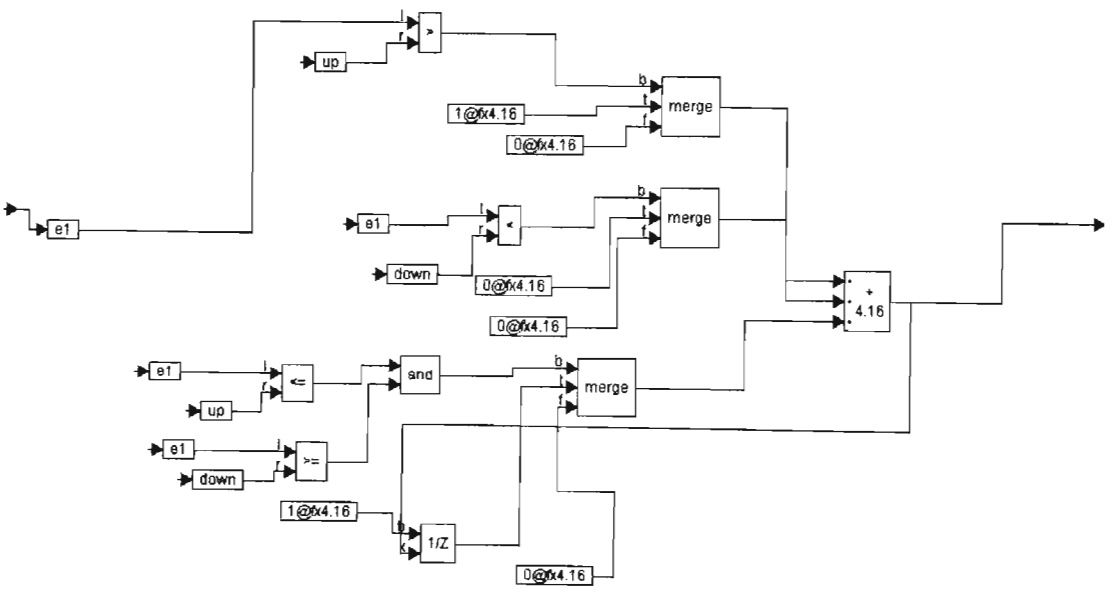

(b) "Hysteresis" block

Fig.D.7 Hysteresis current control

3) *VisSim library functions for rotor angle and speed measurement*

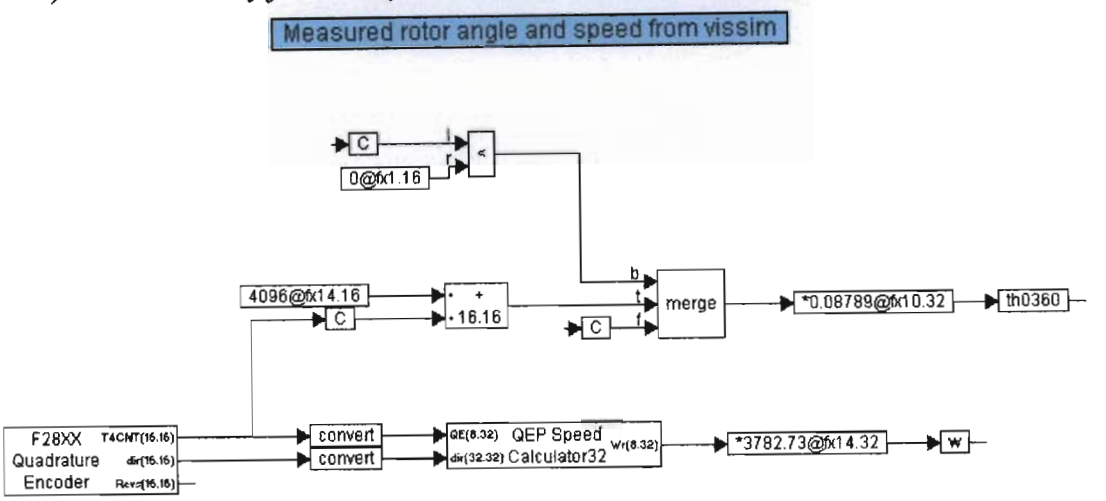

Fig.D.8 rotor angle and speed measurement

'w' is the measured speed.

4) *Wrapping the rotor angle from 0 to 60 degrees*

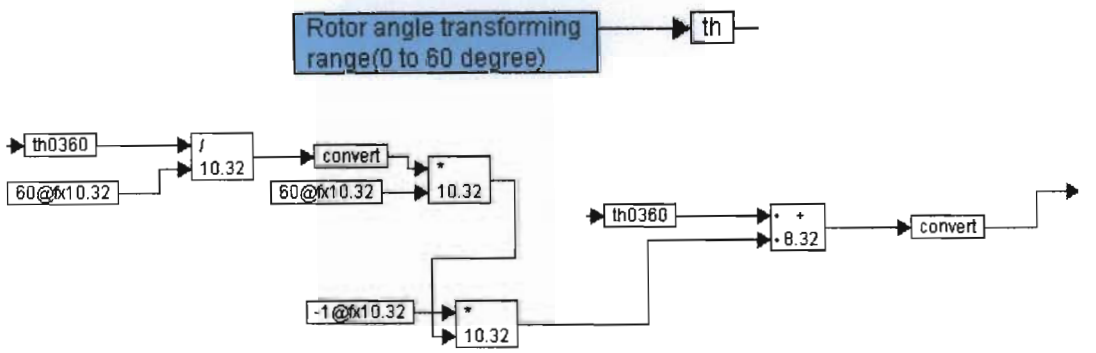

Fig.D.9 wrapping rotor angle from 0 to 60 degrees

'th' is the rotor angle which ranges from 0 to 60 degrees.

5) *Measured torque from transducer for locked rotor test*

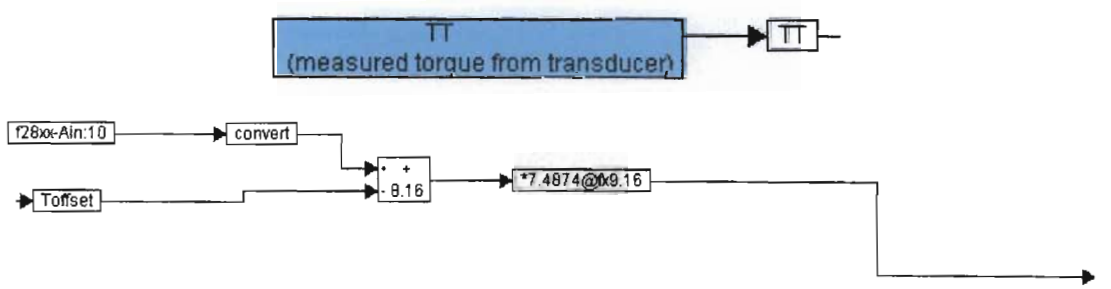

Fig.D.10 Torque transducer measurements

'TT' is the transducer measured torque

6) *Estimated torque from lookup table*

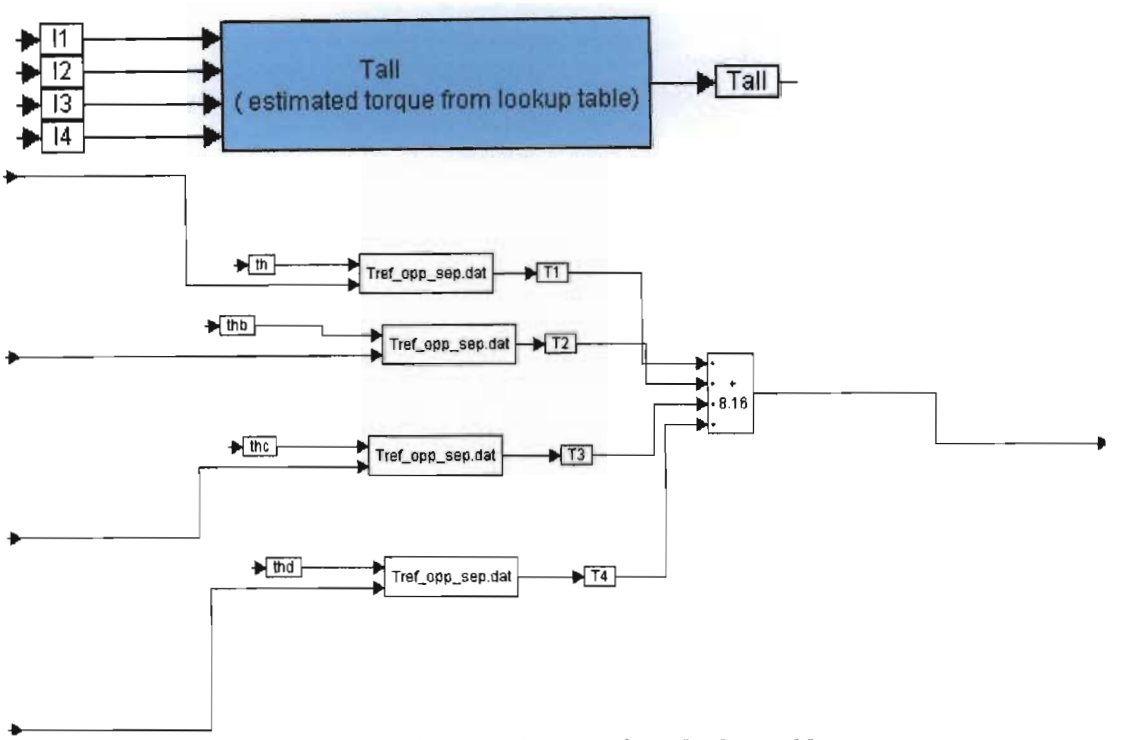

Fig.D.11 Estimated torque from lookup table

'Tall' is the estimated torque.

7) *Torque sharing function and current reference*

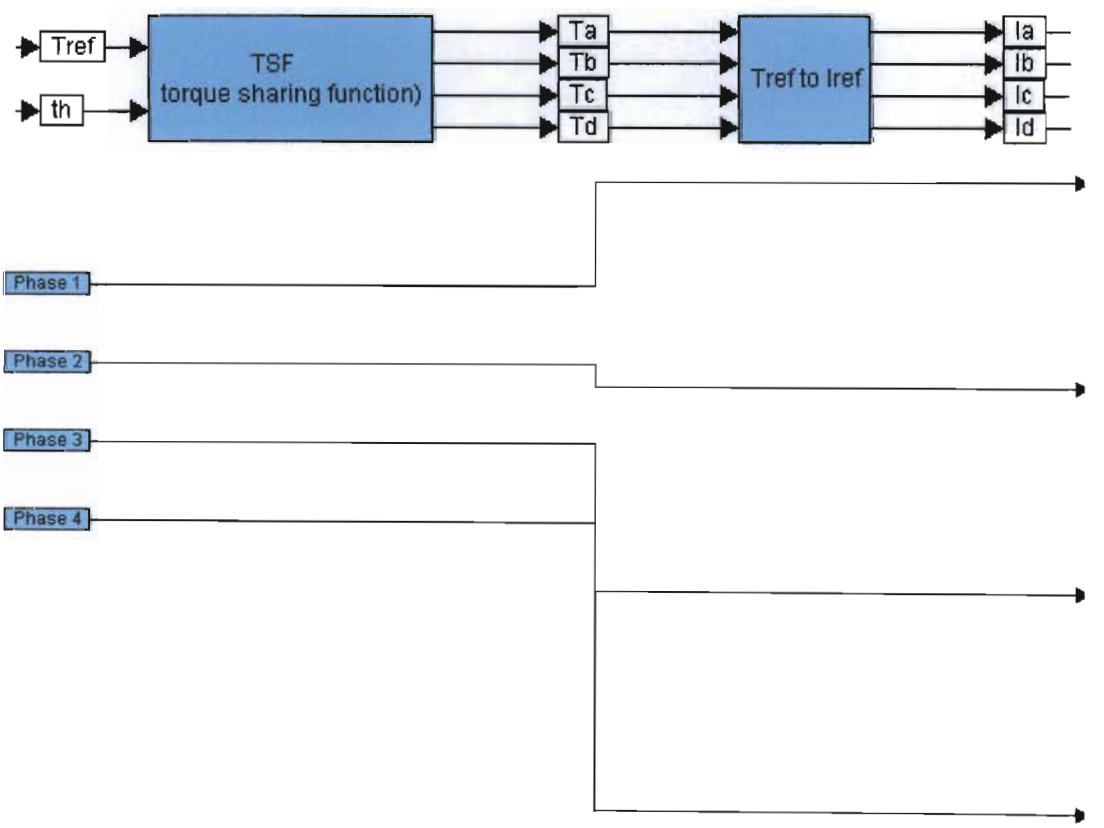

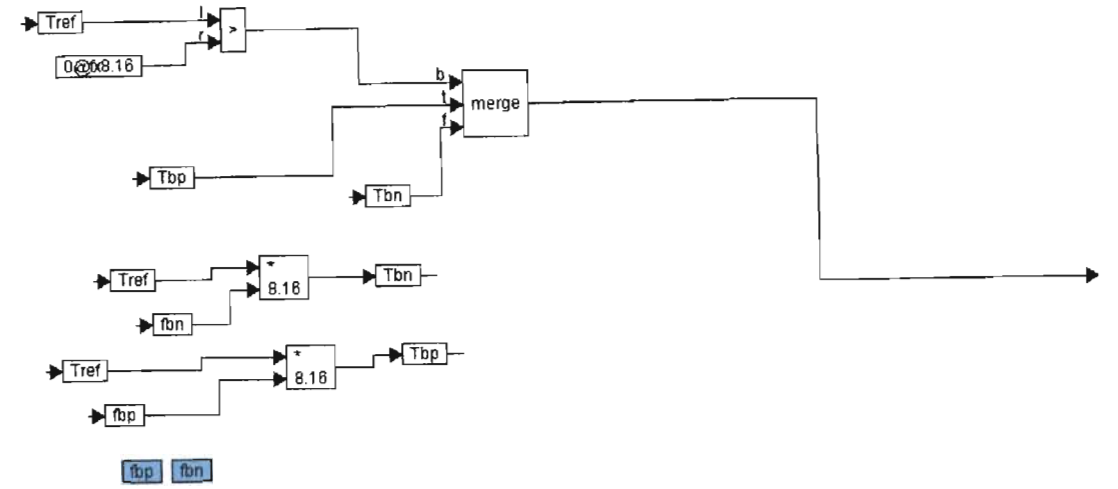

"Phase 2" block

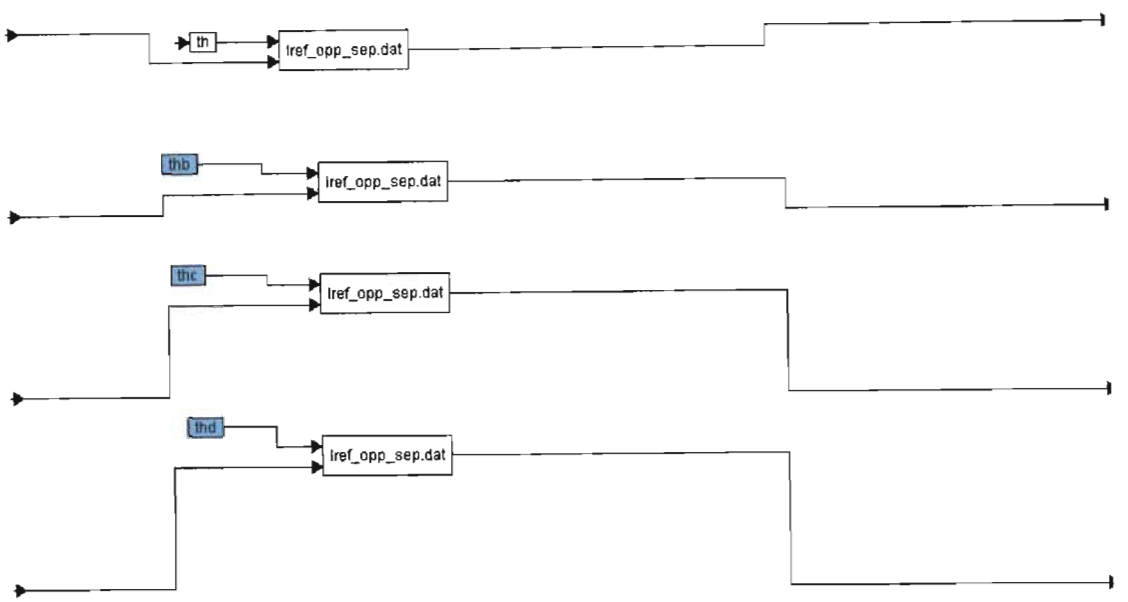

"Tref to Iref" block

Fig.D.12 TSF (torque sharing function) and current reference

'Ta, Tb, Tc, Td' represents the torque reference for phase1 to 4. 'Ia, Ib, Ic, Id' represents the current reference for phase1 to 4.

Comment:

"Tref_opp_sep.dat" and "Iref_opp_sep.dat" are lookup table blocks for estimated torque and current reference respectively. Each phase needs one copy of each of these tables in the diagram. However, the VisSim compiler automatically optimizes the four tables for estimated torque (e.g. Tref_opp_sep.dat) to be one table and it has the same effect for current reference lookup tables [Ref D.1].

D.4 Transducer Measurement of SRM free rotor torque

The setup of transducer measurement of SRM free rotor torque is shown in Fig.D.13. The Induction motor and SRM are via a torque transducer to measure SRM torque. Locked rotor SRM torque is measured by locking the induction motor shaft and observing the resulting torque transducer output directly. Measurement of SRM torque under free rotor conditions cannot be done directly, but can be inferred from the transducer output, based on the following assumptions.

- Couplings have identical mechanical characteristics (torsional stiffness)
- The torque transducer output is negligible when no torque applies on either side
- The moment of inertia of the transducer is negligible

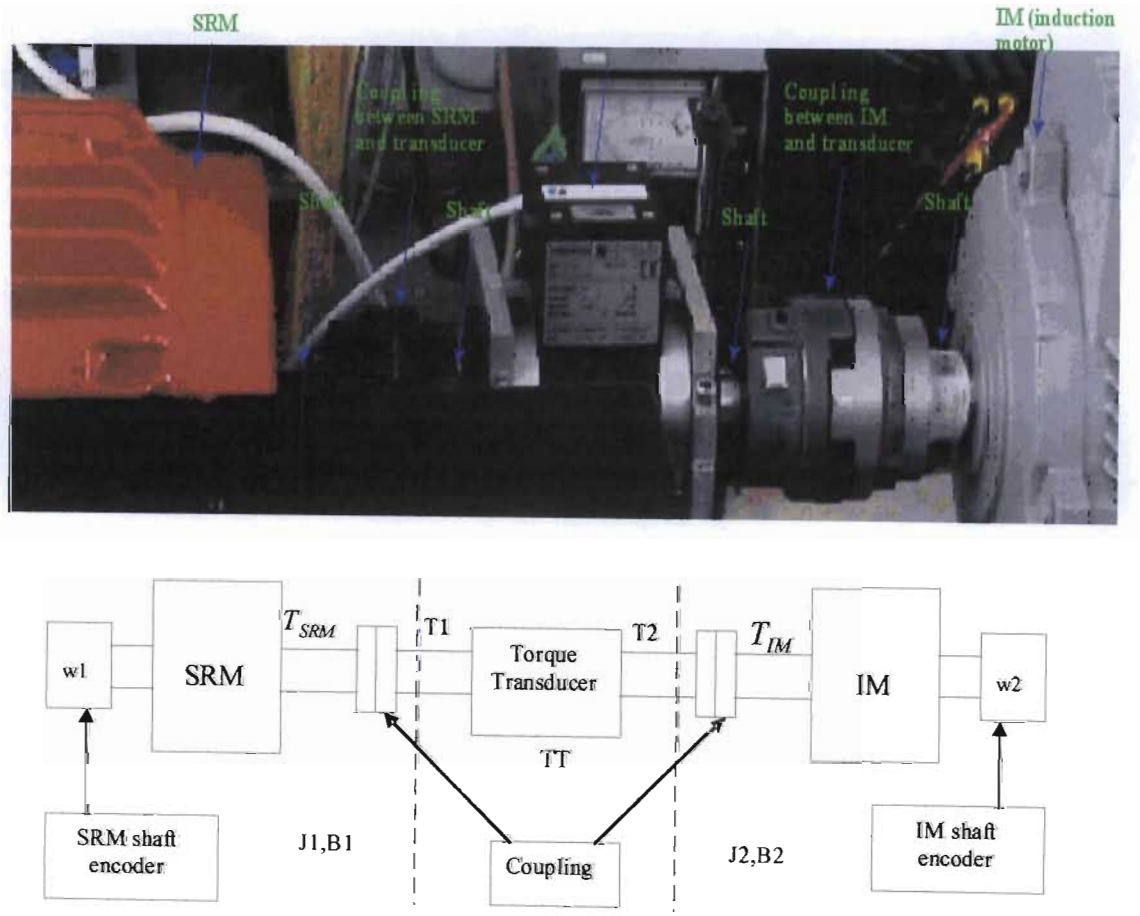

Fig.D.13 Setup of Transducer Measurement of SRM free rotor torque

J1and B1 are the moment of inertia and friction coefficient for the SRM side. J2 and B2 are the moment of inertia and friction coefficient for the IM side. T1 is the torque from the SRM side, and T2 is the torque from the IM side of the transducer. *TT* is the torque transducer

output value. T_{SRM} is the torque produced by the SRM; T_{IM} is the torque applied by the Induction motor. The SRM shaft speed is w1, and the induction motor shaft speed is w2 (the shaft speed has the same direction as the torque for both sides).

The torques developed on the either side of the transducer are

$$T1 = T_{SRM} - J1\frac{dw1}{dt} - B1w1, \text{ and} \tag{D.1}$$

$$T2 = T_{IM} - J2\frac{dw2}{dt} - B2w2. \tag{D.2}$$

The transducer value is

$$TT = T1 - T2. \tag{D.3}$$

The instantaneous SRM torque can therefore be estimated as

$$T_{SRM} = TT + T_{IM} - J2\frac{dw2}{dt} - B2w2 + J1\frac{dw1}{dt} + B1w1, \tag{D.4}$$

but the accuracy of this estimate will depend on the accuracy of the estimates available for J1 and J2, and for B1 and B2 for the corresponding instantaneous values of measured shaft speeds w1 and w2 (i.e. two shaft encoders are required).

D.5 Analysis of Free Rotor Test with No Load

Section D.5 and D.6 shows the analysis for free rotor test with no load for a torque reference of 0.2Nm. Fig.D.14 shows the measured/simulated (a) zoomed phase 1 current, (b) estimated di/dt and (c) re-constructed sampling clock waveforms obtained from Fig.5.14. The accuracy of the di/dt estimates are limited by two factors, namely the fact that the current was only sampled at the turning points, and that this sampling was done manually using the "point&click" ginput () function.

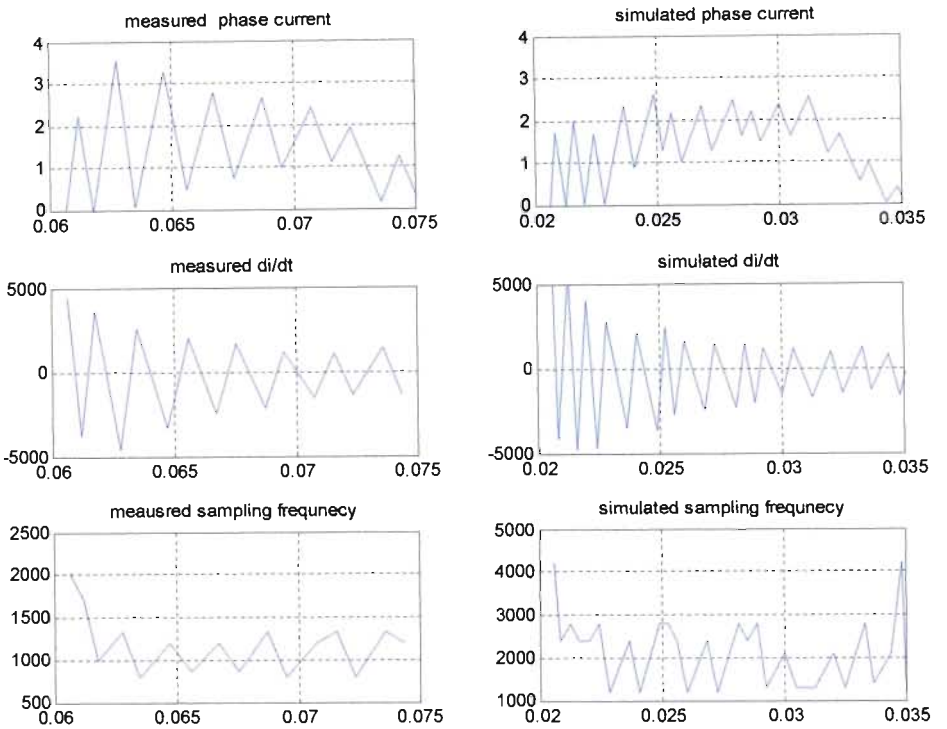

Fig.D.14 Measured/ simulated zoomed phase 1 current, di/dt and sampling frequency results which are obtained from Fig.5.14.

It can be seen from Fig.D.14 that the measured and simulated di/dt estimates have similar envelopes, peak, and "steady state" values. This indicates that the electrical model closely matches the physical system. The average DSP sampling frequency is estimated to be approximately 1.2 KHz, and the average PSCAD sampling frequency is estimated to be 2.2 KHz in this test. It was however observed that the DSP results were most closely matched those produced by PSCAD when a sampling frequency of 1.4kHz was used to simulate this particular case, as shown in Fig. D.15. The nominal DSP sampling rate of 2.5kHz was, however, used to produce all of the comparative simulation results in Chapter 5.

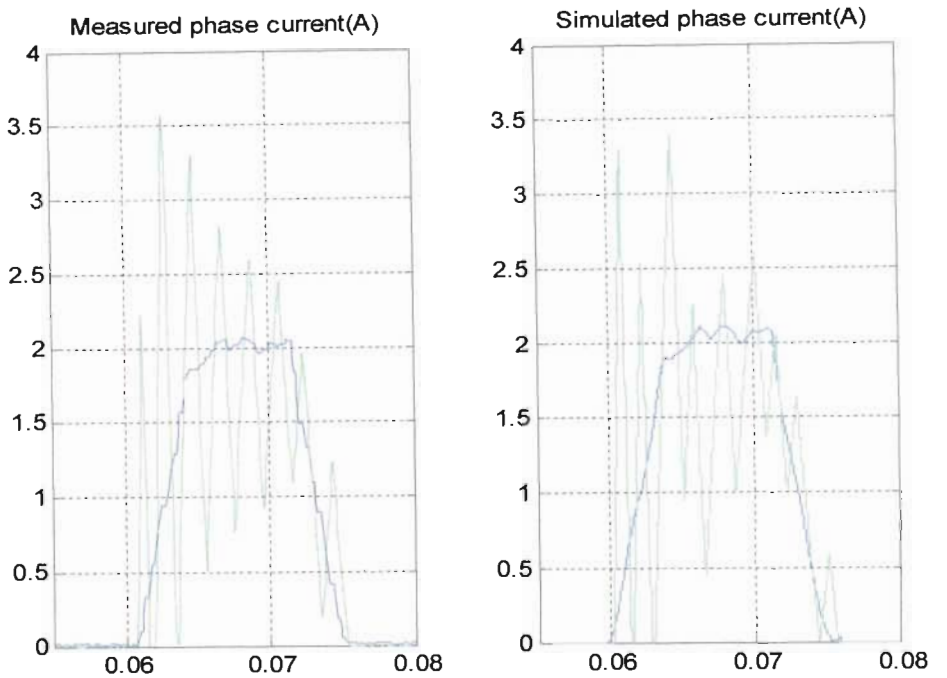

Fig.D.15 Measured/ simulated current when PSCAD sampling frequency is 1.4 KHz

Fig.D.16 shows the measured and simulated current responses, and reconstructions of the corresponding sampling clock waveforms (obtained from the anT02.m program shown on page D.16).

The green circles in Fig. D.16 indicate sampling clock transitions where I1 is too close to Ia to determine whether or not a switching event should have occurred (due to inaccuracies in the sample clock waveform reconstruction and synchronization and plotting resolution, as can be seen from small misalignments between actual switching events and reconstructed sample clock transitions). It is therefore not possible to determine whether these samples were dropped by the DSP or not. The blue circles in Fig.D.16 (a), however, clearly show points where switching events should have occurred but did not due to dropped samples. In all cases, in this test, the required switching action is delayed by one sampling period, which causes significantly higher current ripple and hence torque ripple in the measured results. The next section presents the method used to monitor the sampling rate in real time in order to detect sample dropping.

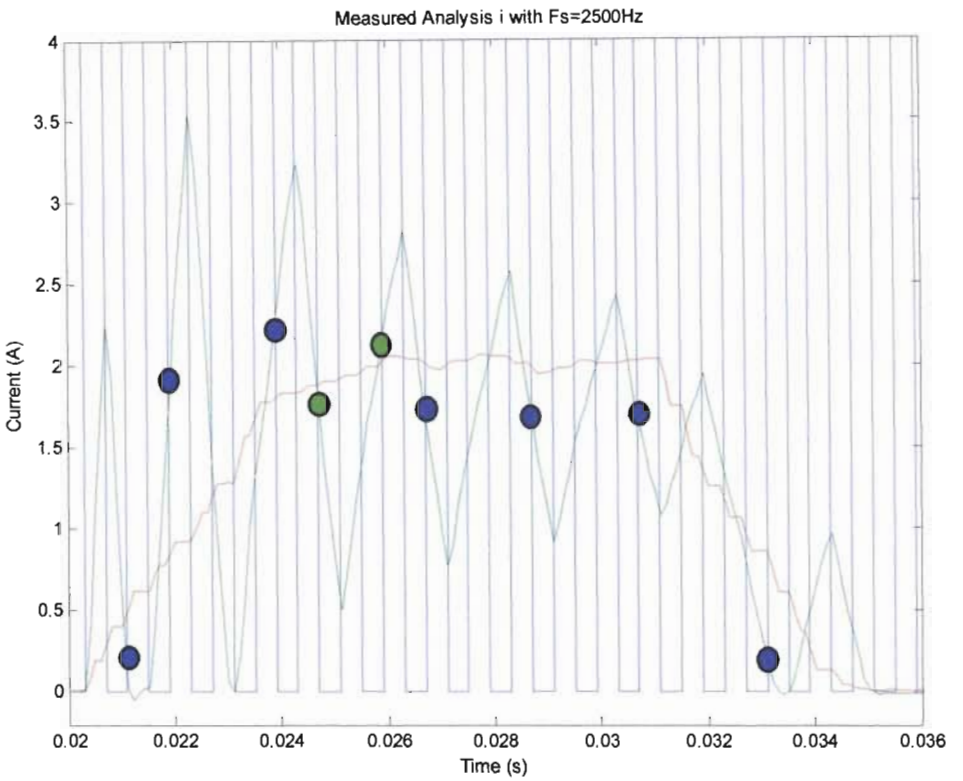

(a) Measured

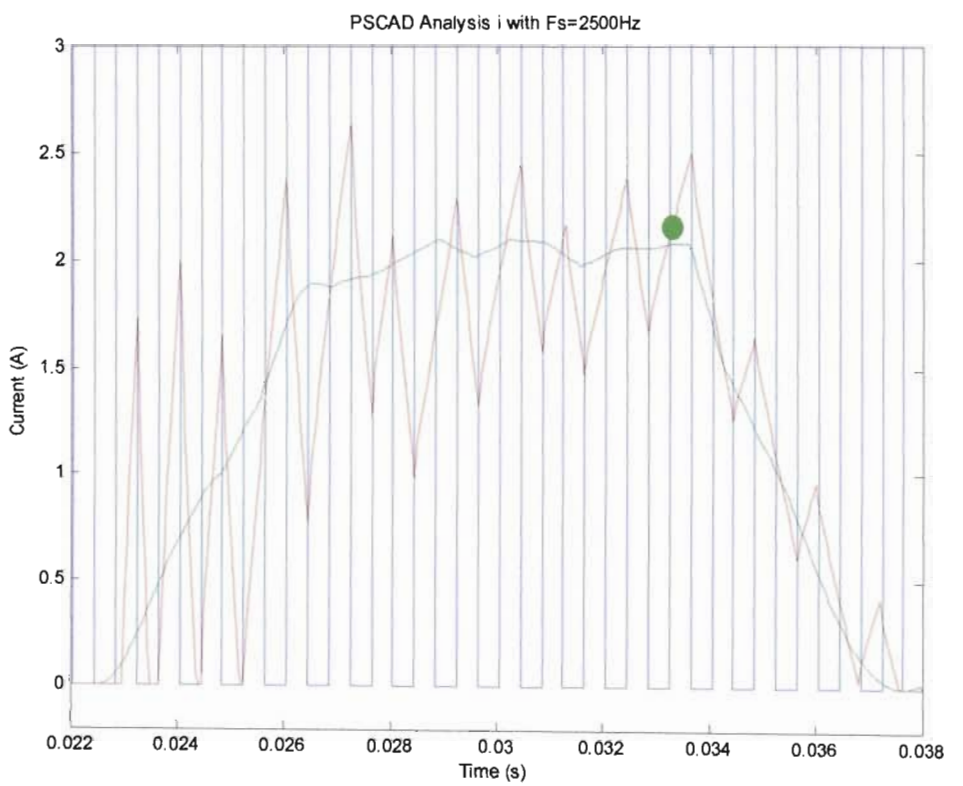

(b) Simulated

Fig, D.16 Measured/simulated current and sampling frequency analysis under free rotor no load test with a Tref of 0.2Nm

```
%anT02.m

load new02
tm=0.0203; %the measured instant of the first switching event
(obtained graphically)
tstart=0;
tend=0.2
tb=linspace(tstart,tend,100000);

s=cos(2*pi*2500*(tb+tm)/2);
S=sign(s);
figure(91);plot(tb,4*(S+1),t,I1_02,t,Ia_02)
title('Measured Analysis i with Fs=2500Hz')

s=cos(2*pi*1250*(tb+tm)/2+pi/4);
S=sign(s);
figure(92);plot(tb,4*(S+1),t,I1_02,t,Ia_02)
title('Measured Analysis i withFs=1250Hz')

tp=.02325; %the PSCADinstant of the first switching event (obtained
graphically)

s=cos(2*pi*2500*(tb+tp)/2+pi/4);
S=sign(s);
figure(93);plot(tb,4*(S+1),t_PSCAD,PSCAD_I2,t_PSCAD,PSCAD_i2)
title('PSCAD Analysis i with Fs=2500Hz')

tp=0.02275;
s=cos(2*pi*1250*(tb+tp)/2+pi/2);
S=sign(s);
figure(94);plot(tb,4*(S+1),t_PSCAD,PSCAD_I2,t_PSCAD,PSCAD_i2)
title('PSCAD Analysis i withFs=1250Hz')
```

D.6 Real time DSP sample rate measuring method and results

Fig.D.17 shows the real time DSP sample rate measuring diagram. This block is included in the main compound block, and should therefore execute at the same rate as all of the other code in the corresponding DSP interface. The measured sample rates in Fig D.18, however, indicate that sampling rates of both 1.25kHz and 2.5kHz are maintained without sample dropping, while the measured current response clearly shows the same dropped sample effect seen in the detailed analysis of Fig.D.16.

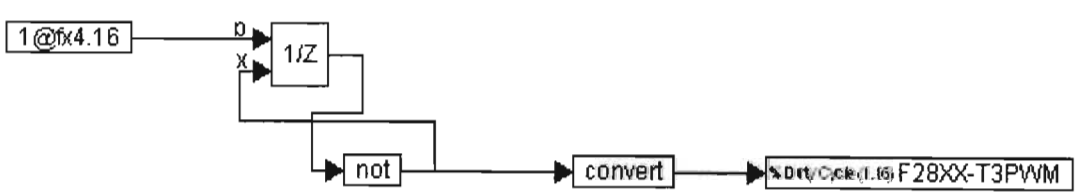

Fig.D.17 DSP sample rate measurement diagram

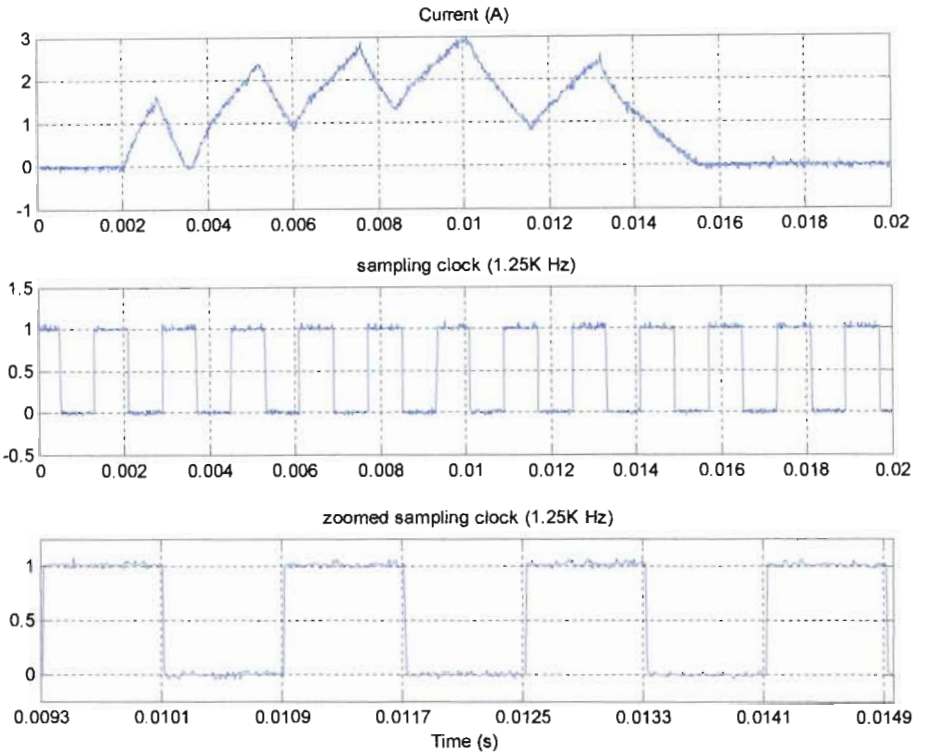

(a)

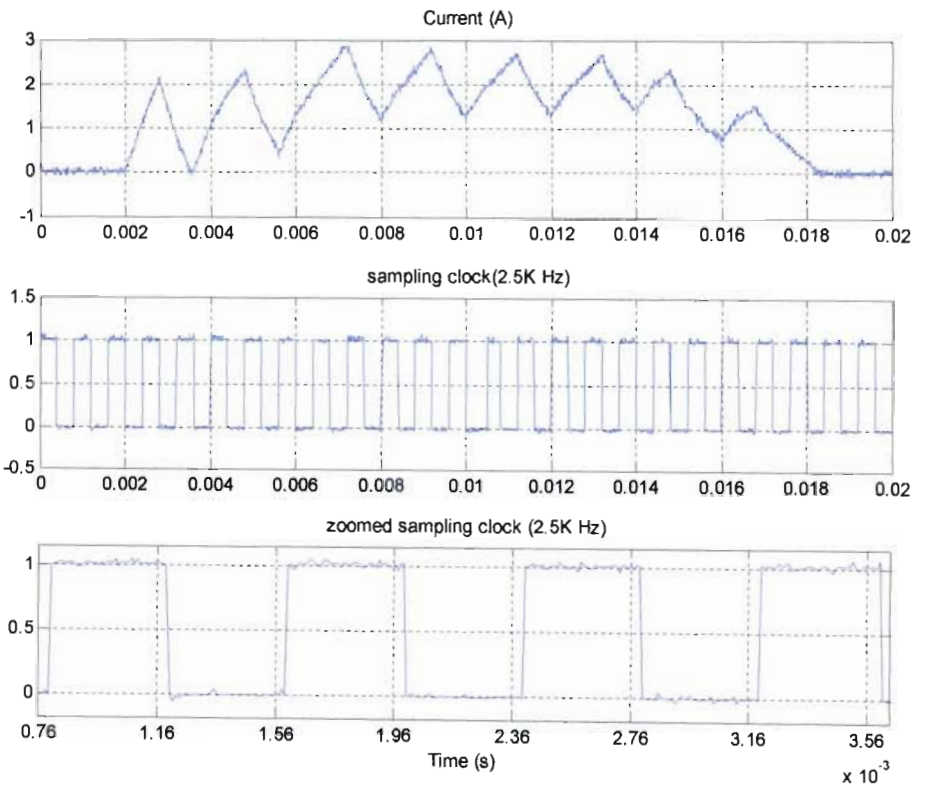

(b)

Fig.D.18 Measured responses with a sample rate at (a) 1.25K and (b) 2.5K Hz under free rotor no load test with a Tref of 0.2Nm

REFERENCES

[1.1] S.A.NASAR, *"DC Switched Reluctance motor"*, Proceedings IEE, Vol.116, N6, 1969, pp.1048-9.

[1.2] R. Krishnan, *"Modeling, Simulation, Analysis, Design, and Applications"*, Industrial Electronics Series, CRC Press, 200.

[1. 3] Adrian Ddavid Ccheok, Tan Siew Chong and Wang Zhongfang, *"Real-time computer-based torque measurement of Switched Reluctance Motors"*, INT. J.ELECTRONICS, 2002, VOL. 89, NO. 9, pp.693–715.

[1.4] Naveen Yadlapalli, "*Implementation of a novel soft-switching inverter for switched reluctance motor drives*", MSc Eng thesis, Virginia Polytechnic Institute and State University, 1999.

[1.5] Sen Wang, Bruce Burton and Ron. G. Harley, *"Switched Reluctance Motor Measurements and Simulation Models"*, SAUPEC2004 (SOUTHERN AFRICAN UNIVERSITIES POWER ENGINEERING CONFERENCE), University of Stellenbosh, South Africa, Jan, 2004, CDROM.

[1.6] Sen Wang, Bruce Burton and Ron. G. Harley, *"Switched Reluctance Motor Modeling and Torque and Current Controller Studies in PSCAD"*, SAUPEC2005, University of the Witwatersrand, South Africa, Jan, 2005, CDROM.

[1.7] Sen Wang, Bruce Burton and Ron. G. Harley, *"Switched Reluctance Motor Measurements and Simulation Models"*, AFRICON, 2004. 7th AFRICON Conference in Africa, Volume 2, 2004 Page(s):1161 - 1167 Vol.2.

[2.1] Buja GS and Valla MI, *"Control Characteristics of Switched-Reluctance Motor Drive"*, Proceedings of the IEEE International Workshop on Intelligent Motion Control, 20-22 August 1990, Vol.2 , pp 675 – 682.

[2.2] D. A. Torrey and J. H. Lang, *"Modeling a nonlinear variable-reluctance motor drive"*, IEE Proceedings on Electric Power Applications, Vol.137, Sep, 1990, pp 314-326.

[2.3] Yinghui, Lu, *"Instantaneous Torque Control of Switched Reluctance Motors"*, MSc Eng Thesis, the University of Tennessee, Knoxville, Aug, 2002.

[2.4] Ramu, Krishnan, *"Switched Reluctance Motor Drives: Modelling, Simulation, Analysis, Design and Applications"*, CRC press, Florida, USA, 2001.

[2.5] Cui P, Zhu JG, Ha QP, Hunter GP and Ramsden VS, *"Simulation of nonlinear switched reluctance motor drives with PSIM"*, Proceedings of the Fifth International Conference on Electrical Machines and Systems, Shenyang, China, 18-20 Aug. 2001, Vol. 2, pp1061 - 1064.

[2.6] Gao Yuan, *"Speed Control of Switched Reluctance Motors"*, MSc Eng Thesis, Hong Kong University of Science and Technology, Aug, 2000.

[3.1] Sayeed Mir, *"Classification of SRM Converter Topologies for Automotive Applications"*, Society of Automotive Engineers, Inc.2000.

[3.2] A.Hava, V.Blasko, and T.A.Lipo, *"A modified C-dump converter for variable reluctance machines"*, Industry Applications, IEEE Transactions on, Volume 28, Issue 5, Sept.-Oct. 1992 Page(s):1017 – 1022.

[3.3] Naveen Yadlapalli, *"Implementation of a Novel Soft-Switching Inverter Topology for Switched Reluctance Motor Drives"*, MSc Eng Thesis, Virginia Polytechnic Institute and State University, July, 1999.

[3.4] *"PSCAD 4.0.3 User's Guide"*, Manitoba HVDC Research Centre, 2003.

[3.5] Mehrad Ehsani, Iqbal Husain, K.R.Ramani and James H.Galloway, *"Dual-Decay Converter for Switched Reluctance Motor Drives in Low-Voltage Application"*, Power Electronics, IEEE Transactions on, Volume 8, Issue 2, April 1993 Page(s):224 – 230.

[3.6] M.Ehsani, J.T.Bass,T.J.Miller,and R.L.Steigerwald, *"Development of a uniploar converter for variable reluctance motor drives"* IEEE Trans. Ind. Appl., vol, IA-23, May/June 1987, pp. 545-553.

[3.7] Yong-Ho Yoon, Sang-Hoon Song, Tae-Won Lee, Chung-Yuen Won, Young-Real Kim , *"High Performance Switched Reluctance Motor Drive for Automobiles using C-dump Converters"*, 2004 IEEE International Symposium on, Volume 2, 04-07 May 2004 Page(s):969 – 974.

[3.8] Sayeed Mir, *"Energy efficient C-dump Converters for Switched Reluctance Motors"*, Power Electronics, IEEE Transactions on, Volume 12, Issue 5, Sept. 1997 Page(s):912 – 921.

[4.1] Iqbal Husain, *"Minimization of Torque Ripple in SRM Drives"*, Industrial Electronics, IEEE Transactions on, Volume 49, Issue 1, Feb. 2002 Page(s):28 – 39.

[4.2] Richard S. Wallace, David G. Taylor, *"A Balanced Commutator for Switched Reluctance Motors to Reduce Torque Ripple"*, Power Electronics, IEEE Transactions on, Volume 7, Issue 4, Oct. 1992 Page(s):617 – 626.

[4.3] Krzysztof Russa, Iqqbal Husain, Malik E. Elbuluk, *"Torque-Ripple Minimization in Switched Reluctance Machines Over a Wide Speed Range"*, Industry Applications, IEEE Transactions on, Volume 34, Issue 5, Sept.-Oct. 1998 Page(s):1105 – 1112.

[4.4] M. Ilic'-Spong, R. Marino, S.Peresada, and D. Taylor, *"Feedback Linearizing Control of a Switched Reluctance motors"*, IEEE Trans. Automat. Contr. Vol. A-32, May 1987, pp. 371-379.

[4.5] L. O. A. P. Henriques, P.J.Costa Branco,L. G. B. Rolim, and W. I. Suemitsu, *"Proposition of an offline learning current modulation for torque-ripple reduction in switched reluctance motors: design and experimental evaluation"*, IEEE Trans. On Industry Electronics, Vol. 49, No. 3, 2002, p. 665-676.

[4.6] Iqbal Husain, M. Ehsani *"Torque Ripple Minimization in Switched Reluctance Motor Drives by PWM Current Control"*, Power Electronics, IEEE Transactions on, Volume 11, Issue 1, Jan. 1996 Page(s):83 – 88.

[4.7] Liang wen Gi, Jing ping Liang, *"New speed control strategy for Switched Reluctance Motors"* PhD Thesis, Zhe Jiang University, China, 2003.

[4.8] D. S. Reay, T. C. Green, and B.W.Williams, *"Neural networks used for torque ripple minimization from a switched reluctance motor,"* in Proc. EPE'93, vol. 6, 1993, pp. 1–6.

[4.9] J. G. O'Donovan J, P. J. Roche, R. C. Kavanagh, M. G. Egan, and J. M. D. Murphy, *"Neural network based torque ripple minimization in a switched reluctance motor,"* in Conf. Rec. IEEE-IAS Annual Meeting, 1994, pp. 1226–1231.

[4.10] S. Mir, M. Elbuluk, and I. Husain, *"Torque ripple minimization in switched reluctance motors using adaptive fuzzy control"* Industry Applications, IEEE Transactions on, Volume 35, Issue 2, March-April 1999 Page(s):461 – 468.

[4.11] Steven E.Schulz and Khwaja M.Rahman, *"High-Performance Digital PI Current Regulator for EV Switched Reluctance Motor Drives"*, Industry Applications, IEEE Transactions on, Volume 39, Issue 4, July-Aug. 2003 Page(s):1118 – 1126.

[4.12] Khwaja M.Rahman and Steven E.Schulz, *"High Performance Fully Digital Switched Reluctance Motor Controller for Vehicle Propulsion"*, Industry Applications, IEEE Transactions on, Volume 38, Issue 4, July-Aug. 2002 Page(s):1062 – 1071.

[4.13] Burton B, Harley RG, Rodgerson JL, Diana G, *"Implementation of a Neural Network to Adaptively Identify and Control VSI Fed Induction Motor Stator Currents"*, IEEE Transactions on Industry Applications, Vol.34, No 3, May/Jun 1998, pp. 580-588.

[5.1] MICROMASTER 440 Operating Instructions, Siemens Corporation, 10/03.

[5.2] TMS320C2000DSP Platform Code Composer Studio DSK v2.12 IDE, TEXAS INSTRUMENTS and Digital Spectrum Incorporated, 09/16/02.

[5.3] VisSim/Embedded Controls Developer 5.0 for TI C2000 manual, 2005.

[5.4] James Ireland, *"Embedded DSP Interface and software for rapid prototyping of Advanced Real time Electric Motor and Power Control Systems"*, Draft MSc Eng Thesis, University of KwaZulu-Natal, South Africa, 2006.

[5.5] PR 30 Current Probe, Max current 20A RMS, LEM, HEME.

[5.6] Agilent storage oscilloscope, 54622A User's Guide.

[5.7] Instruction Manual for Magtrol TorqueMaster TM 200, Janyary, 1997.

[5.8] Private email correspondence with Pete Darnell, at Visual Solutions Inc. June 27, 2005.

[5.9] Private email correspondence with Pete Darnell, at Visual Solutions Inc. Aug, 18, 2005.

[Ref D.1] Private email correspondence with Pete Darnell, at Visual Solutions Inc. Dec, 30-31, 2004.